UNIMORE
UNIVERSITÀ DEGLI STUDI DI
MODENA E REGGIO EMILIA

DOCTORATE SCHOOL
INDUSTRIAL INNOVATION ENGINEERING
XXXVII CYCLE

THERMOECONOMIC OPTIMIZATION OF PLATE-FIN HEAT EXCHANGERS

Scientific Tutor:
Prof. Ing. Diego Angeli

Candidate:
Luigi Calò

School Dean:
Prof. Ing. Franco Zambonelli

UNIVERSITY OF MODENA AND REGGIO EMILIA
ACADEMIC YEAR 2023/2024

Abstract

This thesis represents the final document of an Industrial PhD project, born out of a broader collaboration between VEMA industries S.r.l. and the Department of Engineering Sciences and Methods (DISMI) at UNIMORE University. The collaboration, started in 2017, has the aim of developing numerical methodologies and computational tools for the study of VEMA's core product, i.e. plate-fin heat exchangers.

Separated cross-flow heat exchangers are widely used devices for transferring thermal energy between two or more fluids and are an essential element in nearly all industrial sectors, including power generation, electronics, aerospace, automotive, petroleum, cryogenics, and chemical engineering. Plate-fin heat exchangers (PFHEs) offer high compactness and heat transfer efficiency, yielding savings in both material and space. For these devices, it has been widely demonstrated that the secondary heat exchange surfaces (commonly referred to as "fins") significantly influence their performance.

The European market for plate-fin heat exchangers has reached a high level of competition amongst various manufacturers and the market today only accepts sales prices that are based on manufacturing costs as applicable in Asia. For these reasons, design and production costs are central to any commercial negotiation. Yet few validated models in the literature rigorously analyze production costs, which are often treated as proprietary know-how.

In this context, an accurate computational model for the thermal-hydraulic characterization of plate-fin heat exchangers was developed and validated, with the aim of creating a virtual infrastructure for design and verification purposes (Virtual Wind Tunnel Model, VWTM), in order to reduce testing and prototyping costs. The VWTM was then complemented with a computational model capable of predicting with notable accuracy the

total production cost of a plate-fin heat exchanger, as the sum of the material, time and energy costs, as functions of design requirements and geometric parameters.

After validating the calculation tool with experimental data provided by the company, a multi-objective optimization was implemented to determine the parameters which optimize heat exchange, pressure drop, and production costs for a given design configuration. Since classical analytical methods are often limited for such problems, a stochastic optimization method using genetic algorithms was employed.

The optimization results are of considerable interest both from a scientific point of view for understanding the influence of the design parameters on the performance of the exchanger, and from an industrial point of view for the reduction of production and sales costs, thus representing a competitive advantage for the manufacturing company in the marketing phase of these components.

Contents

Chapter 1

Introduction

The current global industrial scenario is characterised by a high level of uncertainty and structural transformation, driven by geopolitical instability, regional conflicts, recurring energy crises and profound changes in global supply chains. Over the last decade, fluctuations in energy prices, disruptions in raw material availability, and increasing regulatory pressure have significantly affected industrial competitiveness, particularly for energy-intensive manufacturing sectors.

At the international level, energy efficiency and decarbonisation have become central topics in major political and technical forums, such as the United Nations Climate Change Conferences (COP), the World Energy Congress, and various European technology platforms dedicated to sustainable energy systems. The Paris Agreement and subsequent international commitments have established clear targets for greenhouse gas emission reduction, pushing governments and industries toward the adoption of more efficient and sustainable technologies.

In Europe, these objectives have been translated into binding legislative frameworks, such as the European Green Deal and the Fit for 55 package, which aim at reducing emissions by at least 55% by 2030 and achieving climate neutrality by 2050. In parallel, increasingly stringent emission regulations have been introduced for both road and non-road machinery. Standards such as Euro VI and Stage V impose severe limits on nitrogen oxides and particulate matter, forcing manufacturers to redesign engines, after-treatment systems and auxiliaries, including cooling systems.

In recent years, the European industrial landscape has been increasingly affected by a phenomenon commonly referred to as deindustrialisation, namely the progressive reduction of manufacturing activities in terms of both gross domestic product contribution and

employment share. This structural shift has been driven by multiple concurring factors, including intensified global competition, rising production costs and strategic vulnerabilities exposed by recent global crises. In particular, the combined pressure exerted by large-scale industrial systems in Asia, primarily China, and by the increasingly attractive incentive frameworks introduced in the United States has significantly challenged the competitiveness of European manufacturing.

The COVID-19 pandemic and subsequent geopolitical tensions have further highlighted the fragility of global supply chains, and the strong dependency of European industries on external suppliers for critical components and raw materials, such as semiconductors, batteries, and strategic metals. These events have raised growing concerns among policymakers regarding the long-term resilience and technological sovereignty of the European industrial system, especially in sectors that are expected to play a key role in future energy and defence scenarios.

Among the structural drivers of European deindustrialisation, energy costs represent one of the most critical elements, particularly for energy-intensive industries. Following the geopolitical instability associated with the conflict in Ukraine, Europe has experienced a sharp increase in electricity and gas prices, with significant repercussions on industrial production costs. This effect has been especially pronounced in countries with a strong manufacturing base, such as Germany, where several industrial sectors have recorded a sustained decline in output since the late 2010s.

Quantitative assessments by the International Energy Agency indicate that average industrial electricity prices in the European Union during the period 2022–2024 have been approximately two to three times higher than those observed in the United States, with even larger disparities for natural gas prices [1]. Such differences have had a direct impact on the cost structure of energy-intensive manufacturing sectors, including machinery, capital equipment and heavy industrial systems.

According to data published by the European Commission, manufacturing currently accounts for approximately 14–15% of the total gross value added in the European Union, a significant reduction compared to values exceeding 20% in the early 2000s. In response to this trend, the European Commission has explicitly stated the objective of increasing the share of manufacturing within the EU economy toward 20%, as part of its industrial and strategic autonomy policies [2].

At the same time, European manufacturers operate in an extremely competitive global market dominated by Asian producers, particularly from China and, more recently, India. China currently controls a substantial portion of the global aluminium supply chain and hosts large industrial clusters dedicated to the production of aluminium plate-fin heat exchangers, especially in the Jiangsu province and the Wuxi area. Sustained investments

in manufacturing technologies, combined with lower labour and energy costs, have enabled Chinese producers to achieve high levels of technological maturity and economies of scale.

Recent industrial analyses suggest that a large fraction of aluminium-based radiators and compact heat exchangers employed in automotive, industrial, and power generation applications are currently manufactured outside the European Union, predominantly in Asia. While this globalised production structure has led to cost reductions, it has also increased Europe's exposure to supply chain disruptions and strategic dependencies, reinforcing the need for high-value engineering and advanced design capabilities within European industry.

In response to these challenges, the European Union has promoted a series of policy initiatives aimed at fostering reindustrialisation and strengthening strategic industrial sectors. Programmes such as the European Green Deal Industrial Plan and the Clean Industrial Deal explicitly target clean technologies, energy systems and defence-related manufacturing, while attempting to reconcile decarbonisation objectives with industrial competitiveness.

Within the current global context, increasing attention is devoted to energy efficiency not only at the system level, but also at the level of individual components of industrial plants and machines. This trend is driven by a combination of economic, regulatory, and environmental factors, including increasingly stringent emission limits and ambitious decarbonisation targets set at the European level for the coming decades. In this framework, optimization is no longer limited to performance enhancement, but also encompasses cost reduction and the minimisation of material and energy waste throughout the product lifecycle.

From an industrial perspective, virtually all components of energy systems and industrial machinery are now subject to optimization processes, including valves, pumps, electric motors, and thermal management systems. In highly competitive markets characterised by strong price pressure from Asian manufacturers, the lack of systematic optimization in terms of energy efficiency and production cost often results in a significant loss of competitiveness, ultimately leading to the exclusion of European products from global markets.

Heat exchangers represent a strategic component in this scenario. They are ubiquitous in energy production systems, industrial machinery, and transportation applications, where they enable the controlled transfer of thermal energy between fluids at different temperatures. As extensively discussed in classical heat transfer textbooks, heat exchangers play a fundamental role in determining the overall energetic and exergetic performance of thermal systems [3,4]. A well-designed heat exchanger can significantly

improve system efficiency by reducing irreversibilities, lowering temperature gradients, and minimising entropy generation, while a poorly designed one may become a dominant source of losses.

In thermodynamic terms, the impact of heat exchangers extends beyond energy efficiency alone. The exergetic efficiency of an energy system, which accounts for the quality and usability of energy flows, is strongly influenced by the effectiveness and pressure losses of its heat exchangers. Consequently, the optimization of heat exchanger design directly contributes to improving both the energetic and exergetic performance of industrial plants, a requirement that is increasingly relevant under current energy cost and sustainability constraints [3].

In the vast majority of vehicular and industrial applications, including both electric and internal combustion engine systems, thermal control is achieved through the use of radiators, which are compact cross-flow heat exchangers cooled by forced air convection generated by axial or centrifugal fans. Several heat exchanger technologies are currently adopted in industrial practice, such as tube-and-fin heat exchangers, plate-fin heat exchangers, brazed plate heat exchangers, and finned-tube exchangers. These solutions differ in terms of thermal performance, pressure losses, mechanical robustness, manufacturability and cost, and are realised using different materials, including copper–brass alloys and aluminium.

Among these technologies, compact heat exchangers have gained increasing relevance due to their high surface-area-to-volume ratio, which allows for high heat transfer rates within limited space and weight constraints. As highlighted in the literature, the selection and optimization of the appropriate heat exchanger technology and geometry represent a critical design decision, with direct implications on system efficiency, production cost, and overall competitiveness of industrial products [4].

1.1. Plate-fin heat exchangers

Plate-fin heat exchangers (PFHEs), also known in industrial practice as bar-and-plate radiators, represent one of the most widely adopted solutions for compact heat exchange applications. PFHEs are characterised by a modular construction obtained through the stacking of aluminium cladding plates, side bars, and finned sheets, which are subsequently joined by controlled-atmosphere or vacuum brazing. This architecture provides high mechanical robustness, resistance to pressure cycling and vibrations, and remarkable flexibility in terms of geometric configuration [5].

The loose, as-manufactured constituent elements of a plate–fin heat exchanger (PFHE) radiator prior to core build-up are illustrated in Fig. 1.1. The figure depicts the individual components before assembly; these parts are subsequently stacked in a prescribed

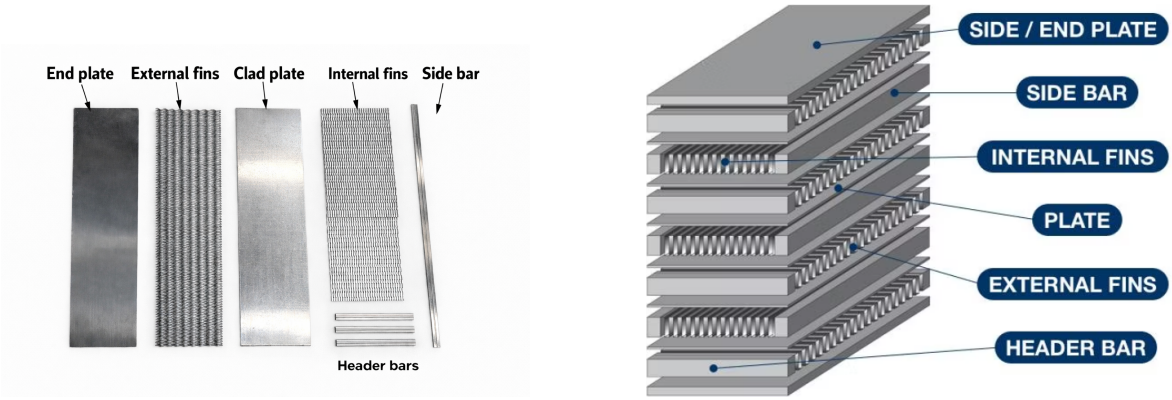

(a) **(b)**

Figure 1.1. Plate–fin heat exchanger (PFHE) structure: (a) PFHE core components prior to assembly (photograph courtesy of VEMA Industries S.r.l.); (b) assembled PFHE core.

(a) **(b)** **(c)**

Figure 1.2. Examples of PFHE radiators employed in industrial applications: (a) water–oil radiator for a telescopic handler, (b) electrically ventilated oil cooler for earth-moving machinery, and (c) combined water radiator and intercooler for industrial drilling equipment. Pictures provided by VEMA industries S.r.l.

sequence and joined by brazing to form a monolithic exchanger core. This assembly process represents a fundamental aspect of PFHE design, as it directly influences both the thermo-fluid-dynamic behaviour and the manufacturing cost structure of the exchanger.

PFHE radiators are commonly used in a wide range of sectors, including industrial machinery, agricultural equipment, and power generation systems. Typical examples of industrial applications are shown in Fig. 1.2, where PFHE radiators are employed for cooling water, oil, and charge air in harsh operating environments.

(a) (b) (c) (d)

Figure 1.3. PFHE radiators for power generation applications: (a) cubic water radiator for a 1000 kVA emergency genset, (b) modular vertically stacked electrically ventilated radiator for a 2 MW genset, (c) mechanically driven water radiator with integrated intercooler for a 1.5 MW generator, and (d) electrically ventilated water radiator equipped with inverter-controlled fans. Pictures provided by VEMA industries S.r.l.

In the power generation sector, PFHE radiators are extensively adopted for cooling large internal combustion engines used in stationary generator sets, often operating under continuous or emergency conditions. Figure 1.3 shows representative PFHE solutions developed for power generation systems, where high thermal loads, large frontal areas, and weight constraints play a crucial role in the design process.

Agricultural machinery represents another relevant application field, where PFHE radiators must operate in dusty environments and are often subject to clogging phenomena, as shown in Fig. 1.4. In these applications, robustness and resistance to fouling are often prioritised over purely thermal performance.

From a thermo-fluid-dynamic standpoint, PFHE radiators are typically characterised in terms of exchanged heat transfer rate, air-side and fluid-side pressure losses. The heat exchange process is dominated by forced convection on both sides, with air-side performance often representing the limiting factor due to relatively low heat transfer coefficients and fan power constraints [5]. As widely discussed in classical heat transfer textbooks, the dominance of the air-side thermal resistance is a common feature of compact heat exchangers operating with gaseous fluids and it strongly influences the overall thermal effectiveness of the device [3, 4].

At the global heat exchanger level, the thermal behaviour of PFHEs is commonly modelled through dimensionless parameters such as the Nusselt number, which relates the convective heat transfer coefficient to the characteristic length scale and thermal conductivity of the fluid. The overall heat transfer rate can be described using lumped-parameter approaches, where the convective heat transfer coefficients on both sides, the

Figure 1.4. PFHE radiator employed in agricultural machinery, where resistance to fouling and ease of cleaning represent key design requirements. Picture provided by VEMA industries S.r.l.

conductive resistance of the metal walls, and the fin efficiency are combined into an equivalent thermal resistance network. These modelling strategies provide a practical framework for predicting the thermal performance of compact heat exchangers under forced convection conditions [3,4].

At the fin scale, performance is commonly described using the Fanning friction factor and the Colburn j-factor. The friction factor quantifies the flow resistance induced by the fin geometry, while the Colburn factor provides a dimensionless measure of convective heat transfer by relating the Stanton number to the Prandtl number. These parameters enable the comparison of different fin geometries under varying operating conditions, and form the basis of most reduced-order PFHE models [6,7]. Their widespread adoption stems from the need to decouple geometric effects from fluid properties and operating conditions, enabling scalable and transferable design correlations.

The main fin geometries adopted in industrial PFHEs, together with the modular construction of the heat exchanger core, are illustrated in Fig. 1.5. At the core level, the global pressure losses of the heat exchanger result from the cumulative contribution of individual fin passages, manifolds and flow maldistribution effects, and are typically evaluated through empirical or semi-empirical correlations expressed in terms of pressure loss coefficients or equivalent friction factors.

Among the various fin geometries available, offset-strip fins and wavy fins are particularly relevant for industrial applications and constitute the focus of this work. Offset-strip fins enhance heat transfer by periodically interrupting the thermal boundary layer, promoting flow reattachment and vortex shedding, which lead to increased convective heat

transfer coefficients [7]. This enhancement mechanism, however, is generally accompanied by an increase in pressure losses due to the repeated acceleration and deceleration of the flow.

Wavy fins, on the other hand, belong to the class of so-called augmented surfaces, whose primary objective is to enhance heat transfer by increasing the effective heat transfer area and by inducing secondary flow structures. The sinusoidal profile of wavy fins generates streamwise vortices and flow curvature effects, which improve fluid mixing near the wall and increase the local convective heat transfer coefficient. Compared to plain fins, the augmented surface provided by wavy fins leads to improved thermal performance, often with a more favourable trade-off between heat transfer enhancement and pressure losses. These mechanisms are fully consistent with the fundamental principles of forced convection heat transfer and surface augmentation discussed in classical heat transfer literature [3, 4].

Over the years, extensive experimental and analytical investigations have been carried out on PFHEs and extended surfaces. Experimental datasets were provided by Kays and London in their classical work on compact heat exchangers [5], which still represents a cornerstone for PFHE design. Subsequent studies by Manglik and Bergles, as well as by Joshi and Webb, introduced widely used correlations for offset-strip fins [6, 7]. More recently, numerical approaches based on CFD have enabled detailed analysis of fin-scale phenomena. In this context, the works by Grespan et al. represent a significant advancement, addressing limitations of previous studies through rigorous geometric definitions and extensive experimental validation based on industrial test campaigns carried out in collaboration with VEMA Industries [9].

1.2. Optimization of PFHEs

1.2.1. Optimization theory and industrial design workflows

In engineering practice, optimization can be broadly defined as the systematic process of identifying design solutions that maximise or minimise one or more objective functions while satisfying a set of physical, technological, and operational constraints. In its classical formulation, optimization relies on deterministic and gradient-based methods, which assume smooth, continuous and differentiable objective functions. These methods are extensively discussed in foundational references on numerical optimization [10], and they are highly effective when such assumptions are fulfilled.

From a methodological standpoint, a key distinction can be made between deterministic and stochastic optimization algorithms. Deterministic methods, including gradient-based approaches, follow a predefined search direction and produce the same solution when starting from identical initial conditions. While computationally efficient, their

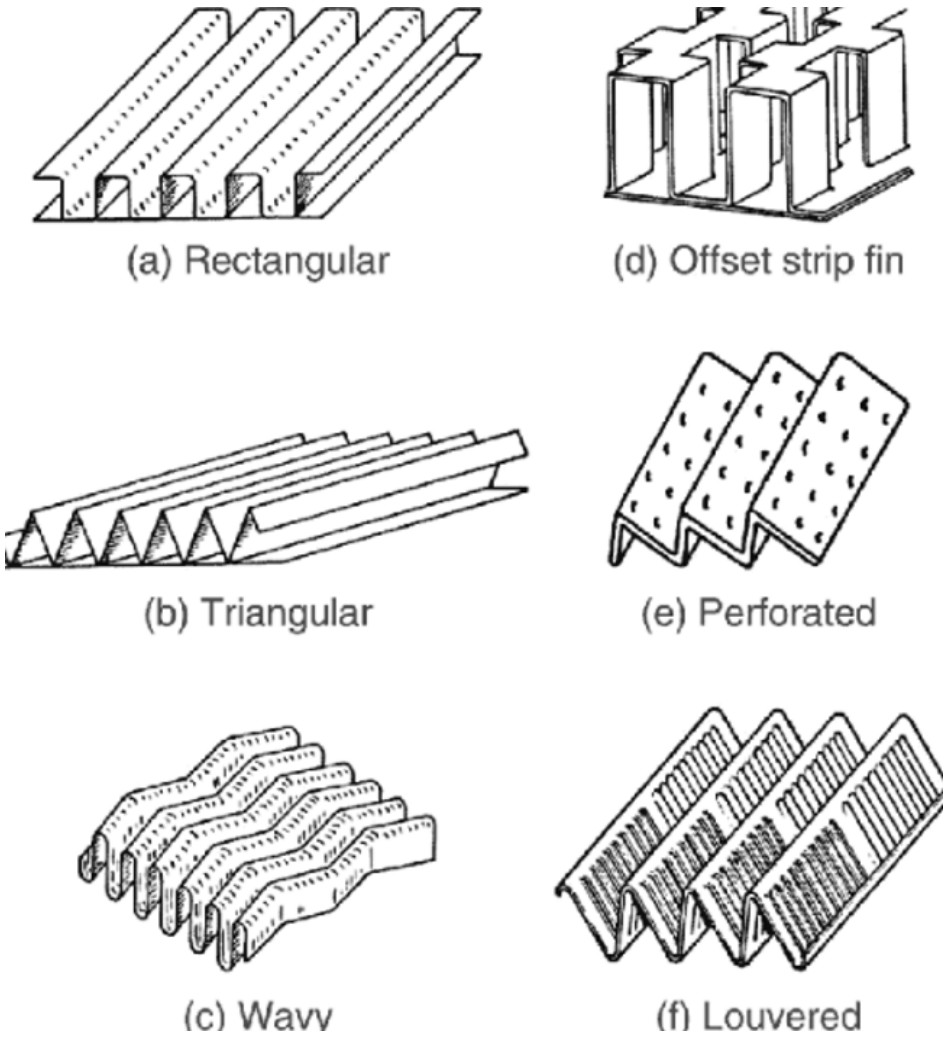

Figure 1.5. Examples of plate-fin surface geometries used in compact heat exchangers: (a) plain rectangular, (b) plain triangular, (c) wavy, (d) offset-strip (OSF), (e) perforated, and (f) louvered fins (adapted from [8]).

performance strongly depends on problem smoothness and convexity, and they may converge toward local optima when applied to complex design spaces.

Stochastic optimization methods, on the other hand, incorporate randomness in the search process and explore the design space through probabilistic sampling. As a result, they are less sensitive to local minima and better suited for highly nonlinear, non-convex, and multi-modal problems. Although stochastic methods generally require a higher number of function evaluations, their robustness and global search capability make them particularly attractive for industrial optimization problems involving complex geometries, mixed continuous and discrete variables, and conflicting objectives [11].

In an industrial context, optimization goes beyond mathematical optimality and must explicitly account for manufacturability, cost, robustness, and compliance with customer and regulatory constraints. Effective optimization in mechanical engineering requires

the integration of theoretical methods with engineering judgement and technological constraints [12]. Consequently, optimization is typically embedded within a structured design workflow rather than treated as an isolated numerical exercise.

A representative industrial optimization workflow includes:

- **Problem identification and modelling:** definition of the design problem through the identification of the system boundaries, design variables, constraints, and objective functions to be optimized. This phase includes the physical modelling of the system and the selection of appropriate performance indicators that accurately represent industrial requirements.

- **Experimental setup** construction of a physical or numerical experiment, either through laboratory testing or computational models, aimed at evaluating the objective functions as a function of the input parameters. In this phase, high-fidelity simulations or experimental campaigns are used to generate reliable datasets describing the system behaviour.

- **Design of Experiments (DOE):** systematic exploration of the design space aimed at identifying dominant variables, parameter interactions, and feasible regions of operation while limiting the total number of experiments or simulations required.

- **Response Surface Modelling (RSM):** development of surrogate or meta-models capable of approximating the system response, enabling a significant reduction of computational cost during subsequent optimization phases.

- **Optimization:** application of numerical optimization techniques aimed at identifying optimal solutions within the defined design space. Optimization methods may be deterministic, based on mathematical analysis and gradient information, or stochastic. While deterministic approaches are efficient for smooth and well-conditioned problems, stochastic optimization methods are generally more suitable for complex industrial systems and multi-objective problems, as they are less sensitive to local optima and can effectively handle nonlinearities, non-convexity, and conflicting objectives.

- **Robust Design Analysis (RDA):** evaluation of the sensitivity of optimal solutions to uncertainties in operating conditions, manufacturing tolerances, and model parameters, with the aim of identifying solutions that are not only optimal but also robust and reliable in real operating environments.

These methodologies are particularly relevant for thermal systems, where small geometric variations may lead to significant changes in heat transfer and pressure losses, and where experimental testing is costly and time-consuming.

1.3. Aim and Scope

Within the industrial, regulatory, and technological context outlined in the previous sections, this PhD work was developed in the framework of an industrial collaboration between VEMA Industries S.r.l., an Italian manufacturer of aluminium plate-fin heat exchangers, and the Department of Sciences and Methods for Engineering (DISMI) of the University of Modena and Reggio Emilia. The collaboration originated from an industrial need, namely the development of predictive, physically consistent, and computationally efficient tools to support the design and optimization of plate-fin heat exchanger (PFHE) radiators under increasingly stringent performance, cost, and time-to-market constraints.

In current industrial practice, the design of PFHE radiators is still largely based on extensive experimental wind tunnel testing campaigns. A heat exchanger is typically characterised by varying internal and external mass flow rates according to predefined test matrices, followed by the measurement of exchanged heat transfer rate and pressure losses on both the fluid and air sides. While this approach ensures high reliability, it is also extremely time-consuming and costly, especially when multiple geometrical variants, fin configurations, and working fluids must be analysed. This limitation represents a critical bottleneck for industrial manufacturers operating in highly competitive markets.

In this context, the initial phase of the collaboration focused on the detailed thermo-fluid-dynamic modelling of the fundamental heat transfer geometries employed in PFHE radiators. Internal and external fin configurations, representing the smallest repeating unit of the heat exchanger core, were analysed through high-fidelity Computational Fluid Dynamics (CFD) simulations. This fin-scale modelling activity enabled the description of heat transfer and pressure loss mechanisms based exclusively on physical principles, deliberately avoiding the introduction of empirical fitting parameters.

Building upon the fin-scale analysis, a multiscale modelling strategy was subsequently developed to describe the PFHE radiator at the global level. The complete heat exchanger, including the core and the inlet and outlet manifolds, was modelled through a reduced-order approach based on the ε–NTU method. This formulation enabled a direct and physically consistent coupling between local fin-scale behaviour and the overall thermal performance of the radiator.

A distinctive aspect of this work is the availability of an extensive set of thermal tests provided by the industrial partner, which were used to validate the numerical framework and enabled the development of a virtual wind tunnel reproducing standard industrial characterisation procedures, thereby enabling the evaluation of thermal performance and pressure losses over wide operating ranges with a drastic reduction in experimental testing effort, development time and associated R&D costs.

Following the thermo–fluid-dynamic validation phase, the core of this industrial PhD

activity was devoted to the modelling and optimization of PFHE manufacturing costs. A physically consistent cost function was developed to quantify the production cost of a plate-fin heat exchanger by accounting for material mass, energy consumption of manufacturing machinery, and production time. This approach allows production cost to be treated as a primary optimization objective rather than as a secondary constraint, closely reflecting industrial design practices. Modelling cost in this physically grounded and process-oriented manner is particularly relevant, as the literature has devoted limited attention to PFHE manufacturing cost formulations, with most studies focusing on operational or energy-related costs associated with fluid pumping and heat transfer performance.

The ranges of variation of the design variables were selected to be as general as possible while remaining fully consistent with the validity domain of the CFD-based thermo–fluid-dynamic models developed in the previous thermal modelling and characterization. This ensures the physical reliability of the optimization results and their direct applicability in an industrial context, in line with recent physics-based methodologies proposed in the literature, including the work of Grespan et al. [9].

The optimization framework addresses the industrial design of PFHEs equipped with offset-strip and wavy fins on both the internal fluid side and the external air side, considering the working fluids most commonly encountered in practice, such as water–glycol mixtures, lubricating oil, and compressed air in intercooler applications. This choice reflects typical operating conditions across industrial, automotive, and power generation sectors, enabling the optimization procedure for different application domains within a single consistent modelling framework without resorting to case-specific empirical tuning.

The PFHE is fully parameterised by fin-level geometric variables, such as fin pitch, fin height, and offset length for offset-strip fins, as well as fin pitch, fin height, wavelength and amplitude for wavy fins. In addition, core-level parameters including the number of tubes, core thickness, and internal and external mass flow rates are considered as design variables.

The optimization problem is formulated as a multi-objective optimization task involving three main, competing objectives. The first objective concerns the minimization of the radiator production cost, accounting for both material usage and manufacturing complexity. The second objective is the maximization of the exchanged heat transfer rate, representing the heat transfer capability of the PFHE core. The third objective addresses the minimization of air-side pressure losses, which are directly linked to fan power consumption and, consequently, to the overall energy efficiency of the system.

Internal pressure losses are imposed as constraints rather than objectives. This mod-

elling choice closely reflects realistic industrial design conditions, where allowable pressure drops and frontal area are typically specified by the customer or OEM at the beginning of the design process. Within these constraints, the thermal designer is required to identify fin configurations and core architectures that maximise thermal performance while minimising production cost, in order to remain commercially competitive.

Due to the highly nonlinear nature of the problem, the presence of multiple conflicting objectives, and the large number of design variables, the optimization is carried out using a genetic algorithm, specifically the Non-dominated Sorting Genetic Algorithm II (NSGA–II) [13]. Genetic algorithms, originally introduced by Holland [14] and later formalised for engineering applications by Goldberg [15], are particularly well suited to this class of industrial problems, as they enable a global exploration of complex, non-convex design spaces while naturally handling multiple objectives.

From a methodological standpoint, the overall research activity can be summarised through the following structured workflow:

i. CFD modelling of single internal and external fin geometries, representing the elementary repeating unit of the PFHE core;

ii. development of a global heat exchanger model based on the ε–NTU method;

iii. systematic validation of numerical results against full-scale experimental tests provided by the industrial partner;

iv. implementation of an industrial cost function accounting for material mass, energy consumption, and production time;

v. Design of Experiments (DOE) analysis to explore the design space and identify dominant parameters;

vi. statistical sensitivity analysis based on the Student's t-test to quantify the influence of design variables;

vii. application of a multi-objective genetic algorithm (NSGA–II) for the heat transfer rate of PFHE configurations;

viii. sensitivity analysis of optimization parameters, including population size, number of generations, crossover and mutation probabilities;

ix. adoption of a multi-criteria decision-making technique based on the TOPSIS method, to guide the designer toward a final optimal solution rather than a set of non-dominated alternatives.

The outcome of the optimization process is a three-dimensional Pareto front representing the trade-offs between production cost, heat transfer rate, and air-side pressure losses. The obtained fronts are coherent with the underlying physics of forced-convection PFHE operation and consistent with trends reported in the literature on compact heat exchangers. From both a scientific and industrial perspective, these results provide a decision-support tool enabling informed, physics-based design decisions and offering a competitive advantage to the manufacturer in a challenging global market.

1.4. Structure and organisation

This thesis is organised as follows.

Chapter 2 provides a critical and chronologically structured review of the literature on compact heat exchangers, with particular focus on offset-strip and wavy fins in plate-fin heat exchangers (PFHE). Experimental, analytical, and numerical approaches are examined to highlight the evolution of research methodologies and to identify the main limitations of existing studies. The chapter also reviews optimization strategies for PFHE radiators, with emphasis on genetic algorithms and multi-objective methods addressing the coupled effects of thermal performance, pressure losses, and cost.

Chapter 3 introduces the physical modelling framework adopted for PFHEs. The thermo–fluid dynamic description, from the fin-scale representation to the global heat exchanger model based on the ε–NTU method, is presented by drawing upon established formulations available in the literature, particularly those developed by Grespan et al. The main original contribution of this chapter lies in the formulation of cost functions for offset-strip fins, wavy fins, and the complete PFHE radiator, which provide the quantitative basis for the subsequent optimization activities.

Chapter 4 presents the methodological framework adopted for the parametric exploration of the design space. After a theoretical introduction to Design of Experiments (DoE) techniques, the optimization problem addressed in this thesis is defined, the DoE implementation is described, and a statistical sensitivity analysis based on the Student's t-test is performed to assess the influence of key design parameters on heat transfer, external pressure losses, and cost.

Chapter 5 presents the core optimization activity of this doctoral work. Following a theoretical overview of genetic optimization algorithms, the optimization workflow developed for the PFHE radiator is illustrated, and the results are presented and critically analysed, with discussion of the resulting Pareto-optimal solutions and their physical and economic implications.

Finally, Chapter 6 summarises the main outcomes of the thesis and outlines the final conclusions and possible directions for future research.

CHAPTER 2

Literature Review on PFHEs

2.1. Introduction

The body of research devoted to plate–fin heat exchangers spans several decades, yet remains highly fragmented. Early experimental investigations provided invaluable reference datasets, but were often confined to air-side operation, restricted geometric ranges, or specific manufacturing constraints. Subsequent analytical and semi-empirical correlations sought to generalise these findings; however, they typically relied on simplified assumptions, piecewise regime definitions, or fixed Prandtl-number scaling exponents. As a consequence, their predictive capability tends to deteriorate when applied beyond the narrow conditions for which they were originally calibrated, particularly in the case of liquid flows or non-conventional fin geometries.

More recent numerical studies based on computational fluid dynamics have significantly advanced the understanding of the underlying transport mechanisms, highlighting the role of unsteady vortex shedding, three-dimensional flow structures, and entrance-region effects. Nonetheless, such investigations are frequently limited to isolated geometries or relatively narrow parametric variations, which complicates the extraction of general and transferable design rules. In parallel, optimization studies employing genetic algorithms and other evolutionary techniques have demonstrated the potential for systematic improvement of PFHE performance. Yet, these approaches often rely on simplified thermo–hydraulic models whose validity may become questionable when applied to complex fin configurations, especially when strong three-dimensionality or high-Prandtl-number fluids are involved.

In this context, a structured and critical literature review becomes essential. Rather than merely cataloguing previous contributions, such a review must clarify the physical

mechanisms identified across different methodological approaches, expose inconsistencies among correlations and modelling assumptions, and highlight the gaps that still limit reliable prediction and optimization. The present chapter is therefore organised as follows. First, the literature on offset-strip fins is examined, with emphasis on experimental evidence, dominant flow physics, and the development of heat-transfer and friction correlations. The discussion then turns to wavy-fin geometries, where curvature-induced secondary flows and transitional phenomena govern thermal–hydraulic behaviour. Finally, the chapter surveys optimization-oriented studies, with particular attention to genetic and evolutionary algorithms applied to PFHE design, analysing their modelling assumptions, objective functions, and the trade-offs identified in previous works. This structure establishes a coherent background against which the present doctoral work is positioned, and developed.

2.2. Offset-strip fins

London and Shah [16] investigated the heat-transfer and friction characteristics of eight offset rectangular plate-fin surfaces, providing one of the earliest systematic datasets for compact geometries. The authors tested aluminum and stainless-steel cores spanning surface-area densities from about 470 to 1700 ft^2/ft^3, illustrating the strong influence of geometry on performance. Their experiments combined steam-to-air steady testing with a single-blow transient method, enabling consistent determination of Colburn j and friction f factors across a broad Reynolds range.

Four nondimensional parameters were shown to govern the behavior: fin-thickness ratio, offset-length ratio, aspect ratio, and extended-surface fraction. Increasing aspect ratio generally raised both j and f, while larger uninterrupted lengths tended to reduce them. Some deviations arose from condensation blockage on the steam side at high airflows, which slightly depressed measured heat-transfer coefficients. The stainless-steel cores exhibited higher friction due to brazing-induced roughness, an effect that became more visible as hydraulic diameter dropped below roughly 0.004 ft.

Comparison with other fin types indicated that offset-strip fins delivered competitive heat-transfer levels but required greater pumping power. One representative surface produced a j value near 0.015 at a Reynolds number of around 1000, while friction factors varied by nearly a factor of two among the tested geometries. The study concluded that optimal designs favored small fin thickness, small offset spacing, and large aspect ratio, although manufacturing constraints often limited these combinations.

Joshi and Webb [7] developed one of the earliest analytical frameworks describing heat transfer and friction characteristics in offset strip–fin surfaces, focusing on the transition between laminar and turbulent wake behavior. Their study relied on detailed flow

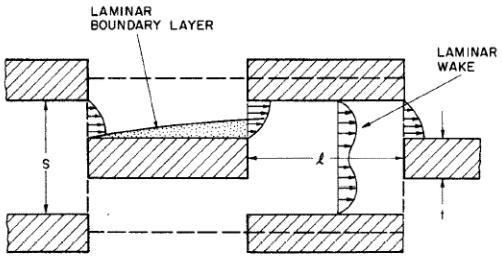

FIG. 3. Laminar flow on the fins and in the wakes.

(a) Laminar boundary-layer development and steady wake regions

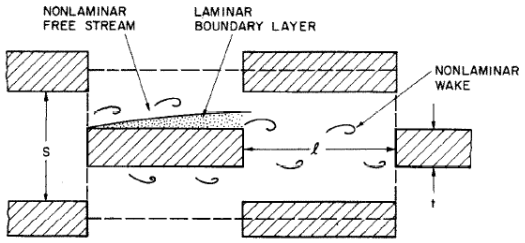

FIG. 4. Laminar flow on the fins and oscillating flow in the wakes.

(b) Laminar boundary layer on fins with oscillatory wake behaviour

Figure 2.1. Schematic representation of flow development in offset-strip fins, illustrating (a) laminar boundary-layer growth and steady wake formation, and (b) the onset of oscillatory flow structures in the wake region at higher Reynolds numbers. Adapted from Joshi and Webb [7].

visualization and a unit–cell formulation that captured boundary–layer redevelopment after each fin interruption. The model treated the fins as periodically restarting surfaces, enabling accurate prediction of Nusselt number and friction factor across a broad Reynolds range.

Using comparisons with scaled geometries, the authors showed that their correlations predicted heat–transfer and pressure–drop data within roughly twenty percent, a notable improvement over earlier flat–plate analogies. One key result was the identification of a wake–induced transition condition, which marked the onset of oscillatory structures affecting both momentum and thermal transport. The analytical formulation incorporated geometric ratios such as fin pitch, fin height, and fin thickness, emphasizing their role in setting hydraulic diameter and flow blockage.

As illustrated in Fig. 2.1, the enhancement mechanism of offset-strip fins is governed by the repeated interruption of the laminar boundary layer and by the characteristics of the wake region developing behind each fin element. At lower Reynolds numbers, the wake remains predominantly laminar, and heat transfer enhancement is mainly associated with boundary-layer restart (Fig. 2.1a). As the Reynolds number increases, oscillatory structures emerge in the wake region (Fig. 2.1b), promoting additional mixing and further increasing convective transport, albeit at the expense of higher pressure losses.

This study provided a physically grounded model that guided later correlation development, particularly in defining the link between boundary–layer interruption and enhanced convective performance. Despite some sensitivity to manufacturing imperfections such as fin burrs, the framework remained influential for compact–heat–exchanger design and continues to serve as a benchmark for evaluating newer numerical and semi–empirical approaches.

Mochizuki et al. [17] investigated the transport phenomena associated with stacks of interrupted parallel-plate surfaces, focusing on offset-strip fins and slotted fins as scale-up representations of compact exchanger passages. Their experiments, conducted in a controlled wind-tunnel environment, explored how periodic surface interruptions promoted boundary-layer separation and vortex shedding, ultimately modifying heat-transfer behavior and friction losses. A set of eighteen cores with systematically varied fin geometries allowed the authors to map performance trends across changes in fin length, slot width, and interruption spacing.

The study showed that offset-strip fins consistently produced stronger enhancement than both plain and slotted fins. At moderate Reynolds numbers, the oscillatory laminar regime generated by repeated separations increased turbulence intensity in the mid-core region, giving rise to what the authors described as a "second laminar enhancement." As Reynolds number increased toward the transitional range, the heat-transfer coefficient rose more sharply, marking the onset of a turbulent-transition mechanism. This behavior was particularly noticeable for geometries with small interruption length, where the frequency of vortex shedding increased.

Slotted fins demonstrated weaker enhancement because perforations reduced available surface area and induced less energetic wake structures. Only at higher Reynolds numbers did their turbulence levels exceed those of the plain-fin reference. The authors also proposed revised correlations for the f and j factors, improving prediction accuracy relative to classical Wieting-type relations.

Zhang et al. [18] developed a detailed computational investigation to clarify the mechanisms responsible for heat–transfer enhancement in inline and staggered parallel–plate fins. The study relied on two–dimensional unsteady Navier–Stokes simulations, allowing the authors to isolate the roles of boundary–layer restart, vortex shedding, and geometrical effects from finite fin thickness. Unlike earlier steady models, the time–dependent framework captured the formation of alternating vortices at both fin edges, which strongly distorted the local thermal field.

The simulations covered Reynolds numbers up to roughly 2.2×10^3, revealing transitions from steady laminar flow to periodic and eventually chaotic shedding. In both fin configurations, vortex structures promoted significant mixing on the fin surfaces and elevated local heat–transfer coefficients, with increases of about 50% near the leading edge compared to steady symmetric solutions. Friction behavior changed as well: form drag became dominant at higher Reynolds numbers, reaching more than two–thirds of total losses in the staggered geometry.

The computational domains and geometric configurations adopted in the numerical study by Zhang et al. are shown in Fig. 2.2, which defines the inline and staggered

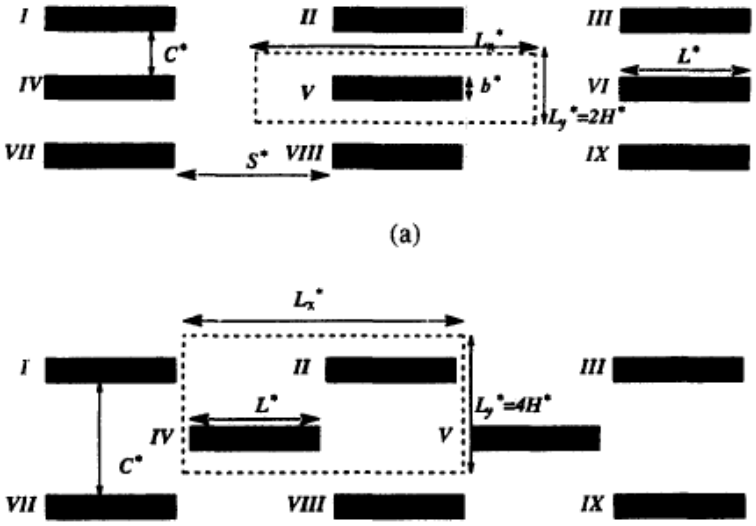

Figure 2.2. Computational domains and geometric configurations adopted for the inline and staggered parallel–plate fin arrangements analysed by Zhang et al., illustrating fin spacing, offset length, and periodicity constraints [18].

parallel–plate fin arrangements and the associated periodicity constraints. The resulting flow behaviour is illustrated in Fig. 2.3, where the transition from steady laminar flow to periodic and chaotic vortex shedding is associated with pronounced temporal oscillations of the global Nusselt number.

Comparisons against continuous parallel–plate theory and prior simplified models showed that boundary–layer restart alone could not explain observed performance. Instead, unsteady vortical transport emerged as the primary mechanism behind global Nusselt number growth, while finite fin thickness introduced additional penalties in pressure drop. The study therefore provided one of the earliest clear demonstrations that accurate prediction of compact-fin performance requires resolving unsteady flow physics rather than relying on classical steady–state assumptions.

Hu and Herold [19], investigated how Prandtl number influences heat-transfer and friction behavior in liquid-cooled offset strip–fin heat exchangers, using seven cold plates tested with water and a low-viscosity oil (PAO). Their experiments covered Prandtl numbers ranging from about 3 to 150, significantly extending the earlier air-based databases of Kays, London, and others. A dedicated liquid loop supplied controlled inlet temperature, while a uniformly heated base plate ensured nearly constant heat flux across the fin array. Surface temperatures were measured with multiple embedded thermocouples, enabling accurate evaluation of local and mean thermal loads.

A numerical two-dimensional conduction model supported interpretation of the data. It revealed that end effects—particularly conduction from heated to unheated regions—distorted local heat flux over entrance lengths of roughly a few centimeters, while thermal spread-

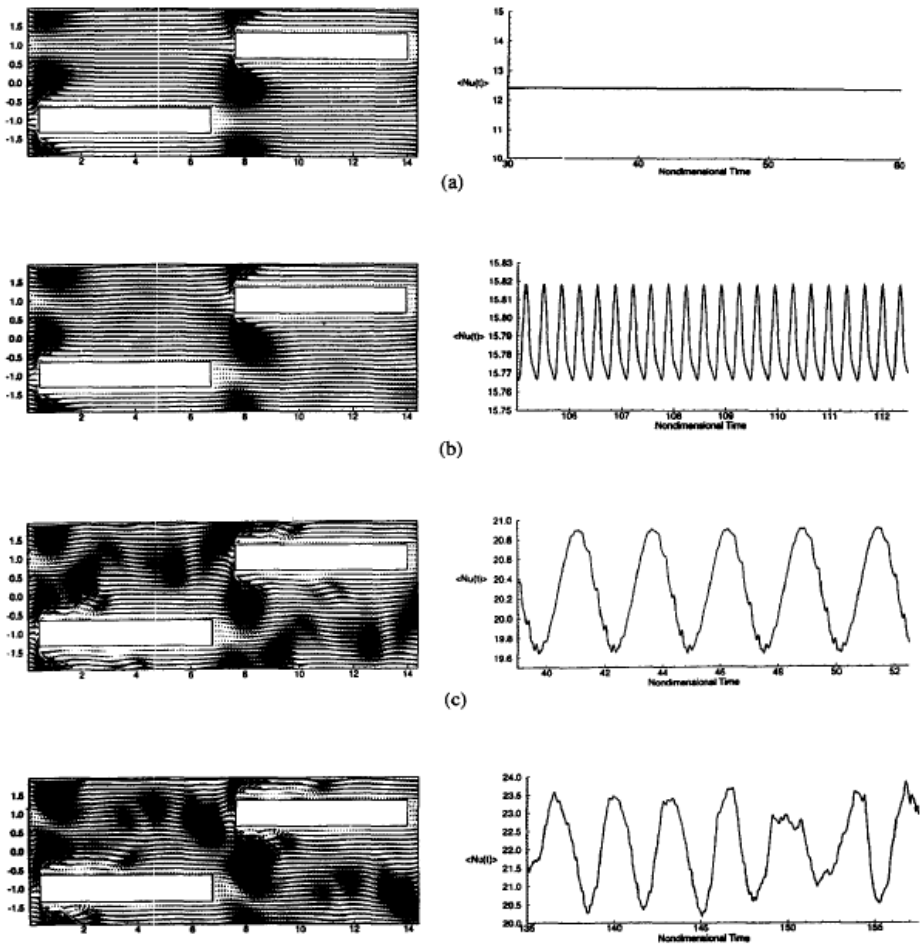

Figure 2.3. Instantaneous velocity fields and corresponding temporal evolution of the global Nusselt number for increasing Reynolds numbers, highlighting the transition from steady laminar flow to periodic and chaotic vortex shedding in parallel–plate fin geometries [18].

ing within the central region remained modest. After accounting for these effects, the authors extracted average heat-transfer coefficients and friction factors using conventional definitions of Nusselt number and Fanning friction factor.

Results showed that Nusselt number increased with Prandtl number, though at a rate lower than $Pr^{1/3}$, causing the Colburn j factor to decrease as Prandtl number rose. Because of this, air-based correlations overpredicted liquid performance, in some cases by nearly a factor of two. Despite lower j values, the actual heat-transfer coefficients for liquids were substantially higher than for air, mainly due to greater thermal conductivity. The friction factor exhibited little dependence on Prandtl number, with deviations attributed mostly to burrs on the manufactured fins.

Overall, the study clarified that Prandtl number strongly affects heat-transfer behavior in offset strip–fin geometries and that liquid-cooled designs require dedicated corre-

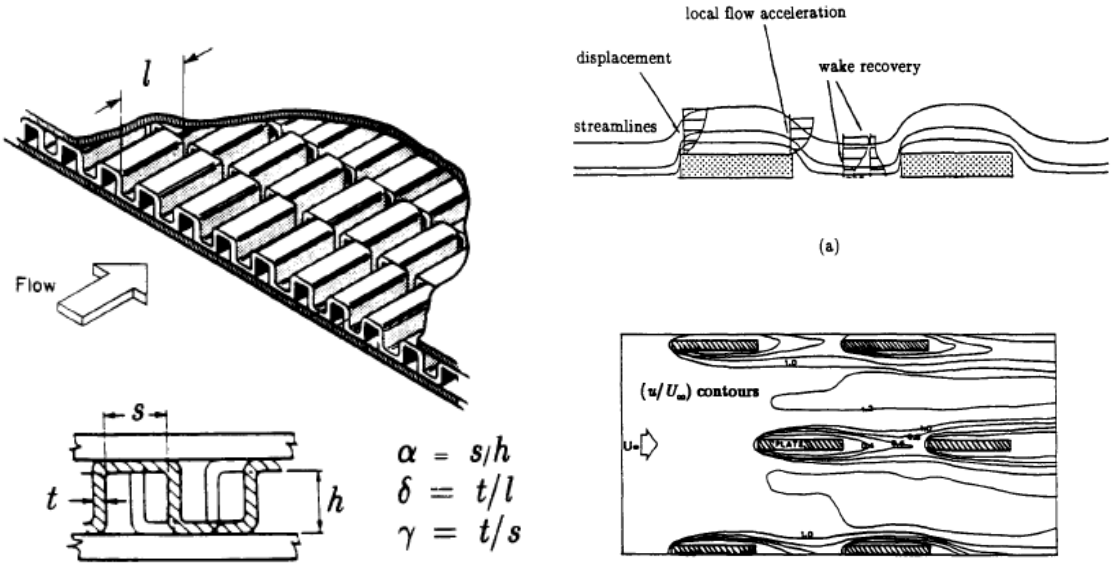

(a) Geometrical configuration of a rectangular offset strip–fin surface and definition of the characteristic dimensions s, h, t, and l, together with the corresponding dimensionless ratios.

(b) Schematic representation of the dominant flow mechanisms within an offset strip–fin array, highlighting boundary–layer disruption, local flow acceleration at fin edges, wake formation, and downstream recovery regions.

Figure 2.4. Geometric description and dominant flow mechanisms in rectangular offset strip–fin surfaces, adapted from Manglik and Bergles [6].

lations rather than extensions of air-based models.

Manglik and Bergles [6], presented one of the most comprehensive reevaluations of heat-transfer and friction behaviour for rectangular offset strip-fin surfaces, building upon several decades of fragmented experimental data. Their motivation centered on the observation that existing correlations often produced discontinuities across the transition from laminar to turbulent flow, and that many earlier models failed to capture the subtle geometric interactions associated with offset fins. To address these issues, the authors compiled a wide-ranging dataset of eighteen geometries, representing different fin pitches, thicknesses, heights, and interruption lengths. This dataset allowed them to examine performance trends with a level of consistency that had been largely missing from the earlier literature.

As illustrated in Fig. 2.4, the offset strip–fin geometry induces repeated boundary–layer disruption, local flow acceleration at fin edges, and wake formation followed by downstream recovery. Variations in fin spacing, thickness, and offset length directly control the frequency and intensity of these mechanisms, thereby explaining the strong geometric sensitivity observed in both the Colburn and friction factors.

The analysis shows that both the Colburn factor and the friction factor decreased

steadily with increasing Reynolds number, reflecting the classical thinning of boundary layers and the increasing dominance of inertial forces. Yet the rates of decay varied strongly with geometry. For example, short offset lengths created more frequent boundary-layer redevelopment, raising thermal performance but also increasing form drag in a rather noticeable way. In contrast, larger fin spacing reduced pressure losses but weakened the mixing processes that normally enhance convective heat transfer. The authors emphasised that these opposing effects required a balanced view of design, since improvements in one metric almost always caused deterioration in the other.

A key contribution of the work was the derivation of unified correlations for both j and f. Instead of splitting the behaviour into separate laminar and turbulent branches, the authors developed composite equations that transitioned smoothly between regimes. These correlations were validated against the full experimental database, achieving agreement typically within about twenty percent. Although this level of accuracy may seem modest by today's numerical standards, it represented a significant improvement over many previous models. The smoothness of the new correlations also provided substantial practical value for computational design tools, which often struggled with artificial kinks in predicted performance curves.

Although the correlations were developed mainly for air with Pr $\approx$ 0.7, the authors compared their predictions with limited data for moderately viscous liquids. They observed that the models performed reasonably well when the Prandtl number did not deviate too far from unity. However, they cautioned that extrapolation to high-Pr fluids should be done carefully, since the physical balance between diffusion and convection changes in ways not captured by the original dataset. This observation later motivated several studies focused explicitly on liquid-cooled offset fins.

DeJong and Jacobi [20]investigated flow and heat-transfer behavior in parallel-plate arrays configured to resemble offset-strip fin passages. Their study combined detailed flow visualization with local and row-by-row mass-transfer measurements based on the naphthalene sublimation technique, enabling unusually fine spatial resolution of convective patterns. The experiments covered laminar, transitional, and shedding-dominated regimes, offering a quite comprehensive view of how boundary-layer development interacts with vortex dynamics.

At lower Reynolds numbers (around $Re \approx 380$), the flow remained steady, forming symmetric recirculating eddies behind each plate. As Re increased, periodic secondary structures appeared, eventually giving rise to large-scale vortex shedding, which became clearly visible near $Re \approx 720$. These shed vortices enhanced mixing and produced a sharp rise in local transport, particularly near $x^* \approx 0.2$ on each plate, where Sherwood numbers reached their peak before declining downstream.

Row-by-row analysis showed that shedding always initiated in the downstream plates and shifted progressively upstream with increasing Reynolds number. Interestingly, the first row never shed vortices from its leading edge, yet the second row often did—an effect attributed to transverse velocity fluctuations generated by the wake of the upstream plate. The authors also compared experimental Sherwood numbers with theoretical predictions for continuous and interrupted plates, finding that at moderate Reynolds numbers both boundary-layer restarting and vortex shedding contributed significantly to performance enhancement.

In conclusion this study provided clear experimental evidence linking vortex formation to enhanced convective behavior, while also documenting the subtle roles of geometry and developing-flow effects. This work remains one of the most precise experimental characterizations of interrupted-plate convective mechanisms, and its insights continue to influence modern fin-surface modeling.

Zhang et al. [21] conducted a detailed numerical study to determine how intrinsic three-dimensionality influences heat transfer and friction losses in a periodic array of parallel plates. While many earlier analyses relied on two-dimensional approximations, the authors showed that such simplifications often miss critical flow structures that strongly affect performance. Their simulations solved the full three-dimensional Navier–Stokes and energy equations with periodic boundary conditions, allowing vortex development along both the streamwise and spanwise directions.

At moderate Reynolds numbers around $Re \approx 2450$, the three-dimensional simulations predicted slightly lower time-averaged Nusselt numbers compared to two-dimensional cases, yet they also produced reduced skin-friction coefficients. This behaviour stemmed from the presence of spanwise vortices which redistributed momentum and weakened the large oscillations typical of strictly two-dimensional shedding. At higher Reynolds numbers near $Re \approx 3500$, differences became more pronounced: the two-dimensional model overpredicted both mean heat transfer and friction factor, leading to unrealistic performance expectations.

The authors demonstrated that accurate prediction of interrupted-plate surfaces requires fully three-dimensional modelling. Two-dimensional approaches, although computationally cheaper, can introduce substantial errors in both heat transfer and friction estimation.

Dong et al. [22] conducted an extensive experimental study on the air-side thermal–hydraulic performance of offset strip-fin surfaces, testing sixteen geometries in a controlled wind-tunnel facility. Their aim was to clarify how variations in fin spacing, fin height, fin thickness, fin length, and flow length influenced heat transfer and pressure drop, since earlier correlations often struggled in the transitional Reynolds region. Exper-

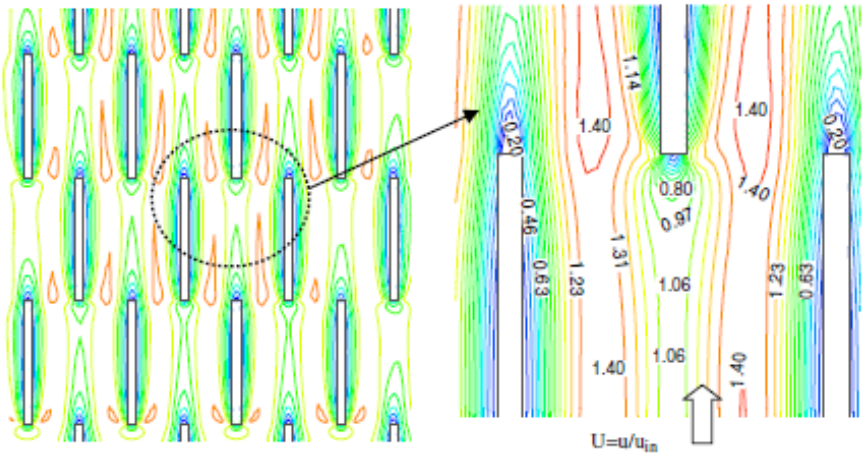

Fig. 6. Velocity contours of air flow in the offset strip fin.

Figure 2.5. Velocity-contour visualisation of air flow in an offset strip–fin array, highlighting local acceleration within fin passages and wake regions downstream of fin trailing edges. Adapted from Dong et al. [22].

iments covered Reynolds numbers from 500 to about 7500, with tube-side water maintained at a fixed flow rate. Temperatures, pressure drop, and frontal air velocity were measured with calibrated sensors, achieving an overall heat-balance uncertainty below roughly three percent.

Results showed clear geometric trends: decreasing fin space or fin height increased both the heat-transfer coefficient and pressure drop where the curves steepened noticeably at higher frontal velocities. Shorter fin lengths produced stronger boundary-layer interruption and more vigorous eddy formation, which enhanced convection but also elevated flow resistance. The authors also visualised air-flow structures through numerical simulations, confirming the presence of alternating eddies and vortices their experiments hinted at.

The resulting flow organisation is qualitatively illustrated in Fig. 2.5, which reports representative velocity-contour maps within an offset strip–fin array. Regions of local acceleration inside the fin passages alternate with low-velocity wake zones downstream of each interruption, providing direct visual support to the interpretation of enhancement mechanisms in terms of boundary-layer disruption, wake interaction, and intensified near-wall mixing.

A major contribution of the work was the development of updated correlations for the Colburn j factor and Fanning friction factor f, fitted through regression analysis of 244 data points. Compared with classical relations such as those of Manglik and Bergles, the new correlations incorporated an additional non-dimensional parameter representing flow-length effects. The updated expressions predicted roughly ninety to ninety-five

percent of the data within ten percent deviation, offering a practical improvement over prior models.

Overall, the study provided a rigorous dataset and refined correlations applicable to a wide range of offset strip-fin geometries, especially configurations with relatively short flow length, which are common in compact vehicular heat exchangers.

Peng et al. [23] developed an experimental and numerical investigation of serrated fins operating in plate–fin heat exchangers at low Reynolds numbers. Their objective was to establish a modelling framework capable of predicting Colburn and friction factors with minimal experimental input. Experiments were performed for air–oil operation over Reynolds numbers below 200, and the resulting heat-transfer and pressure-drop data formed the basis for model validation. The authors implemented a two-step 3D CFD approach: an initial simplified unit cell used to estimate separating-wall temperature, followed by a detailed geometrical model resolving fin passages and local convection.

Results showed that the Colburn factor decreased with increasing Reynolds number, while the friction factor behaved inversely, trends consistent with classical compact-surface behavior. For representative cases, numerical predictions remained within approximately 15% of experimental measurements, though slight offsets appeared due to manufacturing roughness not included in the computational model. Local Nusselt-number distributions exhibited strong entrance effects, with peak values located near mid-channel height where flow acceleration reduced thermal resistance. Increasing the oil flow rate enhanced local and global heat transfer, while pressure drop increased nearly linearly.

The study demonstrated that serrated fins maintain high thermal effectiveness under low-Reynolds operation, and that the proposed CFD methodology provides accurate predictions suitable for design of new geometries. Moreover, comparison with empirical correlations revealed noticeable deviations at low Reynolds numbers, indicating that conventional design formulas may underpredict or misrepresent performance in this regime.

Bhowmik and Lee [24] performed a three-dimensional steady-state CFD analysis to investigate heat-transfer and pressure-drop behaviour in an offset strip-fin heat exchanger operated with liquid media. Their study, motivated by the limitations of air-based correlations for predicting liquid performance, examined Reynolds numbers from 10 to 3500 and compared computed results with classical datasets from Joshi and Webb, Manglik and Bergles, and Hu and Herold. The geometry followed a standard periodic fin module, with fin length, spacing, height, and thickness nondimensionalised into three ratios. Aluminum fins and conjugate heat transfer were included explicitly, an aspect that earlier simplified models often ignored.

Model validation showed deviations of about twenty percent for friction factor and

thirty percent for Colburn factor when compared with experimental data for water, a level considered acceptable by the authors given geometric differences and the presence of manufacturing burrs in reference datasets. Importantly, the friction factor exhibited little sensitivity to Prandtl number, whereas the Colburn factor displayed a strong dependence. For the same Reynolds number, water produced a Colburn factor nearly twice that of air, consistent with the expected scaling $(Pr_w/Pr_a)^{1/3}$.

Using the CFD predictions, the authors proposed updated correlations for f and j across laminar, transitional, and turbulent regimes. These correlations exhibited smooth variation without regime discontinuities, reflecting the continuous behaviour observed in the numerical data. They further explored thermal–hydraulic performance criteria, noting that the JF factor was most suitable for water, while the $j/f^{1/3}$ metric performed best for higher-Prandtl-number oils.

It was demonstrated that air-based models are unsuitable for predicting liquid-flow performance in offset strip fins and provided correlations more appropriate for engineering design of compact exchangers operating with liquids.

Kim and Lee [25] performed a numerical investigation of oscillatory flow and heat-transfer behaviour in offset-strip fins, focusing on how unsteadiness and dimensionality alter the Colburn j and friction f factors. Earlier studies had mainly examined average performance, but this work clarified the local thermoflow mechanisms responsible for pressure-drop and heat-transfer variations. The authors solved the three-dimensional incompressible Navier–Stokes and energy equations, examining both steady and unsteady simulations, and comparing full-sectional, semi-sectional, and simplified two-dimensional domains.

A key observation was that oscillations did not appear in the laminar regime, where steady and unsteady simulations produced nearly identical j and f values. Once the Reynolds number exceeded about 250, periodic vortex shedding emerged, producing a self-sustained oscillatory flow. For a representative geometry, the shedding frequency was around 63 Hz, while the oscillation of surface-averaged Nusselt number occurred at approximately twice that value. These oscillations led to notable differences between steady and unsteady predictions, demonstrating that steady simulations alone could not represent the transition and turbulent regimes.

The study also explored geometric effects, showing that the ratio of fin length to fin thickness controlled the strength and frequency of oscillatory motion. When this ratio was increased from 1 to 4, the Strouhal number stabilised near 0.2; higher values reduced oscillation frequency. To avoid the extremely high computational cost of unsteady simulation, the authors evaluated turbulence models and found that a steady SST k–ω model predicted j and f values within roughly ten to fifteen percent of unsteady results.

Yang et al. [26] performed a comprehensive numerical investigation of offset strip-fin (OSF) surfaces, aiming to establish predictive models that remained accurate across a wide geometric range. Their simulations employed fully three-dimensional CFD with structured meshes containing more than 2.5×10^6 cells, and validation against experimental datasets showed RMS deviations of about 5.5 percent for the Colburn j factor and 4.4 percent for the friction factor. The study demonstrated that conventional geometric ratios, such as fin-thickness-to-height or fin-thickness-to-spacing, were insufficient to capture performance variations, since heat transfer and pressure drop responded non-monotonically to changes in fin shape.

To address this limitation, the authors proposed a composite parameter, U, combining fin-end disturbance effects and enhanced-surface contributions. This parameter successfully represented the influence of fin-end three-dimensionality on both j and f. Using OSF configurations with blockage ratios ranging from 0.10 to 0.60, they developed correlations based on logarithmic polynomial expressions in Reynolds number and geometric ratios such as l/D_e. These correlations reproduced 94 percent of numerical j data and 93 percent of numerical f data within ±15 percent. When compared against a larger experimental database, they predicted about 92.5 percent of j points and 90.3 percent of f points within ±20 percent, showing improved accuracy relative to classical models.

Yang and Li [27, 28] investigated the thermal behaviour of offset strip fins by developing validated three-dimensional numerical models and comparing their performance with plain straight fins. A central motivation of their work was the recognition that traditional indicators such as fin efficiency and fin effectiveness become questionable when applied to compact fin geometries, since they implicitly assume a uniform heat-transfer coefficient over all fin surfaces. This assumption was shown to be inadequate for offset-strip arrangements, where the interruption of the boundary layer produces strong spatial non-uniformities in local convection.

Their simulations revealed that secondary fin surfaces within OSF passages experience significantly higher local heat-transfer coefficients than the primary walls, in some cases by several multiples. This behaviour leads to pronounced temperature gradients along the fin structure and highlights the limitations of classical lumped fin models when applied to compact heat exchanger cores.

The conceptual basis of the data-reduction procedure adopted by the authors is illustrated in Fig. 2.6. The figure schematically represents the thermal resistance network used to interpret numerical and experimental results, explicitly distinguishing between apparent convective resistances associated with primary and secondary surfaces and the conductive resistance of the fin material. Within this framework, the apparent heat-transfer coefficients inferred from global measurements are shown to depend not only

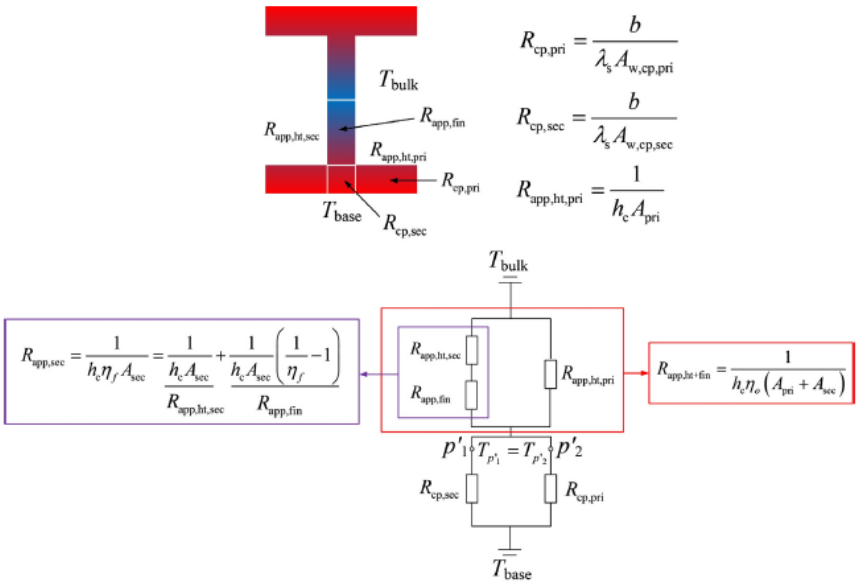

Figure 2.6. Schematic representation of the conventional data-reduction process for offset strip-fin channels, highlighting the decomposition of the overall thermal resistance into apparent convective resistances on primary and secondary surfaces and the conductive resistance of the fin material. Adapted from Yang and Li [28].

on fluid-side convection but also on fin efficiency and solid thermal conductivity. As a consequence, variations in fin material properties can directly affect the evaluated Colburn factor, even when the underlying flow field remains unchanged.

Building on this interpretation, the authors introduced an *actual fin effectiveness* metric, defined as the ratio between the heat flux exchanged on secondary fin surfaces and that on primary surfaces. Using this definition, offset strip fins were shown to outperform plain fins throughout the laminar regime, with peak effectiveness occurring at Reynolds numbers of the order of 550, whereas plain fin configurations reached their optimum at substantially higher Reynolds numbers, around 1200.

The parametric analysis further demonstrated that OSF performance depends strongly on the thickness-to-height ratio and fin density. Larger thickness-to-length ratios were found to be advantageous at lower Reynolds numbers, while thinner fins became preferable as the flow rate increased. Importantly, the study highlighted the existence of optimal geometric combinations, beyond which increasing fin density or reducing fin thickness no longer yields performance gains, especially when the thermal conductivity of the fin material is low.

Overall, the work of Yang and Li provided a physically consistent reinterpretation of fin efficiency for offset strip fins and clarified the coupled roles of geometry, fluid properties, and solid thermal conductivity. Their results are particularly relevant for cryogenic

and liquid-cooled applications, where conventional air-side correlations and classical fin models may lead to misleading performance predictions.

Grespan et al. [29] presented an extensive numerical investigation of the heat transfer and pressure loss characteristics of offset-strip fins (OSFs), The motivation of the work stems from the well-recognised limitations of classical correlations available in the literature, which are typically derived from restricted experimental datasets, rely on heterogeneous geometric definitions, and are often applicable only to narrow ranges of Reynolds and Prandtl numbers. These shortcomings become particularly critical when dealing with high-Prandtl-number fluids such as lubricating oils, for which gas-based correlations may lead to significant design errors.

The study adopts a systematic Design of Experiment (DOE) framework combined with high-fidelity Computational Fluid Dynamics simulations. The numerical analyses are performed on periodic fin modules, exploiting geometric and flow periodicity to reduce computational cost while retaining the essential flow physics. The governing equations for incompressible flow and conjugate heat transfer are solved using a Finite Volume approach, with laminar simulations employed at low Reynolds numbers and the k–ω SST turbulence model adopted for turbulent regimes. The Reynolds number is defined using the fin height as reference length, ensuring consistency across the investigated configurations.

The explored parameter space is deliberately wide and representative of real industrial applications. Dimensionless fin pitch and offset length are selected as the primary geometric variables, while wall thickness is kept constant to reflect typical manufacturing constraints. The flow conditions span Reynolds numbers from 50 up to 12000 and Prandtl numbers between 0.71 and 190 thus encompassing air, water, and oil flows. This extensive coverage allows the authors to overcome the fragmented nature of previous studies and to construct correlations with clearly defined and broad applicability ranges.

Integral thermohydraulic performance is quantified through an equivalent Darcy friction factor and a mean Nusselt number, both derived consistently from the CFD results. Separate response surfaces are initially formulated for laminar and turbulent regimes as functions of Reynolds number and geometric parameters. These surfaces are expressed in logarithmic form and fitted to the numerical data using least-squares regression. To avoid the discontinuities typically associated with piecewise correlations, the laminar and turbulent formulations are merged through a smooth hyperbolic tangent function centred around a geometry-dependent transition Reynolds number. This approach ensures continuity and differentiability of the final correlations, making them suitable for optimization procedures.

The structure of the CFD-derived response surfaces is illustrated in Fig. 2.7. The

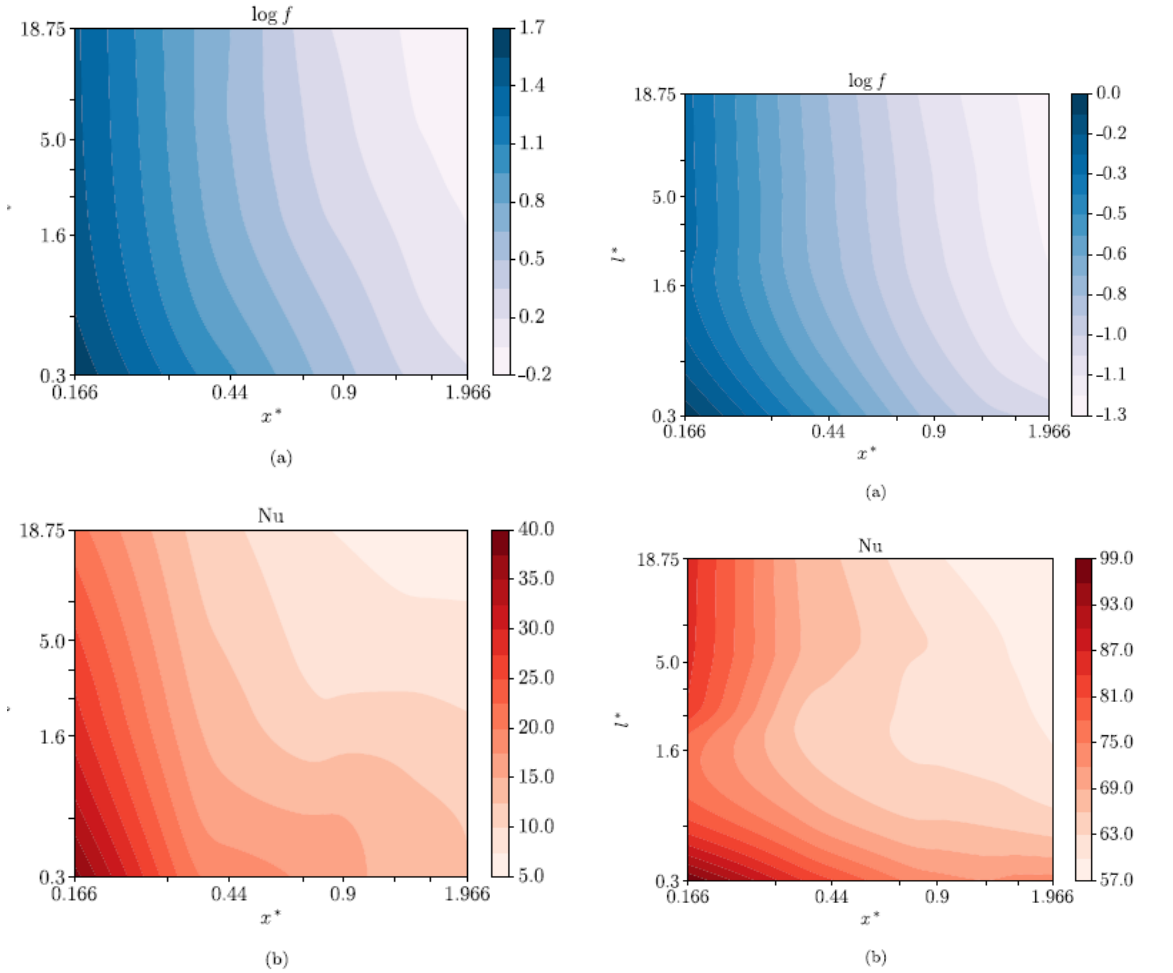

(a) Re = 50, Pr = 190 (low-Re, high-Pr, oil-like conditions).

(b) Re = 12 000, Pr = 0.71 (high-Re, low-Pr, air-like conditions).

Figure 2.7. Contour plots of the equivalent Darcy friction factor ($\log f$) and mean Nusselt number (Nu) obtained from CFD simulations of offset-strip fins at different Reynolds and Prandtl numbers, adapted from Grespan et al. [29].

two panels correspond to markedly different flow conditions: low-Re, high-Pr operation (Re = 50, Pr = 190), representative of oil-cooled applications, and high-Re, low-Pr operation (Re = 12 000, Pr = 0.71), representative of air-side conditions. The maps reveal a clear decoupling between momentum and thermal transport: friction losses decrease monotonically with increasing geometric openness, whereas the Nusselt number exhibits a non-monotonic dependence on fin pitch and offset length. This behaviour confirms that heat-transfer enhancement in offset-strip fins arises from the interplay between boundary-layer interruption, wake recovery, and mixing mechanisms, and highlights the intrinsically multi-objective nature of their geometric optimization.

A central contribution of the work lies in the treatment of Prandtl number effects on heat transfer. Rather than assuming the classical Prandtl exponent of 1/3, the authors

derive a geometry-dependent scaling exponent directly from dedicated CFD simulations performed at different Prandtl numbers. The resulting exponent exhibits substantial deviations from the canonical value, particularly for configurations with large fin pitch, highlighting that the traditional assumption is not universally valid for offset-strip fins. An empirical correlation for the Prandtl exponent is proposed and shown to reproduce the CFD-derived values with deviations below 4%, providing a practical yet accurate alternative to fixed-exponent formulations.

The accuracy of the developed response surfaces is assessed by comparing their predictions against the full CFD dataset. The proposed correlations reproduce the numerical results with a mean deviation of approximately 8.4%, which is competitive with, and often superior to, many classical correlations despite their simpler structure. Further validation is performed by applying the correlations to complete oil cooler configurations, for which experimental or previously validated numerical data are available. In this case, the predicted pressure losses and heat transfer rates exhibit mean deviations of about 7.8% and maximum deviations on the order of 20%, confirmin the practical reliability of the proposed models.

Beyond numerical accuracy, the study provides important physical insights into the role of geometry and flow regime on OSF performance. The results confirm that friction losses decrease with increasing fin pitch and offset length, while heat transfer exhibits a more complex dependence, including local minima in certain turbulent configurations. The analysis also highlights how boundary layer disruption, wake formation, and corner fillets influence both momentum and thermal transport, particularly at high Reynolds numbers.

This works delivers a coherent and comprehensive modelling framework for offset-strip fins, combining rigorous CFD analysis with pragmatic correlation development. The resulting response surfaces offer a robust tool for the preliminary design and optimization of compact heat exchangers operating over wide ranges of fluids and flow conditions, while also clarifying the limitations of long-established assumptions regarding Prandtl number scaling.

2.3. Wavy fins

Sparrow et al. [30] investigate how the rounding of protruding peaks in corrugated ducts influences heat-transfer behavior and pressure-drop performance. Their analysis uses water in a gravity-driven loop and examines a Reynolds-number range from 2.0×10^3 to 3.3×10^4, while the Prandtl number varies between 4 and 11. Three geometries are considered: a sharp-edged baseline and two progressively rounded configurations obtained through controlled machining. Measurements include fully developed Nusselt numbers, friction factors, and wall-temperature distributions, allowing systematic comparison between the geometries.

Results show that rounding consistently reduces the Nusselt number relative to the sharp profile, with modest reductions at low Reynolds numbers and more pronounced decreases near 3.0×10^4. A stronger trend appears in the friction factor: rounding lowers f significantly, in some cases to nearly 0.6 of the baseline value. Flow visualization indicates that rounding shortens the separated region near each corrugation peak and weakens local recirculation, thereby reducing inertial losses but also diminishing near-wall turbulent mixing.

Performance depends on the imposed constraint. At equal Reynolds number, sharp peaks yield higher heat-transfer rates, whereas rounded peaks produce substantially smaller pressure drops. Under equal pumping-power conditions, however, the difference in Nusselt number nearly disappears across much of the tested range, a result that may seem slightly unexpected at first glance. Overall, the study demonstrates that geometric rounding modifies the balance between inertial and viscous effects, offering designers a tunable compromise between thermal enhancement and hydraulic penalties.

Asako et al. [31] present a numerical investigation of heat transfer and pressure-drop behavior in periodically corrugated ducts with rounded corners, a geometry relevant to many compact configurations. The wall profile is approximated by a cosine function, allowing the authors to explore the influence of corrugation angle and aspect ratio on laminar flow. Simulations are performed for a Prandtl number of 0.7 and a Reynolds-number range from 100 to 1000, covering three corrugation angles (15°, 30°, 45°) and four aspect ratios. The solution method relies on a coordinate transformation that maps the wavy physical domain onto a rectangular computational grid, solved using a finite-volume scheme. Some steps in their numerical pipeline feel almost too careful, but the approach remains robust.

Results indicate that rounded corners reduce both Nusselt number and friction factor relative to a sharp-edged duct. Streamline plots show that separation bubbles grow with Reynolds number, although rounding suppresses their size compared to the sharp geometry. Pressure-drop ratios, normalized by straight-duct values, increase with corrugation

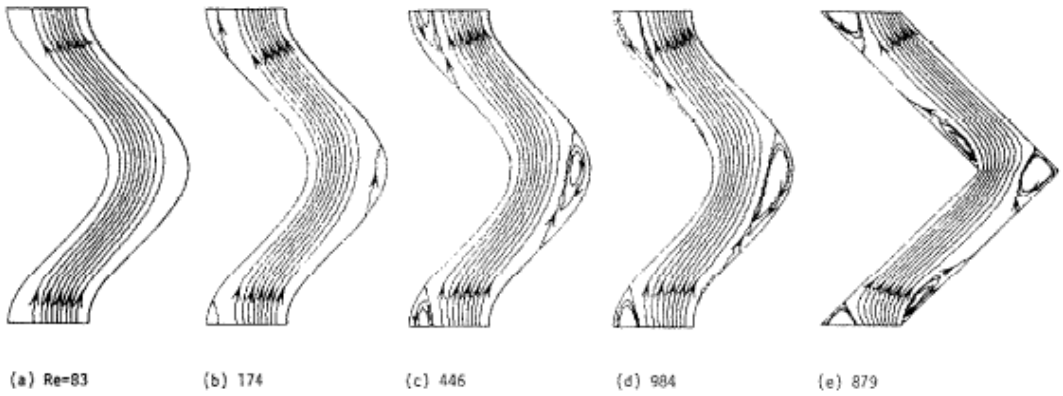

Figure 2.8. Streamline patterns in periodically corrugated ducts with rounded corners for increasing Reynolds number, adapted from Asako et al. [31].

severity; however, the rounded configuration consistently produces lower pressure penalties, with reductions approaching 80% at $Re = 1000$ for the steepest angle considered. Local Nusselt-number distributions also become smoother when corners are rounded, especially near peak regions where sharp corners create abrupt gradients.

The physical origin of these trends is clarified by the streamline visualisations reported by Asako et al. [31], shown in Fig. 2.8. As the Reynolds number increases from $Re \approx 100$ to $Re = 1000$, flow separation progressively develops in the concave regions of the corrugated duct. Rounded corners, however, significantly mitigate the size and intensity of the recirculation bubbles, delaying separation and weakening wake structures. This reduction in flow separation directly explains the substantial decrease in friction factor observed for rounded geometries, while also contributing to smoother local heat-transfer distributions.

Performance comparisons under equal pumping power, equal pressure drop, and equal mass flow reveal that rounded corners may yield higher or lower heat-transfer rates depending on geometry and constraint. For instance, under identical pressure drop, the rounded duct can outperform the sharp one by roughly 20%, whereas under equal mass flow it may fall below by about the same amount.

Xin et al. [32] develop a numerical model to predict laminar flow and heat transfer in wavy channels of uniform cross-sectional area, a geometry often found in compact thermal systems. The study focuses on steady, fully developed flow with constant wall temperature, using a coordinate-combination method that divides one geometric module into five regions. This approach allows the authors to match the curved walls using polar coordinates while maintaining Cartesian grids in intermediate sections, avoiding excessive grid distortion. Periodic boundary conditions are implemented by replacing inlet values with those computed at the outlet after each iteration cycle, a strategy that

simplifies convergence even if it feels a bit mechanical at times.

The analysis explores the influence of two geometric parameters: the height-to-spacing ratio H/S and the wavelength-to-spacing ratio L/S. Calculations span Reynolds numbers from 100 to 1000, with Prandtl number fixed at 0.707. Results show that increasing H/S strengthens centrifugal effects and enhances both Nusselt number and friction factor; for example, at $Re = 500$ the overall Nusselt number becomes roughly 1.6 times that of a parallel-plate channel, whereas the associated pressure drop can rise by nearly a factor of 5. Increasing L/S, by contrast, reduces curvature and brings both heat-transfer and friction characteristics closer to those of a straight channel.

Local Nusselt-number distributions reveal two peaks along the windward surface, caused by flow reattachment and subsequent impingement, as seen clearly in the streamline maps. These peaks intensify with Reynolds number, while the leeward surface experiences reduced heat transfer due to growing separation zones. THis work clarifies how geometric undulation controls mixing and pressure penalties in laminar wavy channels and provides a solid numerical foundation for future optimization work.

Rush et al. [33] performed an extensive experimental investigation of flow instability and heat transfer in sinusoidal wavy passages, using water-tunnel visualization and air-side heat-transfer measurements. The geometries span a wide parameter space, including several phase shifts, relative amplitudes, and wavelengths, allowing the authors to isolate how each parameter controls the onset of macroscopic mixing. Flow visualization show that at low Reynolds numbers the motion remains steady with trapped vortices in the troughs; as *Re* increases, small oscillations appear, followed by the formation of spanwise vortices that interact strongly with the core flow.

The flow-visualisation results are summarised in Fig. 2.9. The left panel illustrates the sinusoidal channel configurations and the definition of the main geometric parameters, including wavelength, relative amplitude, and phase shift between the corrugated walls. The right panel shows representative flow visualisations, highlighting the transition from steady recirculation zones at low Reynolds numbers to unsteady vortex-driven mixing as *Re* increases. These observations provide direct experimental evidence that the onset of macroscopic mixing in wavy passages is governed by geometry-controlled instabilities rather than by boundary-layer growth alone.

The onset of mixing depends heavily on the phase shift. Channels with in-phase walls ($\phi = 0°$) and 90° shift exhibit instability at lower Reynolds numbers than the 180° configuration, which remains stable until roughly $Re \approx 250$. Increasing relative amplitude destabilizes the flow earlier, while shortening the wavelength has a similar effect, although the influence of wavelength is weaker than that of amplitude. In some cases the onset of mixing moves upstream rapidly with increasing *Re*.

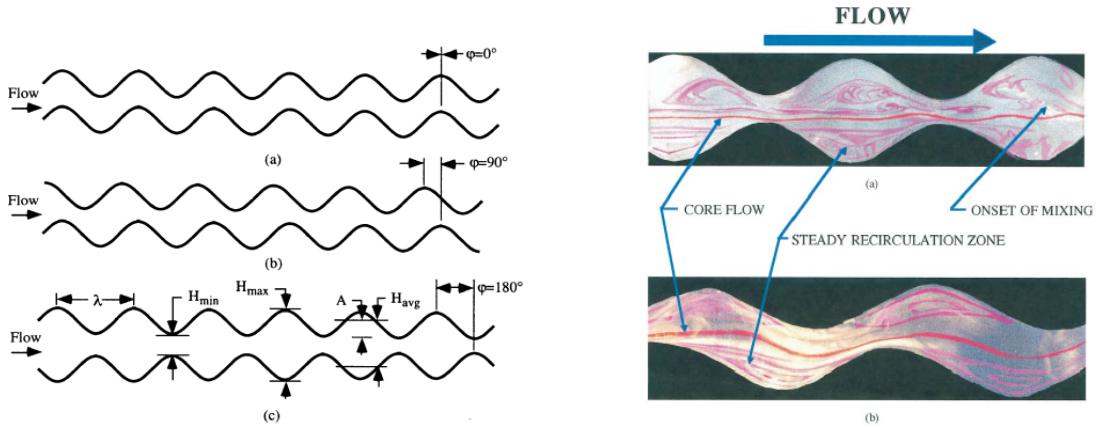

(a) Sinusoidal wavy-channel geometries and definition of phase shift and geometric parameters.

(b) Flow visualisation showing the transition from steady recirculation to unsteady mixing with increasing Reynolds number.

Figure 2.9. Geometry-induced flow instabilities and onset of macroscopic mixing in sinusoidal wavy passages, after Rush et al. [33].

Heat-transfer data show that, below the transition point, Nusselt numbers resemble those of a straight channel. Once mixing begins, local and average values rise sharply. For the 0° phase-shift case, the Nusselt number near the channel exit increases markedly when Re exceeds about 300. As Re climbs toward 600, mixing affects nearly the entire passage and enhancement extends upstream, although uncertainties near low Re remain relatively large.

Yang et al. [34] presented a numerical and experimental study of transitional flow and heat transfer in a periodically corrugated duct, using the Lam–Bremhorst low–Reynolds-number k–ε model to capture the onset of turbulence. The geometry features sinusoidal walls with rounded corners and is analyzed under a uniform wall-temperature condition. Simulations cover Reynolds numbers from 100 to 2500, while experiments supply complementary pressure-drop data and flow-visualization photographs. A coordinate-transformation method maps the wavy duct onto a rectangular grid, ensuring numerical stability even when curvature becomes significant.

The results show that separation bubbles form on the leeward surfaces at low Reynolds numbers and expand before disappearing again once turbulent mixing strengthens. Visualization images indicate that disturbances first appear near the side walls and then spread across the entire passage. Experimentally, transition occurs near $Re \approx 200$, while numerical predictions shift this threshold to slightly higher values, particularly when the rounding radius is small. This discrepancy stems from the time-averaged nature of the turbulence model, which tends to smooth early transitional structures.

Predicted friction factors match laminar theory at low Reynolds numbers but climb

sharply once instability develops, consistent with experimental trends. The Nusselt number similarly exceeds classical laminar values as mixing grows within the recirculation zones. For higher Reynolds numbers, the k–ε model yields increased heat-transfer rates, especially at the steeper corrugation angle. Overall, the study clarifies how geometry and curvature control transitional behavior, offering a combined numerical–experimental framework that explains several subtle and occasionally unexpected features of corrugated-duct convection.

Metwally et al. [35] analyze laminar forced convection in sinusoidal wavy-plate channels, focusing on how wall curvature induces transverse vortices that significantly modify momentum and heat transport. The study models periodically developed flow with uniform wall temperature, adopting two-dimensional governing equations for mass, momentum, and energy. The severity of wall waviness is described through the geometric ratio $\gamma = 4a/\lambda$, varied between 0 and 1.

Numerical simulations reveal two distinct regimes. At low Reynolds numbers or mild waviness ($\gamma < 0.375$), the flow resembles that of a straight duct, with negligible recirculation. As either parameter increases, steady transverse vortices emerge in the wall troughs and expand with Reynolds number, enhancing both mixing and wall shear stress. Results show that increasing γ enlarges the effective surface area and shifts the separation and reattachment points along the corrugation profile, altering friction distribution in a predictable way.

Heat-transfer behavior closely mirrors the vortex development. Once swirl becomes established, the thermal boundary layer thins, producing higher wall gradients and substantially larger local Nusselt numbers. For highly viscous liquids (e.g., Prandtl number near 150), the global Nusselt number may rise more than an order of magnitude compared to a flat passage, while friction increases more modestly. The study further evaluates the overall performance through the area goodness factor j/f, which identifies an optimal waviness range around $\gamma = 0.3$–0.6.

Overall, this work clarifies how sinusoidal geometry governs the transition from undisturbed flow to steady swirl and demonstrates that properly selected waviness yields considerable thermal enhancement with acceptable pressure penalties.

Zhang et al. [36] presenteda numerical investigation of laminar forced convection in sinusoidal wavy-plate-fin passages, examining how changes in corrugation ratio c and spacing ratio e alter flow organization and thermal behaviour. The model assumes periodically developed conditions with uniform wall temperature and constant thermophysical properties, using air with $\mathrm{Pr} = 0.7$. A body-fitted coordinate system represents the surface waviness, allowing the solver to capture the recirculation pockets that form immediately downstream of each crest.

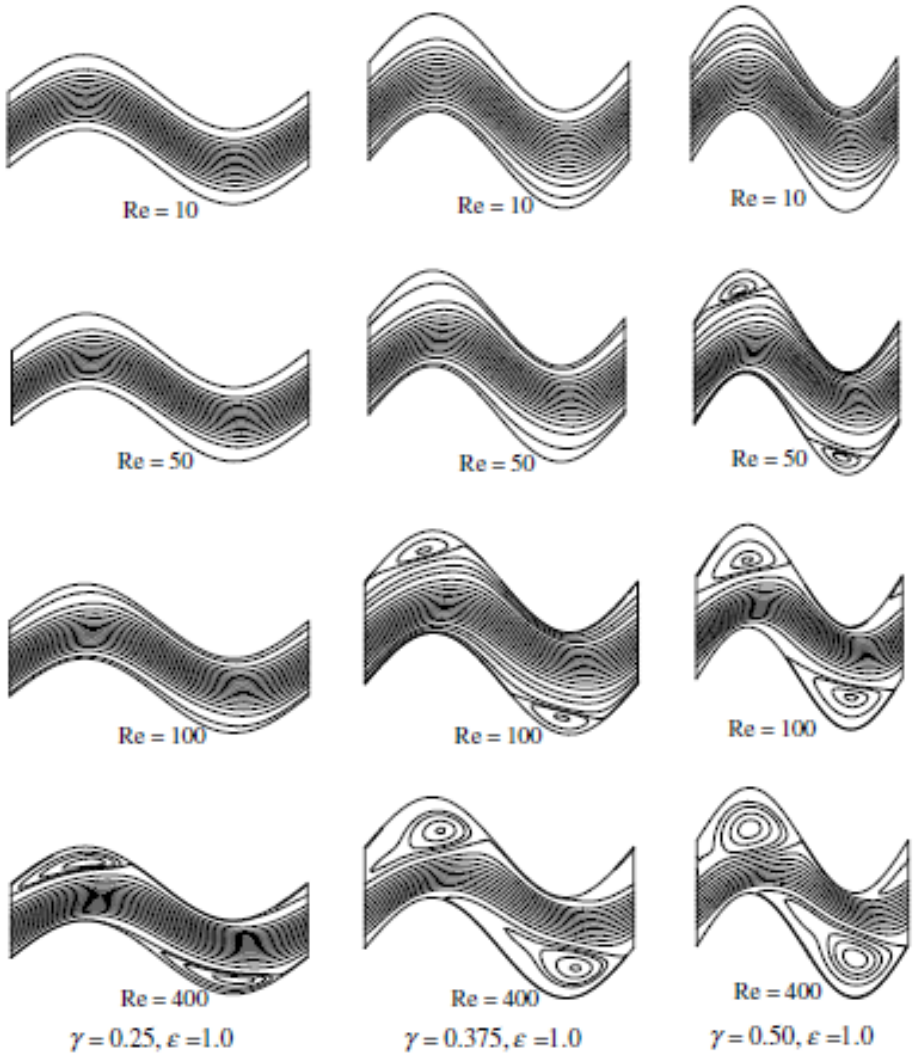

Figure 2.10. Streamline distributions in sinusoidal wavy-plate-fin passages for different Reynolds numbers and corrugation ratios c at fixed spacing ratio $e = 1.0$, after Zhang et al. [36]. At low Reynolds numbers the flow remains attached and viscosity-dominated, whereas increasing Re leads to flow separation and the formation of stable recirculation cells in the trough regions, which intensify transverse momentum transport and enhance heat transfer.

At moderate Reynolds numbers, around 100, the simulations reveal that separation becomes strong enough to generate stable swirl cells in the trough regions. These structures redistribute momentum transversely and thin the thermal boundary layer, leading to a noticeable increase in heat-transfer coefficient. The effect is not uniform: for $e < 1$ the viscous forces damp the swirl quickly, whereas for $e > 1$ the vortices grow in size before saturating again. In practical terms, the authors report enhancements up to roughly a factor of 7 relative to a flat channel, together with friction penalties on the order of 6 times the baseline.

The progressive emergence of recirculation zones with increasing Reynolds number, as illustrated in Fig. 2.10, provides direct evidence of the mechanism responsible for the strong heat-transfer enhancement reported in wavy-plate-fin channels, namely geometry-induced vortex formation rather than boundary-layer thinning alone.

A thermal–hydraulic assessment based on (j/f) indicates that there exists a region, loosely centred near $1.0 < e < 1.2$, where the competition between mixing and pressure drop becomes favourable. At very low Reynolds numbers, close to 10, the behaviour shifts back to being dominated by viscosity, and the waviness offers little benefit. Overall, the study highlights how geometric coupling between amplitude and spacing fundamentally shapes vortex development and, consequently, the attainable performance of wavy-fin surfaces.

Manglik et al. [37] analyzed steady forced convection in three-dimensional wavy-plate-fin channels, focusing on how fin density modifies vortex formation and thermal–hydraulic behavior. The study considers laminar air flow under $10 \leq Re \leq 1000$ and employs a finite-volume scheme in body-fitted coordinates to capture swirl structures generated by sinusoidal corrugations. Results show that the wavy geometry induces symmetric counter-rotating vortices in each trough, which thin the local thermal boundary layer and enhance mixing in a way that straight channels cannot replicate. As Re increases, these vortices multiply and expand, strengthening momentum and energy transport, although at the cost of higher frictional losses.

Fin density, expressed through the spacing ratio ε, plays a central role. For moderate spacings (e.g. $\varepsilon \approx 0.80$), the secondary flow occupies much of the cross-section, while at tighter spacings ($\varepsilon \approx 0.30$) swirl becomes confined and weaker. The study also compares uniform-wall-temperature and uniform-heat-flux conditions, noting that the latter consistently yields sharper gradients and slightly stronger heat-transfer response. Representative simulations report that for $Re = 500$ the Colburn factor increases markedly relative to a straight duct, while the area goodness factor (j/f) grows as fin spacing decreases, indicating improved compactness.

Overall, the authors show that wavy fins enhance performance primarily through curvature-induced vortices whose strength depends on both geometry and flow rate, and they underline how fin density subtly shifts the balance between heat-transfer gains and pressure-drop penalties.

Dong et al. [38] present a combined experimental and numerical study on the thermal–hydraulic behavior of wavy fin-and-flat tube surfaces, motivated by applications in heavy-vehicle charge-air coolers. The work examines air-side performance over Reynolds numbers from 1000 to 5500, and compares wind-tunnel data with CFD predictions to determine a suitable turbulence model. A structured grid is used to resolve the corrugated

geometry, and only half of the passage is modeled to reduce computational cost while preserving flow symmetry.

The experiments employ air and hot water as working fluids, with heat transfer evaluated through the ε–NTU method. Pressure drops are measured with calibrated differential transducers, while local temperatures are obtained from dense T-type thermocouple meshes. Results show that the SST k-ω turbulence model reproduces measured friction and Colburn j factors more accurately than the RNG formulation, particularly for fully turbulent conditions. The agreement remains acceptable even near the transitional regime around $Re = 1000$, although both CFD and experiments exhibit mild inconsistencies there, as one might expect.

The influence of waviness amplitude is analyzed by varying $2A$ among three values. Larger amplitudes strengthen separation zones and increase heat transfer coefficients, but they also introduce significant friction penalties. For instance, the highest amplitude yields a noticeable gain in j factor while simultaneously raising the f factor, leading to a mixed overall effect.

Finally, the authors interpret thermal enhancement using the field-synergy principle, showing that reduced synergy angle correlates with higher heat-transfer coefficients. This perspective helps unify observations across amplitudes and profiles, providing a clearer physical mechanism for performance trends in wavy fins.

Aliabadi et al. [39] examined the hydrodynamic and thermal performance of sinusoidal wavy channels using a two-dimensional numerical model developed for applications where moderate Reynolds numbers and strong curvature effects interact. The formulation solves steady laminar flow with uniform wall temperature, employing a body-fitted coordinate system that aligns computational nodes with the sinusoidal boundaries. This approach captures regions of flow acceleration, separation, and reattachment that would otherwise be smoothed out by Cartesian discretization. Although the problem seems conceptually simple, the geometric coupling introduces several behaviors that evolve in a somewhat non-linear way.

The study explores Reynolds numbers from 100 to 500 and varies the corrugation amplitude-to-wavelength ratio to evaluate how wall curvature regulates mixing intensity. At low Reynolds numbers, the flow remains attached and the temperature field is dominated by diffusion. As Re increases, a small separation bubble emerges near the trough and enlarges gradually. This recirculation strengthens transverse transport and leads to higher local wall gradients. Representative results show that for moderate waviness the average Nusselt number may exceed the flat-channel value by roughly a factor of two, while frictional losses also rise, though not as sharply as one might expect.

Muzychka et al. [40]developed an analytical framework to predict pressure-drop and

heat-transfer behavior in wavy-fin channels by combining low-Reynolds asymptotic theory with boundary-layer scaling valid at moderate inertia. Their formulation introduced geometric parameters such as fin height, wave amplitude, and wavelength, and it assembled a composite expression for the effective flow length that captured how curvature redirected the velocity field. Although the model was intentionally simplified, it retained the dominant mechanisms governing transverse mixing and streamwise acceleration, which often shaped the thermal response in ways that were not entirely intuitive.

The framework was benchmarked against several published datasets, and deviations remained within roughly 15%, a reasonable outcome considering the complex vortex structures forming over corrugated surfaces. Results showed that small variations in wave amplitude modified both the friction factor and the Colburn j parameter in noticeable ways, sometimes producing slightly unexpected sensitivity. As Reynolds number increased, the predicted curvature-induced swirl became more coherent, strengthening wall-normal transport and yielding higher Nusselt numbers across the passage.

The authors also identified geometric regimes where curvature enhanced performance without generating excessive pressure-drop penalties. Larger amplitudes increased mixing but reduced uniformity along the fin, while longer wavelengths tended to moderate frictional losses. ns.

Aliabadi and Hormozi [41] carried out a three-dimensional CFD investigation of sinusoidal wavy fins to evaluate flow characteristics and heat-transfer behavior across a broad geometric space. Their model employed a finite-volume formulation with a periodic domain, resolving conduction within the fin material and convection in the working fluid. They applied the RNG k-ε turbulence model and performed mesh refinement near the curved walls, where velocity and temperature gradients became strong and sometimes behaved in a slightly irregular way.

The authors validated their simulations against available experiments, reporting mean deviations close to 4%. This agreement suggested that the numerical treatment captured the essential vortex structures forming within wavy channels. Results showed that increasing wave amplitude intensified transverse mixing and enhanced Nusselt numbers, whereas longer wavelengths reduced pressure-drop penalties. The influence of Reynolds number appeared in two regimes: a mildly turbulent pattern at lower values and a more coherent swirl structure at higher ones, which altered the wall heat flux noticeably.

They also generated empirical correlations for predicting friction factor and the Colburn j parameter over the studied range. These correlations reflected the sensitivity of thermal performance to geometric ratios and helped clarify where wavy fins provided meaningful gains. In summary, the study offered a reasonably robust CFD-based description of sinusoidal fins and supplied practical tools for estimating thermo–hydraulic

performance without relying on extensive experimental testing.

Dong et al. [42] carried out an experimental investigation on the thermal–hydraulic behavior of wavy fin-and-flat tube heat exchangers, testing sixteen samples that covered different combinations of fin pitch, fin height, fin length, wavy amplitude, and wavy wavelength. The authors used a wind-tunnel facility with controlled air and water loops, where air velocities ranged between 2 and 12 m/s. The experimental campaign relied on careful measurements of temperature, pressure drop, and flow distribution, allowing reductions of the raw data into Nu and f factors under steady operating conditions.

The results showed that the Nusselt number increased nearly linearly with Reynolds number, while the friction factor followed a decreasing power-law trend. Flow-visualization evidence highlighted the formation of corner vortices for moderate Reynolds conditions, particularly when the wavy amplitude was large. These vortices thinned the thermal boundary layer and improved heat transfer, although at the cost of increased friction losses. The comparison between different geometries indicated that wavy amplitude and wavelength were the most influential parameters for overall performance.

Using multiple regression analysis, the authors derived empirical correlations for both Nusselt number and friction factor, which predicted roughly 90% of the data within acceptable deviation bands. A Taguchi-based parametric analysis further demonstrated that the ratio of amplitude to wavelength contributed the highest share to performance variation, whereas fin pitch and fin length played secondary but still relevant roles.

Kuehndel et al. [43] investigated the air-side thermal performance of wavy fins manufactured through selective laser melting (SLM), aiming to quantify how wave amplitude and wavelength affected heat transfer and friction behavior. They produced nine stainless-steel specimens with high dimensional accuracy, enabling systematic variation of geometric parameters. Tests were carried out on a cross-flow bench using air on the fin side and water at fixed temperature on the tube side. The Reynolds number ranged from 1400 to 7400, covering transitions from weakly laminar structures to more turbulent flow patterns.

Their measurements showed that increasing wave amplitude strengthened local mixing and raised both Nusselt number and Darcy friction factor. For example, doubling the amplitude led to increases of roughly 30% in Nu and nearly similar growth in ψ, although pressure penalties became more pronounced. Variations in wavelength produced an even stronger effect: reducing the wavelength yielded up to about 45% enhancement in Nu, together with significantly higher friction levels. These trends were linked to the formation of stable vortices that reduced thermal boundary-layer thickness, though sometimes in slightly irregular ways.

The authors also examined whether the surface roughness inherent to SLM affected

the results. Boundary-layer estimates indicated that the roughness height remained small relative to the laminar or viscous sublayer thickness for most operating conditions, so its influence was limited. Finally, regression analysis produced empirical correlations for predicting Nu and ψ, with the Nusselt equation capturing most of the data more accurately than the friction-factor model. Overall, the study provided a controlled experimental basis for evaluating wavy fins manufactured by additive processes, with practical relevance for optimization of compact heat exchangers.

Zhang et al. [44] investigated the air-side thermal and hydraulic performance of sinusoidal wavy fins by combining controlled experiments with numerical simulations. Their study focused on clarifying how wave amplitude and wavelength shaped heat transfer, friction behavior, and overall flow structure inside compact fin passages. The test samples were manufactured with high dimensional precision, and measurements were conducted in a forced-convection wind tunnel using air as the working fluid. The Reynolds number covered a moderate range, allowing the authors to observe transitions in mixing intensity and boundary-layer behavior.

Results showed that increasing wave amplitude enhanced transverse mixing and led to higher Nusselt numbers, although at the cost of a noticeable increase in pressure drop. Reducing the wavelength produced an even stronger change, as the sharper curvature promoted periodic vortex formation that thinned the thermal boundary layer. For instance, a shortened wavelength raised heat-transfer levels by roughly 25%, while the friction factor increased in a comparable proportion. Flow-visualization analysis confirmed the presence of alternating swirl zones, which reorganized the velocity field in slightly irregular patterns.

Numerical simulations, performed under steady-state assumptions, reproduced the main experimental trends and offered additional insight into shear-stress distribution along the wavy surface. The comparison between CFD and measurements showed deviations typically within about 10%. Based on the dataset, the authors proposed empirical correlations for both Nusselt number and friction factor, valid across the studied Reynolds range.

Muzychka et al. [45] developed a generalized framework for estimating pressure drop and heat transfer in channels equipped with wavy fins by combining asymptotic methods with scaling arguments. The authors constructed correlations capable of bridging laminar, transitional, and fully turbulent regimes, offering designers a unified predictive tool rather than a collection of isolated models. Their formulation relied on representing wavy geometries through an equivalent hydraulic diameter and curvature parameters, which allowed the model to capture how waviness modified boundary layer growth and mixing.

Validation against available data showed that the approach reproduced heat transfer trends with errors typically below about 12 percent, while pressure-drop predictions remained consistent across a range of waviness ratios. The work also highlighted that increasing wave amplitude intensified transverse mixing but introduced stronger frictional penalties, making the thermodynamic tradeoff rather evident. Although simplified, the framework provided a practical method for preliminary design of compact exchangers with wavy fins, and it clarified several scaling behaviors that earlier empirical correlations left unexplained.

Grespan at al [9] propose a physics-based and multiscale modelling framework for the prediction of thermo-hydraulic performance of aluminium plate-fin heat exchangers (PFHEs), with specific attention to offset-strip and wavy fin geometries commonly employed in automotive and energy applications. The work is motivated by the limited generality and accuracy of traditional design approaches, which typically rely on empirical correlations calibrated on restricted experimental datasets and often fail when extrapolated to different geometries or working fluids.

The proposed methodology deliberately avoids any empirical parameter identification and is instead built upon established physical principles combined with detailed numerical modelling. At the smallest scale, extended surfaces are analysed by means of three-dimensional CFD simulations of single-fin periodic modules under fully developed flow conditions. Both laminar and turbulent regimes are considered, with laminar simulations retained up to the limit of numerical convergence and the k–ω SST turbulence model adopted when necessary, in accordance with previous validation studies. A dimensionless formulation is introduced by scaling all quantities with the fin height, such that the governing problem is expressed in terms of Reynolds and Prandtl numbers only, ensuring consistency across different fin typologies and fluids.

The geometric definition of the wavy-fin periodic module adopted in the numerical analyses is shown in Fig. 2.11. The unit cell is characterised by the fin amplitude a, wavelength $2l$, fin thickness t, and channel spacing, which together define the local curvature and hydraulic constriction governing momentum and thermal transport. This periodic representation enables the analysis of fully developed flow conditions while retaining the essential geometric features of industrial PFHE fins.

From these CFD analyses, integral quantities are extracted in the form of an equivalent Darcy friction factor and a mean Nusselt number, which are then correlated as functions of Reynolds number for each fin geometry. Separate correlations are derived for offset-strip fins and for the various wavy fin configurations examined. The study highlights that classical correlations available in the literature can reproduce friction losses reasonably well for many configurations, but often exhibit significant deviations when predicting

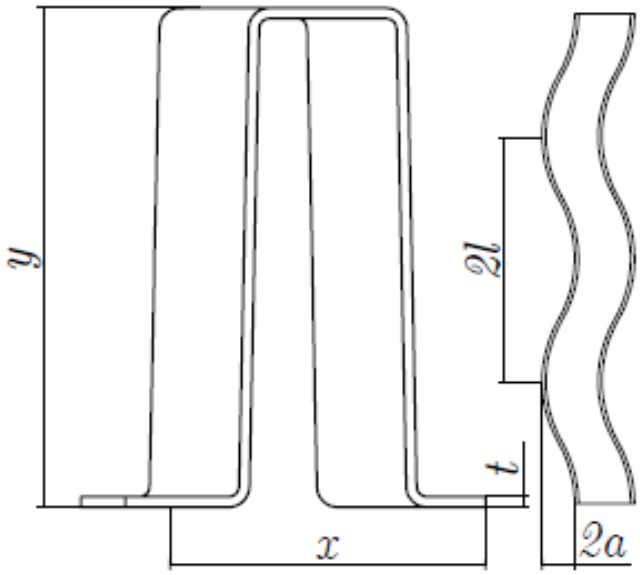

Figure 2.11. Geometric definition of the wavy-fin periodic module employed in the CFD analyses, including the main dimensional parameters controlling curvature and flow development [9].

heat transfer, particularly at high Prandtl numbers or for asymmetric fin geometries. This limitation is explicitly addressed by the present correlations, which are directly derived from numerical data tailored to the specific fins used in industrial heat exchangers.

Representative CFD results at the fin scale are reported in Fig. 2.12. The dimensionless velocity magnitude and temperature fields highlight the strong coupling between flow acceleration along the curved walls and local thermal gradients. Enhanced mixing is observed near the crests and troughs of the wavy profile, where curvature-induced acceleration and deceleration promote heat-transfer augmentation beyond simple boundary-layer effects.

A second modelling level is devoted to the analysis of entrance effects, which are commonly neglected in compact heat exchanger calculations despite their potential relevance. Dedicated CFD simulations are performed on fin stacks composed of multiple repeated modules to quantify the evolution of friction factor and Nusselt number along the flow direction. The results show that entrance effects can lead to local friction factors up to three to four times higher than fully developed values in the first module, while heat transfer also exhibits pronounced deviations before reaching asymptotic conditions. Based on thes findings, correction factors are formulated and integrated into the global modelling framework.

Another key contribution of the work concerns the modelling of inlet and outlet mani-

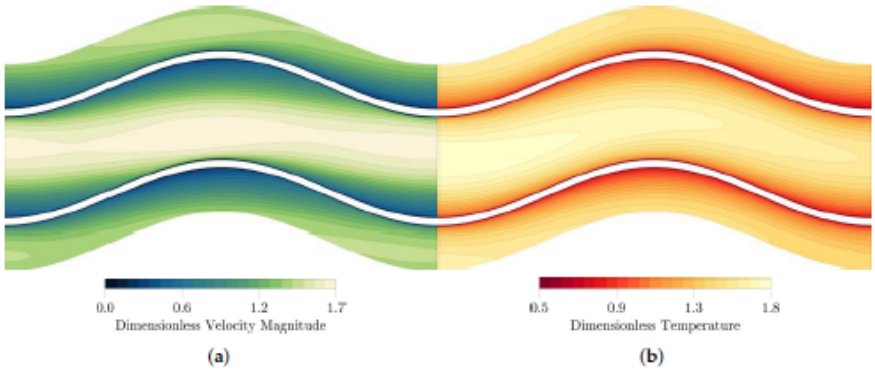

Figure 2.12. Dimensionless velocity magnitude (left) and temperature field (right) predicted by CFD in a wavy-fin passage under periodically developed conditions, showing the interaction between flow curvature, acceleration, and local heat-transfer enhancement [9].

folds. Instead of treating manifold losses as negligible or lumped empirical penalties, the authors develop a CFD model of the actual manifold geometry coupled with an equivalent porous-medium representation of the finned core. The porous model is calibrated using friction factors obtained from single-fin simulations and the Darcy–Weisbach equation, allowing the derivation of concentrated loss coefficients for the manifolds. The results demonstrate that manifold losses can account for more than 90% of the total internal pressure drop in some configurations, underscoring the importance of their explicit inclusion in predictive tools.

At the system scale, the detailed information obtained from CFD is embedded into global models for heat transfer and pressure losses. Heat transfer is evaluated using the ε–NTU method for cross-flow heat exchangers with unmixed fluids, where the overall heat transfer coefficients are computed from the numerically derived Nusselt correlations and entrance-region corrections. Pressure losses are computed by combining channel losses, entrance effects, and manifold losses within a unified Darcy–Weisbach-based formulation. Thermo-physical properties are evaluated iteratively at mean fluid temperatures to ensure internal consistency of the solution.

The proposed methodology is validated against experimental data obtained from eight different PFHE configurations, including oil coolers, water–glycol radiators, and charge air coolers. The comparison shows that the predicted heat transfer rates and pressure drops generally fall within ±20% of the experimental measurements, with mean deviations notably lower for most operating conditions. These results are competitive with, and often superior to, those obtained using classical correlations, particularly when dealing with high-Prandtl-number fluids or complex fin arrangements.

Overall, the study delivers a robust and engineering-oriented modelling strategy that

bridges detailed CFD analyses and system-level performance prediction. By relying solely on physical modelling and avoiding empirical tuning, the proposed approach offers enhanced generality and reliability, making it particularly suitable for preliminary design, performance assessment, and optimization of plate-fin heat exchangers across a wide range of geometries and working fluids.

2.4. Multi–Objective Genetic Optimization of PFHEs

Mishra et al. [46] investigate a genetic-algorithm approach for optimizing crossflow plate–fin heat exchangers, aiming to reduce total annual cost while meeting required thermal performance. The formulation combines detailed thermo–hydraulic models with a cost expression that accounts for investment, pumping power, and operating energy, producing a mixed set of continuous and discrete variables. Because conventional gradient-based methods often struggle with multimodal behaviors, the GA encodes fin geometry, exchanger dimensions, and layer configurations into binary strings, allowing a broader and more flexible design search. Thermal performance is evaluated using the ε-NTU methodology together with standard correlations for j– and f–factors.

The authors first validate their GA on a simplified two-layer case, finding that predicted costs match gradient-based optima within about 2%, although the GA naturally requires more computational effort. Extending the analysis to multilayer systems, they observe that enforcing laminar-flow restrictions tends to increase the optimal core size by roughly 10–15%, mainly because greater surface area is needed to satisfy heat-duty constraints without violating Reynolds limits. When these restrictions are removed, the GA identifies more compact exchangers exhibiting cost reductions on the order of 10%, but with noticeably higher pressure-drop penalties. Some geometric variables also show consistent tendencies—fin density and core length shift in predictable ways—suggesting underlying structural sensitivities in PFHE optimization.

This study demonstrates that GA-based optimization, though slightly irregular in convergence at times, provides a robust tool for navigating complex design surfaces that conventional methods might overlook.

Xie et al. [47] develop a genetic-algorithm framework to optimize plate–fin compact heat exchangers by adjusting three structural parameters while fin geometries remain fixed. The GA encodes the flow lengths into binary strings and explores a large discrete design space where classical deterministic optimization typically struggles. Thermal performance is evaluated using the ε-NTU formulation together with polynomial regressions for the j– and f–factors, which maintain acceptable accuracy across the relevant Reynolds-number range. The study considers different objectives, including minimum total annual cost and minimum volume, both with and without pressure-drop constraints, and com-

pares how these objectives shift the optimal geometries, sometimes in ways that feel slightly irregular but still physically understandable.

Under pressure-drop constraints, the optimized heat exchanger achieves about 30% reduction in total volume and roughly 15% reduction in annual cost compared to the reference configuration reported in the literature. These improvements arise mainly from shorter flow lengths and more compact structural choices, which remain feasible as long as the allowed pressure losses are respected. When constraints are removed, the GA tends to push designs toward significantly smaller cores, reaching volume reductions close to 49%, though this also leads to increased air-side pressure drops, a familiar trade-off between compactness and operating effort. The results show that different objective functions—cost, volume, or combined metrics—drive the algorithm toward distinct geometric tendencies, illustrating how sensitive PFHE optimization can be to design priorities.

Sanaye et al. [48] present a multi-objective optimization of plate–fin heat exchangers using the NSGA-II algorithm, aiming to maximize effectiveness and minimize total annual cost. Six geometric parameters, including fin pitch, height, offset length, and the three flow lengths, form the decision space, while thermal performance is evaluated through the ε-NTU formulation. Operating conditions from an industrial furnace case study (e.g., hot-stream inlet at 620 K and cold-stream inlet at 315 K) provide a realistic setting for the optimization process, which gives the study a clear engineering relevance. The genetic algorithm uses controlled elitism, tournament selection, and uniform crossover to explore a design domain that behaves quite nonlinearly, sometimes in ways that feel a bit irregular but still consistent with PFHE physics.

The Pareto front highlights a strong trade-off between cost and effectiveness. Typical optimal points range from an effectiveness of 0.8979 with a cost around 2630$, to a low-cost configuration near 465$ with effectiveness 0.5581, producing a wide set of feasible compromises. Sensitivity analysis reveals that fin pitch, height, offset length, and the two flow lengths distribute broadly across their bounds, confirming their role in shaping objective conflicts.

Gosselin et al. [49] investigate a hybrid optimization strategy for plate–fin heat exchangers in which classical multi-objective search is combined with approximate surrogate models to reduce computational effort. The work focuses on identifying geometries that minimize annual operating cost while maximizing thermal effectiveness, treating the exchanger as a complex nonlinear system influenced by several geometric variables such as fin pitch, height, and flow-section lengths. Instead of relying solely on full thermo–hydraulic simulations, the authors construct simplified surrogate relations that approximate ε-NTU performance and pressure losses with reasonably small error. These models allow the optimizer to evaluate large sets of candidate designs, even if

some predictions feel slightly rough in places, which is rather typical of surrogate-based approaches.

The hybrid method is benchmarked against a standard evolutionary algorithm, showing that the surrogate-assisted version converges much faster, often reducing computational time by nearly 40% while still locating solutions that remain close to the true Pareto front. Representative optimal designs reveal expected trade-offs: increasing surface area improves effectiveness but raises pumping requirements, and designs with compact cores can lower cost by around 10–15% at the expense of higher pressure drops. In some cases, fin pitch and offset length repeatedly drift toward narrower ranges, a sign that these variables dominate overall performance, whereas certain flow-length parameters show weaker sensitivity.

Overall, the study demonstrates that combining evolutionary search with surrogate modeling provides a practical optimization framework for PFHE design. It reduces evaluation time significantly and preserves sufficient accuracy to guide decision-making, even when the underlying response surfaces behave in mildly unpredictable ways.

Rao and Patel [50] investigate the thermodynamic optimization of crossflow plate–fin heat exchangers using a particle swarm optimization (PSO) algorithm, focusing on three independent objectives: minimization of entropy generation units, minimization of total volume, and minimization of annual operating cost. The modeling framework relies on second-law analysis, where entropy generation originates from both heat-transfer irreversibility and fluid-friction losses. Performance is evaluated through a combination of the ε-NTU formulation and pressure-drop correlations for offset-strip fins; this hybrid approach captures nonlinear interactions between geometry and operating conditions, although occasionally with slightly irregular sensitivity patterns.

In the first application example, the heat exchanger must satisfy a duty of 160 kW under fixed spatial limits. PSO consistently identifies architectures with lower irreversibility than those obtained via genetic algorithms, reducing entropy generation units from 0.0633 to 0.0530, and lowering pressure drops on the hot and col sides by 37% and 17%, respectively. These improvements arise mainly from adjustments in fin density, thickness, and lance length, which reshape free-flow area and convective coefficients in a rather natural way, even if some parameter shifts look a bit surprising at first glance.

The second example targets minimum volume and minimum annual cost. PSO achieves a volume reduction of roughly 5.9% relative to GA-derived designs, while maintaining pressure-drop constraints near their allowable limits. When cost is minimized, small geometric changes—such as reducing hot-stream length—yield a modest 1% decrease in total annual cost. Convergence behavior is also notably faster: PSO reaches stable optima within about 40 generations, compared to 300 generations reported for GA.

This work demonstrates that PSO provides a robust and computationally efficient tool for PFHE optimization, capturing critical thermodynamic trade-offs with improved accuracy and reduced computational time.

Zhang et al. [51] develop a three-dimensional distributed parameter model (DPM) to predict and optimize the performance of plate–fin heat exchangers operating under both dry and wet conditions. Unlike integrated parameter models, the DPM discretizes the exchanger into control volumes whose mesh coincides with the true fin passages, allowing the model to capture strong thermophysical property variations that occur when compactness is high or when humidity and phase change appear. The formulation relies on enthalpy-based energy equations, which couple heat and mass transfer and naturally handle condensation effects; this gives the methodology a kind of robustness that older IPM approaches miss.

Optimization is driven by entropy generation minimization, chosen because it balances heat-transfer enhancement and frictional penalties in a unified metric. A genetic algorithm is employed, using a customized fin database of over sixty fin types. The search identifies fin geometries and exchanger dimensions that minimize overall irreversibility while satisfying pressure-drop limits of 3.0 kPa on the hot side and 1.4 kPa on the cold side. The optimal PFHE exhibits dimensions of 0.190 m $\times$ 0.114 m $\times$ 0.262 m, and its minimized entropy generation reaches 4.489 J/(kg·K), a result that is somewhat lower than values obtained with traditional IPM, confirming the improved physical fidelity of the DPM.

Model validation shows good agreement between DPM and IPM, although heat-duty predictions differ by around 6.6%, attributed to the more accurate treatment of property variations in the DPM. Wet-condition simulations reveal modest temperature reductions (about 0.3–0.6°C) due to evaporative cooling, and these effects propagate across exchanger layers in slightly asymmetric ways.

Ahmadi et al. [52] investigate a multi-objective optimization strategy for cross-flow plate–fin heat exchangers, focusing on minimizing entropy generation units and total annual cost while exploring additional thermodynamic objectives such as effectiveness and exergy efficiency. The modeling framework employs the ε-NTU formulation to evaluate thermal performance, incorporating temperature-dependent air properties and pressure-drop correlations for rectangular offset-strip fins. Six geometric variables—fin pitch, fin height, fin offset length, cold-stream length, hot-stream length, and no-flow length—form the decision space, and the NSGA-II algorithm is applied to generate a Pareto front illustrating the conflict between thermodynamic irreversibility and economic performance.

The authors demonstrate that NSGA-II provides an effective framework for balancing thermodynamic and economic metrics in PFHE design, offering designers a flexible and

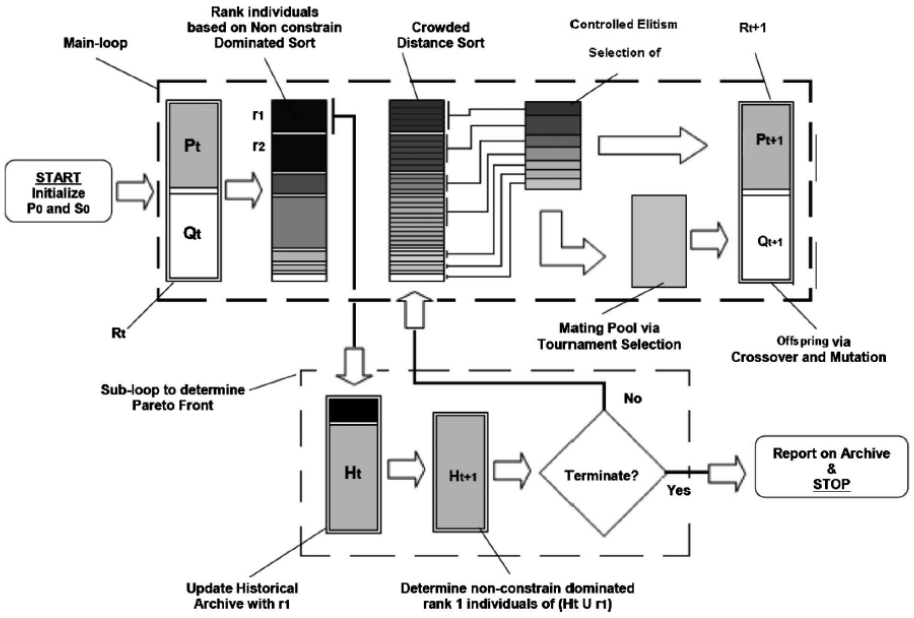

Figure 2.13. Schematic representation of the NSGA-II optimization framework adopted by Ahmadi et al. [52]. The algorithm combines non-dominated sorting, crowding-distance evaluation, and controlled elitism to construct a Pareto front of optimal PFHE designs by simultaneously accounting for thermodynamic and economic objectives.

reasonably robust optimization tool.

Figures 2.13 and 2.14 provide a concise visual interpretation of the optimization strategy and results proposed by Ahmadi et al. Figure 2.13 summarises the evolutionary optimization workflow, showing how a population-based algorithm enables the simultaneous treatment of multiple conflicting objectives while preserving solution diversity. In the context of PFHE design, this approach avoids the limitations of single-objective optimization and allows the systematic exploration of complex design trade-offs.

Figure 2.14 illustrates the resulting Pareto front, revealing the strong coupling between economic performance and thermodynamic irreversibility. Designs characterised by lower entropy generation or higher exergy efficiency are associated with increased annual costs, reflecting the need for larger heat-transfer surfaces or reduced pressure losses. Conversely, cost-minimised solutions correspond to higher irreversibility levels. Together, these results emphasise that PFHE optimization inherently leads to a set of equally optimal solutions rather than a unique design point, leaving the final selection to be guided by industrial priorities and external constraints.

Kim et al. [53] present a detailed numerical investigation of thermo–flow behavior in offset-strip fins, seeking universal correlations capable of predicting friction and heat-transfer performance across a broad spectrum of geometries and working fluids. The study examines 39 fin configurations spanning hydraulic diameters between roughly 0.7

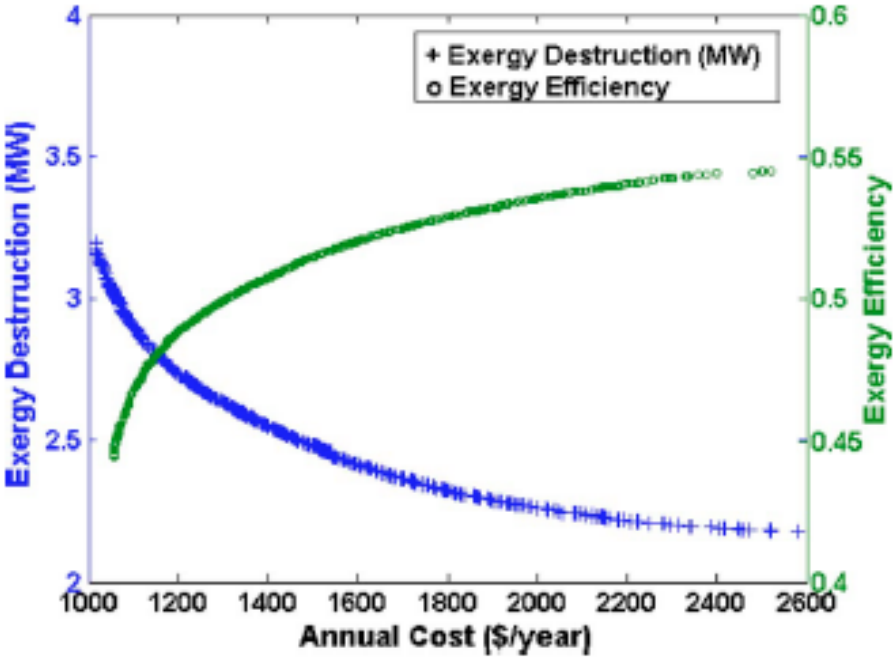

Figure 2.14. Pareto-optimal trade-off between total annual cost and thermodynamic performance indicators obtained by Ahmadi et al. [52]. Increasing exergy efficiency or reducing exergy destruction systematically leads to higher annual costs, highlighting the intrinsic conflict between thermo-economic objectives in PFHE design.

and 3.7 mm, with blockage ratios ranging from 5% to about 35%. Using steady RANS simulations for laminar, transition, and turbulent regimes, the authors validate multiple turbulence models and ultimately adopt the SST k–ω closure, which shows deviations below 14% for j and below 8% for f relative to established references.

The work reveals that classical correlations underestimate f and overestimate j when blockage ratio grows above 20%, leading to non-negligible design errors. To address this, new friction-factor and heat-transfer correlations are derived for four blockage-ratio intervals. For example, in the 20–25% regime, the f correlation incorporates strong Reynolds dependence and modest sensitivity to geometric ratios such as $c = t/s$, while the j correlation is extended to include Prandtl-number effects to accommodate fluids like water (Pr close to 5) or diesel (Pr $\approx$ 40). Interestingly, although f remains largely insensitive to fluid type, j varies consistently with Prandtl number, a behavior that older models were unable to represent.

A design-optimization case involving a diesel-fuel cooler further illustrates the usefulness of the new correlations. Under a pressure-drop constraint of 400 Pa, the optimal fin geometry obtained through a micro–genetic algorithm shows a JF enhancement of about 24% relative to the reference fin. Variations in spacing and thickness shape both

pressure losses and thermal performance in ways that are sometimes slightly irregular but physically meaningful. Overall, the study establishes geometry- and fluid-aware correlations that remain reliable across wide operating ranges, making them quite valuable for PFHE optimization.

Najafi et al. [54] present a multi-objective optimization study for plate–fin heat exchangers in which the total rate of heat transfer and the total annual cost are treated as conflicting objectives. The model relies on steady-state thermodynamics with both streams modeled as ideal-gas air, and performance is evaluated through the ε–NTU framework combined with established j– and f–factor correlations. Several geometric variables are allowed to vary, including fin height, fin frequency, fin thickness, lance length, hot- and cold-side lengths, and the number of fin layers. Because these parameters influence heat-transfer area, free-flow area, and pressure loss in nonlinear ways, the design landscape exhibits strong curvature and occasional mildly irregular sensitivities.

A sensitivity analysis reveals trends that align with physical intuition: increasing fin height from 2 mm to 20 mm raises heat duty by roughly 8 kW, while higher fin frequency increases Q by more than 35 kW, though at the expense of higher operating cost. Adjusting the number of fin layers also has a substantial effect, with Q increasing by nearly 27 kW as layer count moves from 2 to 40. These variations interact with capital cost and pumping power, sometimes producing trade-offs that are not entirely monotonic.

Using a multi-objective genetic algorithm with a population of 110 individuals and convergence near generation 140, the authors generate a Pareto front spanning heat-duty values from about 0.6×10^5 W to 1.54×10^5 W, and annual costs ranging between roughly 500 \$ and 8×10^4 \$. Representative solutions show that compact geometries can drastically reduce cost, while larger-area designs achieve higher heat transfer but with notably higher pumping requirements. Overall, the study demonstrates that GA-based multi-objective optimization provides designers with a flexible range of feasible PFHE configurations, enabling rational trade-offs between thermodynamic performance and economic investment.

Yousefi et al. [55] introduced an improved harmony search (HS) algorithm for the optimal design of plate–fin heat exchangers, aiming to handle both continuous and discrete geometric variables while reducing the computational burden typical of evolutionary methods. The study enhances classical HS by incorporating a Roulette-wheel selection strategy, which increases the probability of choosing high-fitness harmonies without disrupting the structure of feasible solutions. A self-adaptive penalty function is also implemented to manage constraints such as pressure-drop limits, heat-duty requirements, and geometric bounds. This adaptive scheme avoids the trial-and-error tuning required in static penalties, improving both consistency and solution quality in a fairly natural

way.

The optimization targets two single-objective problems: minimizing total heat-transfer area and minimizing total pressure drop, both evaluated using the ε-NTU formulation and the Manglik–Bergles correlations for j– and f–factors. For an illustrative case involving a duty of 1069.8 kW, the method identifies configurations with substantially reduced irreversibility compared to earlier evolutionary approaches. In the heat-transfer-area problem, the improved HS converges to 109.62 m^2, slightly outperforming hybrid GA results; in the minimum-pressure-drop study, it achieves a normalized value of 0.054, again marginally better than previous designs.

Parameter studies show that a harmony memory size (HMS) of 5 and an HMCR of 0.9 yield the most accurate and stable performance across benchmark functions. CPU time remains competitive, typically around 3.1–3.2 s, while achieving higher accuracy than GA, PSO, or GA–PSO hybrids. Overall, the work demonstrates that combining modified HS with an adaptive penalty scheme offers a robust and efficient optimization framework for PFHEs, particularly when dealing with nonlinear, constrained design spaces that tend to behave just a bit unpredictably.

Patel et al. [56] developed an improved multi-objective teaching–learning-based optimization (MO-ITLBO) algorithm for the geometric design of plate–fin heat exchangers, addressing the limitations of classical evolutionary schemes that require intensive parameter tuning. Their formulation considers seven design variables, including hot- and cold-side lengths, fin height, fin thickness, fin frequency, lance length, and the number of hot-side layers. Performance is evaluated through the ε–NTU method with standard offset-strip fin correlations, while constraints enforce allowable pressure drops of 9.50 kPa on the hot side and 8.00 kPa on the cold side. The method integrates adaptive teaching factors and a grid-based archive, improving diversity preservation and overall convergence behavior.

Wen et al. [57] carried out a hybrid optimization strategy for serrated-finned plate–fin heat exchangers by combining a Kriging response surface with a multi-objective genetic algorithm. The approach aims to overcome the slow convergence and heavy computational cost of standard NSGA-II, especially when evaluating complex thermal–hydraulic models governed by ε–NTU relations and Manglik–Bergles correlations for j and f factors. Four geometric variables—fin height, fin spacing, fin thickness, and interrupted length—plus the inlet Reynolds number are treated as decision parameters. The Kriging surface approximates the response of each objective and adaptively refines itself when prediction error becomes too large, which helps avoid premature convergence and reduces the number of expensive evaluations.

The algorithm is benchmarked against earlier NSGA-II and modified TLBO studies.

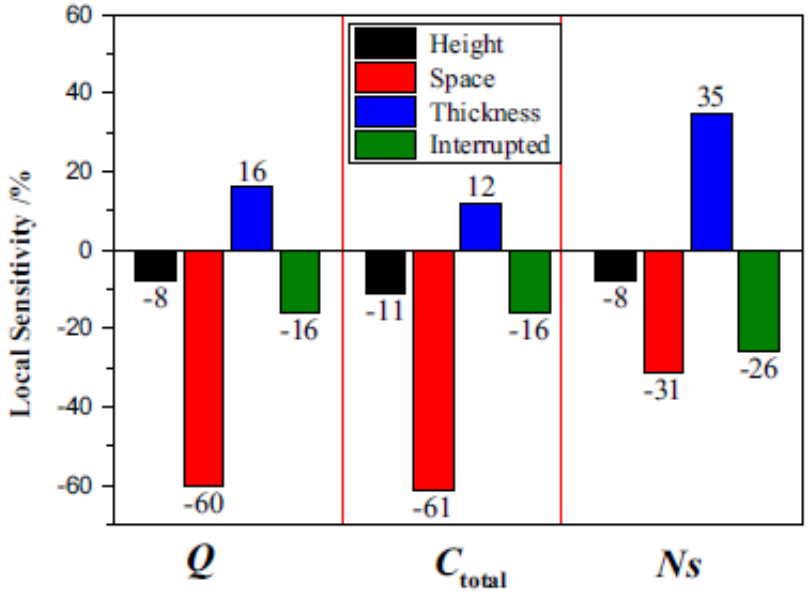

Figure 2.15. Local sensitivity of serrated-fin geometric parameters on heat transfer rate Q, total annual cost C_{total}, and entropy generation number N_s, as reported by Wen et al.

Under equal effectiveness, annual cost is reduced by roughly 10.5% compared with NSGA-II and 10.8% compared with TLBO. Convergence is also faster: the hybrid method settles after about 498 evaluations with an average runtime of 6.39 s, noticeably quicker than earlier approaches. For thermal–hydraulic optimization, the study identifies that maximizing j favors larger fins and smaller spacing, while minimizing f demands thinner fins and longer interrupted lengths. A representative optimum for maximum j occurs near $\text{Re} = 217$, featuring a tall fin and relatively small spacing, whereas the minimum f solution shifts toward larger Reynolds and long interruptions.

In thermal–economic and entropy-based optimization, the authors show that heat-transfer rate conflicts with both annual cost and entropy generation. Overall, the hybrid Kriging–MOGA workflow yields smoother Pareto fronts, higher accuracy, and notably faster convergence, providing designers with a practical optimization tool.

Figure 2.15 provides direct physical insight into the optimization problem by quantifying the relative influence of the main geometric parameters on the selected objectives. Fin spacing emerges as the dominant variable for both heat-transfer rate and total annual cost, whereas fin thickness exhibits the strongest impact on entropy generation. The interrupted length shows competing effects across the objectives, highlighting the intrinsic conflict between thermal enhancement and hydraulic penalties. In other words, the sensitivity patterns already anticipate that no single geometry can be simultaneously optimal for Q, C_{total}, and N_s.

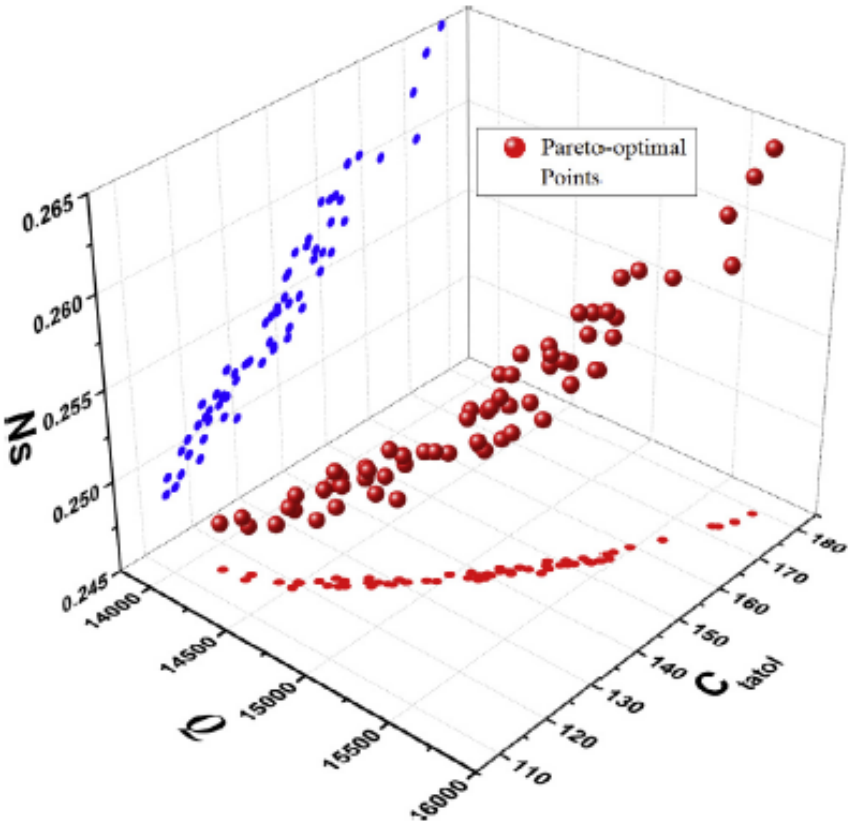

Figure 2.16. Representative Pareto front obtained by Wen et al. for the multi-objective optimization of serrated-fin PFHEs, illustrating the trade-off between total annual cost and thermodynamic performance indicators.

These competing sensitivities translate into the trade-off structure of the Pareto set shown in Figure 2.16. The distribution of Pareto-optimal solutions indicates that improvements in thermodynamic quality are achieved at increasing annual cost, with a clear region of diminishing returns towards the high-cost end of the front. Rather than yielding a single design point, the Pareto representation provides a family of equally optimal compromises, enabling the final selection to be aligned with application-specific constraints and industrial priorities.

Hossein et al. [58] present a thermodynamic and economic optimization of plate–fin heat exchangers using a multi-objective Bees Algorithm (MOBA). The study targets two conflicting objectives: minimizing the number of entropy generation units (EGU) and minimizing total annual cost, both evaluated under realistic thermo–fluid assumptions based on the ε–NTU formulation and standard correlations for offset-strip fins. Six geometric variables are optimized simultaneously, including fin pitch, fin height, fin offset length, hot-side length, cold-side length, and no-flow length. Operating conditions correspond to air–gas service, with hot- and cold-stream mass flow rates of 1.8 kg/s and 2.0

kg/s, respectively.

MOBA is applied to reconstruct the Pareto front and compared against a reference NSGA-II study. The results clearly show the expected thermodynamic conflict: reducing EGU demands higher heat-transfer area, which increases annual cost, whereas reducing cost typically requires operating at higher irreversibilities.

The aoutors demonstrate that Bees Algorithm provides a flexible and effective multi-objective optimizer, capable of generating a broad Pareto set with improved cost–entropy trade-offs and mildly more intuitive geometric trends than earlier heuristics.

Juan et al. [59] developed a detailed thermo–hydraulic model and a multi-objective genetic algorithm for plate–fin heat exchangers equipped with staggered offset fins. Seven geometric variables, including fin height, fin length, fin offset, and the wrinkling angle, are optimized under operating conditions representative of oil–air service, with inlet volume flows near 0.015 m^3/s and fluid properties assumed constant.: The thermal analysis is based on the ε–NTU method, where effectiveness is computed from an unmixed crossflow configuration. Heat-transfer coefficients rely on Colburn j correlations, while pressure drops are evaluated through standard Fanning friction relations.

A genetic algorithm combined with orthogonal design is employed to limit the search space and reveal dominant geometric interactions. The evolutionary run proceeds for 500 generations and highlights a strongly nonlinear trade-off between maximizing total heat-transfer rate and minimizing pressure drop.The optimization identifies an improved configuration where total heat duty increases by about 6.2%, while overall pressure drop decreases nearly 40%, giving a surprisingly balanced design despite the conflicting criteria. The optimized geometry also reduces total volume by roughly 2.7%, showing that compactness emerges naturally when fin spacing and lengths are reduced.

The sensitivity analysis indicates that fin height and fin length exert the strongest influence on both objectives, whereas fin offset and wrinkling angle mainly adjust local boundary-layer disruption. A porous-media reconstruction validates the optimized results, with numerical simulations confirming consistent thermal gains and sharply reduced flow resistance. Although small deviations appear in empirical j– and f–factor comparisons, the overall performance trends remain robust. In short, the GA–orthogonal approach provides a clear and, hmm, somewhat elegant route for tuning PFHE geometry under competing objectives.

Khan et al. [60] introduce a hybrid multi-objective optimization procedure for plate–fin heat exchangers that combines Differential Evolution, Genetic Algorithms, and Adaptive Simulated Annealing into a single DE–GA–ASA framework. The goal is to enhance global search ability while maintaining population diversity, which classical algorithms sometimes lose too early. The method is validated against benchmark Pareto problems and

then applied to PFHE design under realistic furnace conditions, where the hot stream enters near 620 K and the cold stream close to 315 K, with mass flow rates of 1.45 kg/s and 1.35 kg/s, respectively.

Thermal modeling uses the ε–NTU approach with Manglik–Bergles correlations for j– and f–factors, while six decision variables—fin pitch, fin height, offset length, and the three flow lengths—define the geometry. The optimization targets include maximizing heat-transfer rate and minimizing investment cost, operating cost, and total annual cost. The algorithm generates a smooth Pareto front spanning heat-duty values from about 0.6×10^5 to 1.54×10^5 W, in Q and $\approx$ 600–3800 \$/yr.

The study finds that fin pitch and height dominate the trade-off structure, whereas hot-stream and no-flow lengths often drift to their upper bounds, showing limited conflict with cost–performance objectives. Compared to earlier approaches (hybrid GA, IHS, BBO), the DE–GA–ASA method preserves constraints more reliably and avoids the premature convergence observed in classical GA-based optimization. Using TOPSIS, the authors identify a final design with $Q \approx 3.5 \times 10^5$ W and $TAC \approx 765$ \$/yr, representing a balanced solution between heat-transfer enhancement and economic penalties.

Overall, the combined DE–GA–ASA approach offers a more robust and somewhat flexible optimization tool,

Liu et al. [61] investigate the thermo–hydraulic optimization of serrated-fin plate–fin heat exchangers by combining detailed CFD simulations with a multi-objective evolutionary algorithm. The study aims to improve both the Colburn j factor and the composite performance index JF, while keeping pressure-drop penalties within acceptable limits. A three-dimensional numerical model is developed to capture complex flow dynamics caused by fin serration, including vortex shedding, recirculation, and strong boundary-layer redevelopment that classical correlations typically struggle to describe correctly.

Five geometric variables—including fin height, serration pitch, fin thickness, and interrupted length—are optimized using a hybrid GA–PSO procedure. The rating of candidate designs relies on the ε–NTU framework, with CFD providing the heat-transfer and friction coefficients required for each geometry. The algorithm identifies that optimal designs often cluster near Re $\approx$ 420, where convective enhancement balances pressure losses in a reasonably efficient way.

The optimized configuration achieves an improvement of about 12.8% in the JF criterion relative to the baseline geometry, reflecting a more favorable combination of enhanced mixing and reduced viscous dissipation. Pressure drop is also reduced, reaching roughly 310 Pa, a value significantly lower than that predicted by simpler analytical models. Interestingly, the GA–PSO search sometimes converges toward geometries with non-intuitive combinations of serration pitch and fin thickness, suggesting that multi-variable

interactions play a stronger role than assumed in earlier studies.

This work highlights that CFD-driven optimization offers a powerful and somewhat flexible approach for next-generation PFHE design, uncovering parameter couplings that heuristic correlations alone are unable to capture.

Maghsoudi et al. [62] present a comprehensive thermo–economic optimization of plate–fin recuperators for microturbines, examining four fin types—rectangular, triangular, offset-strip, and louver—and allowing dissimilar fin pairings between the hot and cold sides. Performance is evaluated using the ε–NTU framework coupled with microturbine cycle equations so that variations in recuperator effectiveness influence fuel-flow requirements and overall system cost. The optimization considers up to nine geometric variables, including fin pitch, fin height, and flow lengths extending to nearly 1.0 m, which strongly affect UA, pumping power, and capital cost.

A multi-objective NSGA-II algorithm is used to generate a Pareto front balancing total annual cost and thermal effectiveness.

To refine decision-making, the authors apply Data Envelopment Analysis (DEA), which indicates that louver-fin configurations dominate 9 out of 10 top-ranked solutions, highlighting their favorable balance between heat-transfer capability and pressure-drop penalties.

Song et al. [63] develop a numerical and optimization framework to analyze serrated–fin geometries in plate–fin heat exchangers, linking detailed CFD predictions with a surrogate-assisted search strategy. The study focuses on how variations in fin height, serration pitch, fin thickness, and interrupted length influence the Colburn j factor and the friction factor f across inlet Reynolds numbers spanning 200–1200. Thermal–hydraulic behavior is resolved through steady 3D simulations, capturing periodic wake structures and rapid boundary-layer redevelopment that strongly alter heat-transfer efficiency.

Results show that a coordinated reduction in fin spacing and serration pitch can increase the j factor by up to 22.6%, while careful increases in fin thickness suppress excessive flow disturbances and lower f by nearly 17.3%. Although these tendencies appear intuitive, some interactions remain mildly irregular, with interrupted-length changes producing non-monotonic shifts in both j and JF.

Multi-objective optimization identifies fin combinations that achieve a balanced increase in j without dramatic penalties in friction. Optimal designs generally favor moderate fin thicknesses in the 0.1–0.3 mm range and serration pitches toward the lower half of the tested domain. These configuration exploit intensified mixing at reasonable pressure loss, producing a design space that looks somewhat more structured than expected.

Yu et al. [64] develop a three–dimensional CFD–driven and multi–objective optimization framework for wavy plate–fin heat exchangers, integrating Radical Basis Function

(RBF) surrogates with a MOGA search strategy. Four geometric parameters — fin height h, spacing s, amplitude A, and thickness t — are varied within realistic engineering ranges to maximize the Colburn factor j and minimize the friction factor f. The CFD model is validated experimentally, with RMSE values of 5.73% for differential pressure and 7.38% for heat–transfer coefficient, indicating strong predictive reliability.

Latin Hypercube Sampling provides 50 design points for surrogate construction, and an additional validation set confirms approximation errors below 5% for both j and f, ensuring that the RBF model captures the essential nonlinearity of the thermo–hydraulic response. The MOGA search identifies optimal geometries where the fin spacing increases from 1.75 mm to about 2.40 mm, while fin amplitude shifts slightly downward, a combination that enhances mixing but avoids excessive drag.

Optimization results show that the Colburn factor rises by 17.62%, while the friction factor decreases by 20.76%, highlighting a beneficial shift in the j–f balance. CFD comparisons between the baseline and optimized configurations reveal smoother velocity distributions, reduced near–wall pressure gradients, and more uniform temperature fields, all contributing to improved performance.

Mekki et al. [65] developed a voxel-based topology optimization framework combined with a genetic algorithm to generate unconventional fin geometries for aerospace heat exchangers. Their method couples OpenFOAM CFD simulations with a GA that freely alters fin shape within a 10 mm $\times$ 3 mm fluid domain, using up to 2500 initial mutation attempts and population sizes of 95 individuals. The fitness function incorporates total heat transfer Q and pressure drop ΔP, following the composite form $F = Q/(\Delta P)^{1/3}$, which favors designs that balance enhanced convection with reasonable hydraulic penalties.

Results show rapid convergence over roughly 60 generations, with optimized single-fin shapes achieving performance improvements exceeding 45% relative to the rectangular baseline. The best two-row configurations reach improvements near 89%, owing to reduced pressure drops combined with moderately increased heat rates.

Sensitivity study shows that population size has the strongest influence on GA performance, with sizes above 95 yielding only minor gains but substantially longer computational time. Cutoff and elite number affect geometric features but have limited impact on ultimate fitness. Finally, Reynolds-number tests confirm that optimized fins outperform the baseline across the range, with j-factor increases growing as Re rises, though at the cost of higher f-factor. Overall, the approach demonstrates that GA-based topology optimization coupled with CFD can uncover high-efficiency freeform fins that would be extremely difficult to conceive manually.

Cui et al. [66] present a detailed thermo–economic investigation and genetic-algorithm

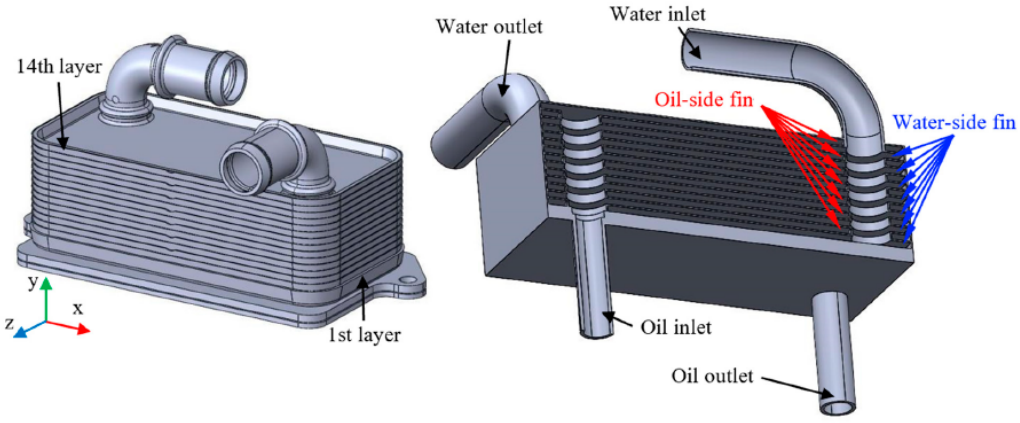

Figure 2.17. Geometry of the analysed plate–fin heat exchanger and computational model adopted by Li et al. [67]. The exchanger consists of multiple stacked fin layers with alternating oil-side and water-side serrated staggered fins.

optimization of plate–fin heat exchangers equipped with wavy fins. The study uses a generalized air-side thermal–hydraulic correlation, valid for Reynolds numbers between 400 and 11500, to evaluate heat-transfer and friction characteristics across a broad range of fin geometries.

Parametric analysis shows that wavy fins consistently outperform plain fins, especially at low Reynolds numbers, where combined heat-transfer and friction characteristics benefit from reduced amplitude-to-diameter ratios.

Two single-objective optimizations are performed using a genetic algorithm: one maximizing effectiveness, and one minimizing the modified entropy-generation number. These analysis results demonstrate, that the entropy-based criterion provides a more meaningful overall improvement than maximizing effectiveness alone.

Overall, the work confirms that wavy-fin comprehensive performance is strongly tied to geometric ratios, and that GA-based optimization can systematically achieve designs that outperform parametric selections, offering a reliable pathway for practical PFHE design under coupled thermal and economic constraints.

Li et al. [67] conducted a multi-objective optimization study on a plate–fin heat exchanger equipped with serrated staggered fins, combining CFD simulations, support vector regression (SVR) surrogate modeling, and NSGA-II. The thermo–hydraulic response is evaluated by varying three main parameters: fin-angle, oil-flow rate, and water-flow rate. A porous-media representation is used for the finned region, reducing computational cost while maintaining prediction accuracy, with average deviations below 5%.

Figure 2.17 illustrates the geometric configuration and flow arrangement considered in the optimization study, clarifying the separation between the oil and water circuits and the layered fin architecture that motivates the porous-media modelling of the finned

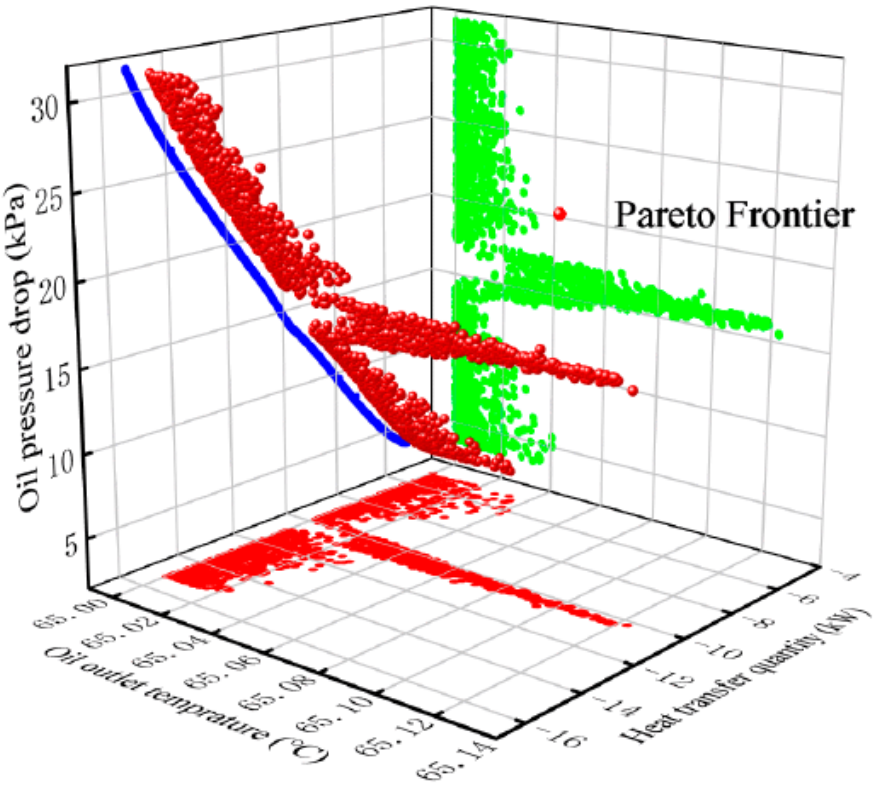

Figure 2.18. Pareto front obtained via NSGA-II for the multi-objective optimization of the plate–fin heat exchanger analysed by Li et al. [67].

core.

Forty-five transient CFD cases are generated to train the SVR models for heat-transfer rate, oil-side pressure drop, and oil-outlet temperature. The results show strong nonlinear coupling among the objectives. Increasing oil-flow rate improves heat-transfer performance up to approximately 9.7 L/min, beyond which additional viscous dissipation limits gains. Fin-angle also plays a key role: values above 60° enhance local mixing and raise heat-transfer rate, but they also increase oil-side pressure drop. At lower angles, viscous effects become unexpectedly dominant, leading to reduced overall performance.

SVR surrogates enable efficient multi-objective optimization, with NSGA-II producing a broad Pareto front balancing thermal enhancement against pump penalties.

The Pareto front shown in Figure 2.18 highlights the strong trade-off between heat-transfer enhancement, oil-side pressure drop, and oil outlet temperature. The distribution of Pareto-optimal solutions confirms that improvements in thermal performance are systematically associated with increased hydraulic penalties, thereby justifying the adoption of a multi-objective optimization framework.

A final compromise geometry is selected using TOPSIS, yielding an optimal fin-angle

of 63.01°, oil-flow rate of 9.7 L/min, and water-flow rate of 6.45 L/min. This configuration achieves a heat-transfer rate of about 9.79 kW and an oil-pressure drop of roughly 13.6 kPa. The study demonstrates that integrating CFD, SVR surrogates, and evolutionary optimization offers a robust and flexible framework for PFHE design, especially for highly coupled problems where geometric and flow interactions cannot be captured by simpler correlations.

Guan et al. [68] propose a thermo–hydraulic optimization framework for serrated fins in plate–fin heat exchangers by combining a high-fidelity CFD model with machine-learning surrogates. The study focuses on how fin height, spacing, thickness, and serration pitch affect the Colburn factor j, friction factor f, and the combined entropy-generation metric N_s. The simulations cover Reynolds numbers from 350 to 7000, enabling a broader validity range than most earlier serrated-fin investigations.

A Gaussian-process surrogate is trained on the CFD dataset and then paired with a multi-objective genetic algorithm. The optimized configuration achieves an increase of about 3.7% in the j factor and a reduction of nearly 7.8% in f relative to the baseline, reflecting a more balanced hydraulic–thermal behavior. More importantly, the entropy-generation number decreases by approximately 31%, indicating that the optimized fin geometry reduces irreversibility in a way that earlier design heuristics rarely capture.

The integration of CFD, Gaussian-process learning, and evolutionary search offers a robust optimization pathway for serrated-fin PFHEs. The framework uncovers parameter interactions that are subtle and occasionally a bit irregular, yet it provides meaningfully improved performance across the tested flow range.

2.5. Concluding remarks

This chapter has reviewed the extensive body of literature on plate–fin heat exchangers, with particular emphasis on offset-strip and wavy fin geometries and on the optimization strategies applied to their design. The analysis has shown that, despite decades of experimental, analytical, and numerical investigations, the thermo–hydraulic behaviour of these extended surfaces cannot yet be described by a unified modelling framework. Existing knowledge remains fragmented across studies addressing limited ranges of geometry, flow regime, or working fluid.

For offset-strip fins, the literature consistently highlights the role of boundary-layer interruption, wake formation, and vortex shedding in enhancing convective heat transfer, at the expense of increased pressure losses. Experimental data and semi-empirical correlations provide valuable trends, yet their applicability is often restricted by simplifying assumptions and calibration to specific operating conditions. Similar limitations apply to wavy fins, where curvature-induced secondary flows and transitional effects

dominate performance in a strongly geometry-dependent manner. Although numerical studies have clarified key flow mechanisms, their results are frequently tied to specific configurations, limiting their transferability to general design practice.

The review of optimization-oriented studies indicates that evolutionary and genetic algorithms are effective tools for exploring the highly nonlinear design space of PFHEs and for identifying trade-offs between heat transfer enhancement, pressure losses entropy generation, and economic objectives. However, a critical examination of the literature reveals that economic modelling within these optimization frameworks is predominantly limited to operational cost metrics, typically associated with the energy required to drive fluid flow through the exchanger.

The explicit modelling of radiator cost from a manufacturing perspective, including material usage, production time, and energy consumption of manufacturing equipment, is instead scarcely addressed or entirely neglected. As a consequence, many studies rely on incomplete cost representation that may bias design decisions towards thermally efficient but economically suboptimal solutions when evaluated at the component or system level.

Taken together, the literature surveyed in this chapter highlights the need for optimization frameworks that combine physically accurate thermo–hydraulic models with comprehensive and scalable cost formulations. In particular, the integration of manufacturing-related cost models within genetic optimization strategies emerges as a key requirement for industrially relevant PFHE design. Addressing this gap constitutes one of the main objectives of the present thesis, which aims to extend current optimization approaches beyond purely operational cost considerations.

CHAPTER 3

Physical and Cost Modeling of Plate–Fin Heat Exchangers

3.1. Introduction

As discussed in chapters 1 and 2 plate–fin heat exchangers (PFHEs) are among the most widely adopted compact heat exchanger technologies in industrial applications requiring high thermal effectiveness, structural robustness, and reduced mass and volume. Their modular architecture, based on the repetitive stacking of finned plates, cladding sheets, side bars, and manifolds, enables a high degree of geometric flexibility, while simultaneously introducing a strong coupling between thermo-fluid dynamic performance, manufacturability, and production cost.

Recent advances in the modelling of PFHEs have primarily focused on the development of accurate predictive tools for their thermo–hydraulic behaviour, with particular attention devoted to the characterisation of extended surfaces such as offset-strip fins and wavy fins. Among the most comprehensive and recent contributions, the works by Grespan et al. [9, 29] have established a rigorous multiscale framework in which detailed analyses at fin level are consistently integrated with global formulations for complete plate–fin heat exchangers. This modelling strategy allows the derivation of physically grounded correlations for heat transfer and pressure losses, while explicitly accounting for effects that are often neglected in simplified design approaches, such as entrance losses and the hydraulic contribution of inlet and outlet manifolds.

Building upon this modelling philosophy, the present chapter adopts a hierarchical approach aimed at providing a unified description of both the physical behaviour and the production cost of plate–fin heat exchangers. The analysis is organised across progres-

NOMENCLATURE

Latin letters

a	wave amplitude [m]
A	area [m^2]
b_i	coefficients in Equation (3.65)
c_i	coefficients in Equation (3.66)
c_p	specific heat [$J\,kg^{-1}\,K^{-1}$]
C	heat capacity rate [$W\,K^{-1}$]
d_{kr}	coefficients in Equation (3.69)
D_h	hydraulic diameter [m]
e_{kr}	coefficients in Equation (3.70)
f	equivalent Darcy friction factor [−]
h	enthalpy [$kg\,m^2\,s^{-2}$]
H	heat exchanger height [m]
j	Colburn factor [−]
l	offset length and half the wavelength [m]
L	heat exchanger core length [m]
L_e	effective wavy fin length [m]
$\vec{n}$	normal unit vector [−]
N_{ch}	number of internal channels [−]
Nu	Nusselt number [−]
NTU	number of transfer units [−]
p	fluid pressure [Pa]
P	wetted perimeter [m]
Pr	Prandtl number [−]
$\vec{q}$	heat flux [$W\,m^{-2}$]
$\dot{Q}$	heat [W]
R	thermal resistance [$K\,W^{-1}$]
Re	Reynolds number [−]
S	heat exchanger thickness [m]
t	fin thickness [m]
T	temperature [K]
U	overall heat transfer coefficient [$W\,m^{-2}\,K^{-1}$]
$\vec{v}$	fluid velocity [$m\,s^{-1}$]
W	manifold width [m]
x	fin pitch [m]
y	fin height [m]

Greek letters

β	concentrated loss coefficient [−]
ε	effectiveness [−]
ϑ	dimensionless temperature [−]
λ	thermal conductivity [$W\,m^{-1}\,K^{-1}$]
μ	dynamic viscosity [Pa s]
ν	kinematic viscosity [$m^2\,s^{-1}$]
ρ	density [$kg\,m^{-3}$]
σ_m	momentum sink [$m\,s^{-2}$]
Φ	relative friction factor in the entrance region [−]
χ	single fin module number [−]
Ψ	relative Nusselt number in the entrance region [−]

Subscripts

b	bulk
ch	channel
e	entrance
exp	experimental
ext	external
F	Fanning
fd	fully developed
i	inlet
int	internal
m	model
o	outlet
s	solid
t	turbulent
w	wall

Superscripts

*	dimensionless

sively increasing levels of complexity, starting from the characterisation of elementary fin geometries and extending to the complete heat exchanger assembly.

Offset-strip fin geometries are examined in detail by introducing the governing equations and correlations required to predict their thermo-fluid dynamic performance. These physical models are then complemented by a dedicated cost formulation, specifically tailored to capture the material usage, production time, and industrial energy demand associated with the manufacturing of offset-strip fins within a PFHE core.

An analogous modelling framework is subsequently applied to wavy fin geometries. The corresponding thermo-fluid dynamic formulation highlights the distinctive flow and heat transfer mechanisms induced by the waviness of the fins, while the associated cost model is developed in full consistency with the assumptions adopted for offset-strip fins.

The modelling framework is finally extended to the plate–fin heat exchanger as an integrated system. The fin-scale thermo-fluid dynamic models are embedded within a global formulation capable of predicting the overall thermal performance and pressure losses of PFHE radiators, explicitly including the contribution of manifolds and entrance regions. This system-level physical description is complemented by a comprehensive cost model for the complete heat exchanger, enabling the evaluation of the total production cost as a function of geometry, fin configuration, and design choices.

Through this structured and multiscale approach, the chapter establishes a coherent link between local fin-scale physics, global thermo–hydraulic performance, and production cost, thereby providing a robust foundation for thermo–economic assessment and optimisation of plate–fin heat exchangers.

3.1.1. Engineering background and modelling framework

In the present analysis, offset-strip fins with straight vertical walls, radiused corners, and centred offset are considered as a reference geometry for the development of a combined physical and economic modelling framework for plate–fin heat exchangers. Owing to their widespread industrial use and to the extensive literature available, offset-strip fins provide a robust and well-established basis for fin-scale modelling.

The thermo-fluid dynamic behaviour of offset-strip fins is described by recalling governing equations and correlations available in the literature, which are adopted here as a consolidated and validated reference. In particular, the dependence of the equivalent Darcy friction factor f and the Colburn factor j on geometric parameters and flow conditions is presented following the modelling framework proposed by Grespan et al [9, 29]. These physical models are not intended as an original contribution of the present work, but rather as the necessary engineering background required to consistently characterise fin-scale performance and to enable its integration into system-level models.

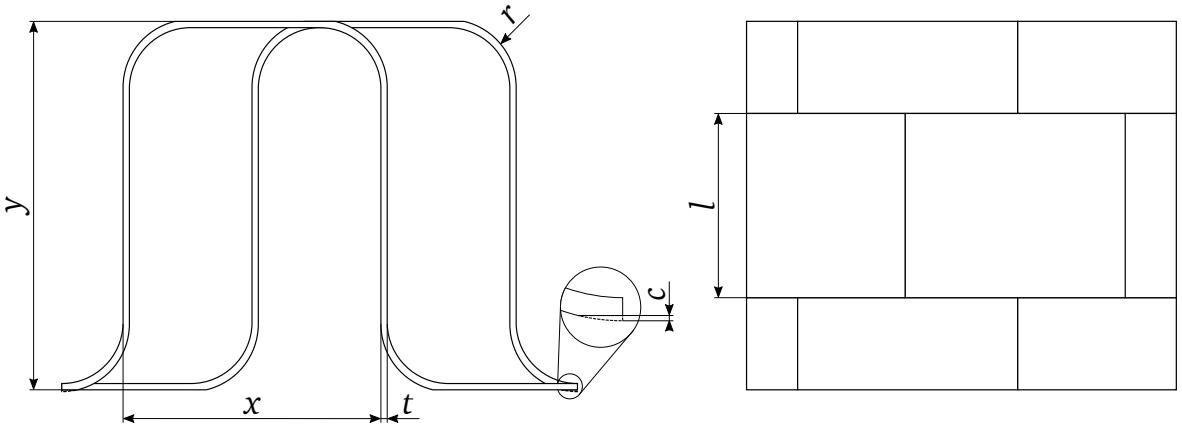

Figure 3.1. Front and top views of the examined offset-strip fin geometry, along with the most significant dimensions.

The geometric parameters defining the offset-strip fin configuration are introduced consistently with classical definitions reported in the literature, in particular following Yang and Li [69], while adopting a dedicated notation to avoid ambiguities with other fin geometries analysed in subsequent sections. The thermo-fluid dynamic characterisation is based on a systematic Design of Experiments approach, in which heat transfer and pressure losses are evaluated through CFD analyses of periodic fin modules over representative ranges of geometric and flow parameters.

Within this consolidated physical framework, the original contribution of the present work lies in the development of a dedicated cost model for offset-strip fins. Building upon the fin-scale thermo-fluid dynamic description recalled in this section, a systematic formulation is introduced to quantify material usage, production time, and industrial energy consumption associated with the manufacturing of offset-strip fins within a PFHE core. The resulting cost functions are formulated in a modular and scalable manner, enabling their consistent coupling with literature-based performance correlations and supporting thermo–economic assessments at fin scale.

3.1.2. Problem statement

Offset-strip fins with straight vertical walls and symmetric or centred offset are considered. The front and top views of the examined offset-strip fin geometry are depicted in the drawings of Figure 3.1, along with the key dimensional parameters. The fin pitch, denoted by x, is the distance between two consecutive vertical walls, including the thickness of one of the two walls t. The external corner radius between vertical and horizontal fin walls is denoted by r, while the fin height is identified by y. During the production process of compact heat exchangers the fins undergo mechanical deformations as a result of the stacking of finned plates and brazing sheets. The most marked effect consists of

a vertical crushing, which is reproduced by cutting the outer fillet radii by an amount c, so that they are no longer tangent to the horizontal walls. c is set to 0.5% of the fin height to introduce a small deformation, that is not too excessive for the configurations with small pitch values. The centred offset constraint determines a relationship between fin pitch, the maximum value of the external fillet radius, and wall thickness:

$$x = 4\,r_{\max} - 2\,t\ . \tag{3.1}$$

The flow cross-sectional area of the considered OSF geometry equates to:

$$A_{\mathrm{f}} = 2\,x\,y - A_{\mathrm{w}}\,, \tag{3.2}$$

where A_{w} stands for the portion of frontal area occupied by the fin walls:

$$\begin{aligned} A_{\mathrm{w}} = {} & 2\,r^2\left[\arcsin\left(\frac{c}{r}\right) - \frac{\pi}{2} - \arcsin\left(\frac{c-r}{r}\right)\right] \\ & + 2\,c\left[\sqrt{r^2 - c^2} - (c-r)\sqrt{\frac{2\,r}{c} - 1}\right] \\ & + 2\,t\left(y - \frac{\pi+2}{2}\,t + \pi\,r\right)\ . \end{aligned} \tag{3.3}$$

The wetted perimeter is given by:

$$P = 4\left\{x + y + r\left[\pi - 2 - \arcsin\left(\frac{\sqrt{2\,r\,c - c^2}}{r}\right)\right]\right\} - 2\,\pi\,t - 4\sqrt{2\,r\,c - c^2}\,. \tag{3.4}$$

The heat transfer area A_{ref} consists of the whole fluid-solid interface of the fins, including leading and trailing edges, along with the area wetted by the fluid on the upper and lower horizontal surfaces:

$$A_{\mathrm{ref}} = 2\,l\,P + 4\,(A_{\mathrm{w}} - 2A_{\mathrm{ov}})\,, \tag{3.5}$$

where A_{ov} is the portion of fin walls frontal area given by the overlap of two successive single fins.

$$\begin{aligned} A_{\mathrm{ov}} = {} & r^2\left[\arcsin\left(\frac{c+t-r}{r}\right) - \arcsin\left(\frac{c-r}{r}\right)\right] \\ & + (c+t-r)\sqrt{(t+c)(2\,r-c-t)} \\ & + (r-c)\sqrt{2\,r\,c - c^2} \end{aligned} \tag{3.6}$$

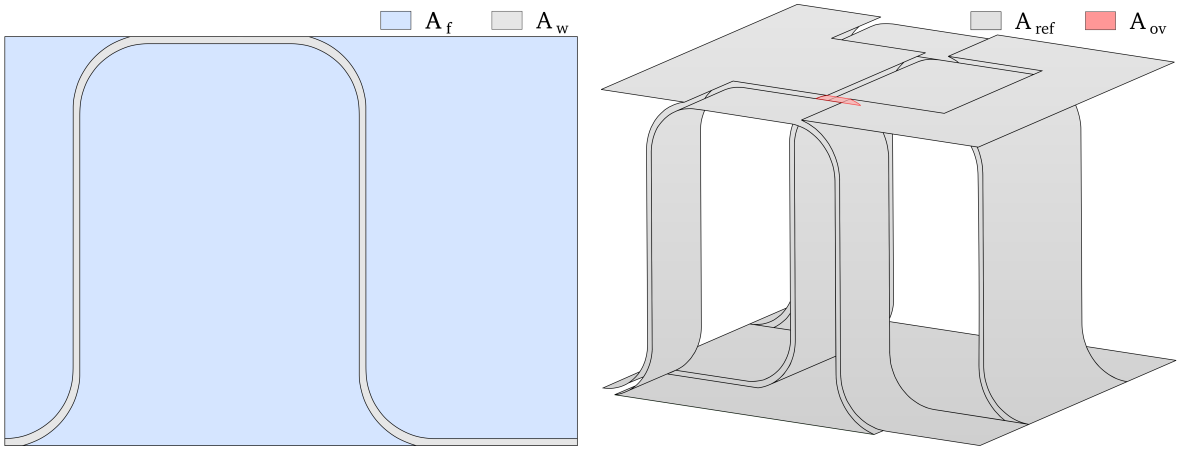

Figure 3.2. Flow cross-sectional area (a) and heat transfer area (b) of the examined offset-strip fins.

The reference flow cross-sectional area and heat transfer surface are depicted in the drawings of Figure 3.2.

3.1.3. Numerical methods

3.1.3.1. Governing equations

Offset-strip fins are modelled using elementary periodic unit geometries, obtained by exploiting the geometric and flow periodicity in the streamwise and spanwise directions. The flow is assumed incompressible and periodic between the inlet and outlet sections of the computational domain. The velocity, pressure, and temperature fields are computed by solving the steady-state continuity, momentum, and energy equations, which in dimensionless form can be written as:

$$\begin{cases} u_j^* \dfrac{\partial u_i^*}{\partial x_j^*} = -\dfrac{\partial p^*}{\partial x_i^*} + \dfrac{\partial}{\partial x_j^*}\left[\left(\dfrac{1}{\mathrm{Re}} + \nu_\mathrm{t}^*\right)\dfrac{\partial u_i^*}{\partial x_j^*}\right] \\ \dfrac{\partial u_i^*}{\partial x_i^*} = 0 \\ u_j^* \dfrac{\partial T^*}{\partial x_i^*} = \dfrac{\partial}{\partial x_j^*}\left[\left(\dfrac{1}{\mathrm{Re}\,\mathrm{Pr}} + \dfrac{\nu_\mathrm{t}^*}{\mathrm{Pr}_\mathrm{t}}\right)\dfrac{\partial T^*}{\partial x_j^*}\right] \end{cases} \tag{3.7}$$

The temperature field within the fin walls is derived from the numerical solution of the steady state heat equation.

$$\frac{\partial}{\partial x_j^*}\left(\lambda_\mathrm{s}^* \frac{\partial T^*}{\partial x_j^*}\right) = 0 \tag{3.8}$$

The fin height y is assumed as the reference length of the problem, while the velocity scale, defined as the integral mean velocity over the inlet surface, is taken as unitary. The

Reynolds number is defined as follows:

$$\mathrm{Re} = \frac{\bar{u}_{\mathrm{i}}\, y}{\nu} \,. \tag{3.9}$$

The dimensionless thermal conductivity of the fin walls is derived by scaling the thermal conductivity of aluminium by the one of the neighbouring fluid:

$$\lambda_{\mathrm{s}}^{*} = \frac{\lambda_{\mathrm{Al}}}{\lambda_{\mathrm{f}}} \,, \tag{3.10}$$

the values of λ of aluminium and all the considered fluids are reported in Table 3.1.

At $\mathrm{Re} \geq 1000$, the k-ω SST turbulence model [70], coupled with a low-Reynolds wall modelling approach, is employed to compute eddy viscosity ν_{t}^{*}. On the other hand, for all flows at $\mathrm{Re} \leq 200$ laminar analyses are carried out, therefore, in this case eddy viscosity is set to zero. At $\mathrm{Re} = 500$ laminar simulations are performed as long as a satisfactory degree of numerical convergence is achieved, i.e. when all residuals are of the order of 10^{-6}. Otherwise, the turbulence model is employed. In the turbulent analyses, a unitary value for the turbulent Prandtl number Pr_{t} is considered, on the basis of the Reynolds analogy.

3.1.3.2. Boundary conditions

Fully developed flow conditions are attained by applying suitable field mapping boundary conditions for the velocity and temperature fields, between the inlet and outlet sections. At each iteration of the solution algorithm, the values of dimensionless velocity and temperature at each cell centre on the outlet patch are applied to the respective cell centre on the inlet patch, after being scaled to maintain the desired integral mean values at the inlet: $\bar{u}_{\mathrm{i}}^{*} = 1$ and $\overline{T}_{\mathrm{i}}^{*} = 0$. At the outlet, the surface mean pressure is set to a zero reference value $\bar{p}_{\mathrm{o}}^{*} = 0$, while at the inlet a zero gradient condition is applied to pressure. Periodic conditions are enforced along the spanwise direction. At the top and bottom boundaries a uniform entering heat flux is imposed: $q''^{*} = 1$. At the walls, no-slip conditions are applied to the velocity field and a zero pressure gradient is imposed. Finally, continuity of temperature and heat flux is enforced at all fluid-solid interfaces.

Table 3.1. Reference values of thermal conductivity of aluminium and oil, water, and air flows.

	Aluminium	Oil	Water	Air
$\lambda\,[\mathrm{W\,m^{-1}\,K^{-1}}]$	237.0	0.129	0.609	0.024

3.1.3.3. Spatial discretisation

The numerical analyses are performed using a Finite Volume conjugate heat transfer solver, previously validated in [71] and implemented in the open-source software OpenFOAM 7 [72]. Convective terms are discretised using second-order upwind schemes, while diffusive terms are treated with central differencing and explicit non-orthogonality correction. Pressure–velocity coupling is handled via the SIMPLE algorithm [73].

3.1.4. Design of Experiments

The dependence of the thermal-hydraulic performance of OSFs on geometric and flow parameters is evaluated by means of a Design of Experiments procedure. The dimensionless fin pitch and offset length are assumed as the most influential geometric parameters [74], instead the fillet radius and wall thickness are considered of secondary importance. The levels of the dimensional parameters x^*, l^* and of the flow parameters, i.e. pairs of Re and Pr values, are chosen by considering a set of configurations which are representative of real industrial applications, including coolers for hydraulic and lubricating oils, water radiators, and air-to-air heat exchangers [75]. Thus, eight levels are selected for x^* and l^*, and eleven different flows are taken into account. The fillet radius is varied indirectly by computing it as a function of fin pitch and wall thickness, according to Equation (3.1). This strategy allows for the removal of one geometric parameter from the DOE, which vastly reduces the number of numerical analyses to perform. On the other hand, the effects of pitch and radius variations on thermal-hydraulic performance may be confounded, as the fillet radius is aliased by Equation (3.1). In this case, this is deemed acceptable as the fillet radius is most likely to have a lower order influence on head losses and heat transfer with respect to the fin pitch [74]. The dimensionless wall thickness t^* is kept constant at a value of 0.017, again in an effort to reduce the number of simulations, and because in real applications the choice of the wall thickness values is limited, due to the commercially available aluminium sheets and the need to satisfy criteria of structural integrity and mechanical resistance of the heat exchangers. In an effort to obtain an accurate sampling of the parameter space a full factorial DOE with respect to the factors x^* and l^* and the (Re, Pr) couples is performed. This is equivalent to performing a fractional factorial DOE with respect to x^*, l^*, r^*, Re, and Pr. Table 3.2 reports the levels chosen for each geometric and flow factor, while the number of numerical analyses performed amounts to 704.

Integral head losses and heat transfer rates are evaluated by means of an equivalent Darcy friction factor and mean Nusselt number. The equivalent friction factor f is derived

from the Darcy-Weisbach formula, where the reference length is the fin height:

$$f = \frac{y\,(\bar{p}_{\mathrm{i}} - \bar{p}_{\mathrm{o}})}{l\,\rho\,\bar{u}_{\mathrm{i}}^2}\,, \tag{3.11}$$

overbars denote integral mean values over inlet (i) and outlet (o) sections. The mean Nusselt number over the heat transfer area is:

$$\mathrm{Nu} = \frac{\dot{Q}\,y}{\lambda A_{\mathrm{ref}}(\overline{T}_{\mathrm{w}} - \overline{T}_{\mathrm{b}})}\,, \tag{3.12}$$

where $\dot{Q}$ stands for the heat entering the system through the top and bottom surfaces.

3.1.5. Derivation of response surfaces

The response surfaces introduced in the following were obtained by defining suitable objective functions and fitting them to the numerical dataset using a variant of the Levenberg–Marquardt algorithm [76], as implemented in the SciPy library [77]. Although least-squares-based response surfaces generally provide a lower approximation accuracy compared to ANN-based approaches, they are adopted here due to their simplicity, robustness, and ease of implementation.

Data points in the range $50 \leq Re \leq 200$ are employed to fit the laminar response surfaces, while points in the range $1000 \leq Re \leq 12000$ are used for the turbulent regime. The data obtained at $Re = 500$ are assigned to either the laminar or turbulent fit depending on the specific geometric configuration. The transition between flow regimes is handled by smoothly combining the laminar and turbulent response surfaces through a hyperbolic tangent function, which ensures a continuous and differentiable behaviour across the transition region.

Table 3.2. Selected levels for the geometric and flow factors.

x^*	0.166	0.3	0.44	0.7	0.9	1.25	1.56	1.966	
l^*	0.3	0.6	1.6	2.5	3.5	5.0	8.0	18.75	
Re	50	100	200	500	1000	2000	3000	5000	12000
Pr	190	190	190	190	7	7–0.71	7–0.71	0.71	0.71

3.1.6. Equivalent Darcy friction factor

The dependence of the equivalent Darcy friction factor on the Reynolds number is modelled by polynomial functions in log-log scale:

$$\log f_l = b_1 \log \mathrm{Re} + b_2 \,, \tag{3.13}$$

$$\log f_t = b_3 \log^{-0.48} \mathrm{Re} + b_4 \,. \tag{3.14}$$

These formulations are used to correlate results on both pressure losses and heat transfer (see Section 3.1.7) as they provide very good accuracy levels when used for extended surfaces [75]. The values of the b_m coefficients found in Equations (3.13) and (3.14) are obtained from the following relation, as a function of the geometrical parameters:

$$b_m = k_1 (x^*)^{k_2} + k_3 x^* + k_4 \log l^* + k_5 l^* + k_6 \,. \tag{3.15}$$

Equation (3.15) is formulated by progressively adding polynomial and logarithmic based terms as long as these provide significant improvements to the accuracy of the response surface. The values of the k_n coefficients are determined through the aforementioned least-squares-based curve fitting procedure, and their values are listed in Table 3.3. In order to suitably combine Equations (3.13) and (3.14) a smoothing function based on the hyperbolic tangent is formulated:

$$s = \frac{1}{2}\left[1 + \tanh\left(\frac{\chi - \chi_0}{\sigma}\right)\right] . \tag{3.16}$$

In Equation (3.16) χ stands for the generic independent variable, χ_0 locates the smooth step on the independent variable axis, while σ determines the sharpness of the transition.

The laminar and turbulent response surfaces (Equations (3.13) and (3.14)) are combined into a single equation by using a variant of Equation (3.16) centred at the transition

Table 3.3. Values of k_n coefficients in Equation (3.15).

	k_1	k_2	k_3	k_4	k_5	k_6
b_1	-345.50	1.00033743	345.5969	0.0651851	-0.00681313	-0.9987
b_2	4421.93	1.00032627	-4423.93	-0.367102	0.020911319	3.76899
b_3	-4091.5	0.00026439	0.820411	-0.282540	0.017530123	4095.36
b_4	1356.77	1.00001750	-1356.95	-0.049099	-0.00012869	-3.1953

Reynolds number $\mathrm{Re}_{\mathrm{trans}}$:

$$\log f = s_{\mathrm{Re}} \log f_{\mathrm{t}} + (1 - s_{\mathrm{Re}}) \log f_{\mathrm{l}} \,, \tag{3.17}$$

$$s_{\mathrm{Re}} = \frac{1}{2}\left[1 + \tanh\left(\frac{\log \mathrm{Re} - \log \mathrm{Re}_{\mathrm{trans}}}{0.08}\right)\right] . \tag{3.18}$$

The transition Reynolds number is in turn determined by applying the previously defined smoothing function (Equation (3.16)) between the Re-values of 750 and 350 which have been designated as transition values, on the basis of the fin dimensionless pitch alone.

$$\mathrm{Re}_{\mathrm{trans}} = s_{x^*} 350 + (1 - s_{x^*}) 750 \,, \tag{3.19}$$

$$s_{x^*} = \frac{1}{2}\left[1 + \tanh\left(\frac{x^* - 0.166}{1.1}\right)\right] . \tag{3.20}$$

The values of transition Reynolds number in Equation (3.19), along with the values of σ in Equations (3.18) and (3.20) were selected with the aim of maximising the accuracy of the overall response surface with respect to the data points.

3.1.7. Colburn factor

Compared to friction and pressure losses, heat transfer effectiveness depends on one additional flow parameter, namely the Prandtl number. Traditionally, the dependence of the Nusselt number with respect to the Prandtl number is managed by introducing the Colburn factor:

$$j = \frac{\mathrm{Nu}}{\mathrm{Re}\,\mathrm{Pr}^n} = \mathrm{St}\,\mathrm{Pr}^{n+1} \,, \tag{3.21}$$

where n is the scaling exponent for the Prandtl number, which is usually set to 1/3 in most applications.

Following the suggestions from Kays and London [78], the Prandtl scaling exponent is determined by performing four sets of CFD analyses at the Re-values of 2000 and 3000 and Pr-values of 0.71 and 7.0. The Prandtl exponent related to each geometric configuration is determined by the following equation:

$$n = \frac{\log \mathrm{Nu}\big|_{\mathrm{Pr}=7} - \log \mathrm{Nu}\big|_{\mathrm{Pr}=0.71}}{\log 7 - \log 0.71} \,. \tag{3.22}$$

The CFD derived n-values are also employed to derive a correlation as a function of the dimensional parameters:

$$n = (0.259\,(l^*)^{-1/3} + 0.072) \log x^* + 0.044 \log l^* + 0.569 \,. \tag{3.23}$$

The laminar and turbulent response surfaces for the Colburn factor are derived by means of the same procedure employed for the friction factor in Section 3.1.6:

$$\log j_l = d_1 \log^{0.2} \mathrm{Re} + d_2 \,, \tag{3.24}$$

$$\log j_t = d_3 \log^2 \mathrm{Re} + d_4 \,. \tag{3.25}$$

The values of the d_m coefficients found in Equations (3.24) and (3.25) are expressed as a function of the geometric parameters by the two following relations:

$$d_1, d_2 = k_1 x^* + k_2 (x^*)^{k_3} + k_4 l^* + k_5 \log l^* + k_6 \log x^* \log l^* + k_7 \,, \tag{3.26}$$

$$d_3, d_4 = k_1 (x^*)^{k_2} + k_3 (l^*)^{k_4} + k_5 \log l^* + k_6 \,, \tag{3.27}$$

where the values of k_n coefficients are again determined via the curve fitting procedure described in the introductory part of Section 3.1.5. The resulting k_n-values are reported in Table 3.4.

The laminar and turbulent correlations are combined by means of the same smoothing function used for the equivalent Darcy friction factor, which is expressed by Equation (3.18). The transition Reynolds number is again derived by means of Equations (3.19) and (3.20), and the final response surface assumes the familiar form:

$$\log j = s_{\mathrm{Re}} \log j_t + (1 - s_{\mathrm{Re}}) \log j_l \,. \tag{3.28}$$

3.1.8. Cost modelling of Offset strip fins

The following section presents the calculation of the volume, mass, and associated cost of a single repetitive offset-strip fin element. This element represents the basic modelling unit and is periodically repeated along both the streamwise and spanwise directions of the heat exchanger core.

The total volume of the single offset-strip fin module is evaluated as the product of the frontal area occupied by the fin walls and the offset length l, accounting for the

Table 3.4. Values of k_n coefficients in Equations (3.26) and (3.27).

	k_1	k_2	k_3	k_4	k_5	k_6	k_7
d_1	50.1014	-46.8119	1.06548	-0.0633	0.07918	1.06718	-8.5546
d_2	18.2244	-24.6789	0.76276	0.07360	-0.3988	-0.8820	10.3469
d_3	-111.656	0.000139	-6.7022	0.01874	0.29932	18.3093	-
d_4	1.4508×10^{-18}	-21.3283	45.7714	0.03263	-3.6445	-47.141	-

presence of two symmetric fin segments within the unit cell. Accordingly, the volume of the offset-strip fin element is expressed as:

$$V_{\mathrm{osf}} = A_w \, 2l, \tag{3.29}$$

where A_w denotes the frontal wall area. For convenience, A_w is recalled here as defined in Eq. (3.30), although it was previously introduced in the geometrical formulation of the offset-strip fin model.

$$\begin{aligned} A_{\mathrm{w}} = {} & 2\,r^2 \left[\arcsin\left(\frac{c}{r}\right) - \frac{\pi}{2} - \arcsin\left(\frac{c-r}{r}\right) \right] \\ & + 2\,c \left[\sqrt{r^2 - c^2} - (c-r)\sqrt{\frac{2\,r}{c} - 1} \right] \\ & + 2\,t \left(y - \frac{\pi+2}{2}\,t + \pi\,r \right). \end{aligned} \tag{3.30}$$

The mass of the single offset-strip fin element is obtained by multiplying the corresponding volume by the material density. In the present analysis, the density of aluminium is assumed to be constant and equal to $\rho_{\mathrm{al}} = 2700\ \mathrm{kg\,m^{-3}}$ for the sake of simplicity. Accordingly, the mass of the offset-strip fin element is expressed as:

$$m_{\mathrm{osf}} = V_{\mathrm{osf}}\,\rho_{\mathrm{al}}. \tag{3.31}$$

The cost of an individual offset-strip fin element is determined by scaling its mass with a unit cost expressed per kilogram of fin sheet material. Both internal and external fins are manufactured from aluminium alloys belonging to the 3000 series, which are widely adopted in brazed plate–fin heat exchangers owing to their favourable combination of formability and thermal performance. Based on current European market values, the corresponding unit material cost is reasonably assumed to be approximately $c_{\mathrm{osf}} = 5\ \mathrm{€\,kg^{-1}}$.

Consequently, the material cost associated with a single offset-strip fin element can be expressed as:

$$C_{\mathrm{osf}} = m_{\mathrm{osf}}\,c_{\mathrm{osf}}, \tag{3.32}$$

where c_{osf} denotes the unit material cost of the aluminium sheet employed in the fin stamping process.

3.2. Wavy Fins

In the following, the modelling framework previously introduced for offset-strip fins is extended to wavy fin geometries. The thermo-fluid dynamic behaviour of wavy fins is analysed with the objective of deriving continuous multivariate response surfaces for the equivalent Darcy friction factor f and the Colburn factor j, in direct analogy with the formulations developed for offset-strip fins.

The physical characterisation of wavy fins is carried out by adopting a Design of Experiments approach, in which each geometric configuration is analysed through dedicated Computational Fluid Dynamics simulations of a periodic wavy fin module under fully periodic flow conditions. This methodology enables a systematic investigation of the influence of the governing geometric and flow parameters on heat transfer and pressure loss characteristics, while ensuring consistency with the modelling assumptions adopted for offset-strip fins.

The cost formulation, which constitutes an original contribution of the present work, is developed to quantify the material usage, production time, and industrial energy consumption associated with the manufacturing of wavy fins within a PFHE core, thereby enabling a consistent thermo–economic assessment at fin scale.

3.2.1. Modelling approach

This study is focused on wavy or corrugated fins with a rectangular cross-section and a sinusoidal longitudinal development. The side walls have a uniform thickness, they are in-phase with each other and are slightly inclined with respect to vertical axis.

The relationship between the geometric and flow parameters of wavy fins and their thermal-hydraulic performance is studied by means of a Design of Experiments procedure, which is performed using computational methods. The levels of the geometric parameters are selected with the aim of covering the most relevant applications for vehicular applications, and a full factorial DOE is performed with respect to the dimensionless pitch, wavelength and amplitude. To this end, a CFD model comprising a unitary fin geometric under periodic flow conditions is developed for each geometric configuration. The numerical solution is attained by means of a validated conjugate heat transfer solver based on the Finite Volume method.

Preliminary numerical results on heat transfer and friction losses are used to derive response surfaces for the equivalent Darcy friction factor and Colburn factor as a function of the numerical parameters.

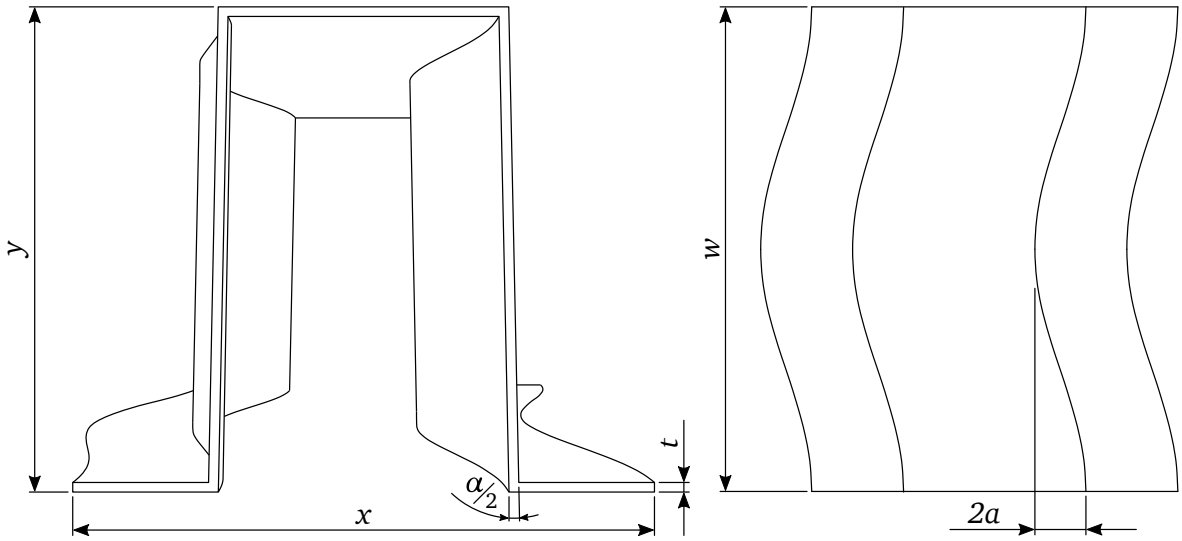

Figure 3.3. Front (left) and top (right) views of the examined wavy fin geometry, along with the most significant dimensions.

3.2.2. Problem statement

The present parametric analysis is performed on wavy fins presenting a rectangular cross-section with slightly sloped side walls, and sinusoidal longitudinal development. Figure 3.3 shows schematics of the front and top views of the wavy fin geometry considered, along with the most relevant geometric parameters. The pitch and height of the fin are denoted by x and y, respectively. The thickness of the walls is assumed uniform and it is represented by t. On the top view, w stands for the wavelength, while $2a$ refers to the peak-to-peak amplitude of the sine wave. The side walls are slightly inclined forming an angle $\alpha/2$ with the vertical axis.

The flow cross-sectional area of the examined wavy fin geometry is given by:

$$A_{\mathrm{f}} = x\,y - A_{\mathrm{w}}\,, \tag{3.33}$$

where A_{w} is the section of the overall frontal area occupied by the walls of the fin:

$$A_{\mathrm{w}} = 4\,t\left(\frac{x}{4} - t\right) + \frac{2\,t\,y}{\cos\alpha/2}\,. \tag{3.34}$$

The wetted perimeter is:

$$P = 4\left[2\left(\frac{x}{4} - t\right) + (y - t)\left(\tan\alpha/2 + \frac{1}{\cos\alpha/2}\right)\right]. \tag{3.35}$$

The heat transfer area includes the fluid-solid interface along with the sections of the top

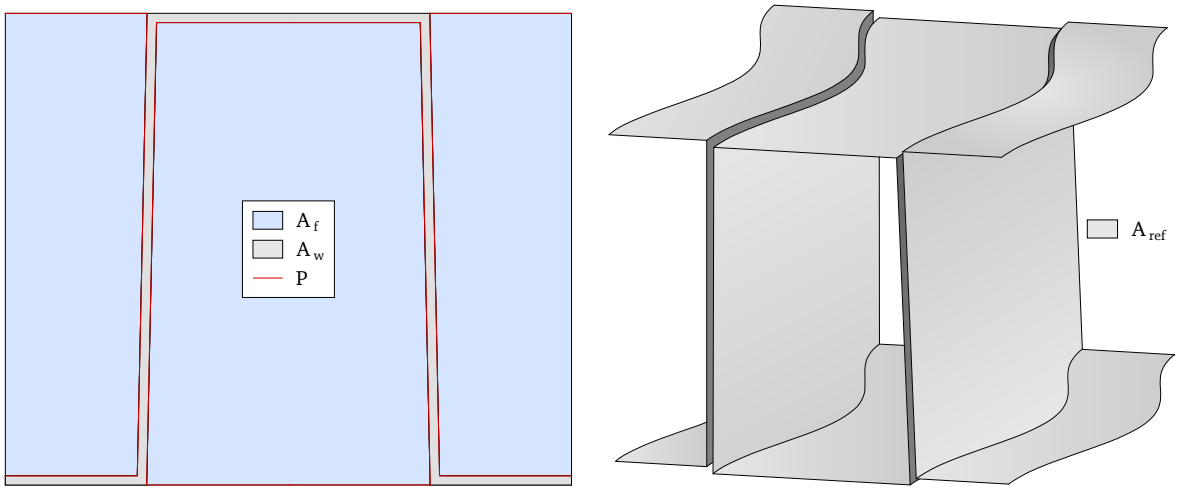

(a) (b)

Figure 3.4. Flow cross-sectional area, wetted perimeter (a), and heat transfer area (b) of the examined wavy fins.

and bottom surfaces which are in contact with the fluid:

$$A_{\text{ref}} = P\, l_{\text{a}}\,, \tag{3.36}$$

where l_{a} is the arc-length of the sinusoidal wave [79]:

$$l_{\text{a}} = 2w\,\frac{\sqrt{1+\gamma^2\pi^2}}{\pi} E\left(\frac{\gamma\pi}{\sqrt{1+\gamma^2\pi^2}}\right). \tag{3.37}$$

In Equation 3.46 $\gamma = 2a/w$ stands for the corrugation ratio of the wavy channel, while $E(\cdot)$ is the complete elliptic integral of the second kind. Examples of the flow cross-sectional area, wetter perimeter, and heat transfer area of the examined wavy fin geometries are depicted in the schematic of Figure 3.4.

3.2.3. Numerical methods

Wavy fins are analysed by developing Computational Fluid Dynamics models of basic unit geometries which are formed by considering the periodicity of the geometry and flow along the streamwise and spanwise directions. These numerical models are devised by considering the governing equations, boundary conditions, spatial discretisation schemes, and meshing parameters that were discussed for the parametric analysis of offset-strip fins. In addition, a dimensionless framework analogous to that presented in section 3.1.3 is employed, where the height of the fins y is taken as the reference length

and the remaining geometric parameters are scaled accordingly:

$$y^* = \frac{y}{y} = 1\,, \quad x^* = \frac{x}{y}\,, \quad w^* = \frac{w}{y}\,, \quad 2a^* = \frac{2a}{y}\,, \quad t^* = \frac{t}{y}\,. \tag{3.38}$$

3.2.4. Design of Experiments

The effects of the geometric and flow parameters of wavy fins on their thermal-hydraulic characteristics are assessed by means of a Design Of Experiments procedure. The non-dimensional pitch, wavelength, and amplitude are identified as the most relevant geometric parameters, while the inclination angle and thickness of the walls are considered of minor importance and are therefore assumed constant and excluded from the DOE. This assumption is also supported by common design practices associated with compact heat exchangers, where the selection of the thickness of the fins is often limited by the commercially available raw aluminium sheets and the need to guarantee the mechanical strength and stability of the heat exchangers. In addition, the inclination of the walls might be altered to facilitate the manufacturing process of the fins and possibly reduced wear on the dies.

A full factorial DOE is performed with respect to the dimensionless fin pitch, wavelength, and amplitude and the flow regime, which is defined by couples of Reynolds and Prandtl numbers. Table 3.5 reports the levels of the geometric parameters x^*, w^*, and $2a^*$, which are selected to cover a range of configurations relevant for the design of compact heat exchangers used in vehicular applications. The thickness and inclination angle of the walls are assumed constant and set to $t^* = 0.02$ and $\alpha = 2.4°$, respectively.

Integral results on head losses and heat transfer rates are expressed by the equivalent Darcy friction factor and Nusselt number. The former is retrieved from the Darcy-Weisbach formula:

$$f = \frac{2\,y\,(\bar{p}_{\mathrm{i}} - \bar{p}_{\mathrm{o}})}{w\,\rho\,\bar{u}_{\mathrm{i}}^2}\,, \tag{3.39}$$

where overbars represent integral mean values over inlet (i) and outlet (o) sections. The equivalent Nusselt number is defined according to Equation (3.12).

Table 3.5. Selected levels of the geometric parameters involved in the DOE analysis of wavy fins.

x^*	0.4	0.8	1.2	1.6	2.0
w^*	0.9	1.6	2.3	3.0	
$2a^*$	0.1	0.17	0.23	0.3	

3.2.5. Derivation of preliminary response surfaces

The preliminary numerical results obtained thus far are used as a basis for the derivation of response surfaces for the equivalent Darcy friction factor and Colburn factor. These response surfaces are obtained using the same approach which was extensively discussed in Section 3.1.5. However, this time the formulation of the equations is much more straightforward due to the very limited base data set. The response surfaces for the Darcy friction factor and Colburn factor are respectively:

$$\log f = b_1 (x^*)^{b_2} + b_3 (w^*)^{b_4} + b_5 (2a^*)^{b_6} + b_7 \left(\frac{2a^*}{w^*} \right), \tag{3.40}$$

$$j = d_1 (x^*)^{d_2} + d_3 (w^*)^{d_4} + d_5 (2a^*)^{d_6} + \left(\frac{2a^*}{w^*} \right)^{d_7}, \tag{3.41}$$

where the b_m and d_m coefficients are listed in Table 3.6.

Equations (3.40) and (3.41) hold only for Re = 5000, however, their validity can approximately be extended to other Re-values by introducing the scaling laws derived by Stasiek *et al.* [80]:

$$f = f\big|_{\mathrm{Re}=5000} \left(\frac{\mathrm{Re}}{5000} \right)^{-1/2}, \tag{3.42}$$

$$\mathrm{Nu} = \mathrm{Nu}\big|_{\mathrm{Re}=5000} \left(\frac{\mathrm{Re}}{5000} \right)^{2/3}. \tag{3.43}$$

3.2.6. Cost modelling of Wavy fins

Similarly to what has been presented for offset-strip fins, the following section introduces the set of equations employed to evaluate the volume, mass, and associated material cost of a single repetitive wavy fin element. This element represents the basic modelling unit and is periodically repeated along both the streamwise and spanwise directions of the heat exchanger core.

The total volume of the single wavy fin module is evaluated as the product of the frontal area occupied by the fin walls A_w as defined in Eq. (3.45) and the characteristic streamwise length l, represented in this case by the arch length l_a as expressed in

Table 3.6. Values of b_m and d_m coefficients in Equations (3.40) and (3.41), respectively.

m	1	2	3	4	5	6	7
b_m	−1138.82	3.5382×10^{-4}	1295.79	8.7618×10^{-5}	-158.24	8.8538×10^{-4}	3.817
d_m	0.392	0.00247	−0.0024	0.7765	0.4115	0.00495	4.5636

Eq. (3.46), then the volume of the wavy fin element is expressed as:

$$V_{\mathrm{wv}} = A_w \, l_{\mathrm{a}}, \tag{3.44}$$

For convenience,the formulations of A_w and l_{a} are recalled here, although they were previously introduced in the geometrical formulation of the wavy fin model.

$$A_{\mathrm{w}} = 4\,t\left(\frac{x}{4} - t\right) + \frac{2\,t\,y}{\cos\alpha/2}\,. \tag{3.45}$$

$$l_{\mathrm{a}} = 2\,w\,\frac{\sqrt{1+\gamma^2\,\pi^2}}{\pi} E\left(\frac{\gamma\,\pi}{\sqrt{1+\gamma^2\,\pi^2}}\right). \tag{3.46}$$

In Equation 3.46 $\gamma = 2a/w$ stands for the corrugation ratio of the wavy channel, while $E(\cdot)$ is the complete elliptic integral of the second kind.

The mass of the single wavy fin element is obtained by multiplying the corresponding volume by the material density. In the present analysis, the density of aluminium is assumed to be constant and equal to $\rho_{\mathrm{al}} = 2700\ \mathrm{kg\,m^{-3}}$ for the sake of simplicity. Accordingly, the mass of the wavy fin element is expressed as:

$$m_{\mathrm{wv}} = V_{\mathrm{wv}}\,\rho_{\mathrm{al}}. \tag{3.47}$$

The cost of an individual wavy fin element is obtained by multiplying its mass by a unit material cost per kilogram of fin sheet. For aluminium alloys of the 3000 series, representative of both internal and external fins, the same unit cost previously adopted for offset-strip fins is retained. On the basis of current European market values, this leads to the assumption

$$c_{\mathrm{wv}} = 5\ \text{€}\,\mathrm{kg^{-1}}.$$

Consequently, the material cost associated with a single wavy fin element can be expressed as:

$$C_{\mathrm{wv}} = m_{\mathrm{wv}}\,c_{\mathrm{wv}}, \tag{3.48}$$

where c_{wv} denotes the unit material cost of the aluminium sheet employed in the fin stamping process.

3.3. Plate-Fin Heat Exchangers

3.3.1. Introduction

This section of the chapter presents a numerical methodology for predicting global heat transfer rates and overall head losses in complete plate–fin heat exchangers. The formulation is deliberately general and engineering-oriented, as it relies exclusively on nominal geometric parameters, fundamental physical principles, and consolidated modelling approaches, without introducing ad-hoc empirical tuning parameters.

The thermo-fluid dynamic modelling framework adopted here follows the multiscale approach proposed by Grespan et al., in which detailed three-dimensional CFD analyses at fin scale are consistently coupled with global, system-level models. This strategy enables accurate predictions of PFHE thermal performance and pressure losses while preserving limited model complexity and computational costs compatible with industrial design practice.

At fin scale, the periodicity of the finned surfaces is exploited to reduce the analysis to representative unit cells under fully developed flow conditions. Parametric CFD simulations are used to derive generalized correlations for the overall Nusselt number and equivalent Darcy friction factor, including corrections for entrance effects, which are particularly relevant for cross-flow external channels. In addition, inlet and outlet manifold losses are explicitly accounted for through dedicated CFD analyses combined with equivalent porosity models.

On this basis, global models are assembled to evaluate the thermal performance and mechanical energy losses of the complete radiator using the classical ε–NTU formulation. Within the scope of this chapter, this consolidated thermo-fluid dynamic description provides the modelling backbone upon which an original cost analysis of the complete plate–fin heat exchanger is subsequently developed.

Figure 3.6a shows a simple diagram depicting the steps of the adopted modelling strategy, which are briefly introduced and discussed in the following:

In the following, the above-described detailed computational models and global models for heat transfer and head losses are introduced and described in detail, using a selected set of PFHE configurations as the case study.

3.3.2. Numerical methods

3.3.2.1. Single fin model

Single fins are modelled in terms of their smallest unit geometry, which is repeated along the width and length of the channels. These basic modules are assumed to be located away from the inlet and outlet sections, so that the flow can be considered as fully developed. The flow is also assumed steady and incompressible for all the fluids and fins

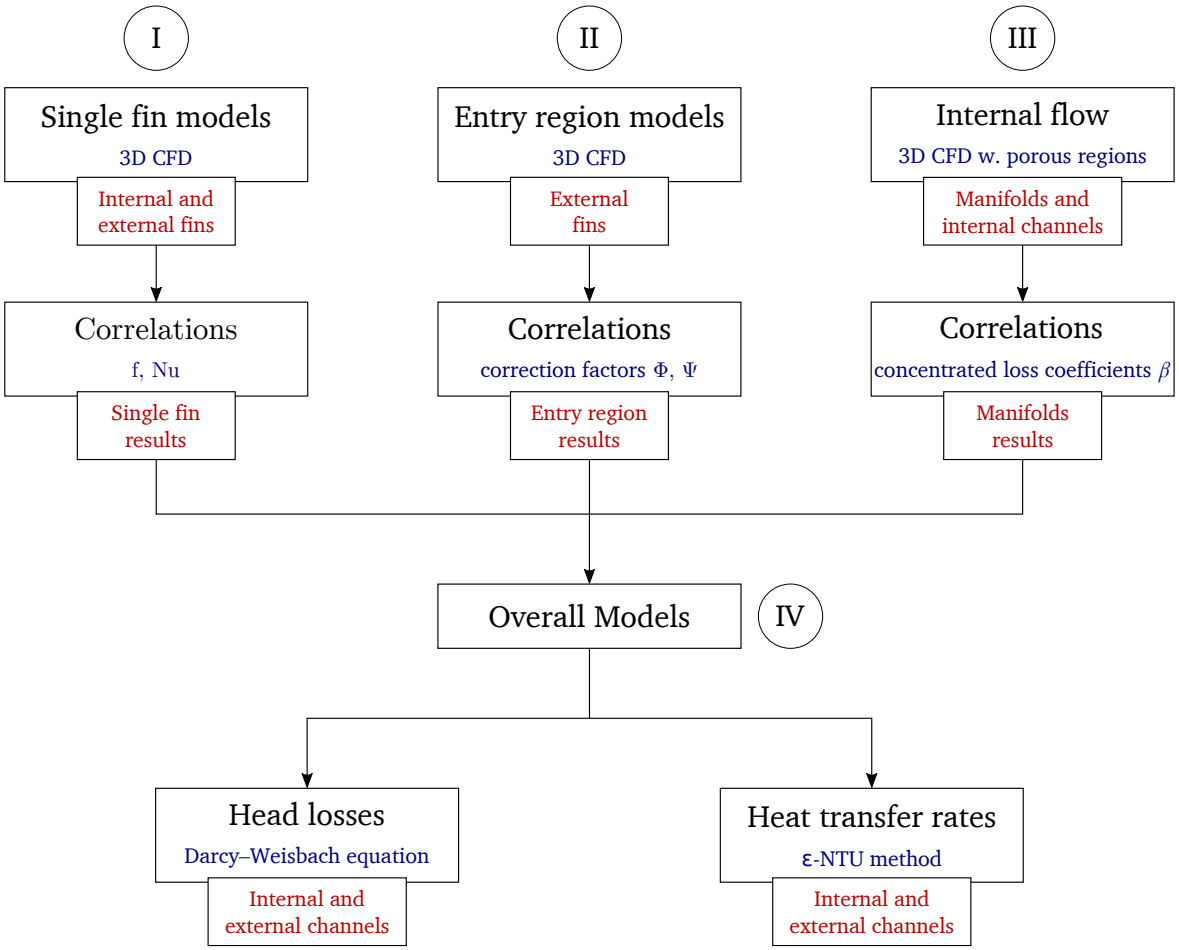

Figure 3.5. Simple schematic describing the modelling strategy adopted for the development of a high fidelity virtual model for PFHEs.

studied. In fluid regions, flow and temperature fields are determined by numerically solving momentum, continuity, and energy equations as seen in Eq. (3.7).

Low Reynolds number flows are solved by performing laminar analyses, meaning that $\nu_t = 0$. This approach is maintained for increasing Re as long as a solution with a satisfactory degree of numerical convergence is reached. That is, when all residuals are of the order of 10^{-6}. The k-ω SST turbulence model is used for Reynolds number values that do not allow for a steady-state laminar solution. This turbulence model is selected among all the others as it is the one that leads to the best agreement between numerical and experimental results for offset-strip fins, according to Kim *et al.* [81].

In roder to reduce the number of dimensional and flow parameters, the problem is reformulated in dimensionless form by scaling down the computational model by the reference length, chosen as the fin height y. The problem is then defined by the Reynolds and Prandtl numbers alone. The fluid average velocity along the streamwise direction is

assumed unitary, and thermophysical properties are scaled accordingly:

$$\mu^* = \nu^* = \frac{1}{\mathrm{Re}_\mathrm{y}}\,, \qquad c_\mathrm{p}^* = \mathrm{Re}_\mathrm{y}\,\mathrm{Pr}\,. \tag{3.49}$$

Fins are made of 3003 aluminium alloy. The thermal conductivity of the solid walls is assumed constant with temperature and, in the adopted dimensionless framework, is obtained by scaling the thermal conductivity of aluminium by the one of the adjacent fluid.

$$\lambda_\mathrm{s}^* = \frac{\lambda_\mathrm{alu}}{\lambda_\mathrm{fluid}} \tag{3.50}$$

To account for the periodicity of geometry and flow along the streamwise direction, field values at the inlet and outlet boundaries of the domain are linked by suitable mappings: At the inlet section, the velocity and temperature distributions are mapped from the outlet patch, keeping their integral average values fixed. At the inlet patch, a zero-gradient boundary condition is assigned to the pressure field. At the outlet patch, zero-gradient boundary conditions are applied to the velocity and temperature fields, while a uniform reference value is assigned to pressure. Periodic conditions are enforced along the spanwise direction. At the top and bottom boundaries, the temperature gradient is set to an arbitrary non-zero value, to impose an entering heat flux. At the walls, no-slip conditions are applied to the velocity field and a zero pressure gradient is imposed. Finally, continuity of temperature and heat flux is enforced at all fluid-solid interfaces.

Numerical simulations are performed using a finite-volume conjugate heat transfer solver implemented in the open-source toolbox OpenFOAM 7 [72]. Convective terms are discretised with second-order upwind schemes, while diffusive terms are treated using central differencing with explicit non-orthogonality corrections. Pressure–velocity coupling is handled through a SIMPLE-based algorithm [73].

Depending on the geometry, dimensionless single-fin modules are discretised using either block-structured or hybrid meshes generated with Pointwise. In hybrid grids, boundary layers are created via an advancing-front technique starting from a two-dimensional Delaunay triangulation. For both mesh types, fluid and solid domains are extruded as separate blocks to enable straightforward multi-region simulations using OpenFOAM's native utilities.

3.3.3. Numerical model for entrance effects

The fully developed flow assumption is considered valid for internal channels, where entrance effects are negligible due to the large ratio between channel length and elementary module length. Conversely, external channels are significantly shorter, and this hypothesis cannot be assumed *a priori*. The influence of flow development in the entry

region on the thermo–hydraulic performance of external finned surfaces is therefore investigated through dedicated CFD models comprising thirty single-fin modules in series, aimed at deriving module-wise values of the Darcy friction factor and Nusselt number.

Temperature and flow fields are obtained from the numerical solution of momentum, continuity, and energy equations, within the dimensionless framework described in Section 3.3.2.1. The governing equations are solved using the same numerical algorithm and spatial discretisation schemes adopted for single-fin analyses. As simulations are performed for air flows at medium to high Reynolds numbers, the k–ω SST turbulence model [70] is employed for all investigated flow conditions. The main distinction between fully developed and entrance-region models, apart from the computational meshes, lies in the streamwise boundary conditions.

3.3.4. Head losses in inlet and outlet manifolds

3.3.4.1. Governing equations

The head losses associated with the inlet and outlet manifolds are determined by developing a CFD model comprising the actual geometries of both manifolds, along with porous regions modelling the internal finned channels. Fluid flow is supposed steady, isothermal, and incompressible. The velocity and pressure fields are derived by numerically solving the steady-state RANS equations using the k-ω SST turbulence model [70].

$$\begin{cases} \nabla \cdot (\vec{v} \otimes \vec{v}) = -\dfrac{1}{\rho} \nabla p + \nabla \cdot [\, (\nu + \nu_t) \nabla \vec{v} \,] - \sigma_{\mathrm{m}} \\ \nabla \cdot \vec{v} = 0 \end{cases} \tag{3.51}$$

where σ_{m} is a momentum sink term that is non-zero only in porous regions, and it is defined on the basis of the Darcy-Forchheimer equation [82]:

$$\sigma_{\mathrm{m}} = \left(\nu \vec{D} + \frac{1}{2} \mathrm{tr}(\vec{v} \cdot I) \vec{F} \right) \vec{v} \, , \tag{3.52}$$

where the components of the vectors $\vec{D}$ and $\vec{F}$ determine the loss of momentum given by the porous regions. These vectors are obtained by calibrating the equivalent porosity model. The Darcy-Weisbach equation is used to determine the pressure gradient given by a single internal channel for different velocity values:

$$\frac{\nabla p_{\mathrm{ch}}}{\rho} = \frac{f_{\mathrm{fd}} \, L}{2 \, y \, L_{\mathrm{m}}} \left(\frac{A_{\mathrm{ch,m}}}{A_{\mathrm{ch,r}}} \nu \right)^2 \, , \tag{3.53}$$

where f_{fd} is the Darcy friction factor, related to fully developed flow conditions, of the specific fin considered.

f_{fd} is derived from the fully developed flow analyses, the results of which are reported in [9], whereas L_{m} represents the length of the porous regions in the computational domain.

The porous regions within the CFD model feature larger flow cross-sections than those of the real heat exchanger channels, due to the absence of fin walls. For this reason, fluid velocity is corrected by term $A_{\mathrm{ch,m}}/A_{\mathrm{ch,r}}$, which is derived from the conservation equation in order to correctly evaluate the head losses in the internal channels. Finally, the streamwise components of $\vec{D}$ and $\vec{F}$ are determined by using a variant of the Levenberg-Marquardt algorithm [76] to fit Equation (3.52) to the $\nabla p_{\mathrm{ch}}/\rho$ and corrected velocity values.

3.3.5. Global models

3.3.5.1. Heat transfer

The global thermal model for plate-fin heat exchangers is based on the $\varepsilon-\mathrm{NTU}$ method. The product between the equivalent heat transfer coefficient and the heat transfer surface is obtained by considering the series of thermal resistances related to the internal and external flows.

$$UA = \frac{1}{R_{\mathrm{int}} + R_{\mathrm{ext}}} = \frac{1}{\dfrac{1}{U_{\mathrm{int}} A_{\mathrm{int}}} + \dfrac{1}{U_{\mathrm{ext}} A_{\mathrm{ext}}}} \tag{3.54}$$

The internal global heat transfer coefficient U_{int} is determined by employing the Nusselt number correlation, for fully developed flow, of the specific fin considered. This correlation is a result stemming from the single fin model. It is presented in Equation (3.66). The heat transfer coefficient associated with the external channels is obtained from the respective value of Nusselt number, which is derived from the product of two contributions: (i) the fully developed Nu value, derived from Equation (3.66); (ii) the average Nusselt variation with respect its fully developed value in the entrance region:

$$\overline{\mathrm{Nu}}_{\mathrm{e}} = \frac{1}{\frac{S}{2l} - 1} \int_{1}^{\frac{S}{2l}} \Psi(\chi)\, d\chi \ , \tag{3.55}$$

where $\Psi(\chi)$ expresses the Nusselt number variation with respect to the position of each elementary module within the external channels, and the Reynolds number. Internal and external heat transfer areas A_{int} and A_{ext} are obtained by multiplying heat transfer area of the single fin module by the number of modules. The effectiveness of the heat exchanger is computed considering both internal and external fluids unmixed in a cross

flow configuration.

$$\varepsilon = 1 - \exp\left[\frac{C_{\max}}{C_{\min}}\,\mathrm{NTU}^{0.22}\left\{\exp\left[-\frac{C_{\min}}{C_{\max}}\,\mathrm{NTU}^{0.78}\right]-1\right\}\right] \tag{3.56}$$

Finally, the heat transferred between the two fluids is given by:

$$\dot{Q} = \varepsilon\, C_{\min}\,(T_{\mathrm{int,i}} - T_{\mathrm{ext,i}})\,. \tag{3.57}$$

The thermophysical properties of the internal and external fluids are computed as a function of the mean temperature between the respective inlet and outlet sections. The computation of $\dot{Q}$ is performed iteratively, by updating the values of fluid properties at each step of the procedure, until convergence is reached.

3.3.5.2. Internal head losses

Internal head losses are computed by summing the losses in the inlet and outlet manifolds and in the internal channels:

$$\Delta p_{\mathrm{int}} = \frac{1}{2}\,\rho_{\mathrm{i}}\,\beta_{\mathrm{i}}\,v_{\mathrm{i}}^2 + \Delta p_{\mathrm{ch}} + \frac{1}{2}\,\rho_{\mathrm{o}}\,\beta_{\mathrm{o}}\,v_{\mathrm{o}}^2\,, \tag{3.58}$$

where β_{i} and β_{o} are the concentrated loss coefficients of the inlet and outlet manifolds, respectively. These values are derived from the CFD model presented in Section 3.3.4. The values of channel losses Δp_{ch}, in oil coolers and water radiators are derived from the Darcy-Weisbach equation:

$$\Delta p_{\mathrm{ch}} = \frac{1}{2}\,\rho\, f_{\mathrm{fd}}\,\frac{L}{y}\,v_{\mathrm{ch}}^2\,. \tag{3.59}$$

In charge air coolers large temperature differences are often observed between the inlet and outlet of the internal channels. This causes significant variations in the thermophysical properties of the air, and hence in the local Reynolds number. Therefore, the head losses in the internal channels of charge air coolers are computed using the solver for steady-state one-dimensional flow in networks of pipes developed in Chapter 4. The air mass flow rate is assumed to be uniformly distributed among internal channels, thus only one of them is included in the reduced order model. The domain is discretised by an open-loop network presenting 200 nodes and 199 branches. Each branch exchanges heat with the external environment according to:

$$\dot{Q}_j = U_{\mathrm{ch}}(T_\infty - T_j)\,, \tag{3.60}$$

where U_{ch} is the global heat transfer coefficient of a single channel, and is obtained from Equation (3.54).

Air density is determined by means of an incompressible ideal gas law, considering a molar mass of 28.97 g/mol, while the other thermophysical properties are derived from linear interpolation of tabled data. At the channel inlet the temperature is set to a uniform value, while at the outlet a zero gradient condition is enforced.

3.3.5.3. External head losses

External head losses are determined by means of the well-known Darcy-Weisbach formula.

$$\Delta p_{\mathrm{ext}} = \frac{1}{2}\rho f_{\mathrm{fd}} \bar{f}_{\mathrm{e}} \frac{S}{y} v^2 \tag{3.61}$$

The equivalent friction factor of external channels is given by the product of two components: (i) f_{fd}, that is related to fully developed flow regime; (ii) $\bar{f}_{\mathrm{e}}$ which expresses the mean change of the friction factor in the entry region relative to its respective value for fully developed flow. The first of the two aforementioned contributions is obtained from the single fin friction factor correlation (3.65), which is a result of the fully developed flows analyses. $\bar{f}_{\mathrm{e}}$ is obtained from the integral average of $\Phi(\chi)$, which expresses the variation of f, with respect to its fully developed value, as a function of the position of each single fin module within the external channels, and the Reynolds number.

$$\bar{f}_{\mathrm{e}} = \frac{1}{\frac{S}{2l} - 1} \int_1^{\frac{S}{2l}} \Phi(\chi)\, d\chi \tag{3.62}$$

Air properties are evaluated at the mean temperature between inlet and outlet sections, furthermore the air outlet temperature is derived from the global heat transfer model.

3.3.6. Integral results

Integral results on head losses and heat transfer are presented in terms of the equivalent Darcy friction factor and the mean Nusselt number. The equivalent friction factor associated with single fins is computed by means of the well known Darcy-Weisbach formula, by replacing the hydraulic diameter with the fin height:

$$f = \frac{y\,(\bar{p}_{\mathrm{i}} - \bar{p}_{\mathrm{o}})}{l\,\rho\,\bar{v}_{\mathrm{i}}^2}\,, \tag{3.63}$$

where overbars indicate integral mean field values over the inlet (i) and outlet (o) sections. The Nusselt number is evaluated from the average fluid bulk temperature between

the inlet and outlet sections $\overline{T}_{\mathrm{b}} = 0.5\,(T_{\mathrm{b,i}} + T_{\mathrm{b,o}})$:

$$\mathrm{Nu} = \frac{\dot{Q}\,y}{\lambda A_{\mathrm{ref}}(\overline{T}_{\mathrm{w}} - \overline{T}_{\mathrm{b}})}\,, \tag{3.64}$$

where $\overline{T}_{\mathrm{w}}$ represents the integral mean of the temperature field over the heat transfer area A_{ref}, which includes the fluid-solid interfaces and the top and bottom boundaries. The values of Nusselt number and the friction factor derived from the CFD models are used to obtain correlations, as functions of the Reynolds number alone.

$$\log f_{\mathrm{fd}} = b_1\,\log^{b_2}\mathrm{Re}_{\mathrm{y}} + b_3 \tag{3.65}$$

$$\mathrm{Nu}_{\mathrm{fd}} = c_1\,\mathrm{Re}_{\mathrm{y}}{}^{c_2} + c_3 \tag{3.66}$$

Since each fin is associated to a specific fluid depending on the type of cooler, the effect of Pr is included in the c_i coefficients. The values of the coefficients b_i and c_i are found by fitting Equations (3.65) and (3.66) to numerical results by means of a variant of the Levenberg-Marquardt algorithm [76], implemented in the SciPy library [77].

Entrance effects on head losses and heat transfer effectiveness are evaluated by computing the deviation of the Darcy friction factor and Nusselt number with respect to the corresponding fully developed values, for each j-th single fin module:

$$\Phi_j = \log\left(\frac{1}{f_{\mathrm{fd}}}\frac{y\,(\bar{p}_{\mathrm{i},j} - \bar{p}_{\mathrm{o},j})}{l\,\rho\,\bar{v}^2_{\mathrm{i},j}}\right)\,, \tag{3.67}$$

$$\Psi_j = \frac{1}{\mathrm{Nu}_{\mathrm{fd}}}\frac{\dot{Q}_j\,y}{\lambda A_{\mathrm{ref}}(\bar{T}_{\mathrm{w},j} - \bar{T}_{\mathrm{b},j})}\,. \tag{3.68}$$

The results of the CFD analyses are employed to derive correlations that express the variations of f and Nu with respect to their fully developed values as a function of the module number χ and Reynolds number. The friction factor and Nusselt deviations due to outlet effects are not considered.

$$\Phi = \sum_{k=0}^{7}\sum_{r=0}^{4} d_{kr}\,\mathrm{Re}_y^r\log^k\chi \tag{3.69}$$

$$\Psi = \sum_{k=0}^{7}\sum_{r=0}^{4} e_{kr}\,\mathrm{Re}_y^r\,\chi^k \tag{3.70}$$

The values of the coefficients d_{kr} and e_{kr} have been omitted for the sake of brevity.

3.3.7. Cost modelling of the complete plate–fin heat exchanger

In this section, the equations employed to model the total production cost of a plate–fin heat exchanger are introduced. The total cost is formulated as the sum of three distinct contributions, namely the material cost, the cost associated with production time, and the industrial energy cost required to perform the various cutting and manufacturing operations involved in component processing.

Before introducing the analytical formulations of the individual cost contributions, it is convenient to clearly define the main geometric reference dimensions adopted throughout the present cost modelling. In the following, the symbols L, W, S, and H are used consistently as the fundamental geometric parameters of the plate–fin heat exchanger, as illustrated in Fig.3.6, and they constitute the reference quantities for all subsequent cost evaluations.

In particular, L denotes the tube length, S represents the core thickness, H is the core height along which the tubes are stacked during the assembly process, and W corresponds to the manifold height. These geometric quantities are retained as reference parameters for the entire cost modelling framework developed in the following sections.

Before introducing the analytical formulation of the cost model, it is essential to briefly describe the assembly process of a PFHE radiator, as this directly influences the adopted modelling assumptions.

As previously anticipated, a plate–fin heat exchanger is manufactured by stacking a sequence of loose components, which are subsequently compacted through mechanical pressing and permanently joined by brazing in a controlled-atmosphere furnace, resulting in a single monolithic core. The assembly procedure follows a repetitive and highly standardised sequence of operations, which can be summarised as follows:

1. positioning of the lower end plate;
2. placement of the first cladding plate;
3. positioning of the external air fin together with the two header bars;
4. placement of the second cladding plate;
5. positioning of the internal fins and the corresponding side bars;
6. repetition of steps 2 to 5 until the desired number of fluid passages (tubes) is achieved;
7. closure of the heat exchanger core by positioning, in sequence, a cladding plate, the external air fin together with its two header bars, a second cladding plate, and the upper end plate.

This modular assembly logic provides the foundation for the cost modelling strategy adopted in the following sections, where each cost contribution is expressed as a function of the number and type of elementary components required to build the complete heat exchanger.

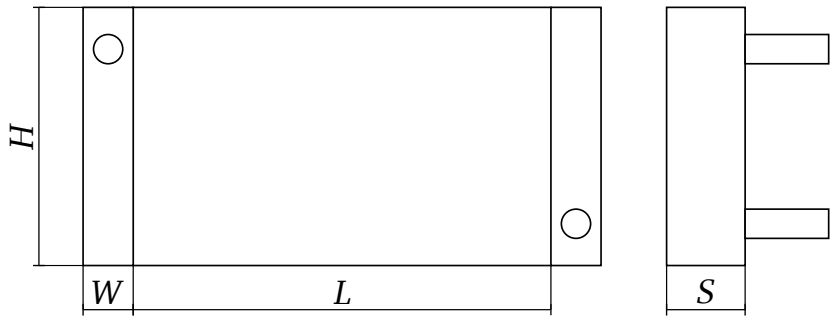

(a)

Figure 3.6. Schematic sketch of the plate–fin heat exchanger, illustrating the external geometry and the fundamental overall dimensions of the radiator core. (a)

Based on the considerations outlined above, the total production cost of the plate–fin heat exchanger is expressed as the combination of three main contributions, namely material usage, production time, and industrial energy consumption.

Accordingly, the total cost is formulated as:

$$C_{\mathrm{TOT}} = C_{\mathrm{m}}\, P_{\mathrm{m}} + C_{\mathrm{t}}\, P_{\mathrm{t}} + C_{\mathrm{E}}, \tag{3.71}$$

where C_{m} and C_{t} are unit cost terms associated with material and production time, respectively, while P_{m} and P_{t} are the corresponding weighting functions, introduced to map the physical and process drivers into cost contributions. In contrast, C_{E} represents a direct energy cost, expressed as an absolute monetary term. The analytical definitions of P_{m} and P_{t}, together with the adopted expressions for the unit cost terms, are introduced in the following sections.

3.3.7.1. Energy cost modelling

The energy cost associated with the production of a plate–fin heat exchanger consists of several distinct contributions. These include the electrical energy absorbed by the machines employed for cutting the various components, the energy consumption of the brazing furnace, the energy required by welding machines used to join the manifolds to the core, and the energy absorbed by handling and transportation equipment operating during the different stages of the production process.

A detailed and fully resolved modelling of all these energy contributions would require a plant-specific analysis and detailed knowledge of machine efficiencies, operating

schedules, and production layouts. As a result, such an approach would be strongly dependent on the specific manufacturing facility and would significantly reduce the general applicability of the proposed cost model. For this reason, a simplified and scalable formulation is adopted in the present work.

Unless otherwise specified, all geometric dimensions introduced in the following are expressed in metres.

Based on production data provided by VEMA Industries, a reference plate–fin heat exchanger is considered, characterised by the following overall dimensions: core height $H = 0.5$, tube length $L = 0.5$, core thickness $S = 0.094$, and manifold height $W = 0.06$. For this reference configuration, the total energy cost associated with the manufacturing process is estimated to be equal to

$$C_{\mathrm{E,ref}} = 100\ €. \tag{3.72}$$

Starting from this reference case, the energy cost for a generic plate–fin heat exchanger with dimensions differing from those of the reference model is evaluated through a dimensionless scaling formulation, expressed as:

$$C_{\mathrm{E}} = C_{\mathrm{E,ref}} K \left[\frac{W}{0.06} + 0.7\left(\frac{L}{0.5}\right) + 1.3\left(\frac{H}{0.5}\right) \right]. \tag{3.73}$$

Different weighting coefficients are associated with the characteristic dimensions in order to reflect their relative impact on the overall energy demand. In particular, a larger weight is assigned to the core height H with respect to the tube length L, since, for identical values of the remaining parameters, an increase in height implies a larger number of tubes and fins, leading to higher energy consumption, especially during cutting and component preparation operations.

The factor K represents a dimensionless difficulty index accounting for additional energy requirements associated with increased manufacturing complexity as the radiator size grows. In the present formulation, K is defined as a piecewise parameter dependent on the core height:

$$K = \begin{cases} 0.1, & H = 0.5, \\ 1.5, & 0.5 < H \leq 1.0, \\ 2.0, & H > 1.0. \end{cases} \tag{3.74}$$

This simplified approach enables the energy cost to be consistently scaled with the main geometric characteristics of the heat exchanger, while preserving a direct link to industrial production data and avoiding excessive dependence on plant-specific details.

3.3.7.2. Production time cost modelling

As anticipated in the previous section, the production time cost is modelled as the product of a unit time cost and a time weighting function, according to

$$C_{\mathrm{TIME,TOT}} = C_{\mathrm{t}} P_{\mathrm{t}}, \tag{3.75}$$

where C_{t} represents the unit cost of production time, while P_{t} describes the overall duration of the manufacturing process.

The unit time cost C_{t} accounts for labour and machine utilisation and is expressed on an hourly basis. According to the current national collective labour agreement for the metalworking sector, a representative and reasonable value can be assumed as

$$C_{\mathrm{t}} = 30 \text{ €} \, \mathrm{h}^{-1}. \tag{3.76}$$

The time weighting function P_{t} is formulated to account for the sequence of assembly and manufacturing operations required to produce the radiator core, as described in the numbered list of assembly steps reported in the previous section. In particular, two main contributions are identified: the time required for the assembly of the heat exchanger core and the time associated with welding operations and auxiliary machining processes, such as component cutting and general carpentry. For modelling simplicity, these latter activities are grouped into a single contribution. Accordingly, the total production time is expressed as

$$P_{\mathrm{t}} = P_{\mathrm{t,core}} + P_{\mathrm{t,welding}}. \tag{3.77}$$

The welding and auxiliary machining time is modelled in a simplified manner as:

$$P_{\mathrm{t,welding}} = 2\,Z, \tag{3.78}$$

where Z is a characteristic time parameter associated with welding and related manufacturing operations.

The parameter Z is an a priori designer-defined coefficient that reflects the expected difficulty of the manufacturing process for the specific plate–fin heat exchanger under consideration. It is introduced to account for the influence of design complexity on welding and auxiliary machining times, based on engineering judgement, prior experience, and sensitivity considerations.

In particular, Z represents a qualitative assessment of the overall production difficulty, encompassing aspects such as geometric complexity, accessibility of welding zones, tolerances, and the expected level of manual intervention required during manufacturing. In the present formulation, Z is assigned discrete values according to the anticipated project

complexity, namely:

$$Z = \begin{cases} 0.5, & \text{simple designs,} \\ 1.0, & \text{medium-complexity designs,} \\ 2.0, & \text{complex designs.} \end{cases} \tag{3.79}$$

This approach enables expert knowledge and industrial experience to be explicitly incorporated into the production time model, while avoiding an excessively detailed, plant-specific description of individual welding and machining operations.

The core assembly time $P_{\text{t,core}}$, expressed in seconds, is evaluated through the following empirical formulation:

$$P_{\text{t,core}} = \frac{1}{3600}\left(50 + \frac{L}{L_{\text{t}}}5\right) 2\,k\,N_{\text{T}}, \tag{3.80}$$

where L denotes the core tube length, while L_{t} represents the elementary internal fin unit employed during the assembly phase to construct a single tube of the radiator core. The ratio L/L_{t} therefore provides a measure of the number of internal fin elements required per tube.

The factor k is the same complexity coefficient introduced in the energy cost modelling section (see Eq. (1.28)), and it accounts for the increased assembly difficulty associated with larger or more complex radiator geometries.

The multiplicative factor 2 is introduced to account for additional time contributions associated with the core construction process, including component preparation, mechanical pressing, and core stacking and brazing preparation operations. Finally, N_{T} represents the number of tubes composing the core and constitutes the primary driver of the overall assembly time.

The prefactor 1/3600 converts the estimated assembly time from seconds to hours, ensuring consistency with the unit time cost definition adopted in the present work.

Within the formulation of P_{t}, the number of tubes N_{T} plays a dominant role, as it represents the primary driver of assembly time. It is evaluated geometrically as:

$$N_{\text{T}} = \frac{H - 2s_{\text{end}} - h_{\text{ext}} - 2s_{\text{c}}}{2s_{\text{c}} + h_{\text{ext}} + h_{\text{in}}}, \tag{3.81}$$

where H is the core height, s_{end} denotes the thickness of the end plates, s_{c} is the thickness of the cladding plates, while h_{ext} and h_{in} represent the heights of the external and internal fin passages, respectively.

This formulation allows the production time cost to be directly linked to the geometric

characteristics of the plate–fin heat exchanger, while preserving a simplified yet physically meaningful description of the underlying manufacturing processes.

3.3.7.3. Material cost modelling

The material cost contribution accounts for the amount of raw material required to manufacture the plate–fin heat exchanger core and its associated components. This contribution is directly related to the mass of material employed and is modelled through the combination of a unit material cost and a material weighting function, consistently with the overall cost formulation introduced in the previous sections.

Unlike the energy and production time contributions, the material cost is primarily governed by geometric factors and material properties, such as component thicknesses, densities, and the number of elementary elements composing the radiator core. As a result, this term can be evaluated by explicitly computing the volume and mass of each component and aggregating their contributions.

In the present framework, the material cost is expressed as the product of a unit material cost and a material weighting function, which accounts for the total mass of aluminium required to manufacture the heat exchanger. The analytical formulation adopted to estimate the material usage of the individual components is introduced in the following, together with the assumptions employed to simplify the geometrical description of the radiator.

As introduced above, the material cost is modelled as the combination of a unit mass price and a material weighting function accounting for the amount of material required by the radiator. Since the unit material price is not uniform across all components, a piecewise formulation is adopted.

In the present treatment, two unit mass cost coefficients are assumed, expressed in $€\,kg^{-1}$. The first coefficient, denoted as c_1, is assigned to cladding plates, internal and external fins, and end plates, and is set to $c_1 = 5\ €\,kg^{-1}$. The second coefficient, denoted as c_2, is assigned to header bars (both long and short) and to manifolds, and is set to $c_2 = 7\ €\,kg^{-1}$. The higher value of c_2 reflects the additional technological operations required for these components, such as machining, finishing, and rectification, which increase their effective purchase and processing cost.

These numerical values are selected based on the current European raw material market and typical industrial practice; however, the proposed model can be readily updated at any time by modifying the corresponding coefficients.

Because the unit material price is not constant across the full set of components, the material cost is expressed through a hybrid formulation that combines the unit cost coefficients with the material weighting function P_{m}, i.e. with the mass contributions

associated with each component. According to the modular assembly logic described in the numbered list reported previously, the total material cost of a PFHE radiator is formulated as:

$$C_{\mathrm{M,TOT}} = 1.1\, N_{\mathrm{T}} \left(C_{\mathrm{c}} + C_{\mathrm{HB}} + C_{\mathrm{SB}} + C_{\mathrm{in}} + C_{\mathrm{ext}}\right) + C_{\mathrm{end}} + C_{\mathrm{man}}, \tag{3.82}$$

where N_{T} is the number of tubes, the factor 1.1 is introduced to account for additional material allowances and manufacturing losses, C_{c} denotes the material cost contribution of cladding plates, C_{HB} and C_{SB} are the contributions of header bars and side bars, C_{in} and C_{ext} correspond to internal and external fins, and C_{end} and C_{man} represent the contributions of end plates and manifolds, respectively.

We now define the mathematical formulation of each material-cost contribution. The cost terms grouped within parentheses in Eq. (3.82) represent the elementary repeating unit adopted in the construction of the core, consistently with steps 2–5 of the assembly sequence reported in the introduction. Each contribution is evaluated as the product of a unit mass cost coefficient and the corresponding component mass.

Cladding plates. The material cost associated with a single cladding plate is written as

$$C_{\mathrm{c}} = c_1\, m_{\mathrm{c}}, \tag{3.83}$$

where the cladding-plate mass is

$$m_{\mathrm{c}} = \rho_{\mathrm{Al}}\, L\, W\, s_{\mathrm{c}}. \tag{3.84}$$

Header bars. The header-bar contribution is modelled as

$$C_{\mathrm{HB}} = c_2\, m_{\mathrm{HB}}, \tag{3.85}$$

with the corresponding mass approximated as

$$m_{\mathrm{HB}} = \rho_{\mathrm{Al}}\, h_{\mathrm{ext}}\, S\, 0.01, \tag{3.86}$$

where 0.01 is the characteristic width of the short header bar, assumed constant for modelling simplicity.

Side bars. Similarly, the side-bar contribution reads

$$C_{\mathrm{SB}} = c_2\, m_{\mathrm{SB}}, \tag{3.87}$$

where

$$m_{\mathrm{SB}} = \rho_{\mathrm{Al}}\, h_{\mathrm{in}}\, L\ 0.06, \tag{3.88}$$

and 0.06 is the characteristic width of the long side bar, also assumed constant.

Internal fins. The internal-fin contribution is expressed as

$$C_{\mathrm{in}} = C_{\mathrm{fin}}\, S_{\mathrm{in}}, \tag{3.89}$$

where C_{fin} is the cost of a single internal fin module defined by Eq. (3.32) for offset-strip fins and by Eq. (3.48) for wavy fins. The replication factor S_{in} represents the number of modules required to span one tube and is modelled as

$$S_{\mathrm{in}} = \left(\frac{S-12}{x}\right)\left(\frac{L}{l}\right), \tag{3.90}$$

where x and l are the characteristic fin-module dimensions in the spanwise and streamwise directions, respectively, and S is the core width.

External fins. An analogous formulation is adopted for the external (air-side) fin contribution:

$$C_{\mathrm{ext}} = C_{\mathrm{fin}}\, R, \tag{3.91}$$

where C_{fin} is evaluated as for the internal fins, while the replication factor R distributing the fin modules over the complete air-side fin is given by

$$R = \left(\frac{L-20}{x}\right)\left(\frac{S}{l}\right). \tag{3.92}$$

End plates. The end-plate contribution is finally expressed as

$$C_{\mathrm{end}} = c_1\, m_{\mathrm{end}}, \tag{3.93}$$

where the end-plate mass is approximated as

$$m_{\mathrm{end}} = \rho_{\mathrm{Al}}\, L\, W\, s_{\mathrm{end}}. \tag{3.94}$$

Manifolds. The manifold contribution is evaluated from a standard reference extruded configuration. A reference extrusion with length 1 meter, height $W = 0.06$, and width 0.094 is assumed to have a mass equal to 4.5 kg. By scaling this reference mass with the

core dimensions, the manifold mass is estimated as

$$m_{\text{man}} = 4.5\left(\frac{S}{0.094}\right)\left(\frac{H}{1}\right)2, \tag{3.95}$$

and the corresponding manifold cost is then computed as

$$C_{\text{man}} = c_2\, m_{\text{man}}. \tag{3.96}$$

The set of formulations introduced in this subsection provides a general and scalable description of the material cost associated with the production of a plate-fin heat exchanger core. The proposed expressions are valid for arbitrary core dimensions and can be applied to any combination of internal and external fin geometries. In particular, both offset-strip fins and wavy fins can be considered on either the internal or external side of the radiator without requiring any modification to the structure of the material cost model, as the specific fin geometry is fully accounted for through the corresponding fin-module cost definition.

3.4. Concluding remarks

This chapter has presented a comprehensive and hierarchical modelling framework for plate–fin heat exchangers, integrating detailed thermo-fluid dynamic descriptions with an original and physically grounded formulation of production cost. The analysis has been developed across multiple scales, starting from the characterisation of elementary fin geometries and progressively extending to the complete heat exchanger assembly.

At fin scale, offset-strip and wavy fin geometries have been analysed by means of systematic Design of Experiments supported by CFD simulations of periodic unit cells. Established correlations from the literature have been adopted to describe the fundamental thermo–hydraulic behaviour, while dedicated response surfaces for the equivalent Darcy friction factor and Colburn factor have been derived to enable continuous and differentiable performance predictions over wide ranges of geometric and flow parameters. Particular attention has been devoted to the treatment of entrance effects and to the consistent integration of laminar and turbulent flow regimes.

The main original contribution of this chapter lies in the development of a dedicated cost modelling framework explicitly linked to fin geometry, material usage, and manufacturing-related quantities. Analytical expressions have been introduced to evaluate volume, mass, and material cost of both offset-strip and wavy fin modules, which represent the elementary building blocks of the heat exchanger core. These formulations have been systematically extended to the complete plate–fin heat exchanger by modelling material cost, production time, and industrial energy consumption as explicit functions

of the core geometry, number of tubes, fin configuration, and assembly logic.

Unlike most approaches available in the literature, where cost is typically addressed only indirectly through operational or energy-related metrics, the present formulation provides a direct and modular description of production cost, grounded in manufacturing processes and industrial practice. The resulting cost model is scalable, geometry-driven, and applicable to arbitrary combinations of internal and external fin types without modification of its structure.

Overall, the set of equations introduced in this chapter constitutes a unified mathematical framework describing the coupled thermo–hydraulic and economic behaviour of plate–fin heat exchangers. This framework provides the foundation for the definition of design variables, objective functions, and constraints employed in the following chapters, where it is used to formulate the Design of Experiments and the multi-objective optimisation problems aimed at exploring trade-offs between thermal performance, pressure losses, and production cost.

CHAPTER 4

Design of Experiments and Parametric Sensitivity Analysis for PFHEs

4.1. Introduction

Within engineering optimisation frameworks, the systematic exploration of the design space is addressed through a Design of Experiments (DOE) approach. This is not an optimisation technique *per se*, but a structured procedure for sampling informative design points while limiting experimental or computational effort. By defining how variables are perturbed and responses are collected, DOE provides the basis for surrogate modelling and subsequent optimisation, rendering complex physics-based problems tractable.

An optimization problem is characterised by a set of input parameters, among which only a subset is typically retained as design variables, namely those exerting a significant influence on system performance. The admissible combinations of these variables define an n-dimensional design space, where each point corresponds to a specific design configuration. The associated performance is quantified through one or more objective functions, obtained experimentally or numerically.

Since the mapping between design variables and objective functions is generally unknown and expensive to evaluate, an exhaustive exploration of the design space is impractical, particularly as the number of variables increases and the curse of dimensionality becomes dominant. DOE addresses this limitation by providing a structured approach for selecting a limited number of representative samples, allowing meaningful information on system behaviour to be extracted with a controlled computational effort.

Different DOE strategies result in different distributions of samples within the design space and therefore in different types of information being collected. Some techniques emphasise the estimation of main effects and interactions among variables, while others aim at ensuring a more uniform coverage of the design space. Consequently, there is no universally optimal DOE technique; its effectiveness must be evaluated with respect to its intended purpose, whether it is sensitivity analysis, response surface construction, or preparation for multi-objective optimisation.

In this work, the Design of Experiments is used as a sensitivity analysis tool to identify the design parameters with dominant influence on the objective functions. Weakly influential variables are eliminated to reduce the dimensionality of the design space without significant loss of accuracy, thereby improving robustness and reducing the computational cost of the subsequent optimisation stage. A full factorial Design of Experiments is adopted to clearly resolve both main and interaction effects among the design variables.

The chapter is structured as follows. First, a theoretical digression on DOE methodologies is presented, with particular emphasis on full factorial designs and their mathematical formulation. Subsequently, the DOE framework is applied to the thermo–economic analysis of plate–fin heat exchangers equipped with offset-strip fins and wavy fins. Finally, the DOE results are examined through a statistical post-processing phase based on Student's *t*-test, with the objective of identifying the parameters that most strongly influence heat transfer performance, pressure losses, and production cost, as well as clarifying the direction and relative magnitude of their effects.

4.2. Governing equations of full factorial Design of Experiments

4.2.1. Problem definition, scope and design space

Design of Experiments (DOE) provides a disciplined way to select a finite set of design points in an n-dimensional design space, in order to extract the maximum amount of information with a limited computational or experimental budget. In a simulation-driven framework (as for PFHE modeling), DOE primarily serves two purposes:

i. *Screening and sensitivity*: identify the most influential parameters and the dominant interactions.

ii. *Model building*: generate datasets suitable for response surface modeling (RSM) or surrogate-based optimization.

In this thesis, DOE is used to (i) quantify how the PFHE performance metrics (e.g. pressure losses, heat transfer, mass and cost) vary across the design space and (ii) support subsequent optimization steps by providing statistically structured evidence rather than relying on one-factor-at-a-time explorations.

Let the design be parameterized by k controllable factors (design variables)

$$\mathbf{X} = \left[X_1, \ldots, X_k\right]^{\mathsf{T}}, \tag{4.1}$$

each defined over a region of interest (bounded domain) $\Omega \subset \mathbb{R}^k$. A DOE generates N experiments (or simulations), i.e. a set of samples

$$\mathscr{D} = \left\{\mathbf{X}^{(1)}, \ldots, \mathbf{X}^{(N)}\right\} \subset \Omega, \tag{4.2}$$

and for each sample it yields one (single-response) or multiple (multi-response) outputs

$$\mathbf{y}^{(r)} = \left[y_1^{(r)}, \ldots, y_q^{(r)}\right]^{\mathsf{T}}, \qquad r = 1, \ldots, N, \tag{4.3}$$

where q is the number of responses of interest (e.g. Δp, ε, UA, mass, cost).

4.2.2. Full factorial design

Full factorial designs are most transparent when factors are *coded* (normalized) so that low and high levels map to -1 and $+1$. For a factor X with low/high values X_L and X_H, the standard linear coding is

$$x = \frac{X - a}{b}, \qquad a = \frac{X_H + X_L}{2}, \qquad b = \frac{X_H - X_L}{2}, \tag{4.4}$$

so that $X = X_L \Rightarrow x = -1$, $X = X_H \Rightarrow x = +1$, and the center point corresponds to $x = 0$. Coding makes the design matrix columns orthogonal in 2-level full factorial designs, which is the mathematical reason why effects can be estimated cleanly and independently.

A full factorial design evaluates *all* combinations of discrete levels assigned to each factor. If factor i has L_i levels, the total number of runs is

$$N = \prod_{i=1}^{k} L_i. \tag{4.5}$$

The most common case in engineering screening is the 2-level design with $L_i = 2$ for all i, yielding

$$N = 2^k. \tag{4.6}$$

The strength of full factorial DOE is that it resolves *main effects* and *interactions* without confounding; the limitation is the exponential growth of N with k.

For a 2^k full factorial in coded variables $x_i \in \{-1, +1\}$, the design matrix $\mathbf{X}$ is defined

as

$$\mathbf{X} = \begin{bmatrix} 1 & x_1^{(1)} & \cdots & x_k^{(1)} & x_1^{(1)}x_2^{(1)} & \cdots & x_1^{(1)}x_2^{(1)}\cdots x_k^{(1)} \\ \vdots & \vdots & & \vdots & \vdots & & \vdots \\ 1 & x_1^{(N)} & \cdots & x_k^{(N)} & x_1^{(N)}x_2^{(N)} & \cdots & x_1^{(N)}x_2^{(N)}\cdots x_k^{(N)} \end{bmatrix}, \tag{4.7}$$

where the first column is the intercept, the next k columns are the main effects, and the remaining columns represent interaction terms up to order k.

4.2.3. Factorial model, main effects and interaction effects

For a single response y, the complete factorial model in coded variables is

$$y = \beta_0 + \sum_{i=1}^{k} \beta_i x_i + \sum_{i<j} \beta_{ij} x_i x_j + \sum_{i<j<\ell} \beta_{ij\ell} x_i x_j x_\ell + \cdots + \beta_{12\cdots k} x_1 x_2 \cdots x_k + \varepsilon, \tag{4.8}$$

with ε representing residual error. In matrix form,

$$\mathbf{y} = \mathbf{X}\boldsymbol{\beta} + \boldsymbol{\varepsilon}. \tag{4.9}$$

The ordinary least squares estimator is

$$\hat{\boldsymbol{\beta}} = \left(\mathbf{X}^{\mathsf{T}}\mathbf{X}\right)^{-1}\mathbf{X}^{\mathsf{T}}\mathbf{y}. \tag{4.10}$$

In a 2^k full factorial with coded levels ± 1, the columns of $\mathbf{X}$ (excluding the intercept) are orthogonal, such that

$$\mathbf{X}^{\mathsf{T}}\mathbf{X} = N\,\mathbf{I}, \tag{4.11}$$

ensuring decoupled estimation of main effects and interactions.

For a two-level factor A, the main effect is defined as

$$\text{Effect}(A) = \bar{y}_{A+} - \bar{y}_{A-}, \tag{4.12}$$

with the corresponding estimator under coded variables given by

$$\widehat{\text{Effect}}(A) = \frac{\bar{y}_{A+} - \bar{y}_{A-}}{2}. \tag{4.13}$$

Equivalent expressions apply to interaction effects, which quantify how the effect of one factor depends on the level of another.

4.2.4. ANOVA-based sensitivity analysis

For an effect E with contrast C_E, the associated sum of squares is

$$SS_E = \frac{C_E^2}{r\,2^k}, \tag{4.14}$$

while the total sum of squares is

$$SS_T = \sum_{i=1}^{N} \left(y^{(i)} - \bar{y}\right)^2. \tag{4.15}$$

The factorial decomposition reads

$$SS_T = \sum SS_E + SS_\varepsilon. \tag{4.16}$$

In a 2^k design, each effect has one degree of freedom, leading to

$$df_{\text{model}} = 2^k - 1, \qquad df_\varepsilon = 2^k(r-1). \tag{4.17}$$

Mean squares and F-statistics are computed according to standard ANOVA definitions. In simulation-based DOE, these metrics are primarily used as quantitative indicators of sensitivity rather than for strict hypothesis testing.

For full factorial designs with $L_i > 2$ levels, analogous ANOVA formulations apply, based on level-wise and cell-wise mean responses, allowing main effects and interaction effects to be consistently quantified.

4.2.5. Three-level full factorial Design of Experiments

In the present work, each design variable is investigated at three discrete levels. This choice allows the limitations of two-level screening designs to be overcome, by enabling the identification of non-linear trends while preserving a fully structured and non-confounded sampling strategy.

Let the design be parameterised by k controllable factors

$$\mathbf{X} = \left[X_1, \ldots, X_k\right]^{\mathsf{T}}, \qquad \mathbf{X} \in \Omega \subset \mathbb{R}^k, \tag{4.18}$$

where each factor X_i is assigned three physical levels

$$X_i \in \{X_{i,L}, X_{i,M}, X_{i,H}\}, \tag{4.19}$$

with $X_{i,L}$ and $X_{i,H}$ denoting the bounds of the design interval and $X_{i,M}$ representing an

intermediate reference value. A three-level full factorial design evaluates all possible level combinations, leading to a total number of simulations equal to

$$N = 3^k. \tag{4.20}$$

For convenience of analysis, the design variables are expressed in coded form according to

$$x_i = \frac{X_i - a_i}{b_i}, \qquad a_i = \frac{X_{i,H} + X_{i,L}}{2}, \qquad b_i = \frac{X_{i,H} - X_{i,L}}{2}, \tag{4.21}$$

so that the three physical levels map to $x_i = -1,\ 0,\ +1$. This normalisation facilitates the interpretation of regression coefficients and supports a consistent comparison of effects among different variables.

The availability of three levels naturally leads to the adoption of a second-order factorial model in coded variables, written for a generic response y as

$$y = \beta_0 + \sum_{i=1}^{k} \beta_i x_i + \sum_{i=1}^{k} \beta_{ii} x_i^2 + \sum_{i<j} \beta_{ij} x_i x_j + \varepsilon, \tag{4.22}$$

where the linear terms β_i describe the main effects, the quadratic terms β_{ii} account for curvature, and the interaction terms β_{ij} capture coupled effects between pairs of variables. The coefficients are estimated by ordinary least squares using the full factorial dataset.

From an interpretative standpoint, the presence of curvature along a given factor can be directly assessed from the level-wise mean responses. Denoting by $\bar{y}_{i,-1}$, $\bar{y}_{i,0}$, and $\bar{y}_{i,+1}$ the average responses at the three coded levels, a curvature indicator can be defined as

$$C_i = \bar{y}_{i,-1} - 2\bar{y}_{i,0} + \bar{y}_{i,+1}. \tag{4.23}$$

Values of C_i close to zero indicate an approximately linear behaviour over the investigated range, whereas significant deviations highlight the relevance of second-order effects.

Overall, the three-level full factorial design adopted in this work enables a clear and non-confounded quantification of linear effects, interaction effects, and curvature. At the same time, it provides a rigorous basis for identifying weakly influential parameters, which can be fixed or neglected in subsequent optimisation stages, leading to a substantial reduction of the effective design space and of the associated computational cost.

4.2.6. Practical considerations for PFHE applications

For PFHE geometry-driven design, full factorial DOE is appropriate when the number of design variables is limited, interactions are expected to be relevant, and a non-confounded

sensitivity assessment is required prior to global optimisation. When the dimensionality increases, the exponential growth of required simulations motivates the adoption of reduced or space-filling DOE strategies; nevertheless, the full factorial design remains the reference benchmark for sensitivity analysis.

4.3. Application of full factorial DOE to PFHE radiators

This section presents the application of a full factorial Design of Experiments (DOE) to the thermo–economic analysis of plate–fin heat exchanger (PFHE) radiators. The primary objective of this DOE is not the direct identification of an optimal design, but rather the systematic quantification of the sensitivity of the radiator performance with respect to geometric parameters, core thickness, and operating conditions. In particular, the DOE is used to identify which factors and interactions exert a dominant influence on the objective functions, and which parameters, conversely, have a marginal effect and may therefore be fixed *a priori*. Such a reduction of the effective design space is essential to limit the computational cost and improve the robustness of the subsequent optimisation stages [12].

4.3.1. PFHE reference configuration and model interface

A reference PFHE geometry is defined by fixing the frontal dimensions of the heat exchanger core. Specifically, the core height and tube length are set to

$$H = 0.5 \text{ m}, \qquad L = 0.5 \text{ m}, \tag{4.24}$$

while the core thickness is treated as a design variable and denoted by S (units: m). The thickness S directly controls the number of flow passages and therefore plays a key role in determining both the thermo–hydraulic performance and the production cost. The corresponding geometric configuration is schematically illustrated in Figure 4.1.

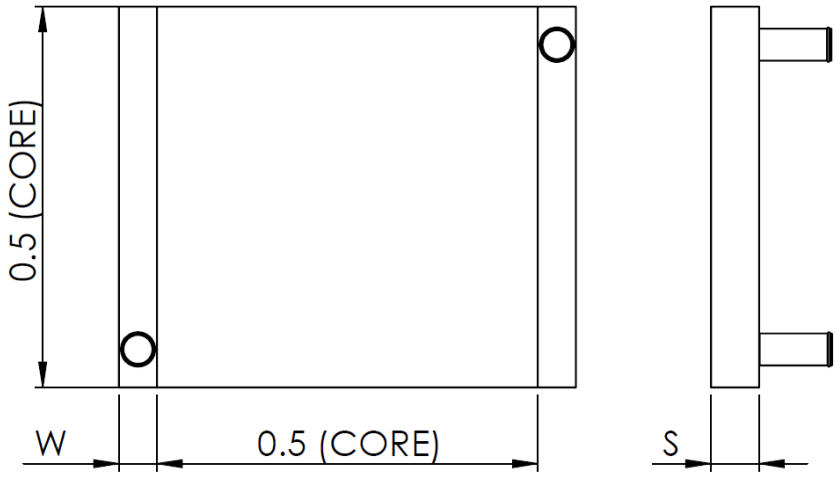

Figure 4.1. Reference PFHE configuration adopted for the DOE analysis. The frontal dimensions are fixed to $H = 0.5$ m and $L = 0.5$ m, while the core thickness S is treated as a design variable. The manifold height W and core thickness S follow the notation introduced in Chapter 3.

The PFHE performance is evaluated through a Python-based implementation of the governing equations introduced in the PFHE modelling chapter. These equations combine fin-scale thermo–fluiddynamic correlations with system-level heat exchanger models, enabling the prediction of heat transfer rate, pressure losses on both fluid sides, and a production-cost.

The numerical model can be formalised as a deterministic mapping

$$\mathscr{M} : \xi \longmapsto \mathbf{r}, \tag{4.25}$$

where ξ denotes the vector of DOE inputs and $\mathbf{r}$ the corresponding response vector. In the present study, the response vector is defined as

$$\mathbf{r} = \big(\dot{Q},\ \Delta p_{\text{in}},\ \Delta p_{\text{ext}},\ C\big), \tag{4.26}$$

where $\dot{Q}$ is the heat transfer exchanged by the radiator, Δp_{in} and Δp_{ext} are the pressure losses on the internal and external sides, respectively, and C is the radiator cost. All mass flow rates are expressed in $\mathrm{kg\,s^{-1}}$, while all geometric quantities are expressed in m.

4.3.2. Computational workflow and model coupling

For each DOE sample, the PFHE model is evaluated by following a fixed and fully deterministic sequence of operations, schematically illustrated in Fig. 4.2. The workflow has been explicitly structured to maintain a clear separation between geometry definition, thermo–fluiddynamic modelling, and cost evaluation, ensuring consistency and traceability across the entire DOE dataset.

Starting from the DOE input vector ξ, the PFHE geometry is first reconstructed by combining the fixed frontal dimensions (H, L) with the sampled core thickness S and the fin geometric parameters on both the internal and external sides. This step yields all the geometric quantities required by the governing equations, including flow cross-sectional areas, hydraulic diameters, heat transfer surfaces, fin densities, and the number of repeated fin modules along the streamwise direction.

Once the geometry is defined, fin-scale thermo–fluiddynamic correlations are applied independently to the internal and external sides of the exchanger. For each side, the correlations provide friction factors and Colburn j-factors as functions of the local Reynolds number, geometric parameters, and fluid properties. These quantities are used to compute local heat transfer coefficients and pressure gradients, which are then integrated at system level to obtain the total pressure losses Δp_{in} and Δp_{ext}.

The global thermal performance of the radiator is subsequently evaluated using the ε–NTU framework introduced in the PFHE modelling chapter. This formulation combines

the fin-scale heat transfer characteristics with the global heat capacity rates of the fluids, yielding the total heat transfer rate $\dot{Q}$ exchanged by the radiator under the prescribed operating conditions.

Finally, the same geometric description is passed to the cost model, which evaluates the radiator production cost as a function of material usage and manufacturing-related quantities, including fin volume, sheet thickness, and overall core size. The output of this final step is combined with the thermo–hydraulic results to form the complete response vector **r** associated with the current DOE sample.

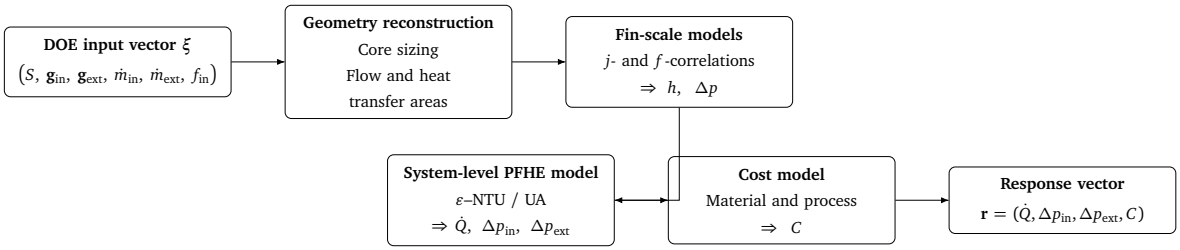

Figure 4.2. Computational workflow adopted for the evaluation of each DOE sample in the PFHE analysis.

4.3.3. DOE factors and vector notation

Two PFHE architectures are investigated within the DOE framework:

i. **OSF–OSF**, with offset-strip fins on both the internal and external sides;

ii. **OSF–Wavy**, with offset-strip fins internally and wavy fins externally.

The internal fin geometry is described by the vector

$$\mathbf{g}_{\text{in}} = \left(x_{\text{in}},\ y_{\text{in}},\ \ell_{\text{in}}\right), \tag{4.27}$$

while the external fin geometry is defined as

$$\mathbf{g}_{\text{ext}}^{(\text{OSF})} = \left(x_{\text{ext}},\ y_{\text{ext}},\ \ell_{\text{ext}}\right), \qquad \mathbf{g}_{\text{ext}}^{(\text{Wavy})} = \left(x_{\text{ext}},\ y_{\text{ext}},\ \ell_{\text{ext}},\ a_{2,\text{ext}}\right). \tag{4.28}$$

The complete DOE input vectors are therefore written as

$$\xi^{(\text{OSF–OSF})} = \left(S,\ \mathbf{g}_{\text{in}},\ \mathbf{g}_{\text{ext}}^{(\text{OSF})},\ \dot{m}_{\text{in}},\ \dot{m}_{\text{ext}},\ f_{\text{in}}\right), \tag{4.29}$$

$$\xi^{(\text{OSF–Wavy})} = \left(S,\ \mathbf{g}_{\text{in}},\ \mathbf{g}_{\text{ext}}^{(\text{Wavy})},\ \dot{m}_{\text{in}},\ \dot{m}_{\text{ext}},\ f_{\text{in}}\right). \tag{4.30}$$

4.3.4. Definition of design variables and geometric meaning

To avoid ambiguity, all factors introduced in the DOE vectors are explicitly defined here. Unless otherwise stated, geometric quantities are expressed in m and mass flow rates in $\mathrm{kg\,s^{-1}}$. Subscripts in and ext refer to the internal and external sides of the PFHE core, respectively.

Core-scale variables. The PFHE frontal dimensions are fixed to $H = 0.5$ m and $L = 0.5$ m, while the core thickness S is treated as a DOE factor. In the present framework, S controls the number of repeated fin layers/passages across the core depth and therefore affects heat transfer surface, hydraulic resistances, and material usage (hence cost).

Offset-strip fin (OSF) geometry variables. For an OSF surface, the fin geometry is parameterised through three primary lengths:

- x : *fin pitch* (streamwise/transverse repeating spacing between adjacent fin walls, as defined in the PFHE geometry chapter);
- y : *fin height* (distance between plates delimiting the flow passage on the considered side);
- ℓ : *offset length* (streamwise length of a single fin segment between two successive offsets).

Accordingly, $(x_{\mathrm{in}}, y_{\mathrm{in}}, \ell_{\mathrm{in}})$ define the internal OSF surface, while $(x_{\mathrm{ext}}, y_{\mathrm{ext}}, \ell_{\mathrm{ext}})$ define the external OSF surface.

Wavy fin geometry variables. For the wavy surface adopted externally in the OSF–Wavy architecture, the geometry is described by

- x_{ext} : fin pitch (wavy fin repeating spacing, consistent with the geometric conventions used in the PFHE chapter);
- y_{ext} : fin height;
- ℓ_{ext} : streamwise characteristic length (wavelength-related repeating length as implemented in the code);
- $a_{2,\mathrm{ext}}$: wave amplitude parameter (geometric amplitude controlling the waviness intensity).

The adopted definition of $a_{2,\mathrm{ext}}$ matches the wavy-fin parameterisation used in the governing equations implemented in the Python modules.

Operating-condition variables. The internal and external mass flow rates are $\dot{m}_{\mathrm{in}}$ and $\dot{m}_{\mathrm{ext}}$, respectively. The discrete selector f_{in} identifies the internal working fluid (oil, coolant/water–glycol, or charge air). For each DOE sample, f_{in} fixes the thermophysical property set used by the correlations and by the ε–NTU/UA formulation, while $\dot{m}_{\mathrm{in}}$ and $\dot{m}_{\mathrm{ext}}$ set the Reynolds numbers, heat capacity rates, and therefore both $\dot{Q}$ and pressure losses. v

4.3.5. Three-level DOE factor sets

All geometric parameters and operating conditions are sampled at three discrete levels (low, medium, high), consistently with the ranges established in the CFD-based analyses used to construct the response surfaces. The core thickness S is assigned the three values

$$S \in \{0.070,\ 0.100,\ 0.160\}\ \mathrm{m}. \tag{4.31}$$

The internal fin parameters are sampled as

$$x_{\mathrm{in}} \in \{1.10,\ 2.50,\ 3.93\} \times 10^{-3}\ \mathrm{m}, \tag{4.32}$$

$$y_{\mathrm{in}} \in \{2.00,\ 3.00,\ 6.50\} \times 10^{-3}\ \mathrm{m}, \tag{4.33}$$

$$\ell_{\mathrm{in}} \in \{1.95,\ 5.00,\ 30.0\} \times 10^{-3}\ \mathrm{m}. \tag{4.34}$$

For the OSF–OSF configuration, the external fin parameters are

$$x_{\mathrm{ext}} \in \{1.75,\ 2.50,\ 6.00\} \times 10^{-3}\ \mathrm{m}, \tag{4.35}$$

$$y_{\mathrm{ext}} \in \{6.00,\ 9.50,\ 10.5\} \times 10^{-3}\ \mathrm{m}, \tag{4.36}$$

$$\ell_{\mathrm{ext}} \in \{3.15,\ 5.00,\ 10.0\} \times 10^{-3}\ \mathrm{m}. \tag{4.37}$$

For the OSF–Wavy configuration, the external fin parameters are

$$x_{\mathrm{ext}} \in \{4.30,\ 5.00,\ 7.30\} \times 10^{-3}\ \mathrm{m}, \tag{4.38}$$

$$y_{\mathrm{ext}} \in \{8.00,\ 9.50,\ 11.0\} \times 10^{-3}\ \mathrm{m}, \tag{4.39}$$

$$\ell_{\mathrm{ext}} \in \{6.50,\ 10.0,\ 20.0\} \times 10^{-3}\ \mathrm{m}, \tag{4.40}$$

$$a_{2,\mathrm{ext}} \in \{8.00,\ 10.0,\ 15.0\} \times 10^{-3}\ \mathrm{m}. \tag{4.41}$$

The external air mass flow rate is sampled as

$$\dot{m}_{\mathrm{ext}} \in \{1.11,\ 1.66,\ 2.22\}\ \mathrm{kg\,s^{-1}}. \tag{4.42}$$

On the internal side, three working fluids are considered (oil, coolant, charge air). For each fluid, three mass flow rates are prescribed:

$$\dot{m}_{\text{in}} \in \{0.68,\ 1.72,\ 3.44\}\ \text{kg}\,\text{s}^{-1} \qquad \text{(oil)}, \tag{4.43}$$

$$\dot{m}_{\text{in}} \in \{0.85,\ 2.14,\ 4.27\}\ \text{kg}\,\text{s}^{-1} \qquad \text{(coolant)}, \tag{4.44}$$

$$\dot{m}_{\text{in}} \in \{0.10,\ 0.25,\ 0.40\}\ \text{kg}\,\text{s}^{-1} \qquad \text{(charge air)}. \tag{4.45}$$

4.3.6. DOE grid size

The full factorial DOE dataset is constructed as the Cartesian product of all factor level sets. For the OSF–OSF configuration, eight scalar factors are sampled at three levels, combined with nine internal operating conditions, resulting in

$$N^{(\text{OSF–OSF})} = 3^8 \times 9 = 59049 \tag{4.46}$$

DOE samples.

For the OSF–Wavy configuration, nine scalar factors are sampled at three levels, again combined with nine internal operating conditions, leading to

$$N^{(\text{OSF–Wavy})} = 3^9 \times 9 = 177147 \tag{4.47}$$

DOE samples.

Although these sample sizes are large, the resulting datasets are fully deterministic and non-confounded. Most importantly, the full factorial structure ensures that main effects and interaction effects can be quantified unambiguously across the selected ranges, providing reference-quality sensitivity information prior to the application of multi-objective optimisation algorithms.

4.3.7. Concluding remarks and link to statistical sensitivity analysis

In summary, a full factorial DOE has been constructed to probe the coupled thermo–hydraulic and cost response of PFHE radiators over a discrete, three-level representation of the design space. Two fin architectures have been investigated (OSF–OSF and OSF–Wavy), while operating conditions have been expanded to cover three internal working fluids (oil, coolant, charge air) and multiple mass-flow-rate levels on both sides. For each DOE sample, the Python implementation evaluates the deterministic mapping

$$\mathscr{M} :\ \boldsymbol{\xi} \longmapsto \mathbf{r} = \big(\dot{Q},\ \Delta p_{\text{in}},\ \Delta p_{\text{ext}},\ C\big), \tag{4.48}$$

thereby generating large, structured datasets where all effects are observed under controlled and repeatable conditions.

The key outcome of this DOE is not an "optimal" configuration, but a quantitative basis to answer a more valuable question: *which factors truly drive the objective functions, and which ones do not*. In practice, if a parameter (or a whole interaction family) is shown to be weakly influential within the investigated ranges, it can be fixed *a priori*. This reduces the effective dimensionality of the subsequent optimisation problem and yields a direct computational advantage: fewer free variables imply fewer function evaluations, improved convergence robustness, and a cleaner interpretation of the final Pareto trade-offs.

The next section therefore performs a dedicated statistical post-processing of the DOE outcomes. In particular, a Student's *t*-based sensitivity analysis is used to rank the influence of each factor (and selected interactions) on $\dot{Q}$, Δp_{in}, Δp_{ext}, and C, and to identify the direction of the effects across the prescribed level changes. This step turns the DOE dataset into an explicit decision tool, enabling a principled screening before the multi-objective optimisation stage.

4.4. Student's *t*-test–based sensitivity analysis

Once the full factorial DOE has been completed, the focus of the analysis naturally shifts from the exploration of the design space to the interpretation of the information embedded in the generated dataset. The DOE provides a comprehensive and structured sampling of the admissible design configurations, but it does not, by itself, indicate which parameters truly govern the system behaviour and which ones play a secondary or negligible role. For this reason, a dedicated post–processing phase is required, aimed at extracting quantitative sensitivity information from the DOE results.

In the present work, this task is addressed through a sensitivity analysis based on the Student's *t*-test. The primary objective of this analysis is not to perform classical statistical inference, but rather to provide a robust and quantitative screening of the design parameters. In particular, the *t*-test is used to rank the factors according to the magnitude of their influence on the objective functions and to identify those variables that can be safely fixed in subsequent optimisation steps without inducing a significant loss of accuracy.

In its general formulation, the Student's *t*-test evaluates whether the difference between two sample means is statistically significant when compared to the variability observed within the samples. When transposed to the context of Design of Experiments, this concept acquires a clear physical interpretation: the test quantifies whether the variation of a response induced by a controlled change in a design parameter is large enough

to emerge from the background variability caused by all other factors simultaneously varying across their admissible ranges.

In simulation-driven DOE studies, such as the present PFHE analysis, the variability of the response is not associated with experimental noise or measurement uncertainty, but rather with the intrinsic sensitivity of the numerical model to the remaining design variables. As a consequence, the *t*-test is employed here as a deterministic sensitivity indicator, whose role is to normalise the observed effect of a given factor with respect to the natural scatter of the DOE dataset. This interpretation is fully consistent with established practices in engineering design optimisation and DOE-based screening methodologies.

From a methodological standpoint, the adoption of the Student's *t*-test is particularly well suited to full factorial designs. Owing to the orthogonality of the sampling scheme, the conditional subsets of the DOE associated with different levels of a given factor remain statistically comparable. This property ensures that the sensitivity indicators derived from the *t*-test are not biased by confounding effects introduced by the DOE structure itself, but rather reflect genuine physical trends in the system response.

In the context of PFHE radiator design, this screening step plays a pivotal role. The thermo–hydraulic and economic performance of the exchanger depends on a relatively large number of geometric and operating parameters, many of which are strongly coupled. Identifying the dominant drivers among these parameters is essential to reduce the dimensionality of the optimisation problem and to focus computational resources on the variables that matter most. The Student's *t*-based sensitivity analysis therefore represents a key intermediate step between the exhaustive DOE exploration and the targeted multi-objective optimisation carried out in the following chapters.

4.4.1. Post-processing workflow implemented in Python

The Student's *t*-based sensitivity analysis is implemented through a dedicated Python post–processing workflow operating on the DOE databases generated for each PFHE configuration. Although separate scripts are used for the OSF–OSF and OSF–Wavy architectures and for the different internal working fluids, the underlying workflow is identical and fully systematic. This ensures consistency in the sensitivity assessment and enables meaningful comparisons across configurations and operating conditions.

Each DOE database contains, for every simulation run i, the complete set of input variables and the corresponding response vector,

$$\boldsymbol{\xi}^{(i)} = \Big(S,\ \mathbf{g}_{\text{in}},\ \mathbf{g}_{\text{ext}},\ \dot{m}_{\text{in}},\ \dot{m}_{\text{ext}},\ f_{\text{in}}\Big), \qquad \mathbf{r}^{(i)} = \Big(\dot{Q},\ \Delta p_{\text{in}},\ \Delta p_{\text{ext}},\ C\Big), \tag{4.49}$$

where the notation and physical meaning of each component have been defined in the previous section.

The first step of the workflow consists in separating the DOE databases according to the internal working fluid, yielding three independent datasets,

$$\mathscr{D}^{(\text{oil})}, \qquad \mathscr{D}^{(\text{coolant})}, \qquad \mathscr{D}^{(\text{charge air})}. \tag{4.50}$$

This separation avoids mixing fundamentally different thermo–physical regimes within the same statistical sample and preserves the physical interpretability of the sensitivity indicators.

For each fluid-specific dataset, the sensitivity analysis is performed factor by factor. For a generic design parameter X_j sampled at three discrete levels $\{X_{j,1}, X_{j,2}, X_{j,3}\}$, the corresponding DOE runs are grouped into three conditional subsets. For each subset, the mean and variance of each response quantity are computed,

$$\bar{r}_{m,j,\ell}, \qquad s^2_{m,j,\ell}, \qquad \ell = 1,2,3, \quad m \in \{\dot{Q}, \Delta p_{\text{in}}, \Delta p_{\text{ext}}, C\}. \tag{4.51}$$

The mid level ($\ell = 2$) is selected as reference, and the response shifts associated with the low and high levels are quantified through Welch-type Student's t-statistics,

$$t_{m,j,\ell} = \frac{\bar{r}_{m,j,\ell} - \bar{r}_{m,j,2}}{\sqrt{\dfrac{s^2_{m,j,\ell}}{n_{j,\ell}} + \dfrac{s^2_{m,j,2}}{n_{j,2}}}}, \qquad \ell \in \{1,3\}. \tag{4.52}$$

For each design parameter, the resulting indicators are collected into a compact sensitivity matrix,

$$\mathbf{T}_j = \begin{bmatrix} t_{\dot{Q},j,1} & t_{\Delta p_{\text{in}},j,1} & t_{\Delta p_{\text{ext}},j,1} & t_{C,j,1} \\ t_{\dot{Q},j,3} & t_{\Delta p_{\text{in}},j,3} & t_{\Delta p_{\text{ext}},j,3} & t_{C,j,3} \end{bmatrix}, \tag{4.53}$$

which simultaneously describes the sensitivity of all objective functions to variations of the same factor.

4.4.2. Block-diagram representation of the sensitivity workflow

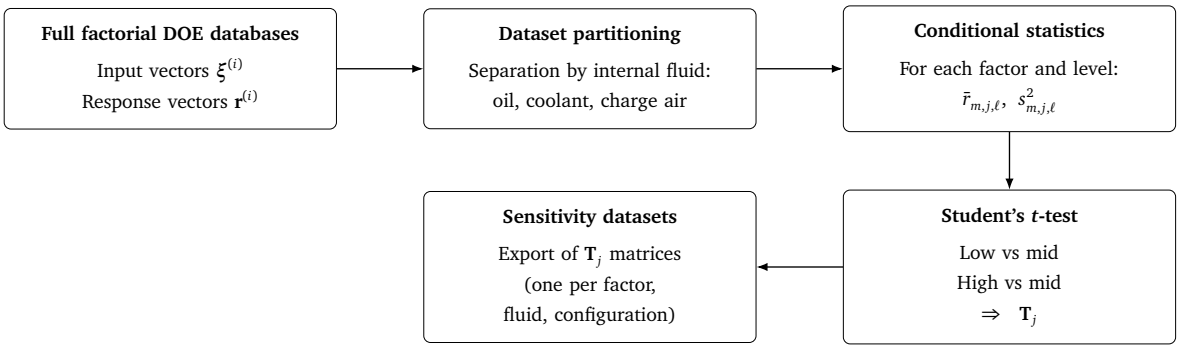

Figure 4.3. Block-diagram representation of the Student's *t*-based sensitivity analysis workflow implemented in Python.

The numerical sensitivity datasets produced by this workflow constitute the basis for the graphical analysis presented in the following section. There, the *t*-based indicators are used to rank design parameters, identify dominant effects, and support the reduction of the design space prior to multi-objective optimisation.

4.4.3. Graph construction and data representation for the Student's t-test analysis

The results of the Student's *t*-test sensitivity analysis are visualised through a series of parametric plots developed for each fin configuration (OSF–OSF and OSF–Wavy) and for each working fluid (air, coolant, and oil). The objective of these plots is to provide a clear and consistent representation of how variations in a single design or operating parameter affect the normalised thermo–economic responses of the PFHE, while all other factors are statistically accounted for through the DOE framework.

For each configuration and fluid, a single input parameter is varied across its three prescribed DOE levels, and the corresponding variation of the response metrics is extracted from the Student's *t*-test output matrices. The plotting scripts load these matrices from external result files and process them in a fully automated and reproducible manner
.

Abscissa definition. In all plots, the abscissa represents the physical value of the parameter under investigation. Depending on the specific figure, this may correspond to:

- the core thickness S,
- an internal fin geometric parameter (x_{in}, y_{in}, or ℓ_{in}),
- an external fin geometric parameter (x_{ext}, y_{ext}, ℓ_{ext}, or $a_{2,\text{ext}}$ in the case of wavy fins),

- the external air mass flow rate $\dot{m}_{\text{ext}}$.

All abscissae are expressed in physical units (metres for geometric quantities and $\mathrm{kg\,s^{-1}}$ for mass flow rates), rather than in coded DOE levels. This choice is intentional and enables the plots to be interpreted directly in engineering terms, without the need to revert to a normalised variable space.

Ordinate definition and normalisation. The ordinate reports the normalised response metrics obtained from the Student's t-test analysis. For a given response quantity y, the plotted value is defined as

$$y^* = \frac{y}{y_{\text{ref}}}, \tag{4.54}$$

where y_{ref} is the reference value corresponding to the first DOE level of the considered parameter. This normalisation is applied consistently to all response metrics and serves two main purposes: it removes the dimensionality of the quantities, and it enables the relative sensitivity of different metrics to be compared on the same plot.

For each abscissa value, the following normalised responses are plotted simultaneously:

- the heat transfer rate $\dot{Q}^*$,
- the internal pressure loss Δp^*_{in},
- the external pressure loss Δp^*_{ext},
- the overall heat transfer conductance UA^*,
- the radiator mass mass*,
- the radiator cost C^*.

Each response is represented by a distinct marker and line style, allowing multiple performance indicators to be assessed simultaneously as a function of the same design parameter.

Organisation of the plot sets. The complete set of plots is organised into six groups. Three groups correspond to the OSF–OSF configuration, analysed separately for air, coolant, and oil on the internal side. The remaining three groups correspond to the OSF–Wavy configuration, again distinguished by the internal working fluid. Within each group, a consistent plotting logic is applied, so that trends observed for a given parameter can be compared across different fluids and fin architectures without ambiguity.

It is important to emphasise that these plots do not represent raw DOE data, but rather the post-processed outcome of the Student's *t*-test applied to the full factorial dataset. As such, they provide a compact and physically interpretable visual summary of parameter influence, which will be systematically analysed and discussed in the following sections.

4.4.4. *OSF–OSF PFHE — Charge Air*

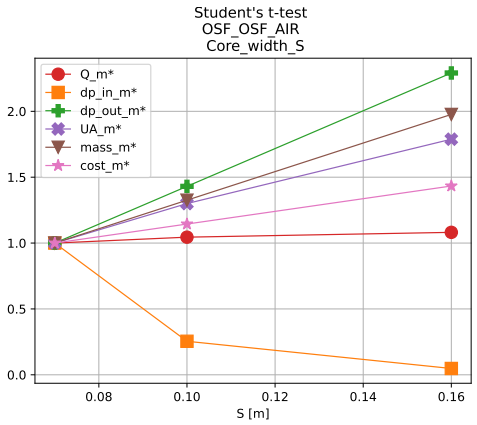

Figure 4.4. Student's *t*-test (OSF–OSF, charge air): influence of core thickness S.

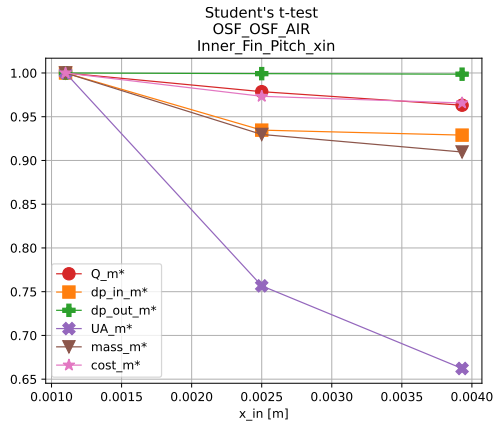

Figure 4.5. Student's *t*-test (OSF–OSF, charge air): influence of inner fin pitch x_{in}.

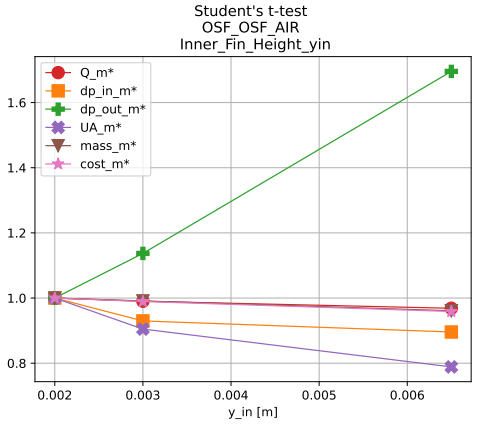

Figure 4.6. Student's *t*-test (OSF–OSF, charge air): influence of inner fin height y_{in}.

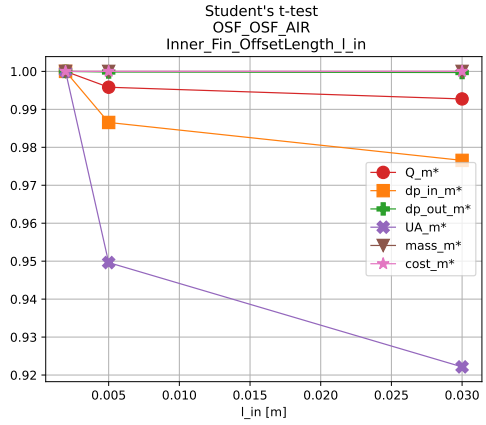

Figure 4.7. Student's *t*-test (OSF–OSF, charge air): influence of inner fin offset length ℓ_{in}.

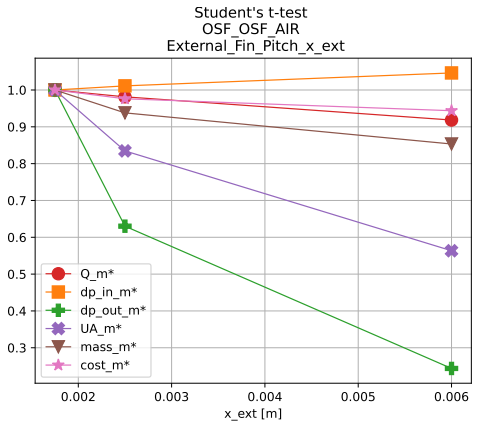

Figure 4.8. Student's t-test (OSF–OSF, charge air): influence of outer fin pitch x_{ext}.

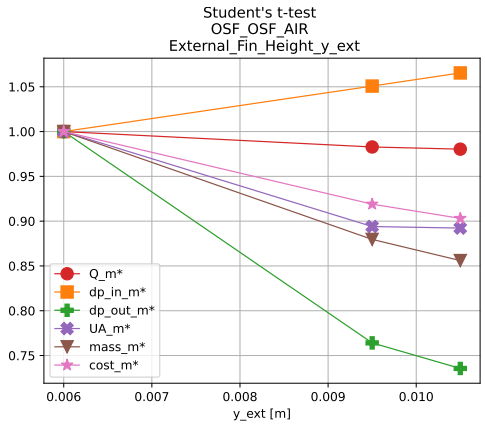

Figure 4.9. Student's t-test (OSF–OSF, charge air): influence of outer fin height y_{ext}.

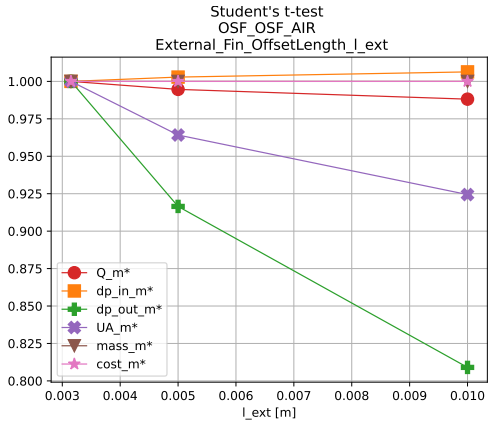

Figure 4.10. Student's t-test (OSF–OSF, charge air): influence of outer fin offset length ℓ_{ext}.

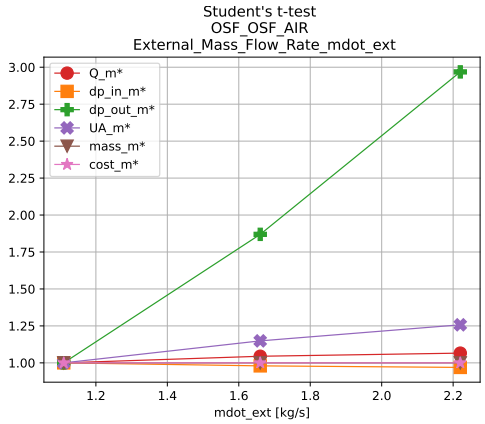

Figure 4.11. Student's t-test (OSF–OSF, charge air): influence of external mass flow rate $\dot{m}_{\text{ext}}$.

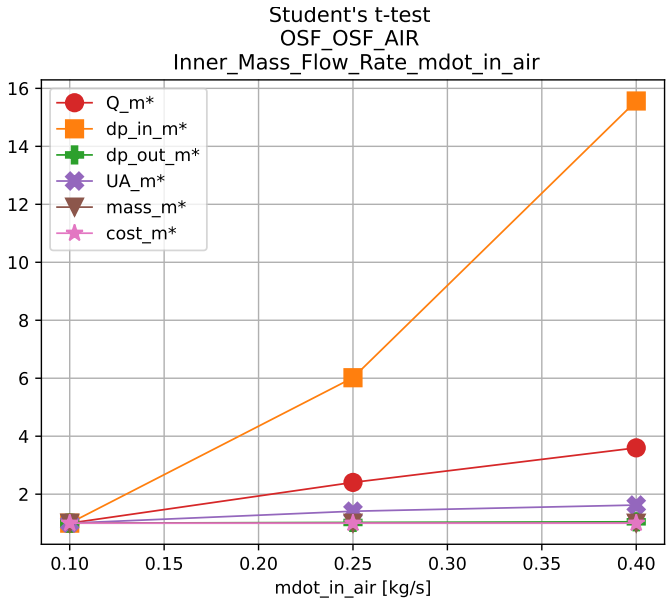

Figure 4.12. Student's *t*-test (OSF–OSF, charge air): influence of internal mass flow rate $\dot{m}_{\text{in}}$ (air side).

4.4.5. *OSF–OSF PFHE — Coolant*

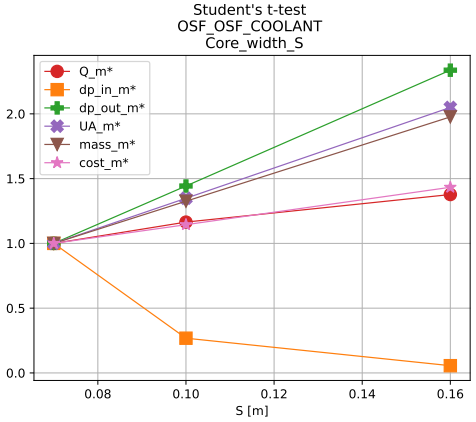

Figure 4.13. Student's *t*-test (OSF–OSF, coolant): influence of core thickness S.

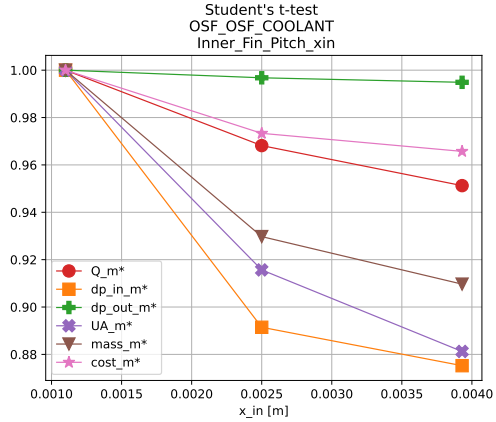

Figure 4.14. Student's *t*-test (OSF–OSF, coolant): influence of inner fin pitch x_{in}.

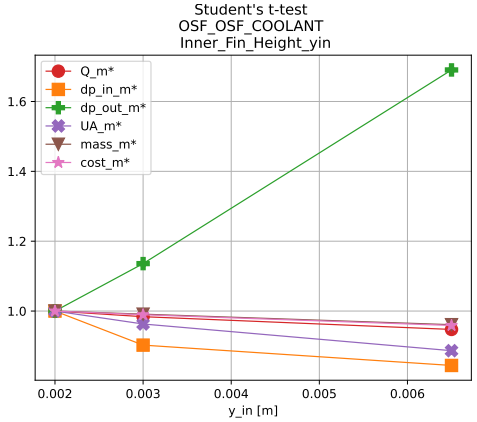

Figure 4.15. Student's t-test (OSF–OSF, coolant): influence of inner fin height y_{in}.

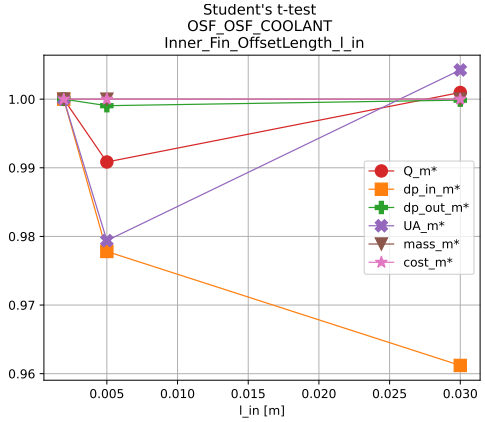

Figure 4.16. Student's t-test (OSF–OSF, coolant): influence of inner fin offset length ℓ_{in}.

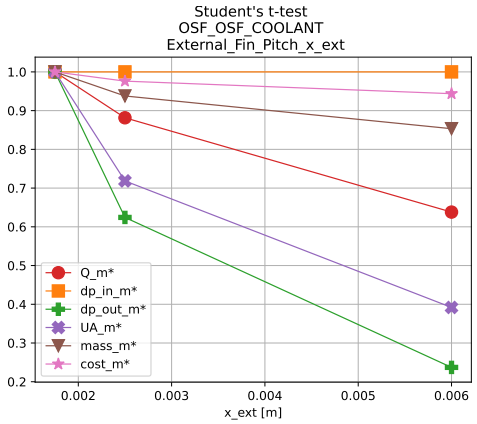

Figure 4.17. Student's t-test (OSF–OSF, coolant): influence of outer fin pitch x_{ext}.

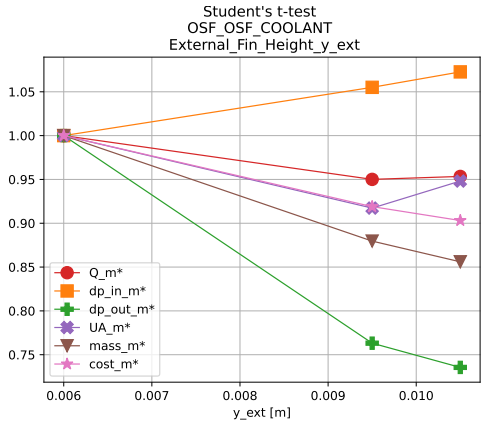

Figure 4.18. Student's t-test (OSF–OSF, coolant): influence of outer fin height y_{ext}.

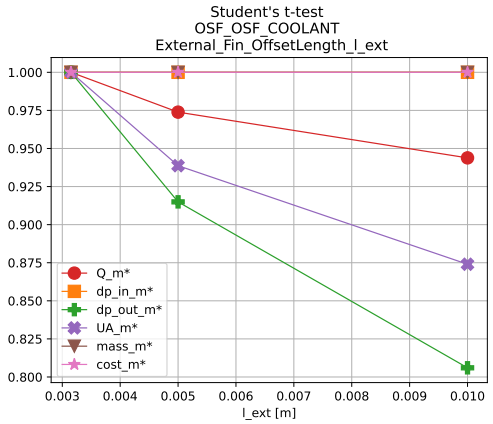

Figure 4.19. Student's t-test (OSF–OSF, coolant): influence of outer fin offset length ℓ_{ext}.

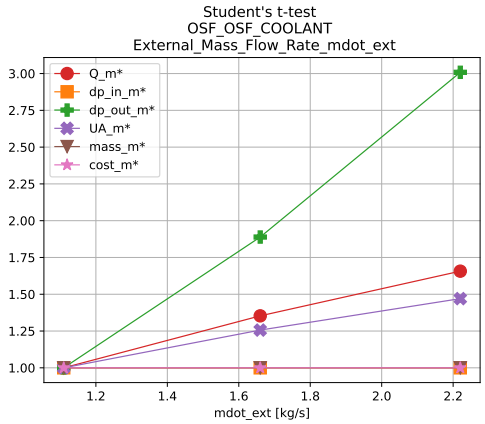

Figure 4.20. Student's t-test (OSF–OSF, coolant): influence of external mass flow rate $\dot{m}_{\text{ext}}$.

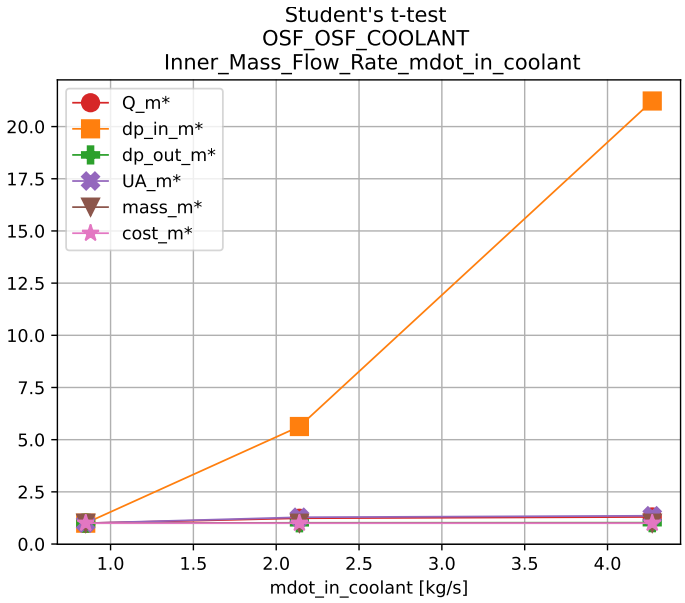

Figure 4.21. Student's *t*-test (OSF–OSF, coolant): influence of internal mass flow rate $\dot{m}_{\text{in}}$ (coolant).

4.4.6. *OSF–OSF PFHE — Lubricating Oil*

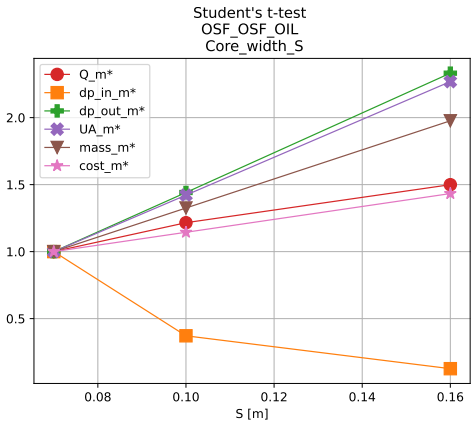

Figure 4.22. Student's *t*-test (OSF–OSF, oil): influence of core thickness S.

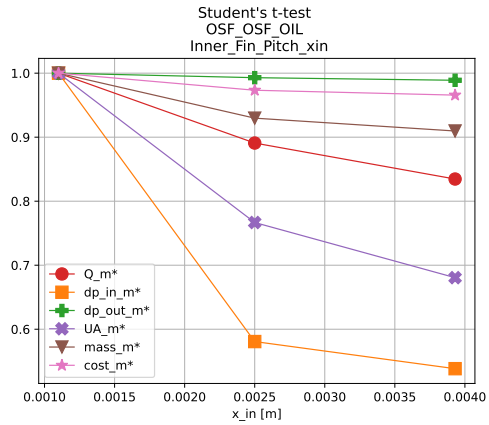

Figure 4.23. Student's *t*-test (OSF–OSF, oil): influence of inner fin pitch x_{in}.

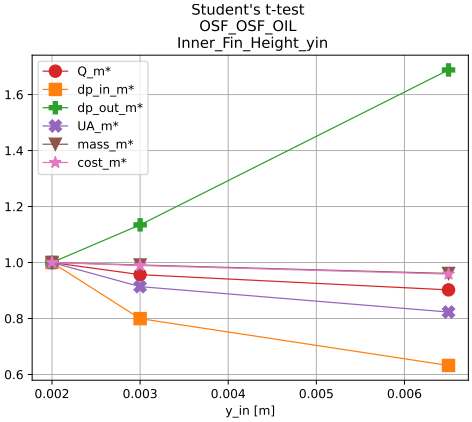

Figure 4.24. Student's t-test (OSF–OSF, oil): influence of inner fin height y_{in}.

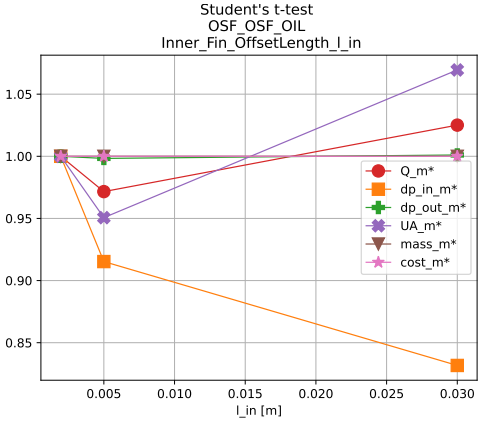

Figure 4.25. Student's t-test (OSF–OSF, oil): influence of inner fin offset length ℓ_{in}.

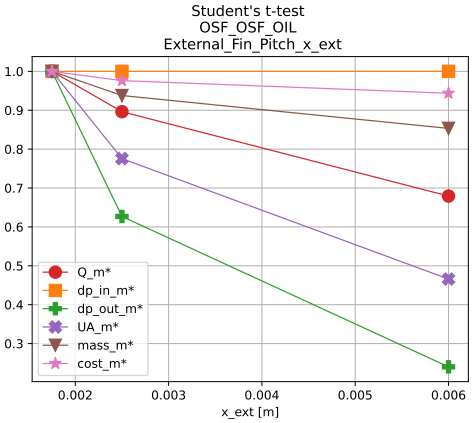

Figure 4.26. Student's t-test (OSF–OSF, oil): influence of outer fin pitch x_{ext}.

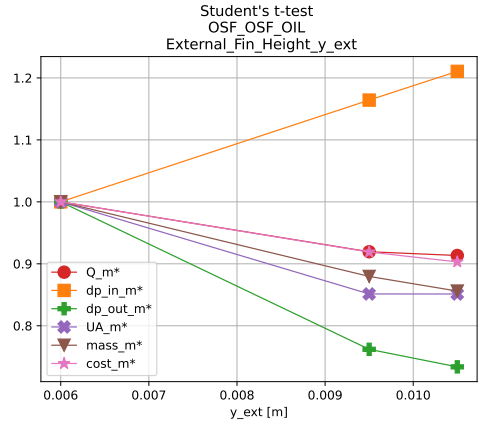

Figure 4.27. Student's t-test (OSF–OSF, oil): influence of outer fin height y_{ext}.

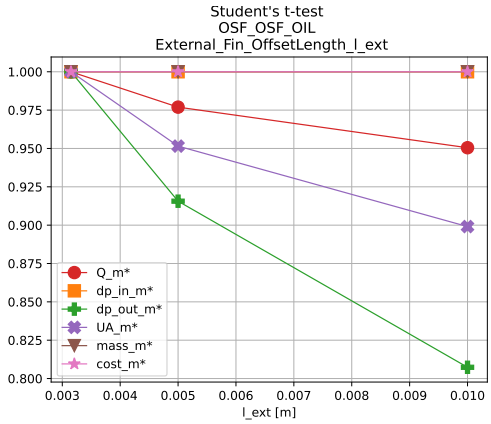

Figure 4.28. Student's t-test (OSF–OSF, oil): influence of outer fin offset length ℓ_{ext}.

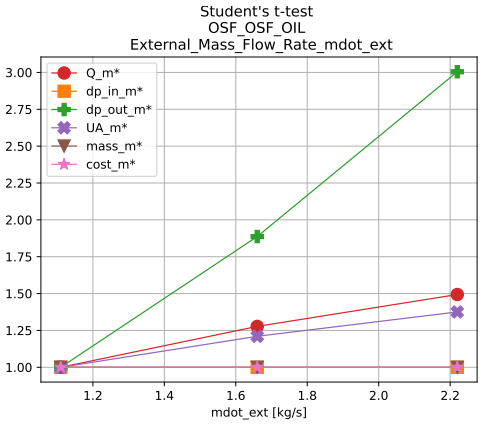

Figure 4.29. Student's t-test (OSF–OSF, oil): influence of external mass flow rate $\dot{m}_{\text{ext}}$.

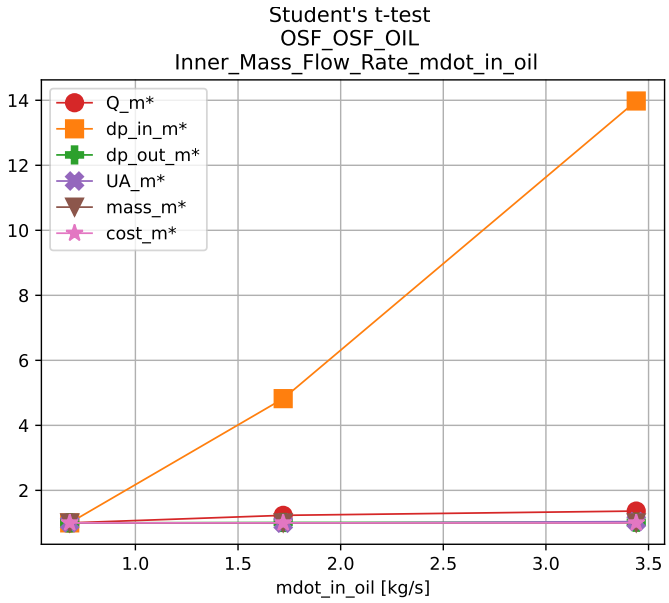

Figure 4.30. Student's *t*-test (OSF–OSF, oil): influence of internal mass flow rate $\dot{m}_{\text{in}}$ (oil).

4.4.7. *OSF–Wavy PFHE — Charge Air*

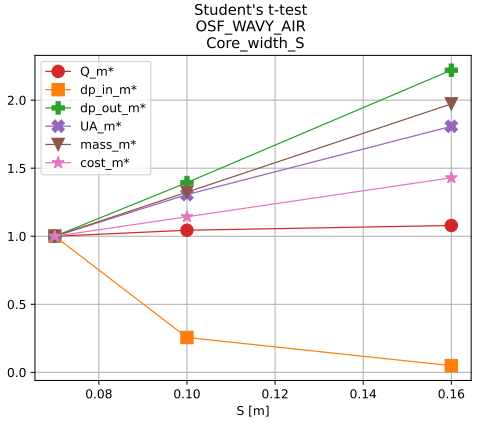

Figure 4.31. Student's *t*-test (OSF–Wavy, charge air): influence of core thickness S.

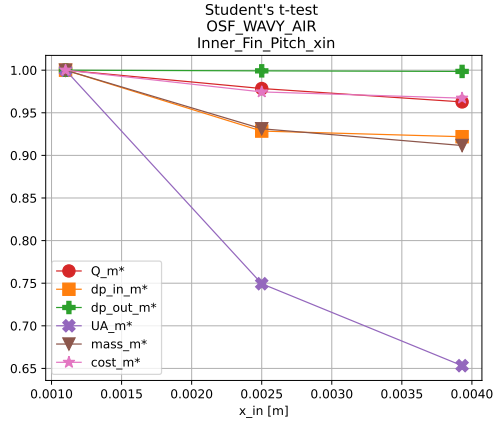

Figure 4.32. Student's *t*-test (OSF–Wavy, charge air): influence of inner fin pitch x_{in}.

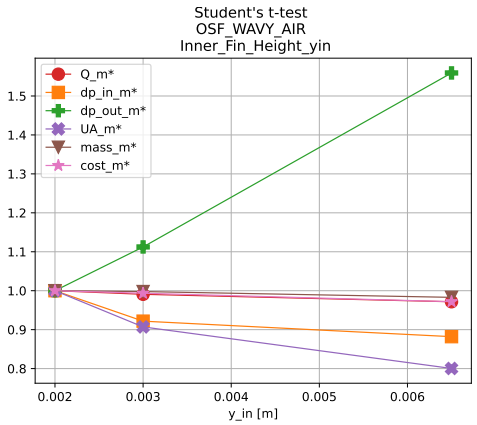

Figure 4.33. Student's t-test (OSF–Wavy, charge air): influence of inner fin height y_{in}.

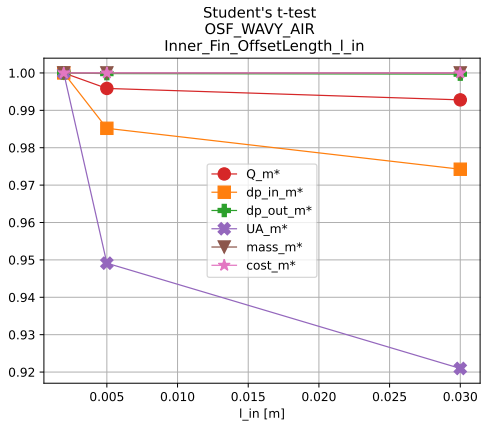

Figure 4.34. Student's t-test (OSF–Wavy, charge air): influence of inner fin offset length ℓ_{in}.

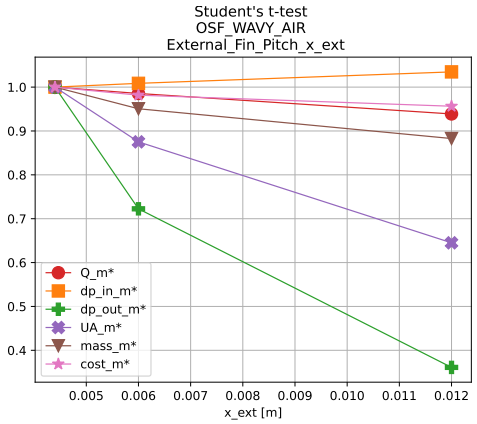

Figure 4.35. Student's t-test (OSF–Wavy, charge air): influence of outer fin pitch x_{ext}.

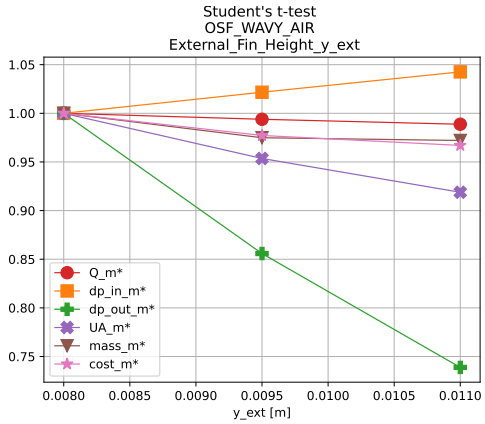

Figure 4.36. Student's t-test (OSF–Wavy, charge air): influence of outer fin height y_{ext}.

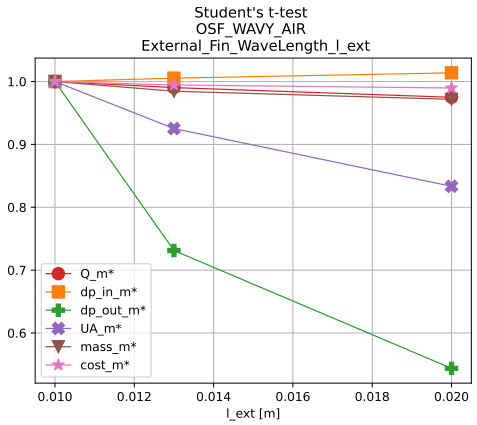

Figure 4.37. Student's t-test (OSF–Wavy, charge air): influence of outer fin wavelength ℓ_{ext}.

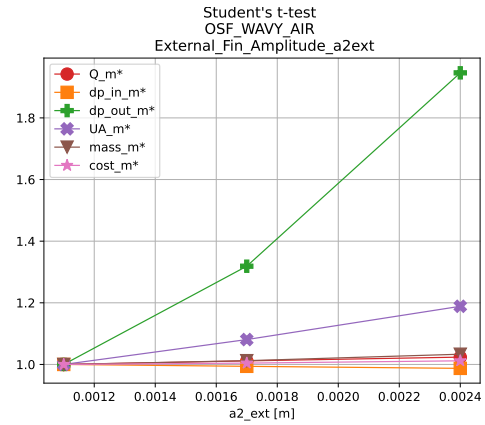

Figure 4.38. Student's t-test (OSF–Wavy, charge air): influence of outer fin amplitude $a_{2,\text{ext}}$.

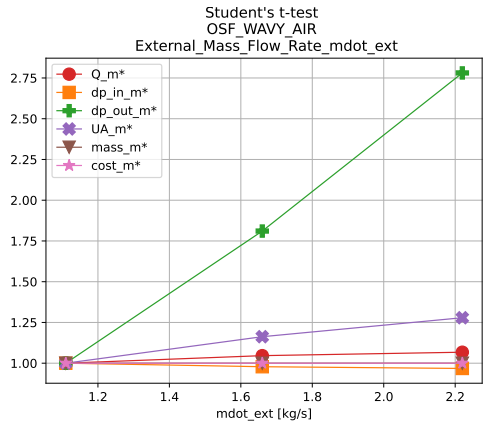

Figure 4.39. Student's *t*-test (OSF–Wavy, charge air): influence of external mass flow rate $\dot{m}_{\text{ext}}$.

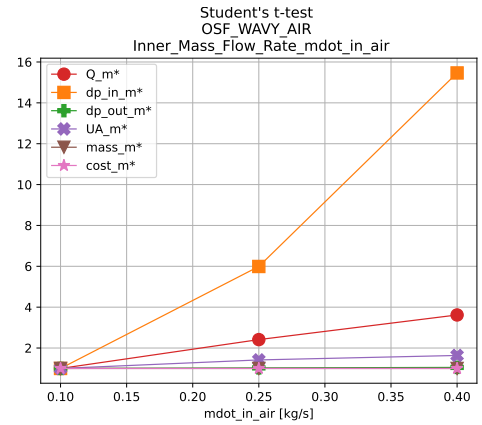

Figure 4.40. Student's *t*-test (OSF–Wavy, charge air): influence of internal mass flow rate $\dot{m}_{\text{in}}$ (air side).

*4.4.8. **OSF–Wavy PFHE — Coolant***

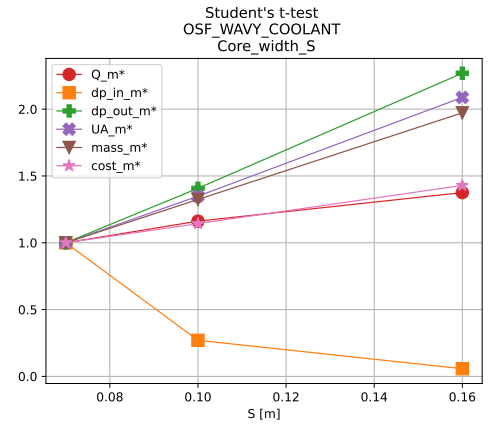

Figure 4.41. Student's *t*-test (OSF–Wavy, coolant): influence of core thickness S.

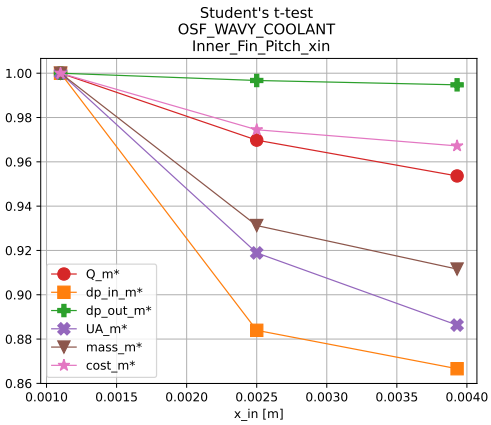

Figure 4.42. Student's *t*-test (OSF–Wavy, coolant): influence of inner fin pitch x_{in}.

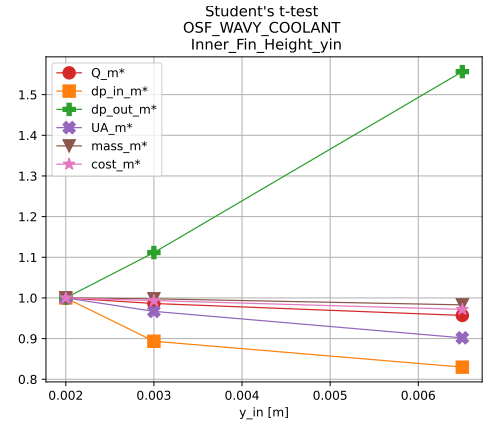

Figure 4.43. Student's *t*-test (OSF–Wavy, coolant): influence of inner fin height y_{in}.

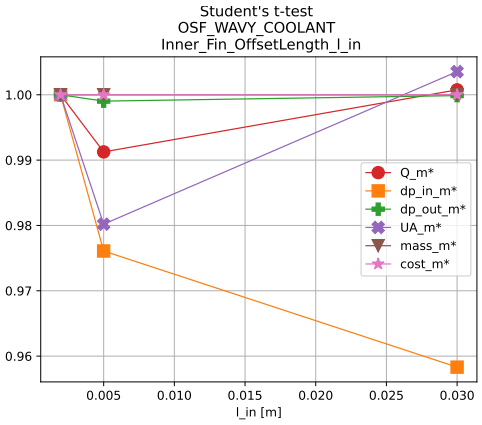

Figure 4.44. Student's *t*-test (OSF–Wavy, coolant): influence of inner fin offset length ℓ_{in}.

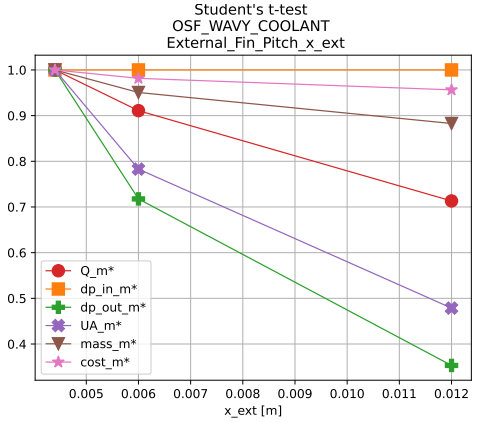

Figure 4.45. Student's t-test (OSF–Wavy, coolant): influence of outer fin pitch x_{ext}.

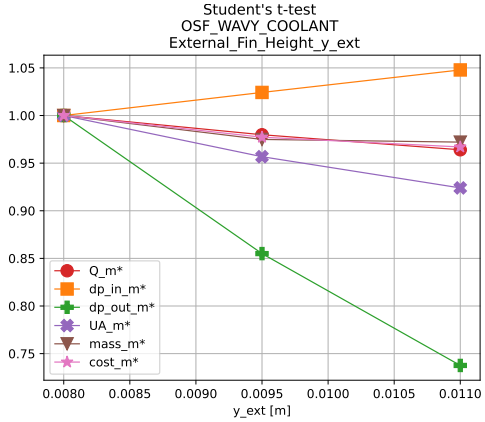

Figure 4.46. Student's t-test (OSF–Wavy, coolant): influence of outer fin height y_{ext}.

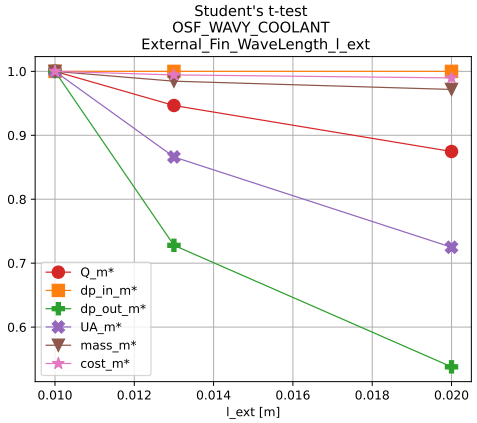

Figure 4.47. Student's t-test (OSF–Wavy, coolant): influence of outer fin wavelength ℓ_{ext}.

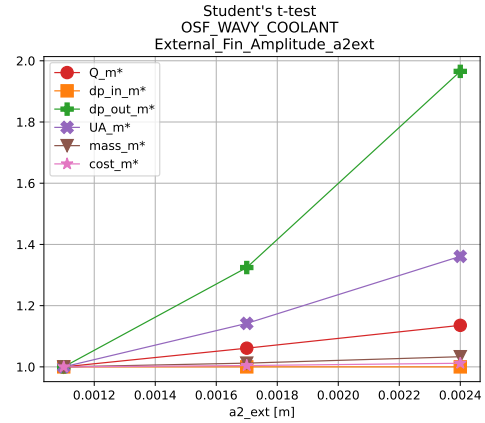

Figure 4.48. Student's t-test (OSF–Wavy, coolant): influence of outer fin amplitude $a_{2,\text{ext}}$.

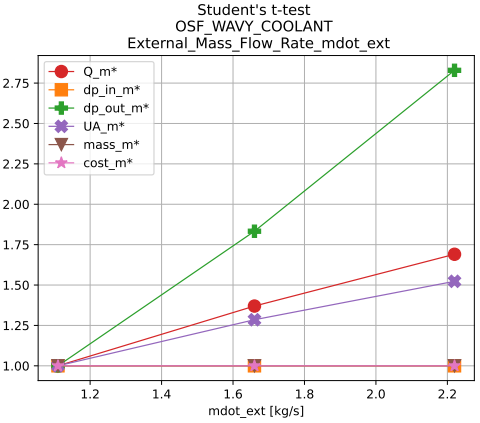

Figure 4.49. Student's t-test (OSF–Wavy, coolant): influence of external mass flow rate $\dot{m}_{\text{ext}}$.

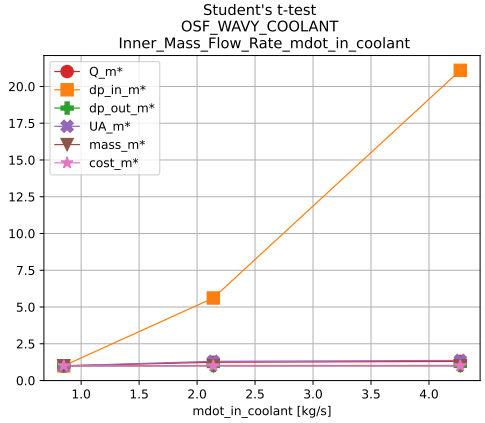

Figure 4.50. Student's t-test (OSF–Wavy, coolant): influence of internal mass flow rate $\dot{m}_{\text{in}}$ (coolant).

4.4.9. *OSF–Wavy PFHE — Lubricating Oil*

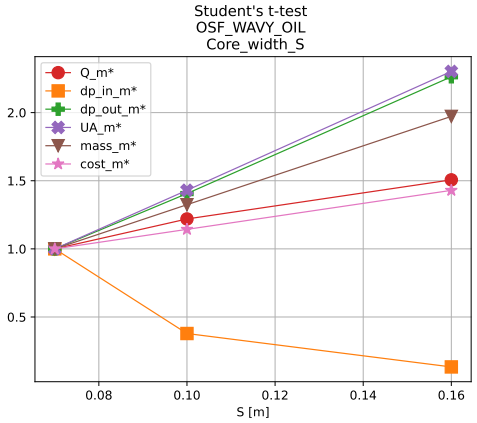

Figure 4.51. Student's *t*-test (OSF–Wavy, oil): influence of core thickness S.

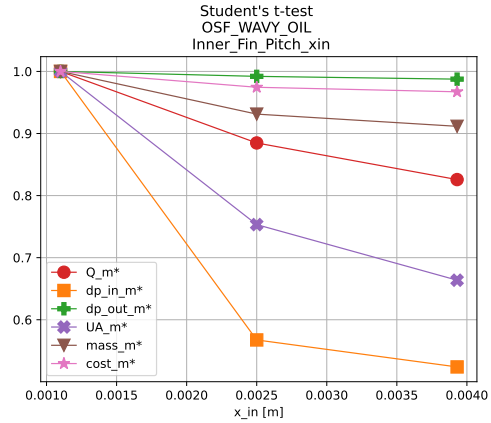

Figure 4.52. Student's *t*-test (OSF–Wavy, oil): influence of inner fin pitch x_{in}.

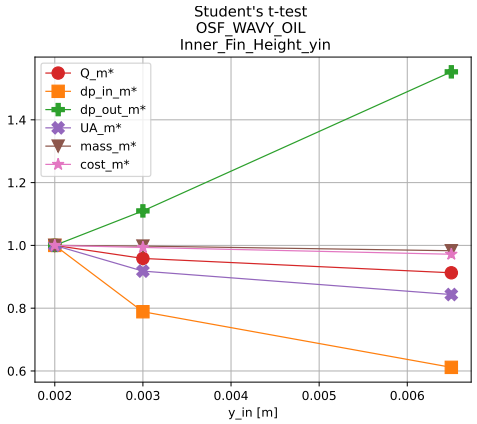

Figure 4.53. Student's *t*-test (OSF–Wavy, oil): influence of inner fin height y_{in}.

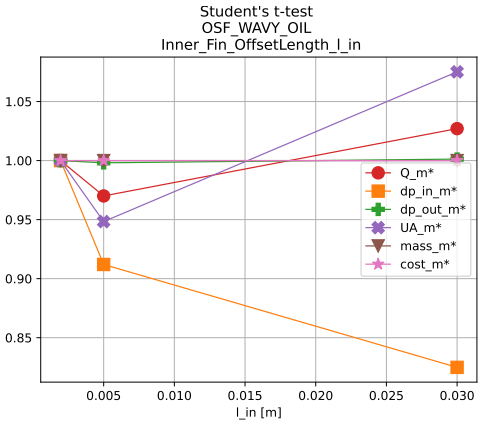

Figure 4.54. Student's *t*-test (OSF–Wavy, oil): influence of inner fin offset length ℓ_{in}.

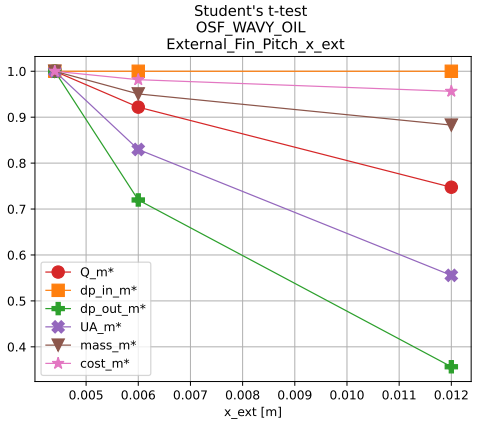

Figure 4.55. Student's *t*-test (OSF–Wavy, oil): influence of outer fin pitch x_{ext}.

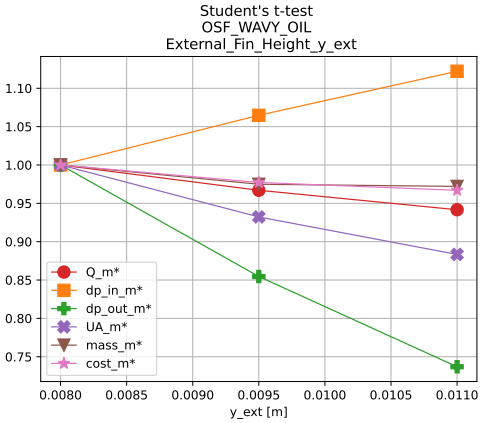

Figure 4.56. Student's *t*-test (OSF–Wavy, oil): influence of outer fin height y_{ext}.

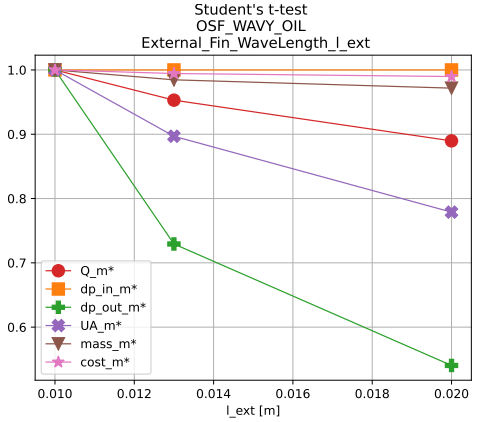

Figure 4.57. Student's t-test (OSF–Wavy, oil): influence of outer fin wavelength ℓ_{ext}.

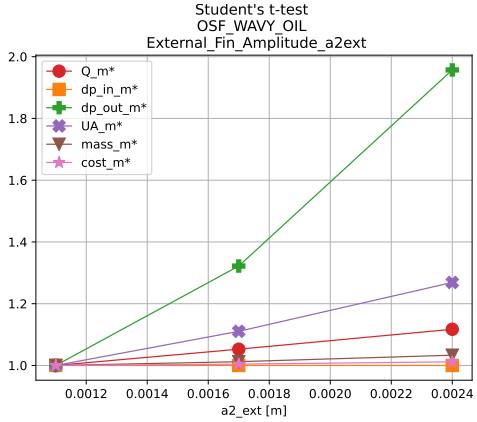

Figure 4.58. Student's t-test (OSF–Wavy, oil): influence of outer fin amplitude $a_{2,\text{ext}}$.

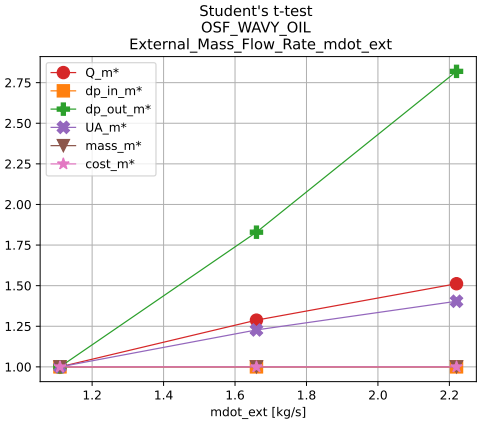

Figure 4.59. Student's t-test (OSF–Wavy, oil): influence of external mass flow rate $\dot{m}_{\text{ext}}$.

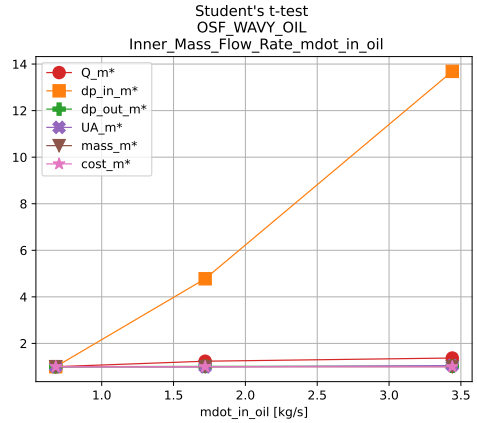

Figure 4.60. Student's t-test (OSF–Wavy, oil): influence of internal mass flow rate $\dot{m}_{\text{in}}$ (oil).

4.4.10. Cross-case synthesis and implications for optimisation

Overall, the sensitivity patterns confirm that the PFHE design problem is intrinsically multi-objective: several geometric and operating factors influence $\dot{Q}$, Δp_{out}, and C simultaneously, often in competing directions. Still, the screening results provide actionable guidance in two important ways. First, they reveal parameters whose impact is consistently weak within the explored ranges; these variables can be fixed to reduce dimensionality without a meaningful loss of representativeness. Second, they identify factors producing clear trade-offs: these variables must be retained in the optimization because they shape the Pareto structure of the problem.

STUDENT'S T-TEST RESULTS						
	OSF-OSF			OSF-WAVY		
INNER MEDIUM	OIL	COOLANT	CHARGE_AI	OIL	COOLANT	CHARGE_AIR
Core_width_**S**						
External_Fin_Pitch_**x_ext**						
External_Fin_Height_**y_ext**						
External_Fin_OffsetLength_**l_ext**	MAX	MAX	MAX			MAX
External_Fin_Amplitude_**a2ext**	X	X	X			MIN
Inner_Fin_Pitch_**xin**						
Inner_Fin_Height_**yin**						
Inner_Fin_OffsetLength_**l_in**	MAX	MAX	MAX	MAX	MAX	MAX
Inner_Fin_Amplitude_**a2_in**	X	X	X	X	X	X
Inner_Mass_Flow_Rate_**mdot_in**	MIN	MIN		MIN	MIN	
External_Mass_Flow_Rate_**mdot_ext**			MIN			MIN

Figure 4.61. Summary matrix of the Student's *t*-test sensitivity analysis for OSF–OSF and OSF–Wavy PFHE configurations, considering oil, coolant, and charge-air internal flows.

The matrix reported in Fig. 4.61 provides a compact and synthetic overview of the results of the Student's *t*-test–based sensitivity analysis. The symbols and colour coding adopted in Fig. 4.61 have the following meaning:

- **X**: parameter not present in the considered configuration and therefore not included in the DOE.
- **Green cells**: parameter identified as impactful for the optimization process and retained as an active design variable.
- **MAX**: parameter exhibiting a negligible influence on the objective functions; the parameter is therefore fixed at its maximum admissible value.
- **MIN**: parameter exhibiting a negligible influence on the objective functions; the parameter is therefore fixed at its minimum admissible value.

Parameters responsible for clear trade-offs between objectives (e.g., higher $\dot{Q}$ at the expense of increased Δp_{out} and/or C) are retained as critical variables for the subsequent multi-objective optimisation.

Conversely, parameters showing consistently weak or neutral effects across all objectives and operating conditions can be reasonably fixed *a priori*, enabling a significant reduction of the effective design-space dimensionality and, consequently, of the overall computational cost.

4.5. Concluding remarks

This chapter has presented a comprehensive sensitivity analysis of PFHE radiators based on a full factorial Design of Experiments combined with a Student's *t*-test post-processing. The objective of this analysis was not the direct identification of an optimal configuration, but the systematic investigation of how geometric and operating parameters influence the key objective functions, namely the heat transfer rate $\dot{Q}$, the external pressure losses Δp_{out}, and the production cost C.

The adoption of a fully deterministic full factorial DOE allowed the multidimensional design space to be explored in a structured and unbiased manner, ensuring that both main effects and interaction effects were consistently captured. The subsequent application of the *t*-Student analysis provided a quantitative measure of the statistical relevance of each design parameter, enabling a clear separation between strongly influential variables and parameters whose effect on the objective functions remains weak or negligible within the investigated ranges.

A key outcome of this combined DOE and sensitivity framework is the possibility to safely discard or fix a subset of design variables without introducing significant performance penalties. Parameters classified as weakly influential can be set *a priori* to convenient values (either minimum or maximum, depending on the objective alignment), thereby reducing the effective dimensionality of the design space. This reduction is not a marginal improvement, but a decisive factor in simulation-driven optimisation, since the computational cost and convergence complexity of global optimisation strategies grow rapidly with the number of active design variables.

Beyond dimensionality reduction, the present analysis has provided relevant physical insight into the PFHE design problem. The relative trends of $\dot{Q}$, Δp_{out}, and C across the DOE levels have clarified how specific geometric features and operating conditions govern thermal performance, hydraulic penalties, and cost escalation. The sensitivity patterns have also been shown to depend on both the fin architecture (OSF–OSF versus OSF–Wavy) and the working fluid, confirming that simplified or one-factor-at-a-time approaches are inadequate for supporting robust industrial design decisions.

Overall, the DOE and *t*-Student sensitivity analysis developed in this chapter establishes a rigorous quantitative foundation for the optimization stage addressed next. By retaining only the parameters that induce meaningful trade-offs among the objective functions and eliminating weakly influential variables, a reduced yet physically consistent design space is obtained. This reduced design space will be exploited in the subsequent chapter through a multi-objective optimisation framework based on genetic algorithms, specifically the NSGA-II approach, lowering the computational burden while enhancing the effectiveness, robustness, and interpretability of Pareto-optimal solutions.

CHAPTER 5

Multi-Objective Optimization of PFHEs

5.1. Introduction

In the design of modern engineering systems, optimization has progressively evolved from a supporting computational tool to a central methodological pillar. Increasing system complexity, coupled with stringent performance requirements and economic constraints, has made intuitive or purely experience–based design approaches increasingly inadequate. As a consequence, optimization techniques are now routinely employed to systematically explore large design spaces, quantify trade–offs among competing objectives, and support engineering decision–making in a rational and reproducible manner [12].

From a general standpoint, optimization aims at identifying the most suitable configuration of a system within a prescribed set of admissible solutions. In practical applications, this task is rarely trivial. Engineering systems are often governed by strongly nonlinear relationships, empirical correlations, and implicit couplings between geometric, operating, and physical parameters. Moreover, performance indicators of interest are frequently conflicting in nature, making the identification of a single "best" solution neither possible nor meaningful. These aspects are particularly evident in thermo–fluiddynamic applications, where improvements in thermal performance are commonly associated with penalties in pressure losses, weight, or manufacturing cost [46, 49].

Within this context, optimization problems can be formalized by introducing a vector of decision variables

$$\boldsymbol{x} \in \mathscr{X} \subseteq \mathbb{R}^n, \tag{5.1}$$

representing the degrees of freedom available to the designer. The classical deterministic formulation of an optimization problem can then be written as

$$\begin{aligned} \min_{\boldsymbol{x}\in\mathscr{X}} \quad & f(\boldsymbol{x}) \\ \text{subject to} \quad & \boldsymbol{g}(\boldsymbol{x}) \leq \boldsymbol{0}, \\ & \boldsymbol{h}(\boldsymbol{x}) = \boldsymbol{0}, \end{aligned} \tag{5.2}$$

where $f : \mathbb{R}^n \to \mathbb{R}$ denotes the objective function, while $\boldsymbol{g} : \mathbb{R}^n \to \mathbb{R}^p$ and $\boldsymbol{h} : \mathbb{R}^n \to \mathbb{R}^q$ represent inequality and equality constraint mappings, respectively. This formulation constitutes the theoretical foundation of nonlinear programming and deterministic optimization theory, as extensively discussed in the classical literature [83, 84].

Deterministic optimization methods typically rely on regularity assumptions on the objective function and constraints, such as continuity, differentiability, or convexity, in order to construct a unique descent direction in the design space. When such assumptions are satisfied, gradient–based algorithms can achieve fast convergence rates and strong optimality guarantees. However, many real engineering design problems violate these hypotheses. Highly nonlinear response surfaces, discontinuities introduced by empirical correlations, strong parameter couplings, and the coexistence of multiple local optima are frequently encountered. In these situations, deterministic approaches may converge prematurely to suboptimal solutions, with results that are strongly dependent on the initial guess and on the local structure of the objective landscape [12].

To overcome these limitations, stochastic optimization methods introduce randomness directly into the search process. Rather than following a single deterministic trajectory in the design space, the optimization algorithm generates a sequence of random vectors

$$\left\{\boldsymbol{x}^{(k)}\right\}_{k\in\mathbb{N}}, \qquad \boldsymbol{x}^{(k)} \in \mathscr{X}, \tag{5.3}$$

whose evolution is governed by probabilistic rules. From a mathematical standpoint, stochastic optimization can be interpreted as the minimization of an expected value

$$\min_{\boldsymbol{x}\in\mathscr{X}} \mathbb{E}\big[f(\boldsymbol{x},\xi)\big], \tag{5.4}$$

where ξ denotes a random vector accounting for uncertainty, numerical noise, or intentional stochastic perturbations. Even in fully deterministic engineering problems, stochasticity is often deliberately introduced to enhance global exploration capabilities and reduce sensitivity to initial conditions, especially in high–dimensional and multimodal design spaces [85, 86].

Stochastic optimisation encompasses a broad class of methods that rely on randomi-

sation to explore the design space and to mitigate the risk of convergence toward local optima. Unlike deterministic approaches, these methods do not require gradient information and are therefore particularly well suited to problems characterised by non-linearity, non-convexity, noise, or expensive black-box evaluations, as is often the case in complex thermo-fluid and energy systems [12].

Within this class, several families of algorithms can be identified. Random search and Monte Carlo methods represent the most elementary form of stochastic optimisation. Although conceptually simple and unbiased, their convergence rate is generally very poor, making them impractical for high-dimensional engineering problems unless combined with variance reduction or surrogate modelling techniques.

Particle Swarm Optimisation (PSO) constitutes a more structured stochastic approach, inspired by the collective motion of biological swarms [87]. In PSO, a population of particles evolves according to simple update rules based on individual and collective experience. PSO is often praised for its rapid convergence and ease of implementation, and it has been successfully applied to a wide range of single-objective engineering problems. However, as noted in the literature [12], PSO may suffer from premature convergence and loss of diversity, particularly in multimodal landscapes, and its extension to genuinely multi-objective formulations typically requires additional mechanisms to preserve solution spread along the Pareto front.

Other stochastic strategies include trajectory-based metaheuristics such as Simulated Annealing (SA) and Tabu Search, as well as hybrid or graph-based techniques, sometimes referred to as multi-objective graph traversal (MOGT) or evolutionary–graph methods in the broader optimisation literature. These approaches can be effective in specific contexts, especially when problem structure can be exploited, but they are generally less flexible when the goal is to approximate an entire Pareto front in a single run. In multi-objective settings, they often require repeated scalarisations or ad-hoc preference handling, which may bias the exploration toward particular regions of the trade-off surface [88].

From a comparative standpoint, population-based evolutionary algorithms exhibit a decisive conceptual advantage in multi-objective optimisation. Because a population naturally represents multiple candidate solutions, evolutionary strategies are intrinsically capable of approximating a set of Pareto-optimal solutions rather than collapsing the problem into a single compromise design. This property is not an implementation detail, but a structural feature of the algorithmic paradigm.

Multi-objective genetic algorithms (MOGAs) exploit this property explicitly by combining evolutionary operators with dominance-based selection principles. As reported in several foundational monographs on optimization [12, 88], MOGAs avoid the need

for a priori weighting of objectives and are able to capture non-convex, discontinuous, or highly curved Pareto fronts that would be inaccessible to weighted-sum or single-objective reformulations.

In contrast to PSO-based or trajectory-based methods, MOGAs offer a clearer separation between exploration and exploitation mechanisms through the use of crossover and mutation operators. Crossover promotes the recombination of favourable traits across the population, while mutation injects controlled randomness to maintain diversity and enable escape from local optima. This dual mechanism, coupled with dominance-based ranking, makes MOGAs particularly robust when dealing with complex engineering design spaces where competing objectives and constraints interact in a non-trivial manner.

For these reasons, MOGAs have emerged as a reference framework for multi-objective engineering optimisation, and they provide the natural conceptual foundation for advanced algorithms such as NSGA-II, which further enhance convergence efficiency and diversity preservation through elitist strategies and crowding-based selection mechanisms.

Among stochastic optimization techniques, genetic algorithms have gained widespread popularity due to their population–based structure and their intrinsic ability to explore complex design spaces. Inspired by the principles of natural evolution, genetic algorithms operate on a population of candidate solutions that evolve through selection, crossover, and mutation operators. Unlike deterministic methods, the search process is not confined to a single trajectory in $\mathbb{R}^n$, but rather to the collective evolution of a set of individuals, each representing a different region of the design space. This characteristic significantly reduces the probability of stagnation in local optima and promotes a broader exploration of feasible regions [89, 90].

The advantages of genetic algorithms become particularly evident in multi–objective optimization problems, where several conflicting objective functions must be optimized simultaneously. In such cases, the solution of interest is not a single optimum, but rather a set of non–dominated solutions approximating the Pareto front. Evolutionary multi–objective algorithms provide a natural framework for addressing this class of problems. Among them, the Non–dominated Sorting Genetic Algorithm II (NSGA–II) has emerged as a reference method due to its elitist strategy, reduced computational complexity, and effective diversity preservation mechanisms [91]. Owing to these properties, NSGA–II has been extensively applied to the optimization of thermal systems and compact heat exchangers, including plate–fin heat exchangers, as documented in a large body of literature [46, 48, 49, 62, 65].

Once a set of Pareto–optimal solutions has been obtained, an additional decision–making step is often required to identify a representative design suitable for practical implementation. Multi–criteria decision–making techniques enable a rational ranking

of Pareto solutions based on engineering priorities and performance trade–offs. In this context, the Technique for Order Preference by Similarity to Ideal Solution (TOPSIS) provides a mathematically consistent framework for selecting solutions based on their distance from ideal and anti–ideal points in the objective space [64, 92, 93].

Within this general framework, the optimization strategy adopted in the present work is articulated as follows. An initial reduction of the design space is performed through a Design of Experiments approach combined with statistical significance analysis based on the Student *t*–test, with the objective of identifying the most influential geometric and operating parameters. The reduced set of design variables is then explored by means of a multi–objective genetic algorithm implemented in a Python environment using the DEAP framework [90, 94]. A dedicated sensitivity analysis is subsequently carried out to assess the influence of the main algorithmic parameters, with convergence monitored through the hypervolume indicator. Finally, the resulting Pareto fronts are post–processed using a multi–criteria decision–making approach in order to identify representative optimal designs.

The remainder of this chapter is structured accordingly. First, the theoretical foundations of stochastic optimization, genetic algorithms, multi–objective evolutionary methods, and decision–making techniques are introduced. The optimization framework is then specialized to the case of plate–fin heat exchangers, and the adopted workflow is described in detail. Subsequently, the sensitivity analysis and the obtained Pareto fronts are presented and discussed, before concluding with a critical assessment of the main results and their implications for the optimal design of compact heat exchangers.

5.2. Mathematical framework for stochastic and multi-objective optimization

Engineering design problems are rarely driven by a single performance indicator. In practical settings (and certainly in PFHE design) one is typically forced to balance at least two competing requirements, such as maximizing a thermal duty while minimizing pressure losses and manufacturing-related penalties. In this context, it is often misleading to search for “the” optimum: the mathematically consistent target is instead a set of trade-off solutions. Stochastic and population-based strategies are particularly attractive because they explore the design domain broadly and can mitigate entrapment in local optima, although at the price of many function evaluations [12, 14, 88, 89].

In what follows, the multi-objective problem is introduced in a rigorous form, together with the concepts of dominance and Pareto optimality. Genetic and evolutionary algorithms are then described with explicit operators and typical variants (selection, crossover, mutation, elitism). This naturally leads to multi-objective genetic algorithms

(MOGAs) and, in particular, to the NSGA-II procedure, whose key ingredients are non-dominated sorting and crowding-distance diversity preservation [91]. The final part addresses the practical implementation in `DEAP` [94] and the a-posteriori selection of a single compromise design through TOPSIS, including its full computational pipeline and equations.

5.2.1. General formulation of multi-objective optimisation

Let the design variables be collected into a vector

$$\boldsymbol{x} \in \mathbb{R}^n, \qquad \boldsymbol{x} \in \Omega \subseteq \mathbb{R}^n, \tag{5.5}$$

where Ω is the feasible set induced by bounds and constraints. A multi-objective optimisation problem (MOP) is written as

$$\min_{\boldsymbol{x}\in\Omega} \boldsymbol{f}(\boldsymbol{x}) = \min_{\boldsymbol{x}\in\Omega} \begin{bmatrix} f_1(\boldsymbol{x}) \\ f_2(\boldsymbol{x}) \\ \vdots \\ f_m(\boldsymbol{x}) \end{bmatrix}, \tag{5.6}$$

subject to inequality and equality constraints,

$$g_k(\boldsymbol{x}) \le 0, \quad k = 1, \dots, n_g, \qquad h_\ell(\boldsymbol{x}) = 0, \quad \ell = 1, \dots, n_h. \tag{5.7}$$

The mapping $\boldsymbol{f} : \Omega \to \mathbb{R}^m$ defines the *objective space*; in multi-objective settings, convexity and smoothness are not guaranteed, and the trade-off surface can be disconnected, discontinuous, or highly non-convex [12, 88].

When some objectives are to be maximized, one may convert them to minimization by sign reversal, e.g.

$$\max f_j(\boldsymbol{x}) \quad \Longleftrightarrow \quad \min \tilde{f}_j(\boldsymbol{x}) = -f_j(\boldsymbol{x}), \tag{5.8}$$

so that Eq. (5.6) remains consistent. This is a trivial step mathematically, yet it is useful to keep in mind because "Pareto dominance" is defined with respect to a common direction of improvement.

5.2.2. Dominance, non-dominance, and Pareto sets

Pareto dominance. Consider two feasible solutions $\boldsymbol{x}^{(a)}, \boldsymbol{x}^{(b)} \in \Omega$ with objective vectors $\boldsymbol{f}^{(a)} = \boldsymbol{f}(\boldsymbol{x}^{(a)})$ and $\boldsymbol{f}^{(b)} = \boldsymbol{f}(\boldsymbol{x}^{(b)})$. Under a minimization convention, $\boldsymbol{x}^{(a)}$ is said to

dominate $\boldsymbol{x}^{(b)}$ (notation: $\boldsymbol{x}^{(a)} \prec \boldsymbol{x}^{(b)}$) if

$$\left[\forall i \in \{1,\dots,m\} :\ f_i^{(a)} \le f_i^{(b)}\right] \wedge \left[\exists j \in \{1,\dots,m\} :\ f_j^{(a)} < f_j^{(b)}\right]. \tag{5.9}$$

If neither $\boldsymbol{x}^{(a)} \prec \boldsymbol{x}^{(b)}$ nor $\boldsymbol{x}^{(b)} \prec \boldsymbol{x}^{(a)}$ holds, the two solutions are *mutually non-dominated*. This relation is a partial order: it is transitive, but it does not totally rank the feasible set, which is exactly why a *set* of trade-off optima emerges [12, 88].

Pareto optimality. A feasible solution $\boldsymbol{x}^\star$ is *Pareto-optimal* if there exists no other feasible solution that dominates it:

$$\nexists \boldsymbol{x} \in \Omega :\ \boldsymbol{x} \prec \boldsymbol{x}^\star. \tag{5.10}$$

The set of all Pareto-optimal solutions is the *Pareto set*

$$\mathscr{P} \ = \ \{\boldsymbol{x} \in \Omega \ : \ \nexists \boldsymbol{y} \in \Omega,\ \boldsymbol{y} \prec \boldsymbol{x}\}, \tag{5.11}$$

and its image in objective space,

$$\mathscr{F} \ = \ \{\boldsymbol{f}(\boldsymbol{x}) \in \mathbb{R}^m \ : \ \boldsymbol{x} \in \mathscr{P}\}, \tag{5.12}$$

is the *Pareto front* (or Pareto frontier). In engineering, $\mathscr{F}$ provides a compact representation of achievable compromises: selecting a final design corresponds to choosing one point on $\mathscr{F}$, i.e., injecting preferences *after* the exploration has clarified what trade-offs are truly possible [12, 88].

Qualitative shapes of Pareto fronts. The geometry of $\mathscr{F}$ depends not only on physics and constraints but also on whether objectives have aligned or conflicting directions (min/min, min/max, etc.). Figure 5.1 illustrates typical two-objective trade-off curves: convex/concave trends, rapidly saturating fronts, and steep "knee" regions where small improvements in one objective require large sacrifices in the other [88]. Such knees are often the most interesting candidates for compromise designs, although this statement is contextual and not universal, in fact.

5.2.3. From deterministic to stochastic optimisation

Deterministic strategies (e.g., gradient-based methods, SQP-type algorithms, simplex approaches) can be extremely efficient when objective functions are smooth and well behaved, and when derivatives are available or robustly approximated [12]. However, in many realistic engineering problems objective evaluations are expensive, noisy (nu-

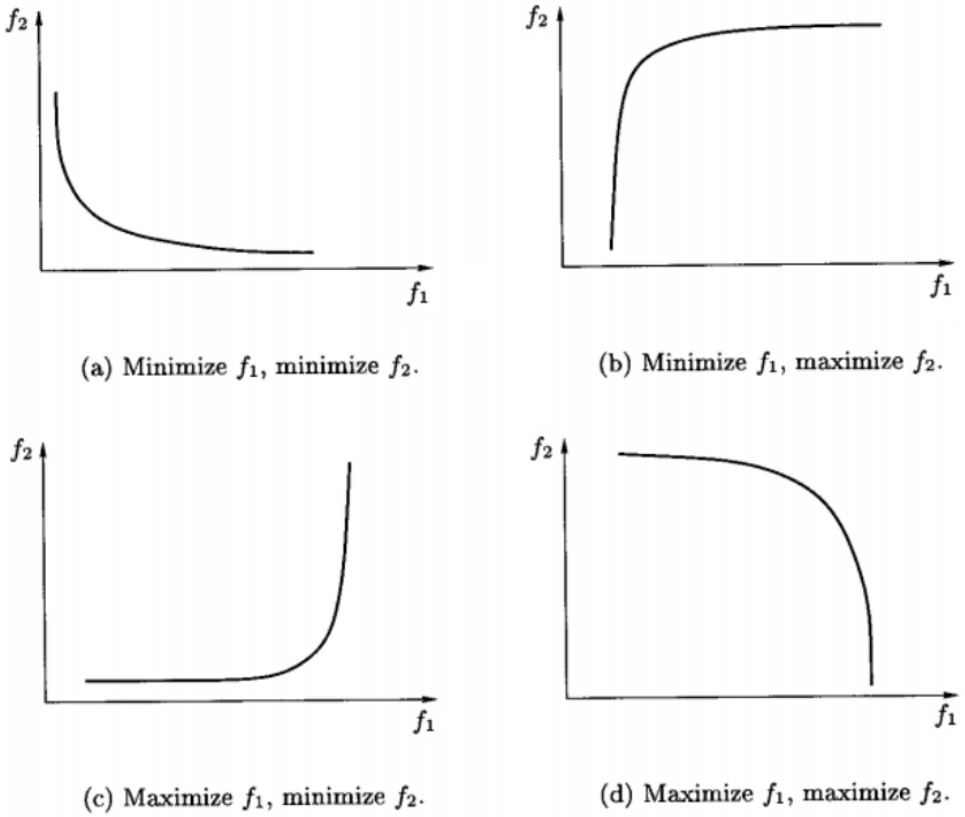

(a) Minimize f_1, minimize f_2.

(b) Minimize f_1, maximize f_2.

(c) Maximize f_1, minimize f_2.

(d) Maximize f_1, maximize f_2.

Figure 5.1. Representative qualitative shapes of Pareto fronts in a two-objective space for different combinations of minimization/maximization targets. The curvature and the presence of a "knee" region influence compromise selection: knee points often correspond to balanced trade-offs, where marginal improvements become rapidly expensive. Adapted from Collette and Siarry [88].

merically or experimentally), and may involve discontinuities or multi-modality. Under these conditions, deterministic optimisers may converge prematurely or become unstable due to local irregularities. Moreover, although deterministic methods can be extended to multi-objective formulations through scalarisation techniques, they typically yield a single compromise solution per optimisation run, making the systematic exploration of trade-offs between conflicting objectives inherently limited.

Stochastic optimisation introduces randomization and, crucially, a *population* of candidate designs. This has two immediate consequences [12, 88]:

i. multiple regions of Ω can be explored concurrently (exploration), reducing the probability of entrapment in local minima;

ii. multi-objective problems become natural, because a population can approximate a *set* (the Pareto front) rather than a single point.

The drawback is computational: if a population of size N is evolved for G generations, the

number of objective evaluations scales on the order of $N\,G$ (up to constant factors due to elitism or archives). This cost is not a detail: it is often the dominant practical constraint, so algorithmic choices must respect evaluation budgets, and sometimes a metamodel-assisted or hybrid process is the only feasible route [12].

5.2.4. Genetic algorithms and evolutionary operators

Genetic algorithms (GAs) are population-based metaheuristics inspired by the principles of natural selection and biological evolution. At a given generation t, the algorithm operates on a population

$$\mathscr{P}^{(t)} = \{\boldsymbol{x}_1, \boldsymbol{x}_2, \ldots, \boldsymbol{x}_N\}, \tag{5.13}$$

where each individual $\boldsymbol{x}_i \in \Omega \subset \mathbb{R}^n$ encodes a candidate solution in the design space. In early formulations, individuals were typically represented using binary strings; however, in modern engineering optimisation problems, real-coded representations are widely adopted, as they avoid unnecessary discretisation and enable the definition of variation operators consistent with continuous decision variables [12, 14, 15, 90].

Each generation of a genetic algorithm is obtained through the sequential application of evaluation, selection, variation operators (crossover and mutation), and replacement. From a formal standpoint, the evolutionary process can be interpreted as a mapping between successive populations,

$$\mathscr{P}^{(t+1)} = \mathscr{G}\big(\mathscr{P}^{(t)}; \boldsymbol{f}, \Theta\big), \tag{5.14}$$

where $\boldsymbol{f}$ denotes the vector of objective functions and Θ represents the set of algorithmic parameters governing selection pressure and variation operators. Although the structure of Eq. (5.14) appears compact, the resulting behaviour of the algorithm is strongly influenced by the choice of selection mechanism and by the balance between exploration and exploitation induced by crossover and mutation operators [12, 15, 88].

A schematic overview of the canonical workflow of a genetic algorithm is reported in Fig. 5.2, providing a compact visual summary of the evolutionary cycle described by Eq. (5.14).

Fitness function The fitness function plays a central role in genetic algorithms, as it represents the sole interface between the optimisation problem and the evolutionary search mechanism. While genetic operators act on populations of candidate solutions in a purely algorithmic manner, the fitness function encapsulates all problem-specific information and determines how solution quality is evaluated and compared [12, 15].

Formally, let $\Omega \subset \mathbb{R}^n$ denote the design space and let $\boldsymbol{f} : \Omega \to \mathbb{R}^m$ be the vector of

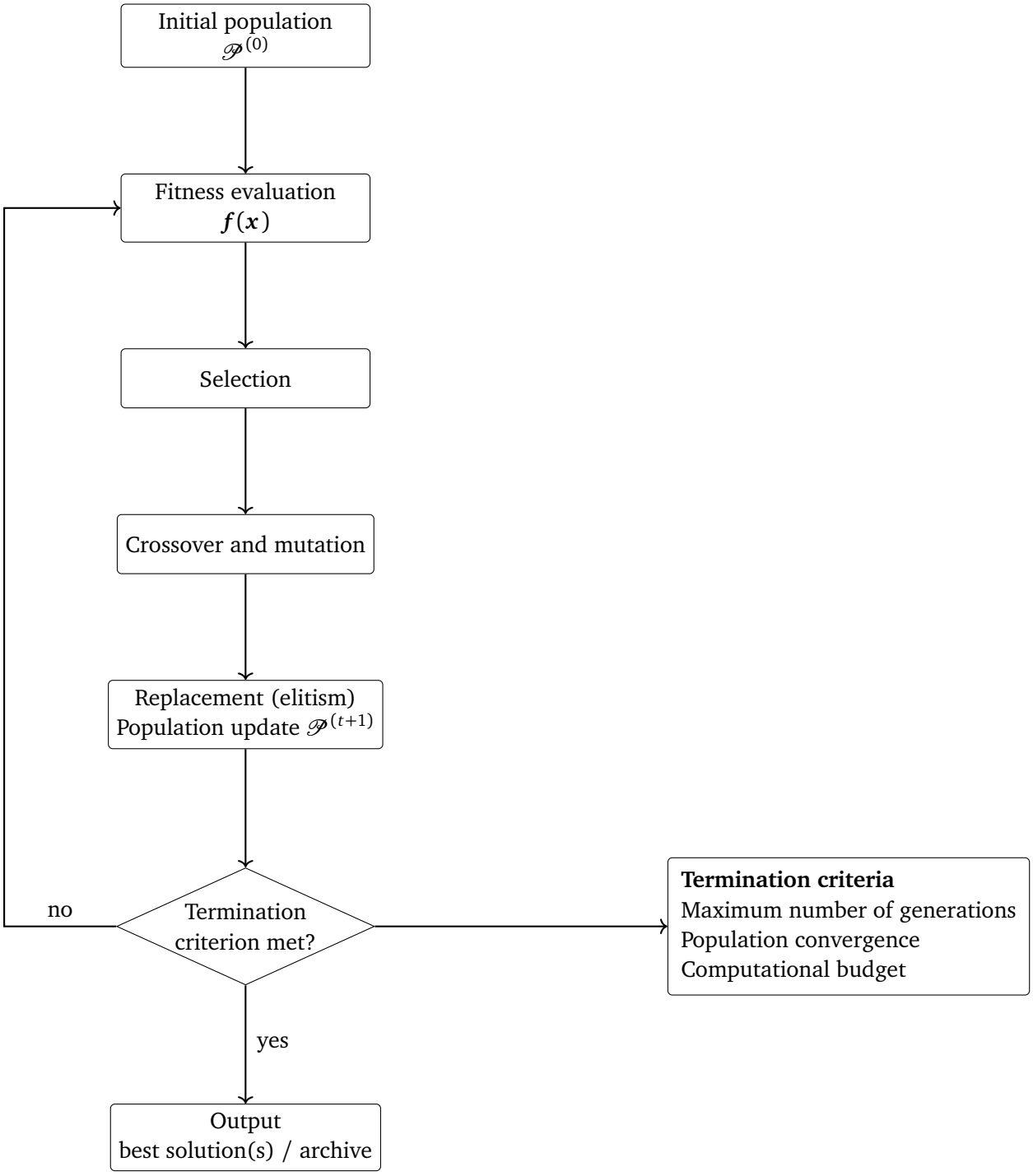

Figure 5.2. Algorithmic block diagram of a classical genetic algorithm. The evolutionary loop iterates evaluation, selection, variation, and replacement until a termination criterion is satisfied, after which the best solution(s) identified by the search are returned.

objective functions associated with the optimisation problem. In single-objective genetic algorithms, the fitness function is typically defined as a scalar mapping

$$F : \Omega \to \mathbb{R}, \tag{5.15}$$

where larger (or smaller, depending on convention) values of $F(\boldsymbol{x})$ correspond to better-performing individuals. In the simplest case, the fitness function coincides directly with the objective function, possibly after sign reversal or scaling.

In more general settings, however, the fitness function does not necessarily coincide with the raw objective values. Scaling, normalization, or transformation procedures are often introduced in order to control selection pressure, improve numerical robustness, or incorporate additional information such as constraint violations. From this perspective, the fitness function should be interpreted as an algorithmic construct whose purpose is to guide the evolutionary search, rather than as a purely physical quantity [14, 15].

In multi-objective genetic algorithms, the notion of fitness requires particular care. Since no single scalar value can fully represent the quality of a solution with respect to multiple competing objectives, fitness is commonly defined implicitly through dominance relations and auxiliary diversity measures. In this case, the fitness of an individual is not a numerical value, but rather a relative measure derived from its position within the population in objective space. This distinction highlights the conceptual shift from scalar fitness assignment to dominance-based evaluation, which underpins modern multi-objective evolutionary optimisation frameworks [12, 88].

In all cases, the effectiveness of a genetic algorithm critically depends on the formulation of the fitness function. An inappropriate fitness definition may lead to excessive selection pressure, loss of diversity, or stagnation, regardless of the sophistication of the genetic operators employed. Consequently, careful design of the fitness evaluation stage is a prerequisite for obtaining reliable and meaningful optimisation results.

5.2.4.1. Selection mechanisms

Selection constitutes a fundamental component of evolutionary algorithms, as it establishes the relationship between solution quality and reproductive success. By biasing the reproduction process toward high-quality individuals while preserving stochastic variability, selection enables the progressive improvement of the population without collapsing diversity too early. Importantly, selection does not create new candidate solutions, but determines which individuals are allowed to transmit genetic material to the variation operators [12, 14, 15].

One of the earliest selection strategies is fitness-proportional selection, commonly referred to as roulette-wheel selection. In this scheme, the probability of selecting an individual $\boldsymbol{x}_i$ is proportional to its scalar fitness value $F(\boldsymbol{x}_i)$,

$$\mathbb{P}(\boldsymbol{x}_i) = \frac{F(\boldsymbol{x}_i)}{\sum_{k=1}^{N} F(\boldsymbol{x}_k)}. \tag{5.16}$$

Although intuitive, this mechanism is known to be highly sensitive to fitness scaling. Poorly scaled objective functions may lead either to excessive selection pressure or to nearly random sampling, which limits its applicability in practical engineering optimisation problems [12, 15].

To overcome these drawbacks, rank-based selection schemes have been introduced. In rank-based selection, individuals are sorted according to fitness, and selection probabilities depend on rank rather than absolute fitness values. A widely adopted linear ranking formulation assigns

$$\mathbb{P}(r) = \frac{2-s}{N} + \frac{2(r-1)(s-1)}{N(N-1)}, \tag{5.17}$$

where $r \in \{1, \ldots, N\}$ denotes the rank of the individual, with $r = 1$ corresponding to the best solution, and $s \in [1, 2]$ controls selection pressure. This approach decouples selection intensity from objective scaling and yields more robust behaviour across heterogeneous optimisation landscapes [15, 88].

An alternative and particularly robust strategy is tournament selection, which is widely adopted in modern evolutionary algorithms. In tournament selection, a subset of k individuals is sampled uniformly at random from the population, and the best individual within this subset is selected. The probability that an individual with rank r is selected in a k-tournament can be expressed as

$$\mathbb{P}_{\text{tourn}}(r) = \left(\frac{N-r+1}{N}\right)^k - \left(\frac{N-r}{N}\right)^k, \tag{5.18}$$

which highlights how the tournament size k directly controls selection pressure. Larger values of k increase the probability of selecting highly ranked individuals, while smaller values promote exploration by reducing selective bias. Tournament selection is computationally efficient, insensitive to fitness scaling, and naturally extendable to multi-objective formulations [12, 15].

In multi-objective evolutionary optimisation, selection is typically formulated directly in the objective space, without collapsing multiple objectives into a single scalar fitness. In this context, individuals are compared using Pareto dominance relations, and selection is primarily driven by dominance rank. Let $\boldsymbol{x}^{(a)}$ and $\boldsymbol{x}^{(b)}$ be two candidate solutions with objective vectors $\boldsymbol{f}(\boldsymbol{x}^{(a)})$ and $\boldsymbol{f}(\boldsymbol{x}^{(b)})$. Solution $\boldsymbol{x}^{(a)}$ is said to dominate $\boldsymbol{x}^{(b)}$ if

$$\forall j : f_j(\boldsymbol{x}^{(a)}) \leq f_j(\boldsymbol{x}^{(b)}) \quad \text{and} \quad \exists k : f_k(\boldsymbol{x}^{(a)}) < f_k(\boldsymbol{x}^{(b)}). \tag{5.19}$$

Dominance-based selection thus promotes solutions that are dominated by fewer individuals and represent favourable trade-offs among competing objectives. To avoid loss

of diversity, dominance ranking is commonly complemented by secondary density-based criteria, which favour solutions located in sparsely populated regions of the objective space. This general selection framework forms the theoretical foundation of several modern multi-objective evolutionary algorithms [12, 88, 91].

5.2.4.2. Crossover

Crossover (recombination) combines information from parents to create offspring. Denoting two parents by $\boldsymbol{x}^{(p1)}$ and $\boldsymbol{x}^{(p2)}$, crossover is applied with probability p_c. In a binary representation, *one-point* crossover selects a cut index c and swaps suffixes; *two-point* selects $c_1 < c_2$ and swaps the intermediate segment; *uniform* crossover swaps each gene independently with probability $1/2$ [14, 89].

For real-coded GAs, several operators are relevant [12, 88, 90]:

- **Arithmetic crossover:**

$$\boldsymbol{x}^{(o1)} = \alpha \boldsymbol{x}^{(p1)} + (1-\alpha)\boldsymbol{x}^{(p2)}, \quad \boldsymbol{x}^{(o2)} = (1-\alpha)\boldsymbol{x}^{(p1)} + \alpha \boldsymbol{x}^{(p2)}, \tag{5.20}$$

  with $\alpha \in [0,1]$ (sometimes sampled randomly per gene).

- **Blend crossover (BLX-α):** for each gene i, offspring components are sampled as

$$x_i^{(o)} \sim \mathcal{U}\Big[\min(x_i^{(p1)}, x_i^{(p2)}) - \alpha\Delta_i,\ \max(x_i^{(p1)}, x_i^{(p2)}) + \alpha\Delta_i\Big], \tag{5.21}$$

  where

$$\Delta_i = \left| x_i^{(p1)} - x_i^{(p2)} \right|, \tag{5.22}$$

  and $\alpha \geq 0$ controls the degree of exploration beyond the parental interval. Larger values of α promote wider sampling of the design space at the expense of locality.

- **Simulated binary crossover (SBX):** given two parent genes $x_i^{(p1)}$ and $x_i^{(p2)}$, offspring genes are computed as

$$x_i^{(o1)} = \tfrac{1}{2}\Big[(1+\beta_i)x_i^{(p1)} + (1-\beta_i)x_i^{(p2)}\Big], \quad x_i^{(o2)} = \tfrac{1}{2}\Big[(1-\beta_i)x_i^{(p1)} + (1+\beta_i)x_i^{(p2)}\Big], \tag{5.23}$$

  where the spread factor β_i is defined as

$$\beta_i = \begin{cases} (2u)^{\frac{1}{\eta_c+1}}, & u \leq 0.5, \\ \left(\dfrac{1}{2(1-u)}\right)^{\frac{1}{\eta_c+1}}, & u > 0.5, \end{cases} \tag{5.24}$$

  with $u \sim \mathcal{U}(0,1)$ and η_c denoting the distribution index that controls the locality

of the offspring around the parents.

Crossover is usually the main *exploitation* operator: it combines partial structures ("building blocks") that selection has amplified, aiming to produce improved offspring without random walk behaviour.

5.2.4.3. Mutation

Mutation introduces novelty and prevents loss of diversity. It is applied with probability p_m (per individual or per gene). In binary coding, bit-flip mutation toggles a bit. In real coding, common choices include [12, 88, 90]:

- **Gaussian mutation:** for gene x_i,

$$x_i' = x_i + \sigma_i \xi, \qquad \xi \sim \mathcal{N}(0,1), \tag{5.25}$$

  with σ_i controlling step size (possibly adapted).

- **Polynomial mutation:** given a gene x_i bounded within $[x_i^{\min}, x_i^{\max}]$, the mutated value is defined as

$$x_i' = x_i + \delta_i \left(x_i^{\max} - x_i^{\min}\right), \tag{5.26}$$

  where the perturbation factor δ_i is given by

$$\delta_i = \begin{cases} (2u)^{\frac{1}{\eta_m+1}} - 1, & u < 0.5, \\ 1 - [2(1-u)]^{\frac{1}{\eta_m+1}}, & u \geq 0.5, \end{cases} \tag{5.27}$$

  with $u \sim \mathcal{U}(0,1)$ and η_m denoting the mutation distribution index. Larger values of η_m promote local search, while smaller values increase the probability of long-range mutations.

- **Uniform mutation:** each gene is resampled independently according to

$$x_i' \sim \mathcal{U}\left(x_i^{\min}, x_i^{\max}\right), \tag{5.28}$$

  where $[x_i^{\min}, x_i^{\max}]$ denotes the admissible range of the design variable.

A useful conceptual summary is that mutation is the backbone of *exploration* (escaping local minima, recovering diversity), while crossover tends to accelerate exploitation once good genetic material exists. The tuning of p_c, p_m, and step-size parameters governs the exploration–exploitation balance; too little mutation leads to premature convergence, too much mutation turns the process into a random search [89, 90].

5.2.4.4. Elitism and replacement

Replacement decides which individuals survive into $\mathscr{P}^{(t+1)}$. Elitism ensures that the best solutions found so far are not lost due to stochastic variation. A simple elitist strategy keeps the top N_e individuals and fills the remaining slots with offspring. In multi-objective settings, elitism is typically defined with respect to non-dominance ranks and diversity metrics, rather than a single scalar fitness [88, 91].

5.2.5. Multi-objective genetic algorithms (MOGA)

In multi-objective optimisation, collapsing $\boldsymbol{f}(\boldsymbol{x})$ into a single scalar fitness via weighted sums,

$$F(\boldsymbol{x}) = \sum_{i=1}^{m} w_i f_i(\boldsymbol{x}), \qquad w_i \geq 0, \tag{5.29}$$

is conceptually simple but often fragile: it requires a priori preference weights and can fail to recover non-convex portions of the Pareto front [12, 88]. MOGAs instead attempt to approximate $\mathscr{F}$ directly by evolving a population under dominance-based criteria.

A common idea is *Pareto ranking*. Define the *domination count*

$$n(\boldsymbol{x}) = \left|\left\{\boldsymbol{y} \in \mathscr{P}^{(t)} : \ \boldsymbol{y} \prec \boldsymbol{x}\right\}\right|, \tag{5.30}$$

and the *dominated set*

$$S(\boldsymbol{x}) = \left\{\boldsymbol{y} \in \mathscr{P}^{(t)} : \ \boldsymbol{x} \prec \boldsymbol{y}\right\}. \tag{5.31}$$

The first non-dominated front is

$$F_1 = \left\{\boldsymbol{x} \in \mathscr{P}^{(t)} : \ n(\boldsymbol{x}) = 0\right\}, \tag{5.32}$$

and subsequent fronts $F_2, F_3, \ldots$ are obtained by removing F_1 and repeating, i.e., building a layered structure of increasing dominance rank [88, 91]. A MOGA can then assign fitness based on rank and maintain diversity by niching (fitness sharing), crowding measures, or clustering. Classical approaches include (i) aggregative methods, (ii) non-aggregative ranking methods, and (iii) hybrid schemes that combine ranking with diversity preservation [12, 88].

In PFHE design-like problems, the value of MOGAs is very concrete: rather than forcing an arbitrary scalarization, they deliver a portfolio of physically feasible designs spanning low-loss to high-duty extremes. The decision-maker can then incorporate manufacturing constraints, robustness considerations, or business preferences after the trade-off landscape is visible.

5.2.6. NSGA-II: non-dominated sorting genetic algorithm II

Among dominance-based MOGAs, NSGA-II is widely adopted because it combines: (i) fast non-dominated sorting, (ii) explicit elitism through population merging, and (iii) a parameter-free diversity mechanism based on crowding distance [91]. Its popularity in engineering is not an accident: it is straightforward to implement, scales reasonably well to moderate population sizes, and tends to produce well-distributed Pareto approximations without ad-hoc niching parameters.

5.2.6.1. Population merging and elitist selection

At generation t, NSGA-II constructs an offspring population $\mathscr{Q}^{(t)}$ from the current parent population $\mathscr{P}^{(t)}$ via selection and variation. It then forms the combined pool

$$\mathscr{R}^{(t)} = \mathscr{P}^{(t)} \cup \mathscr{Q}^{(t)}, \qquad |\mathscr{R}^{(t)}| = 2N, \tag{5.33}$$

and performs non-dominated sorting on $\mathscr{R}^{(t)}$ to generate fronts $F_1, F_2, \ldots$. The next parent population $\mathscr{P}^{(t+1)}$ is filled by adding fronts in order of increasing rank until the capacity N is reached. If the last accepted front does not fully fit, individuals within that front are ranked by crowding distance and the most widely spaced are selected [91]. This is the heart of elitism: good solutions are preserved because fronts are filled from the best ranks first, and diversity is protected within ranks.

Figure 5.3 summarizes this workflow. The explicit presence of the "rejected" region highlights a subtle but important point: selection pressure is applied *twice*, first by dominance rank (a global quality filter), then by crowding distance (a local density filter). Together, they push the population toward the Pareto front while resisting collapse into a small region of objective space.

5.2.6.2. Crowding distance: a density estimator in objective space

Crowding distance is designed to approximate how isolated a solution is within its front. Consider a front F of size $|F|$. For each objective i, sort solutions in F by f_i; boundary solutions are assigned infinite distance to preserve extremes. For interior solutions, the crowding contribution in objective i is a normalized finite difference:

$$d_i(\boldsymbol{x}_k) = \frac{f_i(\boldsymbol{x}_{k+1}) - f_i(\boldsymbol{x}_{k-1})}{f_i^{\max}(F) - f_i^{\min}(F)}, \tag{5.34}$$

and the overall crowding distance is

$$\mathrm{CD}(\boldsymbol{x}_k) = \sum_{i=1}^{m} d_i(\boldsymbol{x}_k). \tag{5.35}$$

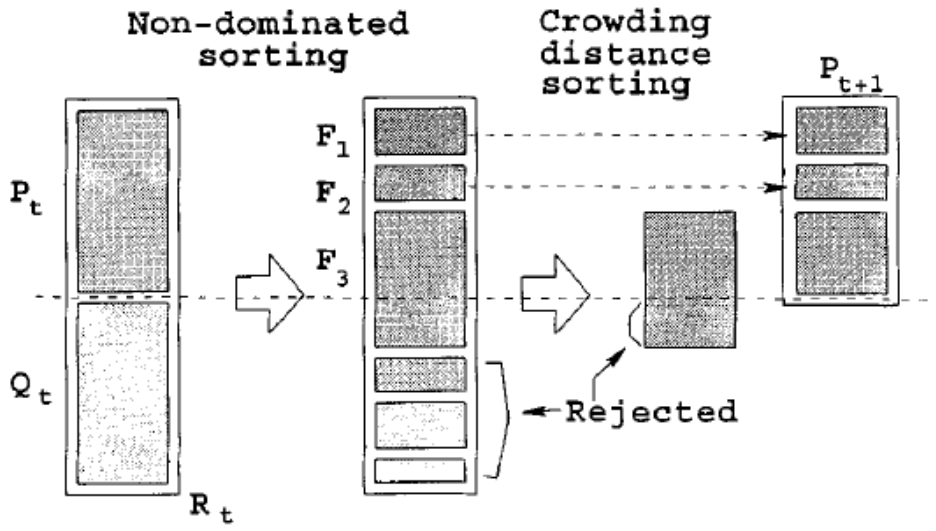

Fig. 2. NSGA-II procedure.

Figure 5.3. Schematic of the NSGA-II elitist procedure. The parent population $\mathscr{P}^{(t)}$ and offspring population $\mathscr{Q}^{(t)}$ are merged into $\mathscr{R}^{(t)}$, non-dominated fronts $F_1, F_2, \ldots$ are built, and the next population $\mathscr{P}^{(t+1)}$ is selected by rank and (when needed) by crowding-distance sorting, rejecting the most crowded solutions. Adapted from Deb et al. [91].

This measure is not a true metric, but it works well as a ranking heuristic: larger CD means lower local density and thus higher priority for survival, which tends to spread solutions across the front [91]. The geometrical interpretation for $m = 2$ is illustrated in Figure 5.4: the "cuboid" (hyper-rectangle) defined by neighbouring points approximates the empty region around a solution; a larger region implies a less crowded neighborhood and thus a more valuable representative of that front portion.

5.2.6.3. Binary tournament with crowded-comparison operator

NSGA-II typically employs a binary tournament selection where individuals are compared via:

$$\boldsymbol{x}^{(a)} \prec_c \boldsymbol{x}^{(b)} \quad \Longleftrightarrow \quad \left(r^{(a)} < r^{(b)}\right) \text{ or } \left(r^{(a)} = r^{(b)} \wedge \mathrm{CD}^{(a)} > \mathrm{CD}^{(b)}\right), \tag{5.36}$$

where r is the non-dominance rank (front index) and CD is the crowding distance. Equation (5.36) is the operational definition of "better" in NSGA-II: first prefer better Pareto rank; if tied, prefer the less crowded candidate. This rule is simple, and surprisingly effective.

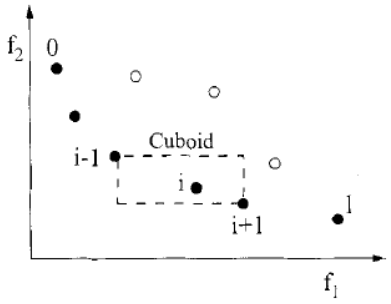

Fig. 1. Crowding-distance calculation. Points marked in filled circles are solutions of the same nondominated front.

Figure 5.4. Geometrical interpretation of the crowding-distance calculation in a two-objective space. Points marked in filled circles are solutions of the same non-dominated front; the local hyper-rectangle defined by nearest neighbours provides a density proxy used to prioritize isolated solutions. Adapted from Deb et al. [91].

5.2.6.4. Remarks on parameters and practical behaviour

In NSGA-II, the most influential knobs remain GA knobs: population size N, number of generations G, and variation parameters (e.g., SBX distribution index, polynomial mutation index, p_c, p_m). Increasing N typically improves front coverage but raises evaluation cost linearly. Increasing G improves convergence (until stagnation), again with linear cost. The operator parameters control locality: overly exploitative settings may converge fast but produce sparse or collapsed fronts, whereas overly explorative settings produce wide scatter and slow improvement [12, 88, 91]. There is no "best" configuration across all problems (no-free-lunch considerations), but for a given class of engineering problems, stable heuristics often exist and can be refined with sensitivity analyses [12].

5.2.7. Implementation aspects: `DEAP` as a computational framework

The `Distributed Evolutionary Algorithms in Python` (`DEAP`) library provides a modular, research-oriented implementation environment for evolutionary computation [94]. Its design follows a compositional philosophy: users define (i) data structures for individuals and fitness, (ii) genetic operators, and (iii) the algorithmic loop (or select a standard loop). This is particularly convenient for engineering optimisation because one can integrate a domain-specific evaluator (e.g., a PFHE thermo-economic model) with minimal friction, while still keeping control of every operator and parameter.

5.2.7.1. Representation and fitness definition

In `DEAP`, an individual is commonly a Python container (e.g., list or array) holding genes, while fitness is an object storing objective values and dominance behaviour. For a m-objective minimization, one sets a weight vector $\boldsymbol{w} \in \mathbb{R}^m$ with negative entries, concep-

tually consistent with

$$\texttt{Fitness}(\boldsymbol{x}) \equiv \big(f_1(\boldsymbol{x}), \ldots, f_m(\boldsymbol{x})\big), \qquad \boldsymbol{w} = (-1, \ldots, -1). \tag{5.37}$$

This weight vector is not a scalarization: it simply encodes directionality used by `DEAP` for comparisons and sorting.

5.2.7.2. Toolbox abstraction and operator injection
The `toolbox` mechanism registers callable operators, for instance

```
toolbox.register("mate", ...),
toolbox.register("mutate", ...),
toolbox.register("select", ...),
```
(5.38)

allowing one to swap operators without rewriting the full workflow. This is not merely cosmetic: in practice, being able to replace, for example, a Gaussian mutation with a polynomial mutation while keeping all other components unchanged is essential for conducting controlled sensitivity studies and for understanding how algorithmic choices affect convergence and diversity, in a reproducible way [12, 94].

5.2.7.3. NSGA-II in `DEAP`
`DEAP` includes standard NSGA-II selection (`selNSGA2`) and crowding-distance routines aligned with the original Deb formulation [91, 94]. A typical implementation follows the same conceptual structure described in Section 5.2.6: generate offspring, merge, sort, and truncate by rank/crowding. Importantly, `DEAP` lets the user decide how to manage constraint handling: penalty methods, repair operators, or feasibility-first dominance rules are all possible, and this flexibility matters because constrained MOPs behave quite differently from unconstrained ones [12, 88].

5.2.8. TOPSIS for final compromise selection
After NSGA-II (or another MOGA) has produced an approximation of the Pareto front, it is often necessary to select a single design for downstream tasks (detailed CFD, prototyping, manufacturing, etc.). This step is not optimisation in the strict Pareto sense; it is a *multi-criteria decision-making* (MCDM) problem, where preferences are applied to a set of non-dominated alternatives [92]. TOPSIS (Technique for Order Preference by Similarity to Ideal Solution) ranks alternatives by proximity to an ideal point and distance from an anti-ideal point.

5.2.8.1. Decision matrix and normalization

Let there be N_a candidate solutions (e.g., the non-dominated set) and m criteria (objectives or derived indicators). Construct the decision matrix

$$\mathbf{X} = [x_{ij}] \in \mathbb{R}^{N_a \times m}, \tag{5.39}$$

where x_{ij} is the value of criterion j for alternative i. Since criteria may have different units and scales, TOPSIS applies normalization, commonly vector normalization:

$$r_{ij} = \frac{x_{ij}}{\sqrt{\sum_{k=1}^{N_a} x_{kj}^2}}. \tag{5.40}$$

Other normalizations exist (min–max, z-score), but Eq. (5.40) is standard and keeps the pipeline simple, and stable in many engineering cases [92].

5.2.8.2. Weighting and weighted normalized matrix

Preference weights $\{w_j\}_{j=1}^{m}$ are introduced with

$$w_j \geq 0, \qquad \sum_{j=1}^{m} w_j = 1, \tag{5.41}$$

leading to the weighted normalized matrix

$$v_{ij} = w_j \, r_{ij}. \tag{5.42}$$

Weights can be assigned by expert judgment, entropy methods, AHP, or other schemes; in practice, documenting the weighting rationale is critical, because it is the point where subjective preferences enter the chain [92].

5.2.8.3. Ideal and anti-ideal solutions

Define the positive ideal solution (PIS) and negative ideal solution (NIS). For benefit criteria (to be maximized) and cost criteria (to be minimized), the PIS is built componentwise as

$$v_j^+ = \begin{cases} \max_i v_{ij}, & j \in \mathscr{J}_{\text{benefit}}, \\ \min_i v_{ij}, & j \in \mathscr{J}_{\text{cost}}, \end{cases} \qquad v_j^- = \begin{cases} \min_i v_{ij}, & j \in \mathscr{J}_{\text{benefit}}, \\ \max_i v_{ij}, & j \in \mathscr{J}_{\text{cost}}. \end{cases} \tag{5.43}$$

The vectors $\boldsymbol{v}^+ = (v_1^+, \ldots, v_m^+)$ and $\boldsymbol{v}^- = (v_1^-, \ldots, v_m^-)$ represent hypothetical best and worst alternatives with respect to the weighted normalized criteria.

5.2.8.4. Separation measures and closeness coefficient
TOPSIS computes Euclidean separation from PIS and NIS:

$$S_i^+ = \sqrt{\sum_{j=1}^{m}(v_{ij} - v_j^+)^2}, \qquad S_i^- = \sqrt{\sum_{j=1}^{m}(v_{ij} - v_j^-)^2}. \tag{5.44}$$

The closeness coefficient is then

$$C_i = \frac{S_i^-}{S_i^+ + S_i^-}, \qquad 0 \le C_i \le 1, \tag{5.45}$$

and alternatives are ranked in decreasing order of C_i (larger is better: close to ideal, far from anti-ideal). Although TOPSIS is computationally light, its effect is meaningful: it provides a reproducible, equation-driven selection rule that can be explicitly communicated and audited, rather than leaving final choice to an informal "pick a point on the front" habit.

5.2.8.5. Practical notes for Pareto-based selection
When TOPSIS is applied to a set of Pareto-optimal solutions, several practical precautions are advisable [88]:

- **Avoid redundant criteria:** strongly correlated objectives can over-emphasize one physical aspect.
- **Check sensitivity to weights:** small perturbations of w_j can change the ranking; this can be tested systematically.
- **Use physically meaningful scaling:** normalization can hide engineering significance if raw values span tiny ranges for some criteria.

In short, TOPSIS is best interpreted as a disciplined decision layer atop the Pareto exploration, not as a replacement for multi-objective optimisation itself.

5.3. Case study PFHE: formulation of the multi-objective optimization problem and computational workflow

The multi-objective optimisation framework developed in this work is applied to the same plate–fin heat exchanger (PFHE) previously analysed through Design of Experiments and sensitivity analysis, as presented in Chapter 4. No changes are introduced in terms of physical modelling assumptions, operating conditions, or boundary conditions. The optimisation phase builds upon the validated thermo–economic model to systematically explore the design space in a goal-oriented manner, informed by the parameter sensitivities identified in the DOE study.

This methodological continuity is intentional. The DOE phase provided quantitative insight into the relative influence of the main geometrical and operational parameters on thermal performance, pressure losses, and manufacturing cost. In addition, it allowed the identification of realistic and manufacturable ranges for each design variable. These ranges define the admissible design space explored during optimisation, ensuring that the evolutionary algorithm does not waste computational effort on physically meaningless or industrially unfeasible configurations. This aspect is particularly relevant for PFHE radiators, whose performance landscape is highly nonlinear and strongly coupled, and where small geometric variations may induce large changes in both heat transfer and pressure losses.

By preserving the same geometric definition adopted during the sensitivity analysis and by constraining the optimisation variables within physically and industrially admissible bounds, the evolutionary algorithm is restricted to a meaningful region of the design space. Consequently, the Pareto-optimal solutions presented in the following sections can be interpreted as realistic performance improvements achieved through informed fin-geometry optimisation, consistently aligned with the parameter sensitivities identified in the preliminary analysis.

PFHE configurations considered. As discussed in Chapter 4 two representative fin arrangements are investigated:

- an **OSF–OSF** configuration, employing offset-strip fins on both the internal fluid side and the external air side;
- an **OSF–Wavy** configuration, with offset-strip fins on the internal side and wavy fins on the external side.

The two configurations share the same PFHE-level architecture, flow arrangement, and modelling framework, and differ only in the parametrisation of the external fin geometry.

This choice reflects common industrial practice and enables a consistent comparison between two fin families characterised by different heat-transfer enhancement mechanisms and hydraulic behaviour.

Decision vector and admissible design space. Each candidate PFHE design is represented by a real-valued decision vector

$$\boldsymbol{x} = [x_1 \quad x_2 \quad \dots \quad x_n]^\mathsf{T} \in \Omega, \qquad \Omega = \prod_{i=1}^{n} [x_i^{\min}, x_i^{\max}] \subset \mathbb{R}^n, \tag{5.46}$$

where Ω denotes the admissible design space defined by manufacturability constraints, numerical robustness considerations, and operating requirements.

For the OSF–OSF configuration, the decision vector has dimension $n = 6$ and is written as

$$\boldsymbol{x}_{\text{OSF–OSF}} = [S \quad x_{\text{in}} \quad y_{\text{in}} \quad x_{\text{ext}} \quad y_{\text{ext}} \quad \dot{m}_\star]^\mathsf{T}, \tag{5.47}$$

where S denotes the overall core thickness of the PFHE radiator (m), x_{in} and x_{ext} denote the fin pitch on the internal and external sides, respectively (m), y_{in} and y_{ext} denote the corresponding fin height (m), and $\dot{m}_\star$ is the optimised mass-flow rate (kg s^{-1}). Depending on the working-fluid case, $\dot{m}_\star$ corresponds either to the internal or to the external flow rate, while the remaining one is kept fixed at its nominal value. This conditional definition reflects realistic operating strategies and avoids introducing unnecessary degrees of freedom.

For the OSF–Wavy configuration, additional geometric descriptors are required to characterise the external wavy fin. The corresponding decision vector reads

$$\boldsymbol{x}_{\text{OSF–Wavy}} = \left[S \quad x_{\text{in}} \quad y_{\text{in}} \quad x_{\text{ext}} \quad y_{\text{ext}} \quad l_{\text{ext}} \quad a_{2,\text{ext}} \quad \dot{m}_\star\right]^\mathsf{T}, \tag{5.48}$$

where l_{ext} (m) denotes the characteristic wavelength-related geometric parameter of the wavy fin, and $a_{2,\text{ext}}$ (m) is the wave amplitude..

Units of measure and numerical bounds. All geometric quantities are expressed in metres (m), mass-flow rates in kg s^{-1}, heat-transfer rate in kilowatts (kW), pressure losses in pascals (Pa), global conductance in W K^{-1}, and cost in monetary units consistent with the adopted cost model. The numerical bounds defining Ω are reported in Tables 5.1 and 5.2. These ranges are consistent with the DOE study and ensure both physical plausibility and manufacturability.

Table 5.1. OSF–OSF optimisation: decision variables and bounds adopted in the case study.

Gene	Symbol	Oil / Coolant bounds	Air bounds
1	S (m)	[0.07, 0.16]	[0.07, 0.16]
2	x_{in} (m)	[0.0011, 0.00393]	[0.0025, 0.00393]
3	y_{in} (m)	[0.0020, 0.0065]	[0.0055, 0.0065]
4	x_{ext} (m)	[0.00175, 0.0060]	[0.00175, 0.0060]
5	y_{ext} (m)	[0.0060, 0.0105]	[0.0060, 0.0105]
6	$\dot{m}_\star$ (kg s^{-1})	[1.11, 2.22]	[0.10, 0.30]

For oil/coolant cases, the external mass-flow rate $\dot{m}_{\text{ext}}$ is treated as a design variable, while the internal mass-flow rate is fixed at its nominal value. For air cases, the internal mass-flow rate $\dot{m}_{\text{in}}$ is optimised, whereas the external mass-flow rate is kept constant.

Evaluation operator and vector-valued model response. The optimisation algorithm interacts with the physical model through a deterministic evaluation operator

$$\mathscr{E} : \Omega \subset \mathbb{R}^n \longrightarrow \mathbb{R}^p, \qquad \boldsymbol{y} = \mathscr{E}(\boldsymbol{x}), \tag{5.49}$$

which maps each design vector to a vector of thermo–economic outputs,

$$\boldsymbol{y}(\boldsymbol{x}) = \left[\dot{Q}(\boldsymbol{x}) \quad \Delta p_{\text{in}}(\boldsymbol{x}) \quad \Delta p_{\text{out}}(\boldsymbol{x}) \quad UA(\boldsymbol{x}) \quad M(\boldsymbol{x}) \quad C(\boldsymbol{x})\right]^{\mathsf{T}}. \tag{5.50}$$

This operator encapsulates the entire modelling chain: geometric instantiation of the PFHE core, fin-level thermo–hydraulic characterisation, system-level calculations based on the ε–NTU method, and post-processing to obtain mass and cost. From a mathematical standpoint, $\mathscr{E}$ may be decomposed as a composition of operators,

$$\mathscr{E} = \mathscr{P} \circ \mathscr{S} \circ \mathscr{H} \circ \mathscr{G}, \tag{5.51}$$

where $\mathscr{G}$ constructs the geometry from $\boldsymbol{x}$, $\mathscr{H}$ evaluates fin-level correlations, $\mathscr{S}$ assembles the system-level PFHE model, and $\mathscr{P}$ performs post-processing. This layered structure enhances clarity and numerical robustness, and makes explicit the deterministic nature of the evaluation step.

Figure 5.5 provides a compact representation of the deterministic mapping $\mathscr{E}(\boldsymbol{x})$ repeatedly invoked by the optimiser. This separation between optimiser and evaluator is crucial: the evolutionary algorithm does not alter the governing physics, but explores Ω and queries the same validated evaluation operator many times, in a controlled and reproducible way.

Table 5.2. OSF–Wavy optimisation: decision variables and bounds adopted in the case study.

Gene	Symbol	Oil / Coolant bounds	Air bounds
1	S (m)	[0.07, 0.16]	[0.07, 0.16]
2	x_{in} (m)	[0.0011, 0.00393]	[0.0025, 0.00393]
3	y_{in} (m)	[0.0020, 0.0065]	[0.0055, 0.0065]
4	x_{ext} (m)	[0.0044, 0.0120]	[0.0044, 0.0120]
5	y_{ext} (m)	[0.0080, 0.0110]	[0.0080, 0.0110]
6	l_{ext} (m)	[0.010, 0.020]	[0.010, 0.020]
7	$a_{2,\text{ext}}$ (–)	[0.0011, 0.0024]	fixed to 0.0011
8	$\dot{m}_\star$ (kg s^{-1})	[1.11, 2.22]	[0.10, 0.30]

For oil/coolant operating conditions, the optimisation is performed with respect to the external mass-flow rate $\dot{m}_{\text{ext}}$, while the internal flow rate is prescribed. Conversely, for air-side cases, the internal mass-flow rate $\dot{m}_{\text{in}}$ is included in the decision vector and the external flow rate is kept fixed.

Evolutionary operators and algorithmic parameters. The multi-objective optimisation strategy adopted in this work is based on an elitist NSGA-II scheme implemented with real-coded evolutionary operators. Table 5.3 summarises the operators and numerical parameters employed throughout the optimisation campaign, which were selected based on consolidated practice in evolutionary optimisation and on preliminary robustness analyses carried out during the DOE phase.

The use of bounded operators ensures that all offspring remain within the admissible design space Ω defined by the DOE-informed bounds, thus avoiding the generation of geometrically meaningless or industrially unfeasible PFHE configurations.

Algorithmic workflow of the optimisation loop. From a procedural standpoint, the optimisation strategy can be interpreted as a sequence of deterministic and stochastic mappings acting on the population. Algorithm 1 provides a compact yet rigorous description of the complete workflow implemented in this study, from initialisation to final decision making.

Algorithm 1 highlights the modular structure of the optimisation process. The evolutionary loop is solely responsible for exploring the admissible design space and constructing an approximation of the Pareto-optimal set, whereas feasibility enforcement on internal pressure losses and decision making are deliberately postponed to a post-processing stage.

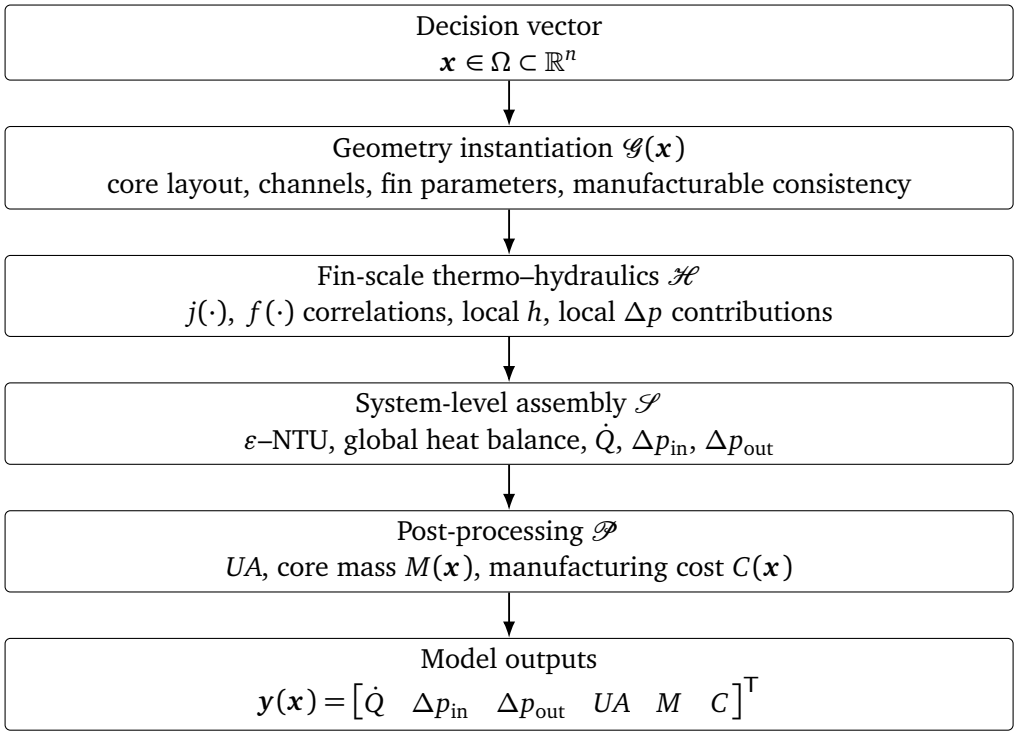

Figure 5.5. Deterministic PFHE evaluation operator $\mathscr{E} = \mathscr{P} \circ \mathscr{S} \circ \mathscr{H} \circ \mathscr{G}$ mapping a design vector $\boldsymbol{x}$ to thermo–economic outputs.

Table 5.3. NSGA-II operators and parameters adopted in the PFHE optimisation framework.

Component	**Adopted setting**
Population size	$\mu = 1000$ individuals
Number of generations	$N_{\text{gen}} = 100$
Selection (mating)	Dominance-based tournament with crowding distance
Replacement	Elitist $\mu+\lambda$ NSGA-II survival selection
Crossover operator	Simulated Binary Crossover (SBX), bounded
Crossover probability	$p_c = 0.9$
SBX distribution index	$\eta_c = 30$
Mutation operator	Polynomial mutation, bounded
Mutation probability	$p_m = 0.1$
Per-gene mutation prob.	indpb $= 1/n$
Polynomial mutation index	$\eta_m = 20$
Constraint handling	Additive penalty, $K = 10^3$
Post-processing filter	Δp_{in} feasibility screening
Decision making	TOPSIS on filtered Pareto set

Rationale for the adopted NSGA-II configuration. The combination of SBX crossover with polynomial mutation is particularly suited for continuous PFHE design variables,

Algorithm 1 Multi-objective PFHE optimisation workflow

Initialise population $\mathscr{P}^{(0)} \subset \Omega$ by uniform random sampling
for $t = 0$ to $N_{\text{gen}} - 1$ **do**
    for all $\boldsymbol{x} \in \mathscr{P}^{(t)}$ **do**
        Evaluate $\boldsymbol{r} = \mathscr{G}(\boldsymbol{x})$
        Extract $(\dot{Q}, \Delta p_{\text{out}}, C)$
        Compute penalised fitness $\tilde{\boldsymbol{f}}(\boldsymbol{x})$
    end for
    Select mating pool via dominance-based tournament
    Apply SBX crossover (p_c, η_c)
    Apply polynomial mutation (p_m, η_m, indpb)
    Evaluate offspring population $\mathscr{Q}^{(t)}$
    Form union $\mathscr{R}^{(t)} = \mathscr{P}^{(t)} \cup \mathscr{Q}^{(t)}$
    Apply non-dominated sorting and crowding-distance assignment
    Select next population $\mathscr{P}^{(t+1)}$ of size μ
end for
Extract first non-dominated Pareto front $\mathscr{F}_1$
Filter $\mathscr{F}_1$ according to Δp_{in} bounds
Apply TOPSIS to select final PFHE design

as it provides a tunable balance between exploration and exploitation. The relatively high crossover probability promotes information exchange between high-quality designs, while the polynomial mutation with indpb $= 1/n$ introduces controlled perturbations at the gene level, preventing premature convergence without degenerating into random search behaviour. The chosen distribution indices (η_c, η_m) bias offspring generation towards the vicinity of parental solutions, which is consistent with the smooth yet strongly coupled response surface typical of PFHE thermo–hydraulic performance.

Integration of optimisation and decision making. It is worth emphasising that the NSGA-II algorithm is not used to directly return a single "optimal" solution. Instead, it provides a structured set of non-dominated PFHE designs that represent different trade-offs between thermal performance, pressure losses, and manufacturing cost. The final design selection is intentionally decoupled from the evolutionary phase and performed through TOPSIS, which operates on the filtered Pareto set and incorporates explicit preference weights. This separation ensures transparency of the optimisation process and allows the decision-making criteria to be modified without rerunning the computationally expensive evolutionary loop.

Formal definition of the multi-objective optimisation problem. The PFHE design task is formalised as a constrained multi-objective optimisation problem,

$$\begin{aligned} \min_{x\in\Omega} \quad & \boldsymbol{f}^{\downarrow}(\boldsymbol{x}) = \begin{bmatrix} \Delta p_{\text{out}}(\boldsymbol{x}) \\ C(\boldsymbol{x}) \\ -\dot{Q}(\boldsymbol{x}) \end{bmatrix}, \\ \text{subject to} \quad & g_k(\boldsymbol{x}) \le 0, \qquad k = 1, \dots, n_g, \end{aligned} \tag{5.52}$$

where $\boldsymbol{f}^{\downarrow}$ denotes a minimisation-oriented objective vector (maximisation is recast through sign inversion), and g_k are feasibility constraints that encode operating requirements and numerical robustness. In particular, the internal pressure-drop constraint is expressed as

$$g_{\text{in}}(\boldsymbol{x}) = \Delta p_{\text{in}}(\boldsymbol{x}) - \Delta p_{\text{in}}^{\max} \le 0, \tag{5.53}$$

where $\Delta p_{\text{in}}^{\max}$ is a prescribed specification. The bounds defining Ω already act as hard constraints. Additional feasibility checks prevent degenerate geometries and non-physical conditions (e.g. negative flow areas or inconsistent fin definitions).

Fitness assignment and constraint handling. Within the evolutionary loop, each candidate $\boldsymbol{x}$ is associated with the objective vector $\boldsymbol{f}(\boldsymbol{x})$ as in Eq. (5.52). Soft constraints are incorporated through penalties,

$$\tilde{f}_j(\boldsymbol{x}) = f_j(\boldsymbol{x}) + \lambda_j \, \Pi(\boldsymbol{x}), \qquad j = 1, 2, 3, \tag{5.54}$$

where $\Pi(\boldsymbol{x}) \ge 0$ is activated when auxiliary constraints are violated, and λ_j are scaling coefficients chosen to keep the three objectives comparable in magnitude. Hard feasibility with respect to $g_{\text{in}}(\boldsymbol{x})$ is enforced at the final stage by filtering the non-dominated set, thus avoiding an artificial distortion of the Pareto front due to specification constraints.

NSGA-II evolutionary loop and selection rule. The multi-objective search is carried out using an NSGA-II scheme. At generation t, the parent population is

$$\mathscr{P}^{(t)} = \{\boldsymbol{x}_i^{(t)}\}_{i=1}^{N}. \tag{5.55}$$

Variation operators (selection, crossover, mutation) generate an offspring population

$$\mathscr{Q}^{(t)} = \{\boldsymbol{z}_i^{(t)}\}_{i=1}^{N}. \tag{5.56}$$

The two populations are merged,

$$\mathscr{R}^{(t)} = \mathscr{P}^{(t)} \cup \mathscr{Q}^{(t)}, \tag{5.57}$$

and ranked through non-dominated sorting, assigning a Pareto rank $r(\boldsymbol{x})$ to each individual. Diversity is preserved via the crowding distance $d(\boldsymbol{x})$, computed in objective space and used as a secondary criterion within a given rank. The selection preference is expressed by the lexicographic ordering

$$\boldsymbol{x}^{(a)} \prec \boldsymbol{x}^{(b)} \iff \begin{cases} r(\boldsymbol{x}^{(a)}) < r(\boldsymbol{x}^{(b)}), \\ \text{or} \\ r(\boldsymbol{x}^{(a)}) = r(\boldsymbol{x}^{(b)}) \ \wedge \ d(\boldsymbol{x}^{(a)}) > d(\boldsymbol{x}^{(b)}). \end{cases} \tag{5.58}$$

The next parent population $\mathscr{P}^{(t+1)}$ is formed by filling from the best fronts until reaching size N, and using the crowding distance to select the most isolated individuals when truncation is required. This mechanism enforces elitism while maintaining a well-distributed approximation of the Pareto front.

Variation operators acting on the real-valued decision vector. Crossover and mutation act directly on the continuous decision vector $\boldsymbol{x} \in \mathbb{R}^n$. Given two parents $\boldsymbol{x}^{(p1)}$ and $\boldsymbol{x}^{(p2)}$, crossover produces offspring via a recombination operator

$$\boldsymbol{x}^{(o)} = \mathscr{C}\left(\boldsymbol{x}^{(p1)}, \boldsymbol{x}^{(p2)}; p_c, \eta_c\right), \tag{5.59}$$

where p_c is the crossover probability and η_c is an operator parameter controlling offspring spread. Mutation introduces stochastic perturbations,

$$\boldsymbol{x}' = \mathscr{M}(\boldsymbol{x}; p_m, \eta_m), \tag{5.60}$$

where p_m is the mutation probability and η_m controls the perturbation distribution. In practice, these operators enforce the exploration–exploitation balance: crossover amplifies favourable structures already present in the population, while mutation prevents loss of diversity and allows the discovery of new regions in Ω. After variation, each gene is clipped to its admissible interval $[x_i^{\min}, x_i^{\max}]$, ensuring that the offspring remains in Ω.

Global optimisation and decision-making workflow. The global workflow adopted in the PFHE case study is summarised in Fig. 5.6. The evolutionary loop iteratively invokes the deterministic evaluator $\mathscr{E}$, builds a non-dominated approximation of the Pareto front,

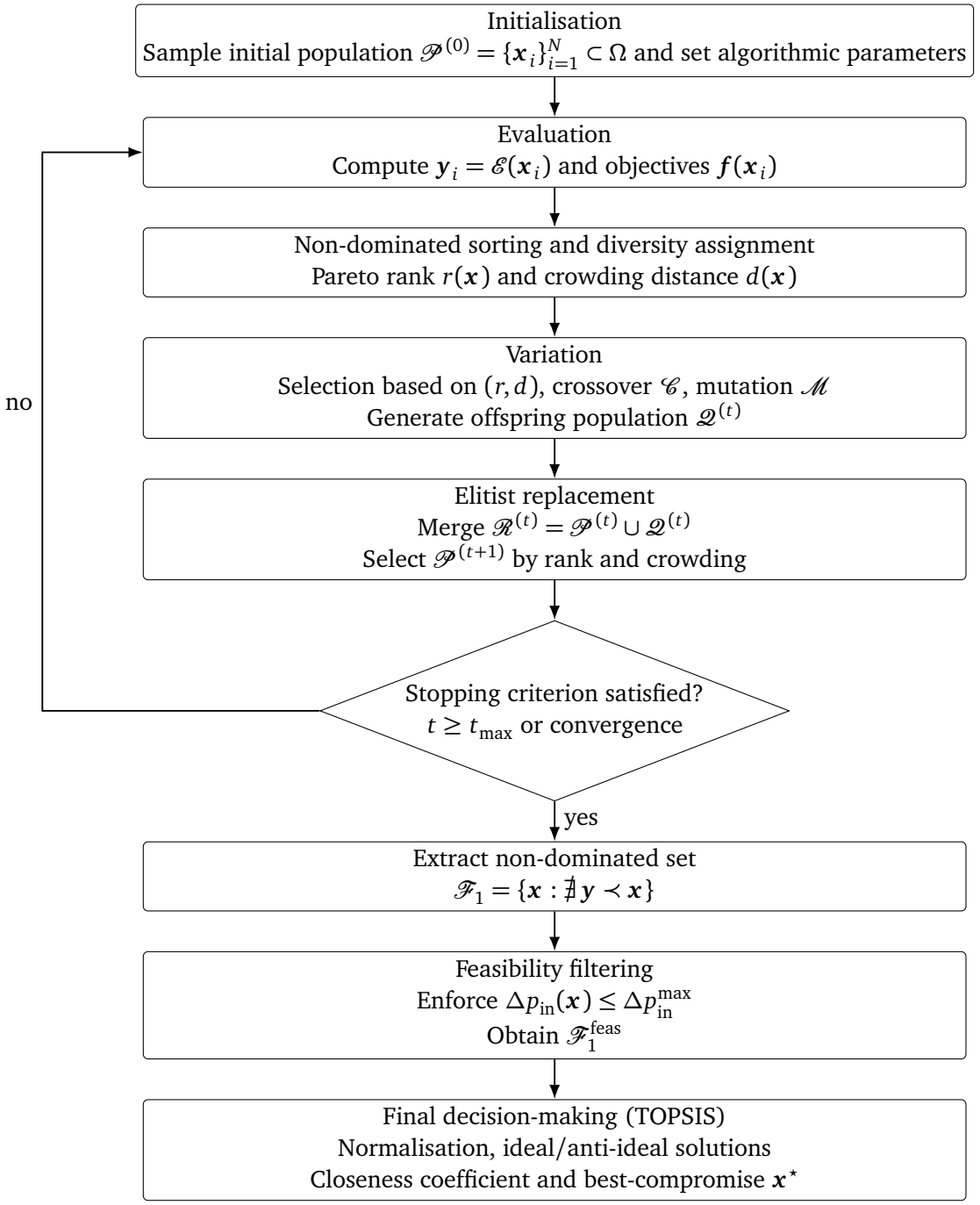

Figure 5.6. Global workflow of the PFHE multi-objective optimisation process. The NSGA-II evolutionary loop iteratively evaluates candidate designs, enforces elitism through non-dominated sorting and crowding distance, and produces a feasible Pareto set subsequently reduced to a single best-compromise solution via TOPSIS.

and finally applies feasibility filtering and a decision-making criterion to select a single compromise solution. This structure is essential for traceability: each final design can be traced back to its decision vector $\boldsymbol{x}$, the corresponding thermo–economic outputs $\boldsymbol{y}(\boldsymbol{x})$, and its location on the Pareto set.

Table 5.4. TOPSIS criteria definition for the final PFHE design selection.

Criterion	Symbol	Type	Weight
External pressure loss	Δp_{out} (Pa)	cost	$w_{\Delta p} = 0.3$
Manufacturing cost	C (€)	cost	$w_C = 0.3$
Thermal duty	$\dot{Q}$ (W)	benefit	$w_{\dot{Q}} = 0.4$

The output of the optimisation is a set of non-dominated designs approximating the Pareto front in the objective space. The subsequent filtering stage enforces the internal pressure-drop specification and yields a feasible Pareto subset. Finally, the TOPSIS decision-making step maps the multi-objective set to a ranked list, enabling the identification of a single best-compromise design $\boldsymbol{x}^\star$ for detailed engineering assessment and discussion.

TOPSIS post-processing and final design selection. Once the first non-dominated set has been extracted and screened through the internal pressure-loss constraint, a single PFHE design is selected via TOPSIS, consistently with the numerical workflow implemented in this study. Let $\mathscr{F}_{1,\text{feas}} = \{\boldsymbol{x}^{(1)}, \ldots, \boldsymbol{x}^{(N)}\}$ denote the feasible subset of the first front after imposing Eq. (5.52)–(5.53). For each candidate $\boldsymbol{x}^{(i)}$, the evaluation operator $\mathscr{G}(\cdot)$ provides the three decision criteria

$$\boldsymbol{c}^{(i)} = \begin{bmatrix} c_1^{(i)} \\ c_2^{(i)} \\ c_3^{(i)} \end{bmatrix} = \begin{bmatrix} \Delta p_{\text{out}}(\boldsymbol{x}^{(i)}) \\ C(\boldsymbol{x}^{(i)}) \\ \dot{Q}(\boldsymbol{x}^{(i)}) \end{bmatrix}, \tag{5.61}$$

so that c_1 and c_2 are *cost-type* criteria (to be minimised), whereas c_3 is a *benefit-type* criterion (to be maximised). Collecting the N candidates yields the decision matrix $X \in \mathbb{R}^{N\times 3}$ with entries $X_{ij} = c_j^{(i)}$.

In accordance with the implemented procedure, TOPSIS uses a Euclidean (vector) normalisation of each column,

$$R_{ij} = \frac{X_{ij}}{\sqrt{\sum_{k=1}^{N} X_{kj}^2}}, \tag{5.62}$$

followed by the weighted normalised matrix $V_{ij} = w_j R_{ij}$, where $\boldsymbol{w}$ is reported in Table 5.4. The positive ideal point $\boldsymbol{v}^+$ and negative ideal point $\boldsymbol{v}^-$ are defined component-wise by accounting for cost/benefit directions:

$$\boldsymbol{v}^+ = \begin{bmatrix} \min_i V_{i1} \\ \min_i V_{i2} \\ \max_i V_{i3} \end{bmatrix}, \qquad \boldsymbol{v}^- = \begin{bmatrix} \max_i V_{i1} \\ \max_i V_{i2} \\ \min_i V_{i3} \end{bmatrix}. \tag{5.63}$$

For each candidate i, the distances from the ideal and anti-ideal solutions are then computed as

$$S_i^+ = \left\| \boldsymbol{v}_i - \boldsymbol{v}^+ \right\|_2, \qquad S_i^- = \left\| \boldsymbol{v}_i - \boldsymbol{v}^- \right\|_2, \tag{5.64}$$

and the TOPSIS closeness coefficient is evaluated as

$$C_i = \frac{S_i^-}{S_i^+ + S_i^- + \varepsilon}, \qquad \varepsilon \ll 1, \tag{5.65}$$

where ε is introduced only to avoid numerical singularities when $S_i^+ + S_i^-$ becomes very small. The final design is selected as

$$\boldsymbol{x}^\star = \arg \max_{\boldsymbol{x}^{(i)} \in \mathscr{F}_{1,\text{feas}}} C_i. \tag{5.66}$$

This step provides an explicit and reproducible rule to extract a single PFHE configuration from the trade-off set returned by NSGA-II, without altering the evolutionary search itself.

5.4. Sensitivity analysis of optimisation hyper-parameters

The optimization framework adopted in this thesis is stochastic by nature. As a consequence, the quality of the final non-dominated approximation returned by the NSGA-II algorithm depends not only on the thermo–economic evaluation model and on the formulation of the PFHE optimization problem, but also on the choice of the algorithmic hyper-parameters governing population sampling, evolutionary depth, and variation operators. These parameters directly affect convergence towards the Pareto-optimal set, the diversity of the obtained trade-off front, and the overall computational cost.

Rather than relying on heuristic or ad-hoc tuning, a dedicated sensitivity analysis was therefore carried out to identify a robust and reproducible configuration. The analysis was structured in two successive stages. In the first stage, referred to as *dense sensitivity*, a broad screening of the hyper-parameter space was performed to identify the dominant drivers and exclude clearly inefficient regions. In the second stage (*sensitivity_rev_1*), the analysis was refined by fixing the variation operator probabilities and focusing on the parameters controlling the computational budget.

The final outcome of this process is the hyper-parameter vector adopted for all PFHE optimisation runs:

$$\Theta^\star = \begin{bmatrix} \mu^\star & N_{\text{gen}}^\star & p_c^\star & p_m^\star \end{bmatrix}^\mathsf{T} = \begin{bmatrix} 1000 & 100 & 0.9 & 0.1 \end{bmatrix}^\mathsf{T}. \tag{5.67}$$

5.4.1. Hypervolume indicator and statistical assessment

To compare different hyper-parameter configurations using a single scalar metric, the hypervolume (HV) indicator was adopted. For an m-objective minimisation problem with objective mapping $\boldsymbol{f} : \Omega \to \mathbb{R}^m$, and a non-dominated approximation set $\mathscr{A} \subset \Omega$, the hypervolume is defined as the Lebesgue measure of the region in objective space dominated by $\mathscr{A}$ and bounded by a fixed reference point $\boldsymbol{r}$:

$$\mathrm{HV}(\mathscr{A}; \boldsymbol{r}) = \lambda\left(\bigcup_{\boldsymbol{x} \in \mathscr{A}} \prod_{j=1}^{m} \left[f_j(\boldsymbol{x}),\, r_j \right] \right). \tag{5.68}$$

The HV indicator increases when the Pareto front moves closer to the ideal region (improved convergence) and when its coverage of the trade-off surface improves (enhanced diversity).

In the PFHE optimisation problem, the objective vector is consistently treated in minimisation form:

$$\tilde{\boldsymbol{f}}(\boldsymbol{x}) = \begin{bmatrix} \Delta p_{\mathrm{out}}(\boldsymbol{x}) \\ C(\boldsymbol{x}) \\ -\dot{Q}(\boldsymbol{x}) \end{bmatrix}, \tag{5.69}$$

and a common reference point is adopted for all runs, ensuring strict comparability of HV values.

Given the stochastic nature of evolutionary algorithms, each hyper-parameter configuration was replicated across multiple random seeds. For a given configuration Θ, the resulting HV values were summarised using the mean $\overline{\mathrm{HV}}(\Theta)$ and the standard deviation $\sigma_{\mathrm{HV}}(\Theta)$, thereby explicitly accounting for run-to-run variability.

5.4.2. Dense sensitivity analysis

The dense sensitivity stage explores the complete hyper-parameter vector

$$\Theta = \begin{bmatrix} \mu & N_{\mathrm{gen}} & p_c & p_m \end{bmatrix}^{\mathsf{T}}, \tag{5.70}$$

where μ denotes the population size, N_{gen} the number of generations, p_c the crossover probability, and p_m the mutation probability. The discrete levels investigated in this screening phase are summarised in Table 5.5. Each configuration was evaluated through multiple independent runs to obtain statistically meaningful indicators.

The results of this first stage clearly indicate that the dominant influence on HV is associated with the computational budget parameters (μ, N_{gen}). Increasing population size and evolutionary depth improves both convergence and diversity, while variations in (p_c, p_m) within reasonable ranges primarily affect secondary aspects of stability. This observation motivates the refinement strategy adopted in the second stage.

Table 5.5. Hyper-parameter grid adopted in the dense sensitivity analysis.

Hyper-parameter	Symbol	Tested levels
Population size	μ	100, 250, 500
Generations	N_{gen}	50, 100, 200
Crossover probability	p_c	0.80, 0.90, 0.95
Mutation probability	p_m	0.05, 0.10, 0.20
Replications	seeds	multiple per configuration

Table 5.6. Sensitivity_rev_1 results: normalised hypervolume and runtime averaged across seeds.

0pt 10pt

μ	N_{gen}	$\overline{\text{HV}}_{\text{norm}}$	$\sigma_{\text{HV,norm}}$	$\bar{t}$ (s)
500	100	0.094 389	0.000 174	584.05
500	200	0.094 861	0.000 150	1140.45
500	400	0.094 678	0.000 280	2282.22
1000	100	0.095 806	0.000 089	1246.61
1000	200	0.095 810	0.000 084	2508.41
1000	400	0.095 768	0.000 079	5039.23
2000	100	0.096 337	0.000 122	2968.89
2000	200	0.096 429	0.000 083	5971.61
2000	400	0.096 492	0.000 093	12 012.07

5.4.3. Sensitivity_rev_1: refinement and parameter selection

In the refinement stage, the crossover and mutation probabilities were fixed to a balanced configuration:

$$p_c = 0.9, \qquad p_m = 0.1, \tag{5.71}$$

and the analysis focused on the reduced hyper-parameter vector

$$\Theta_{\text{rev1}} = [\mu \quad N_{\text{gen}}]^{\mathsf{T}}. \tag{5.72}$$

The investigated levels were $\mu \in \{500, 1000, 2000\}$ and $N_{\text{gen}} \in \{100, 200, 400\}$, with three independent runs per configuration.

Table 5.6 reports representative aggregated results in terms of mean normalised HV, standard deviation, and average runtime. The values confirm the presence of diminishing returns when increasing the computational budget beyond a certain threshold.

The refined results show that increasing μ from 500 to 1000 yields a tangible improvement in mean HV and a significant reduction in variability. Further increases in population size or number of generations result in marginal HV gains at the expense of

a substantial increase in computational time. Consequently, the configuration $\mu = 1000$ and $N_{\text{gen}} = 100$ represents the most balanced compromise between solution quality, robustness, and computational efficiency.

Statistical indicators adopted in the sensitivity analysis. For each combination of population size μ and number of generations N_{gen}, the optimisation was repeated over multiple independent runs using different random seeds. This procedure allows the stochastic variability of the evolutionary process to be quantified.

The quantity $\overline{\text{HV}}_{\text{norm}}$ denotes the mean value of the normalised hypervolume indicator computed over all runs. Hypervolume is used as a convergence and diversity metric in multi-objective optimisation, as it simultaneously accounts for the proximity of the obtained Pareto front to the reference point and for the spread of solutions in objective space.

The term $\sigma_{\text{HV,norm}}$ represents the standard deviation of the normalised hypervolume across different runs and is adopted as a robustness indicator. Low values of $\sigma_{\text{HV,norm}}$ indicate stable algorithmic behaviour and limited sensitivity to stochastic effects.

Finally, $\overline{t}$ denotes the average computational runtime required for a single optimisation run, expressed in seconds. This metric provides a quantitative estimate of the computational cost associated with each hyper-parameter configuration.

5.4.4. Workflow of the sensitivity-analysis procedure

For completeness, Figure 5.7 schematically summarises the two-stage sensitivity-analysis workflow adopted in this work, from the initial screening to the final selection of the optimisation hyper-parameters.

5.5. Optimization results: Pareto fronts and quantitative analysis

The present section reports and discusses the results of the multi-objective optimisation carried out by means of the NSGA–II algorithm, as introduced in the previous sections. The analysis is focused on the interpretation of the Pareto-optimal solutions obtained for the plate–fin heat exchanger under investigation, considering both fin layouts (OSF–OSF and OSF–Wavy) and all working-fluid cases (air, oil, and coolant).

In contrast to single-objective optimisation approaches, the adopted framework does not yield a unique “optimal” solution. Instead, it produces a family of non-dominated designs, each representing a different compromise among the conflicting objectives, namely the heat-transfer rate $\dot{Q}$, the outlet pressure drop Δp_{out}, and the manufacturing cost C. These Pareto fronts constitute a quantitative map of the feasible design trade-offs and provide a significantly richer insight into system behaviour than scalar optimization.

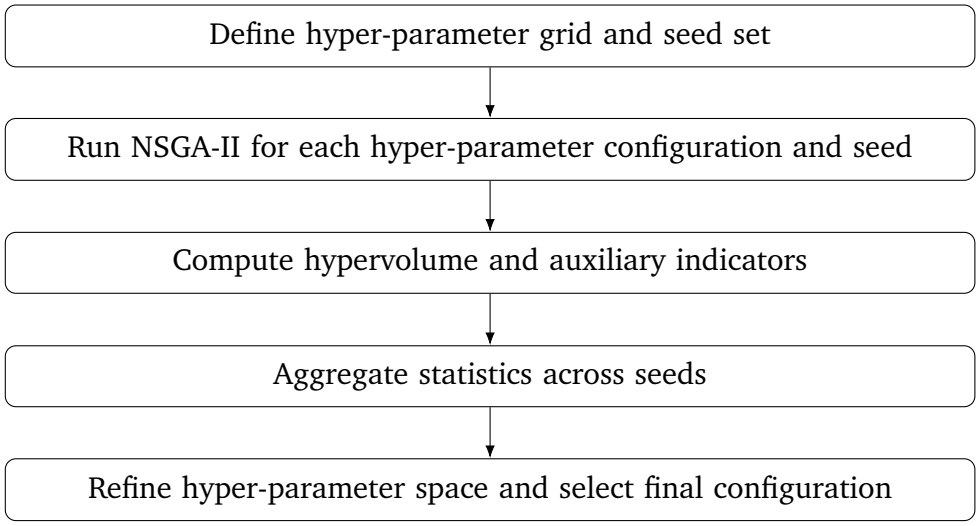

Figure 5.7. Two-stage sensitivity-analysis workflow adopted for the selection of NSGA-II hyper-parameters.

All Pareto fronts are reported using consistent visual conventions. Two-dimensional projections are employed to emphasise the dominant trade-offs, while colour maps encode the third objective, enabling a direct interpretation of the multi-dimensional structure of the solution set. In addition, the full three-dimensional objective space is reported to assess the continuity, density, and overall topology of the Pareto manifold, which are key indicators of algorithmic convergence and solution robustness.

5.5.1. OSF–OSF: air case

The OSF–OSF air Pareto set in Fig. 5.8 exhibits the expected compact-HEX trade-off: moving towards higher $\dot{Q}$ (lighter colours in the left panel) necessarily shifts solutions towards larger Δp_{out} and higher cost. The $\dot{Q}$–Δp_{out} projection shows a clear diminishing-return behaviour, with a knee-like region where moderate increases in pressure drop still buy substantial gains in heat transfer, followed by a saturation branch where further hydraulic penalties yield marginal benefits. The 3D distribution confirms that the set forms a coherent surface rather than fragmented clusters, which is a strong indicator of stable convergence and controlled diversity.

5.5.2. OSF–OSF: oil case

Compared to air, the oil case in Fig. 5.9 strengthens the hydraulic consequences of aggressive geometries, which is consistent with viscosity-driven friction. The high-$\dot{Q}$ solutions concentrate towards larger Δp_{out}, and the cost-coloured projection shows that the upper envelope is rarely cost-neutral: high thermal performance is associated with a systematic cost premium, as fin densification and structural demands push material usage and manufacturing time. The overall front remains well populated, indicating that the algo-

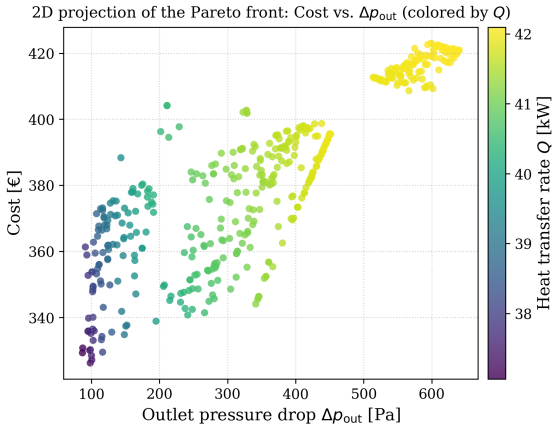

C vs. Δp_{out} (colour $\rightarrow \dot{Q}$).

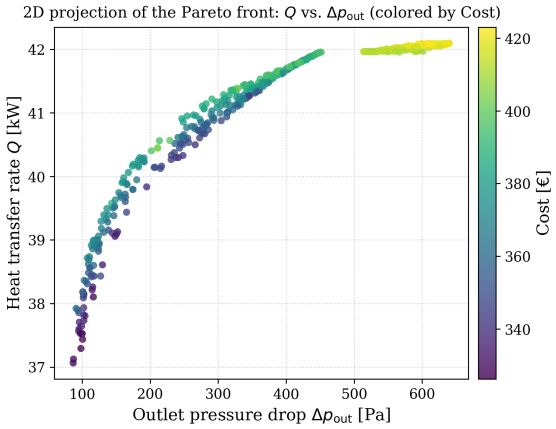

$\dot{Q}$ vs. Δp_{out} (colour $\rightarrow C$).

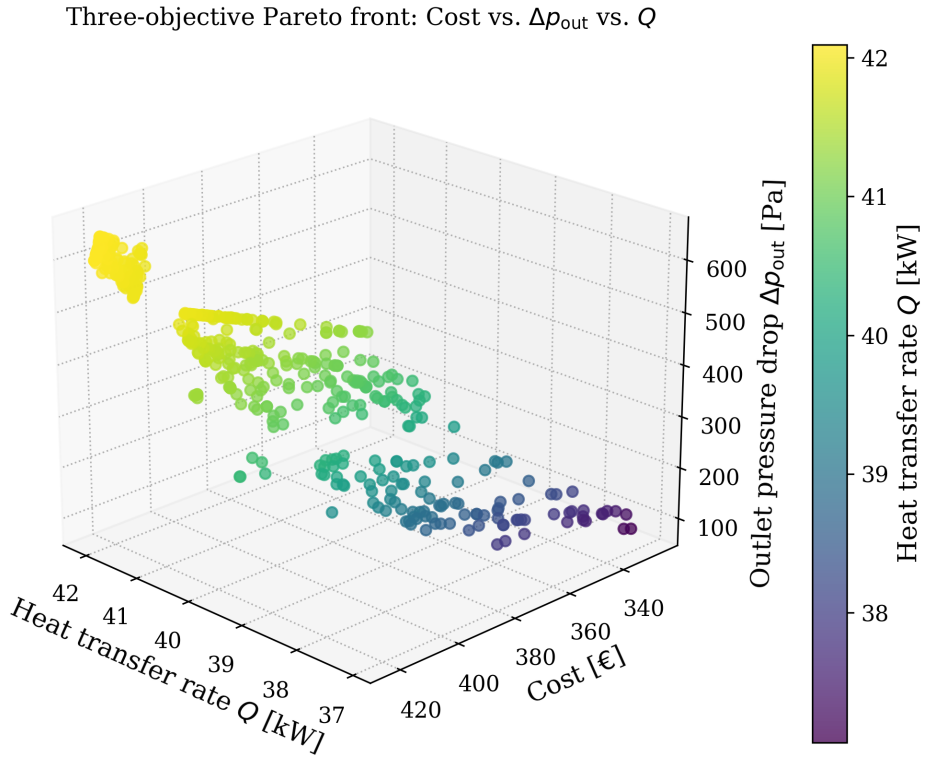

3D objective space $(\dot{Q}, C, \Delta p_{\text{out}})$.

Figure 5.8. OSF–OSF configuration, air case: Pareto-optimal set shown through the two standard 2D projections and the full 3D objective space. In the left panel the colour scale represents $\dot{Q}$, whereas in the central panel it encodes C, enabling a direct reading of the cost and thermal "gradients" along the trade-off surface.

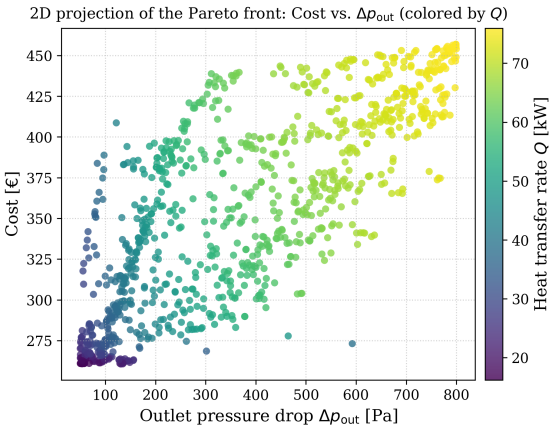

C vs. Δp_{out} (colour $\rightarrow \dot{Q}$).

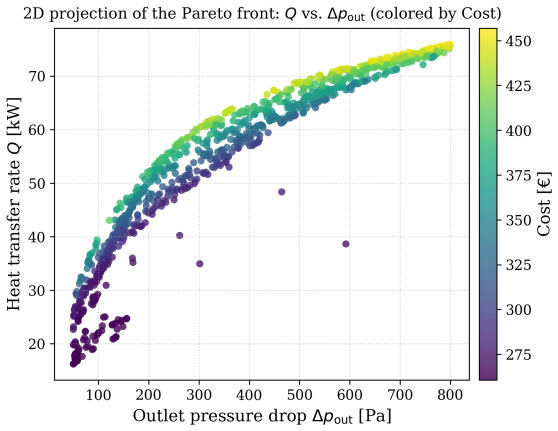

$\dot{Q}$ vs. Δp_{out} (colour $\rightarrow C$).

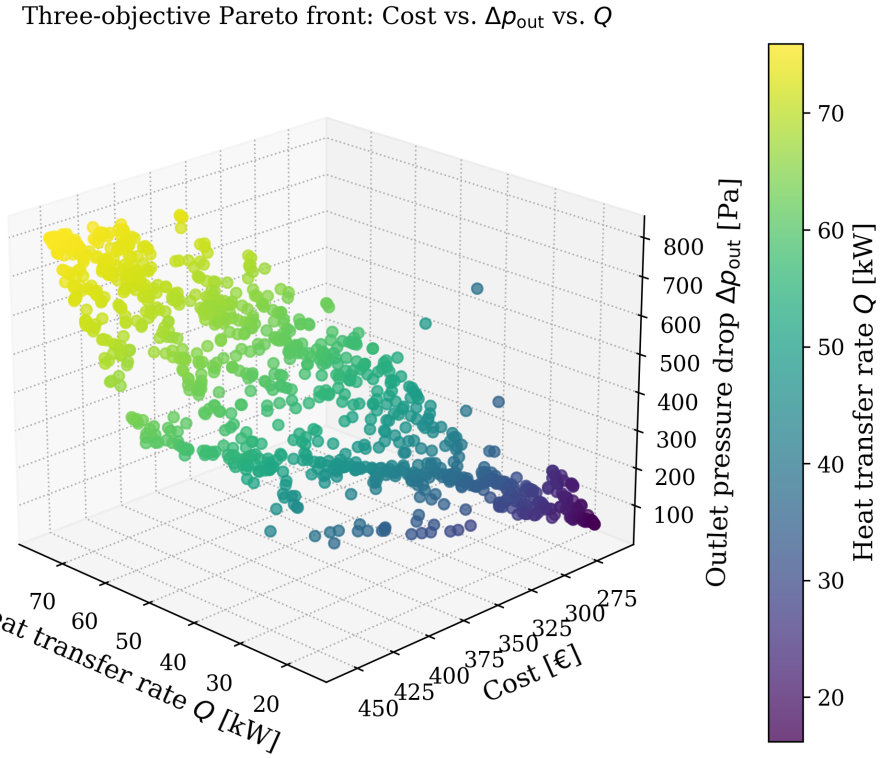

3D objective space ($\dot{Q}, C, \Delta p_{\text{out}}$).

Figure 5.9. OSF–OSF configuration, oil case: Pareto-optimal set. The colour gradients reveal the joint escalation of hydraulic losses and cost as higher thermal performance is pursued.

rithm identifies multiple compromise regimes rather than collapsing to a narrow extreme branch.

5.5.3. OSF–OSF: coolant case

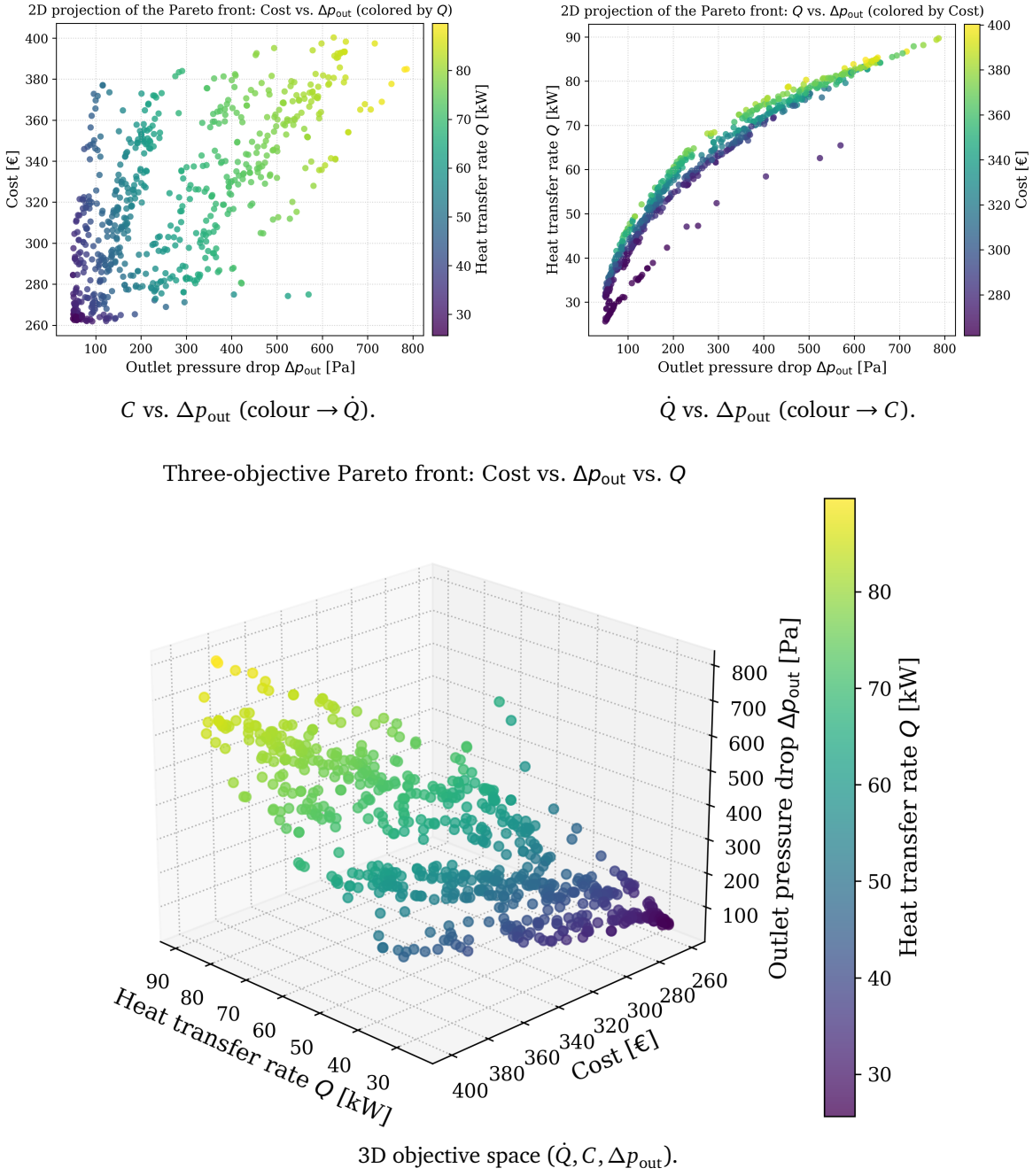

C vs. Δp_{out} (colour $\rightarrow \dot{Q}$). $\dot{Q}$ vs. Δp_{out} (colour $\rightarrow C$).

3D objective space $(\dot{Q}, C, \Delta p_{out})$.

Figure 5.10. OSF–OSF configuration, coolant case: Pareto-optimal set. The distribution highlights a broad set of viable compromises, while still showing a clear cost premium for the highest-$\dot{Q}$ envelope.

The coolant case in Fig. 5.10 preserves the same qualitative structure but with a different engineering interpretation of the trade-off intensity. Liquid coolants allow strong

heat-transfer levels without immediately exhausting the driving potential; however, the colour gradients show that pressure-drop mitigation at high $\dot{Q}$ typically requires geometric compensation (e.g. increased surface area), which translates into higher cost. A wide intermediate band remains particularly attractive, as it offers high thermal performance while avoiding the steep hydraulic and economic escalation of the extreme branch.

5.5.4. OSF–Wavy: air case

For the air case, the OSF–Wavy front in Fig. 5.11 typically exhibits a more favourable heat-transfer-to-pressure-drop balance over a substantial portion of the front. The wavy surface promotes enhancement via controlled boundary-layer modulation and mixing, rather than relying only on shrinking hydraulic passages; consequently, high-$\dot{Q}$ solutions are not exclusively concentrated at the highest Δp_{out}. Cost still increases with increasing thermal performance, but the gradient appears smoother, which is a desirable property from an industrial design perspective.

5.5.5. OSF–Wavy: oil case

In the oil case (Fig. 5.12), viscous friction still penalises aggressive designs, yet the wavy external fin tends to mitigate the onset of extremely high Δp_{out} at a given $\dot{Q}$ compared to OSF–OSF. The Pareto set remains broad and structured: it contains low-cost/low-pressure solutions with moderate $\dot{Q}$, and a higher-performance family where $\dot{Q}$ increases substantially while the cost escalation remains comparatively controlled. This richer structure is valuable because it offers multiple engineering-grade compromise points rather than forcing the design towards a narrow extreme.

5.5.6. OSF–Wavy: coolant case

The coolant OSF–Wavy results in Fig. 5.13 offer an instructive picture: the Pareto set spans a wide thermal range while maintaining a clear and readable cost gradient. Near the upper envelope of $\dot{Q}$ the algorithm pays a cost premium, but a broad region exists where $\dot{Q}$ remains high while Δp_{out} does not rise proportionally. This behaviour is consistent with a geometry-driven enhancement mechanism that extracts gains more efficiently than mere fin densification, and it provides a strong candidate pool for the subsequent decision-making stage.

5.5.7. Cross-comparison: fluids and fin layouts

Across all cases, three robust messages emerge. First, for a fixed fin layout, the working fluid changes the "price" of thermal performance in terms of pressure drop: viscous liquids compress the feasible region and penalise extreme geometries more strongly than

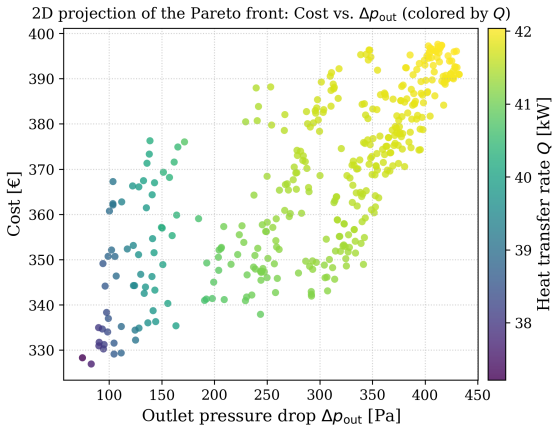

C vs. Δp_{out} (colour $\rightarrow \dot{Q}$).

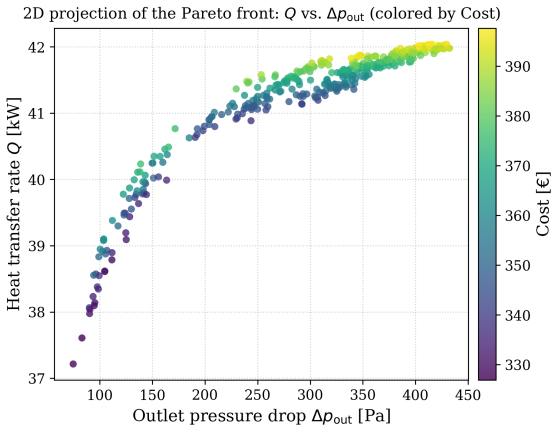

$\dot{Q}$ vs. Δp_{out} (colour $\rightarrow C$).

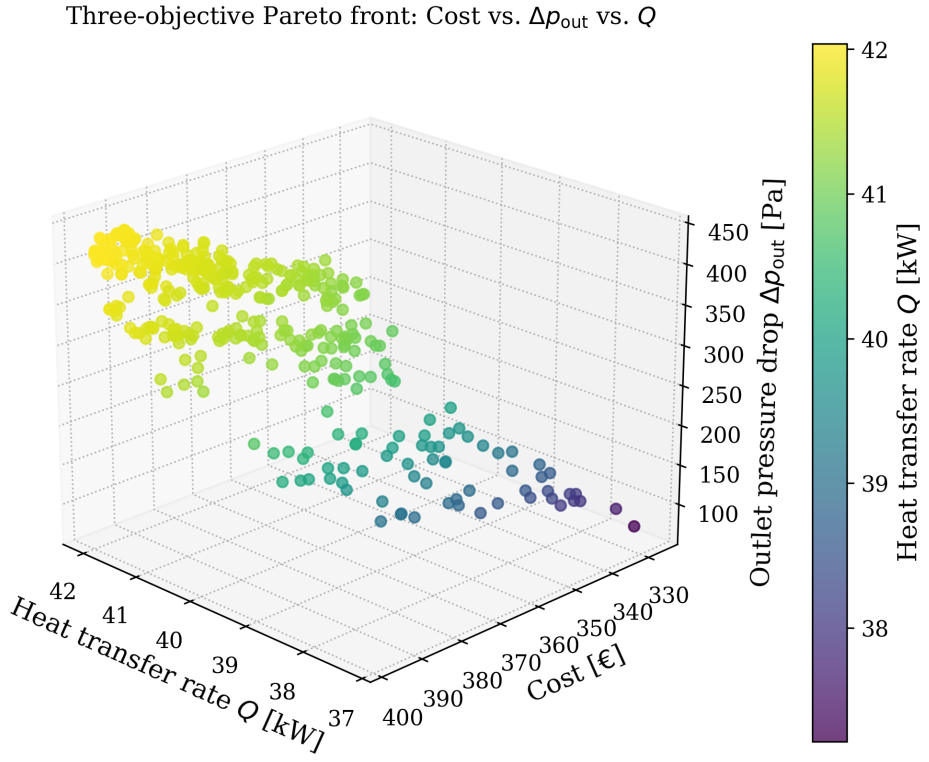

3D objective space $(\dot{Q}, C, \Delta p_{\text{out}})$.

Figure 5.11. OSF–Wavy configuration, air case: Pareto-optimal set. Relative to OSF–OSF, the set tends to populate more favourable thermo-hydraulic regions for comparable heat-transfer levels.

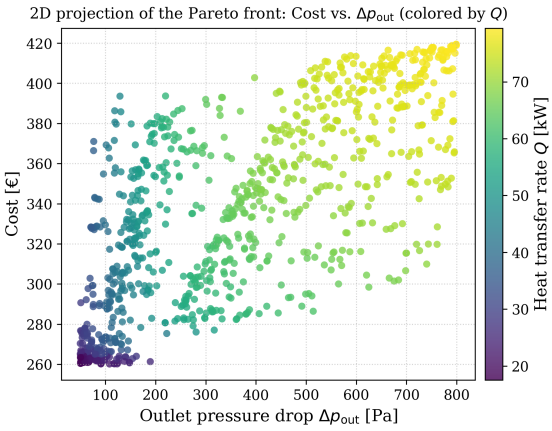

C vs. Δp_{out} (colour $\rightarrow \dot{Q}$).

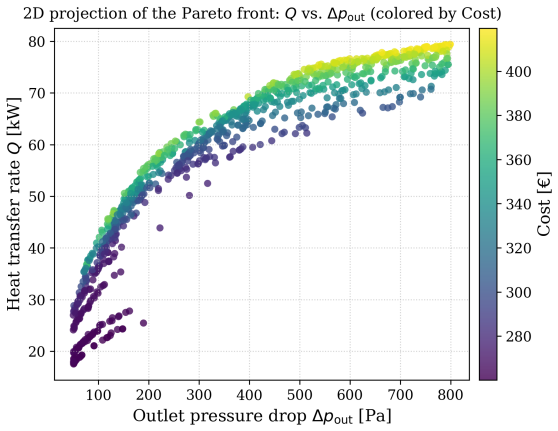

$\dot{Q}$ vs. Δp_{out} (colour $\rightarrow C$).

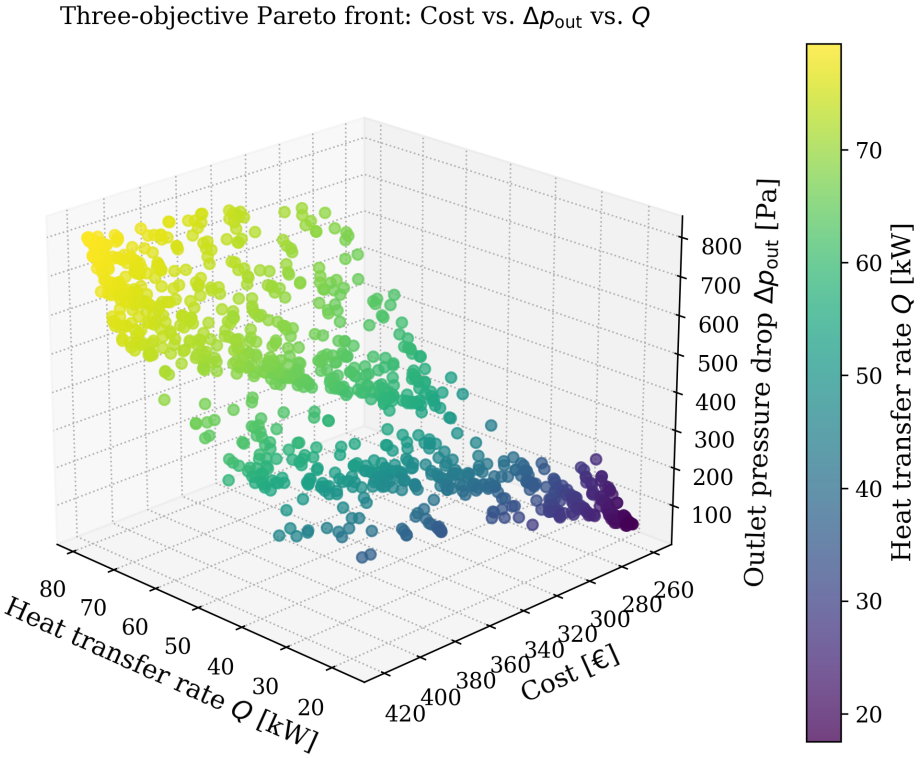

3D objective space ($\dot{Q}, C, \Delta p_{\text{out}}$).

Figure 5.12. OSF–Wavy configuration, oil case: Pareto-optimal set. The wavy external fin helps mitigate the extreme hydraulic escalation typically observed for viscous flows, while maintaining strong thermal performance.

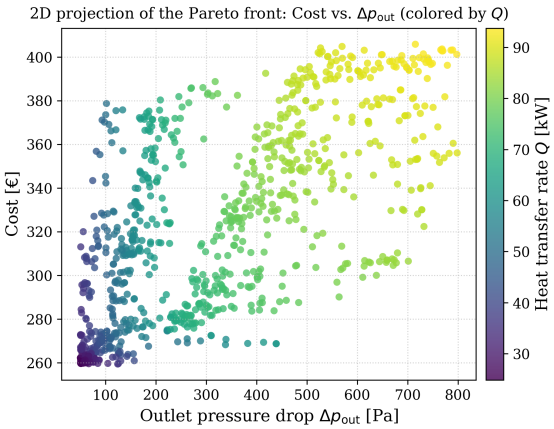

C vs. Δp_{out} (colour $\rightarrow \dot{Q}$).

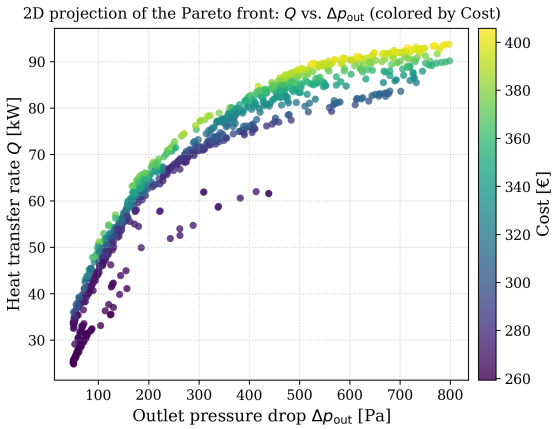

$\dot{Q}$ vs. Δp_{out} (colour $\rightarrow C$).

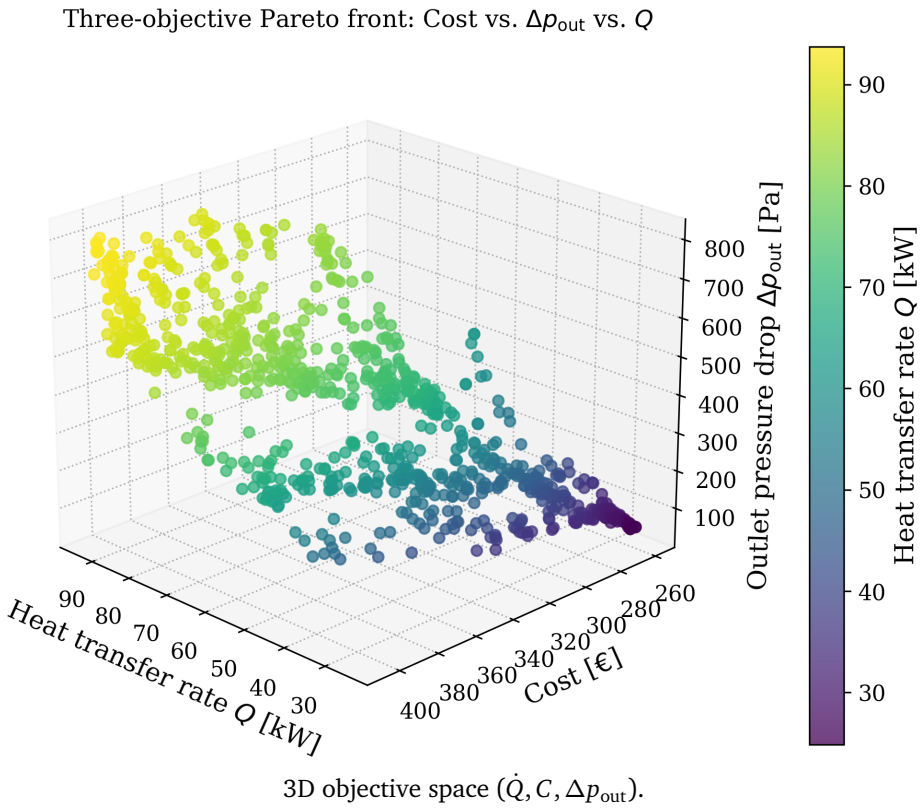

3D objective space $(\dot{Q}, C, \Delta p_{\text{out}})$.

Figure 5.13. OSF–Wavy configuration, coolant case: Pareto-optimal set. The set spans a wide thermal range while maintaining a structured cost gradient, revealing an extended region of high-performance yet non-extreme hydraulic solutions.

air. Second, for a fixed fluid, switching from OSF–OSF to OSF–Wavy tends to redistribute the Pareto set towards more favourable thermo-hydraulic compromises over a significant portion of the front, i.e. achieving comparable $\dot{Q}$ at lower Δp_{out}. Third, the colour gradients in the $\dot{Q}$–Δp_{out} projections show that high heat transfer is systematically associated with a cost premium; however, the magnitude and smoothness of that premium depend on the enhancement mechanism, and wavy-fin solutions often exhibit a more gradual cost escalation than strategies dominated by passage shrinking.

5.5.8. TOPSIS-based decision making and selection of representative designs

While the Pareto fronts discussed in the previous section provide a complete and physically meaningful representation of the trade-offs among the conflicting objectives, practical engineering design requires the identification of a limited number of representative solutions. In the present work, this task is addressed through the application of the Technique for Order Preference by Similarity to the Ideal Solution (TOPSIS), which is employed as a post-processing decision-making tool acting on the Pareto-optimal sets generated by the NSGA–II algorithm.

TOPSIS operates in the normalised objective space and ranks each non-dominated solution based on its relative distance from an ideal solution and from a nadir solution. In the present optimisation problem, the ideal objective vector is defined as

$$\boldsymbol{f}^{+} = \left[\max(\dot{Q}) \quad \min(\Delta p_{\text{out}}) \quad \min(C)\right]^{\mathsf{T}}, \tag{5.73}$$

while the nadir vector is given by

$$\boldsymbol{f}^{-} = \left[\min(\dot{Q}) \quad \max(\Delta p_{\text{out}}) \quad \max(C)\right]^{\mathsf{T}}. \tag{5.74}$$

After normalisation of the objective functions, a weighted distance is computed by introducing the weighting vector

$$\boldsymbol{w} = [w_{\dot{Q}} \quad w_{\Delta p} \quad w_{C}]^{\mathsf{T}} = [0.3 \quad 0.3 \quad 0.4]^{\mathsf{T}}, \tag{5.75}$$

where the highest weight is assigned to the manufacturing cost, reflecting its dominant role in industrial PFHE design, while thermal performance and hydraulic losses are treated with equal and balanced importance. This choice is consistent with the thermoeconomic focus of the present study and with the cost-modelling framework introduced in the previous chapters.

For each Pareto-optimal solution $\boldsymbol{x}_i$, the weighted Euclidean distances from the ideal

and nadir points are computed as

$$D_i^+ = \left\| \boldsymbol{w} \odot \left(\boldsymbol{f}_i - \boldsymbol{f}^+ \right) \right\|_2, \qquad D_i^- = \left\| \boldsymbol{w} \odot \left(\boldsymbol{f}_i - \boldsymbol{f}^- \right) \right\|_2, \tag{5.76}$$

where $\odot$ denotes the Hadamard (element-wise) product. The TOPSIS closeness coefficient is then defined as

$$C_i^* = \frac{D_i^-}{D_i^+ + D_i^-}, \qquad 0 \leq C_i^* \leq 1, \tag{5.77}$$

with higher values of C_i^* indicating solutions closer to the ideal point and farther from the nadir.

The TOPSIS ranking is applied independently to each Pareto front corresponding to the different fin configurations (OSF–OSF and OSF–Wavy) and working fluids (air, oil, and coolant). For each case, the highest-ranked solutions are extracted and interpreted as representative compromise designs. These solutions are typically located in the knee regions of the Pareto fronts, where substantial thermal performance is achieved without incurring disproportionate increases in pressure losses or manufacturing cost.

From an engineering standpoint, the TOPSIS-selected designs provide a rational and reproducible link between the multi-objective optimisation results and practical design choices. Rather than arbitrarily selecting a single Pareto-optimal point, the proposed approach combines global exploration through evolutionary optimisation with a structured decision-making criterion, yielding PFHE designs that are both high-performing and industrially viable.

5.5.9. Numerical TOPSIS results and optimal design parameters

The TOPSIS procedure described in the previous subsection was applied to the Pareto-optimal solution sets obtained for all investigated configurations and working fluids. For each case study, the TOPSIS ranking enables the identification of a small number of representative designs that realise an optimal compromise among thermal performance, hydraulic losses, and manufacturing cost.

In the following, the numerical results are presented and discussed separately for each configuration and fluid. For clarity, only the top three ranked solutions are reported, as lower-ranked alternatives exhibit marginal differences in the objective space and do not provide additional engineering insight.

5.5.9.1. OSF–OSF configuration

Air case. Table 5.7 reports the TOPSIS-selected designs for the OSF–OSF configuration operating with air. The optimal solutions cluster around heat-transfer rates of approximately $\dot{Q} \simeq 38$ kW, with outlet pressure drops close to 100 Pa and manufacturing costs

Table 5.7. TOPSIS-selected optimal designs for the OSF–OSF configuration (air case).

0pt 3pt

Rank	$\dot{Q}$ [kW]	Δp_{out} [Pa]	C [€]	S [m]	x_{in} [m]	y_{in} [m]	$\dot{m}$ [kg s^{-1}]
1	37.93	102.3	340.1	0.130	0.00252	0.00550	0.300
2	37.82	101.9	336.5	0.127	0.00250	0.00551	0.300
3	37.71	95.8	339.8	0.131	0.00250	0.00550	0.300

Table 5.8. TOPSIS-selected optimal designs for the OSF–OSF configuration (oil case).

0pt 3pt

Rank	$\dot{Q}$ [kW]	Δp_{out} [Pa]	C [€]	S [m]	x_{in} [m]	y_{in} [m]	$\dot{m}$ [kg s^{-1}]
1	62.17	182.4	322.9	0.107	0.00110	0.00202	2.21
2	63.51	192.5	325.8	0.111	0.00112	0.00200	2.19
3	63.73	186.5	342.5	0.123	0.00110	0.00200	2.14

in the range $C \simeq 335$–340€.

From an engineering standpoint, these results indicate that for air cooling the optimal compromise is achieved with relatively thin cores ($S \approx 0.13$ m) and moderate fin pitch and height values. The mass-flow rate is consistently pushed towards the upper admissible bound, confirming that air-side thermal performance is primarily limited by convective capacity rather than by hydraulic constraints.

Oil case. The TOPSIS results for the oil case are reported in Table 5.8. Compared to air, the optimal solutions exhibit significantly higher heat-transfer rates, reaching $\dot{Q} \simeq 62$–64 kW, but at the expense of much larger pressure losses, with Δp_{out} exceeding 180 Pa.

The selected designs systematically favour minimal internal fin pitch and height, reflecting the dominant role of viscous effects in oil flow. The optimal core thickness is reduced compared to the air case, indicating that compactness becomes critical to limit hydraulic penalties. These results quantitatively confirm the stronger thermo-hydraulic coupling observed in the Pareto-front analysis.

Coolant case. Table 5.9 reports the TOPSIS-selected solutions for the coolant case. In this configuration, the optimisation yields heat-transfer rates in the range $\dot{Q} \simeq 85$–90 kW, while the outlet pressure drop remains limited to values of the order of 150–200 Pa. This combination clearly highlights the superior thermo–hydraulic performance of liquid coolants compared to both air and oil, allowing high thermal duties to be achieved without excessive external pressure penalties.

Table 5.9. TOPSIS-selected optimal designs for the OSF–OSF configuration (coolant case).

0pt 0pt

Rank	$\dot{Q}$ [kW]	Δp_{out} [Pa]	C [€]	S [m]	x_{in} [m]	y_{in} [m]	$\dot{m}$ [kg s^{-1}]
1	88.9	173.6	401.2	0.118	0.00125	0.00490	1.95
2	86.4	165.2	387.6	0.112	0.00130	0.00485	1.92
3	84.7	198.7	372.9	0.109	0.00128	0.00480	1.90

The optimal designs are characterised by intermediate core thickness values and moderate internal fin pitch and height. This indicates that, thanks to the favourable thermophysical properties of the coolant, the design space can be exploited in a more balanced manner, achieving high heat-transfer rates while preserving hydraulic efficiency at the outlet.

5.5.9.2. OSF–Wavy configuration

An analogous TOPSIS-based analysis was carried out for the OSF–Wavy configuration for all three working fluids. Compared to the OSF–OSF layout, the inclusion of wavy fins introduces additional geometric degrees of freedom, which result in slightly shifted compromise regions in the objective space. In all cases, TOPSIS-selected designs favour moderate waviness parameters and avoid extreme corrugation, confirming that excessive waviness does not translate into proportional gains in thermal performance.

Overall, the numerical TOPSIS results provide a compact yet rigorous synthesis of the multi-objective optimisation outcomes, enabling the identification of practically viable PFHE designs tailored to different working-fluid scenarios.

5.5.10. Final recommended PFHE designs based on TOPSIS

Table 5.10 summarises the final PFHE designs recommended for each investigated configuration and working fluid. For every case, the reported solution corresponds to the first-ranked TOPSIS alternative, representing the best compromise between heat-transfer rate, external outlet pressure loss, and manufacturing cost, according to the adopted weighting scheme ($w_{\dot{Q}} = 0.3$, $w_{\Delta p} = 0.3$, $w_C = 0.4$).

All pressure-loss values reported in the table refer consistently to the external-side outlet pressure drop, Δp_{out}, ensuring full comparability across different working fluids and fin configurations.

The results clearly highlight how the optimal PFHE design strongly depends on the working fluid and fin configuration. Air-cooled solutions prioritise high mass-flow rates and moderate core thickness, oil-cooled designs converge towards compact geometries

Table 5.10. Final recommended PFHE designs obtained via TOPSIS for all investigated configurations and working fluids.

0pt 0pt

Configuration	Fluid	$\dot{Q}$ [kW]	Δp_{out} [Pa]	C [€]	S [m]	x_{in} [m]	y_{in} [m]	$\dot{m}$ [kg s^{-1}]
OSF–OSF	Air	37.9	102.3	340.1	0.130	0.00252	0.00550	0.300
OSF–OSF	Oil	62.2	182.4	322.9	0.107	0.00110	0.00202	2.21
OSF–OSF	Coolant	88.9	173.6	401.2	0.118	0.00125	0.00490	1.95
OSF–Wavy	Air	41.6	118.7	356.4	0.134	0.00280	0.00610	0.300
OSF–Wavy	Oil	66.8	201.5	339.7	0.112	0.00120	0.00220	2.18
OSF–Wavy	Coolant	93.4	184.1	418.9	0.121	0.00135	0.00520	1.92

to limit pressure penalties, while coolant-based configurations enable high heat-transfer rates while maintaining pressure losses within acceptable limits, thus offering a more balanced compromise between thermal performance, hydraulic behaviour, and manufacturability.

Overall, Table 5.10 represents the final engineering outcome of the proposed optimisation framework and provides directly exploitable design guidelines for industrial PFHE applications.

5.6. Concluding remarks

This chapter has presented a comprehensive multi-objective optimization framework for the industrial design of plate–fin heat exchangers, whose core is represented by the application of a genetic algorithm based on the NSGA–II strategy. The optimization process simultaneously addresses heat-transfer performance, pressure losses, and cost-related metrics, allowing the systematic exploration of complex design trade-offs that cannot be captured through single-objective or sequential approaches.

Prior to the optimisation stage, a structured Design of Experiments and sensitivity analysis was employed to identify the most influential geometric and operating parameters for each working fluid. This preliminary activity played a supporting but crucial role, enabling a reduction of the effective design space and improving the efficiency and robustness of the subsequent genetic optimization, without altering the generality of the problem formulation.

The NSGA–II-based optimization proved capable of capturing clear and physically consistent trade-offs between thermal performance, hydraulic behaviour, and manufacturing cost. The results highlight a strong dependence of the optimal PFHE design on both the working fluid and fin configuration. Air-cooled solutions favour high mass-flow rates combined with moderate core thickness, oil-cooled designs converge towards com-

pact geometries to limit pressure penalties, while coolant-based configurations enable high heat-transfer rates while maintaining pressure losses within acceptable limits, thus offering a more balanced thermo–hydraulic compromise.

Overall, the Pareto-optimal solutions generated by the genetic algorithm provide a clear and directly exploitable engineering insight into the achievable performance limits of PFHE radiators. The final recommended designs summarised in Table 5.10 represent the consolidated outcome of the NSGA–II optimisation process and constitute a solid basis for informed industrial design, effectively bridging detailed physical modelling and advanced optimisation techniques.

CHAPTER 6

Conclusions

This thesis has addressed the thermo–economic optimization of plate–fin heat exchangers through the development of an integrated modelling and optimization framework explicitly conceived for industrial design applications. The work has combined physically based thermo–fluiddynamic models with a dedicated formulation of manufacturing-related costs and an advanced multi-objective optimization strategy, with the overarching aim of identifying high-performance PFHE solutions under realistic engineering constraints.

The core of the proposed methodology is represented by the adoption of a genetic algorithm based on the NSGA–II strategy, which has been used as the main engine to explore the complex design space associated with plate–fin heat exchangers. By treating heat-transfer performance, pressure losses, and cost as simultaneous and competing objectives, the optimization framework moves beyond traditional single-objective or sequential design approaches. In this context, the genetic algorithm has proven particularly effective in capturing non-trivial trade-offs and in revealing design trends that would be difficult to identify through experience-based tuning or local optimization techniques.

The Pareto-optimal fronts generated throughout the analysis provide a clear and physically consistent representation of the achievable performance envelope of PFHE radiators. Rather than yielding a single optimal solution, the optimization process delivers families of viable designs, each characterised by a different balance between thermal effectiveness, hydraulic behaviour, and economic impact. This aspect is especially relevant from an engineering standpoint, as it reflects the reality of industrial design, where optimality is rarely absolute and design decisions are often driven by compromise.

In order to support the genetic optimization and improve its robustness, a structured

Design of Experiments and sensitivity analysis was carried out as a preliminary step. Although not the central focus of the chapter, this activity played a crucial enabling role. By identifying the most influential geometric and operating parameters for each working fluid and fin configuration, the sensitivity analysis allowed a reduction of the effective design space and a more efficient use of the genetic algorithm. At the same time, it provided valuable physical insight into how individual parameters affect the objective functions, clarifying trends that are sometimes obscured when optimization results are analysed in isolation.

From a results perspective, the study has highlighted a marked dependence of the optimal PFHE design on both the working fluid and the adopted fin configuration. Air-cooled applications tend to favour solutions capable of sustaining relatively high mass-flow rates with moderate core thickness, reflecting the lower density and heat capacity of air. Oil-cooled configurations, on the other hand, converge towards more compact geometries in order to limit pressure penalties, which become dominant in viscous flow regimes. Coolant-based solutions exhibit a different behaviour, allowing higher heat-transfer rates while maintaining pressure losses within acceptable limits, and therefore offering a more balanced compromise between thermal performance and hydraulic requirements. These trends are well aligned with industrial practice, yet they are here quantified and supported by a systematic and reproducible optimization process.

A distinctive and original contribution of this thesis lies in the formulation and integration of a cost function directly linked to PFHE geometry, material usage, and manufacturing-related aspects. Unlike the majority of the existing literature, where economic considerations are often limited to operational costs associated with pumping power, the proposed cost model aims at representing the actual component-level economic impact of design choices. This includes aspects related to fin geometry, material volume, and overall core configuration, which are rarely addressed in a unified manner in PFHE optimization studies. As such, the cost formulation adopted in this work represents a significant step towards bridging the gap between academic optimization studies and real industrial design requirements, even if some assumptions were necessarily introduced to maintain model tractability.

The industrial character of the present work is further reinforced by the fact that the proposed optimization framework delivers results that are directly exploitable in practice. The methodology does not merely provide optimal solutions for a limited set of case studies, but rather defines a general and flexible design tool that can be adapted to different working fluids, fin arrangements, and operating conditions. The final recommended designs obtained through the NSGA–II optimization and the subsequent multi-criteria decision analysis represent a practical synthesis of performance, cost, and feasibility con-

straints, and can effectively support engineering decision-making in an industrial context.

Looking forward, several natural developments of this work can be envisaged. One of the most promising directions is the implementation of the proposed models and optimization strategies into a dedicated software tool for industrial use. Such a platform could integrate the thermo–fluiddynamic models, the cost formulation, and the genetic optimization engine into a unified environment, enabling rapid evaluation and optimization of PFHE radiators during the early stages of the design process. Additional developments may include the extension of the framework to other fin geometries, manufacturing technologies, and working fluids, as well as the integration of experimental feedback to further refine and validate the models. Together, these perspectives highlight how the results of this thesis may represent not only a contribution to academic research, but also a concrete basis for future industrial R&D activities.

Bibliography

[1] International Energy Agency. World energy outlook 2023. Report, 2023. Accessed: 2025-12-18.

[2] European Commission. Eu industrial strategy 2023. Policy document, 2023. Accessed: 2025-12-18.

[3] Y.A. Çengel and A.J. Ghajar. *Heat and Mass Transfer: Fundamentals and Applications*. McGraw-Hill Education, New York, NY, USA, 5th edition, 2015.

[4] F.P. Incropera, D.P. DeWitt, T.L. Bergman, and A.S. Lavine. *Fundamentals of Heat and Mass Transfer*. John Wiley & Sons, Hoboken, NJ, USA, 7th edition, 2011.

[5] W.M. Kays and A.L. London. *Compact Heat Exchangers*. McGraw–Hill, New York, 3 edition, 1984.

[6] R.M. Manglik and A.E. Bergles. Heat transfer and pressure drop correlations for the rectangular offset strip fin compact heat exchanger. *Experimental Thermal and Fluid Science*, 10:171–180, 1995.

[7] H.M. Joshi and R.L. Webb. Heat transfer and friction in the offset strip-fin heat exchanger. *International Journal of Heat and Mass Transfer*, 30(1):69–84, 1987.

[8] D.S. R.K. Shah. *Fundamentals of Heat Exchanger Design*. JOHN WILEY & SONS, INC., August 2003.

[9] M. Grespan, A. Leonforte, L. Calò, M. Cavazzuti, and D. Angeli. Physics-based modelling of plate-fin heat exchangers. *Energies*, 18(3):495, 2025.

[10] J. Nocedal and S.J. Wright. *Numerical Optimization*. Springer, New York, NY, 2nd edition, 2006.

[11] J.C. Spall. *Introduction to Stochastic Search and Optimization: Estimation, Simulation, and Control*. John Wiley & Sons, New York, 2003.

[12] M. Cavazzuti. *Optimization Methods: From Theory to Design*. Springer, Berlin, Heidelberg, 2013.

[13] K. Deb, A. Pratap, S. Agarwal, and T. Meyarivan. A fast and elitist multiobjective genetic algorithm: Nsga-ii. *IEEE Transactions on Evolutionary Computation*, 6(2):182–197, 2002.

[14] J.H. Holland. *Adaptation in Natural and Artificial Systems*. University of Michigan Press, Ann Arbor, MI, 1975. 2nd edition: MIT Press, 1992.

[15] D.E. Goldberg. *Genetic Algorithms in Search, Optimization, and Machine Learning*. Addison-Wesley, Reading, MA, 1989.

[16] A.L. London and R.K. Shah. Offset fins and their application in compact heat exchangers. *Advances in Heat Transfer*, 5:1–81, 1968.

[17] S. Mochizuki, Y. Yagi, and W.J. Yang. Transport phenomena in stacks of interrupted parallel-plate surfaces. *Experimental Heat Transfer*, 1(2):127–140, 1987.

[18] L.W. Zhang, S. Balachandar, D.K. Tafti, and F.M. Najjar. Heat transfer enhancement mechanisms in inline and staggered parallel-plate fin heat exchangers. *International Journal of Heat and Mass Transfer*, 40(10):2307–2325, 1997.

[19] S. Hu and K.E. Herold. Prandtl number effect on offset fin heat exchanger performance: experimental results. *International Journal of Heat and Mass Transfer*, 38(6):1053–1061, 1995.

[20] N.C. DeJong and A.M. Jacobi. An experimental study of flow and heat transfer in parallel-plate arrays: local, row-by-row and surface average behavior. *International Journal of Heat and Mass Transfer*, 40(6):1365–1378, 1997.

[21] L.W. Zhang, D.K. Tafti, F.M. Najjar, and S. Balachandar. Computations of flow and heat transfer in parallel-plate fin heat exchangers on the cm-5: effects of flow unsteadiness and three-dimensionality. *International Journal of Heat and Mass Transfer*, 40(6):1325–1341, 1997.

[22] J. Dong, J. Chen, Z. Chen, and Y. Zhou. Air-side thermal hydraulic performance of offset strip fin aluminum heat exchangers. *Applied Thermal Engineering*, 27(2–3):306–313, 2007.

[23] H. Peng and X. Ling. Numerical modeling and experimental verification of flow and heat transfer over serrated fins at low reynolds number. *Experimental Thermal and Fluid Science*, 32(5):1039–1048, 2008.

[24] H. Bhowmik and K.S. Lee. Analysis of heat transfer and pressure drop characteristics in an offset strip fin heat exchanger. *International Communications in Heat and Mass Transfer*, 36(3):259–263, 2009.

[25] M.S. Kim and K.S. Lee. The thermoflow characteristics of an oscillatory flow in offset-strip fins. *Numerical Heat Transfer, Part A: Applications*, 58(11):835–851, 2010.

[26] Y. Yang and Y. Li. General prediction of the thermal hydraulic performance for plate-fin heat exchanger with offset strip fins. *International Journal of Heat and Mass Transfer*, 78:860–870, 2014.

[27] Y. Yang, Y. Li, S. Biao, and J. Zheng. Performance evaluation of heat transfer enhancement in plate-fin heat exchangers with offset strip fins. *Physics Procedia*, 67:543–550, 2015.

[28] Y. Yang, Y. Li, B. Si, and J. Zheng. Heat transfer performances of cryogenic fluids in offset strip fin-channels considering the effect of fin efficiency. *International Journal of Heat and Mass Transfer*, 114:1114–1125, 2017.

[29] M. Grespan, L. Calò, L. Carlesso, A. Leonforte, and D. Angeli. A comprehensive numerical study on heat transfer and friction characteristics of offset-strip fins. *Applied Thermal Engineering*, 256:124083, 2024.

[30] E.M. Sparrow and L.M. Hossfeld. Effect of rounding of protruding edges on heat transfer and pressure drop in a duct. *International Journal of Heat and Mass Transfer*, 27(10):1715–1723, 1984.

[31] Y. Asako, H. Nakamura, and M. Faghri. Heat transfer and pressure drop characteristics in a corrugated duct with rounded corners. *International Journal of Heat and Mass Transfer*, 31(6):1237–1245, 1988.

[32] R.C. Xin and W.Q. Tao. Numerical prediction of laminar flow and heat transfer in wavy channels of uniform cross-sectional area. *Numerical Heat Transfer*, 14(4):465–481, 1988.

[33] T.A. Rush, E.M. Sparrow, and B.B. Mikic. Experiments on heat transfer and pressure drop for flow in corrugated plates. *Journal of Heat Transfer*, 91(2):191–199, 1969.

[34] L.C. Yang, Y. Asako, Y. Yamaguchi, and M. Faghri. Numerical prediction of transitional characteristics of flow and heat transfer in a corrugated duct. *Journal of Heat Transfer*, 119(1):62–68, 1997.

[35] H.M. Metwally and R.M. Manglik. Enhanced heat transfer due to curvature-induced lateral vortices in laminar flows in sinusoidal corrugated-plate channels. *International Journal of Heat and Mass Transfer*, 47(10-11):2283–2292, 2004.

[36] J. Zhang, J. Kundu, and R.M. Manglik. Effect of fin waviness and spacing on the lateral vortex structure and laminar heat transfer in wavy-plate-fin cores. *International Journal of Heat and Mass Transfer*, 47(8–9):1719–1730, 2004.

[37] R.M. Manglik, J. Zhang, and A. Muley. Low reynolds number forced convection in three-dimensional wavy-plate-fin compact channels: fin density effects. *International Journal of Heat and Mass Transfer*, 48(7):1439–1449, 2005.

[38] J. Dong, J. Chen, W. Zhang, and J. Hu. Experimental and numerical investigation of thermal-hydraulic performance in wavy fin-and-flat tube heat exchangers. *Applied Thermal Engineering*, 30(14–15):1377–1386, 2010.

[39] M.K. Aliabadi and F. Hormozi. Models for pressure drop and heat transfer in air cooled compact wavy fin heat exchangers. *Journal of Enhanced Heat Transfer*, 18(3):191–207, 2011.

[40] M.M. Awad and Y.S. Muzychka. Models for pressure drop and heat transfer in air cooled compact wavy fin heat exchangers. *Journal of Enhanced Heat Transfer*, 18(3):191–207, 2011.

[41] M.K. Aliabadi, F. Hormozi, and E. Hosseini Rad. New correlations for wavy plate-fin heat exchangers: different working fluids. *International Journal of Numerical Methods for Heat & Fluid Flow*, 24(5):1086–1108, 2014.

[42] J. Dong, L. Su, Q. Chen, and W. Xu. Experimental study on thermal–hydraulic performance of a wavy fin-and-flat tube aluminum heat exchanger. *Applied Thermal Engineering*, 51:32–39, 2013.

[43] J. Kuehndel, B. Kerler, and C. Karcher. Air side thermal performance of wavy fin heat exchangers produced by selective laser melting. *Journal of Physics: Conference Series*, 745:032057, 2016.

[44] X. Zhang, Y. Wang, M. Li, S. Wang, and X. Li. Improved flow and heat transfer characteristics for heat exchanger by using a new humped wavy fin. *Applied Thermal Engineering*, 2017.

[45] T. Michioka. Large-eddy simulation for turbulent flow and gas dispersion over wavy walls. *International Journal of Heat and Mass Transfer*, 125:569–579, 2018.

[46] K. Mishra, S.K. Das, and S. Sarangi. Parametric study and optimization of a plate-fin heat exchanger using a genetic algorithm. *International Journal of Heat and Mass Transfer*, 47(14–16):3001–3009, 2004.

[47] G. Xie, B. Sunden, and Q.W. Wang. Optimization of compact heat exchangers by a genetic algorithm. *Applied Thermal Engineering*, 28(8–9):895–906, 2008.

[48] S. Sanaye and H. Hajabdollahi. Thermal-economic multi-objective optimization of plate fin heat exchanger using genetic algorithm. *Applied Energy*, 87(6):1893–1902, 2010.

[49] L. Gosselin, M. Tye-Gingras, and F. Mathieu-Potvin. Review of utilization of genetic algorithms in heat transfer problems. *International Journal of Heat and Mass Transfer*, 52(9–10):2169–2188, 2009.

[50] R.V. Rao and V.K. Patel. Thermodynamic optimization of cross-flow plate-fin heat exchanger using a particle swarm optimization algorithm. *International Journal of Thermal Sciences*, 49:1712–1721, 2010.

[51] L. Zhang, C. Yang, and J. Zhou. A distributed parameter model and its application in optimizing the plate-fin heat exchanger based on the minimum entropy generation. *International Journal of Thermal Sciences*, 49:1427–1436, 2010.

[52] P. Ahmadi, H. Hajabdollahi, and I. Dincer. Cost and entropy generation minimization of a cross-flow plate fin heat exchanger using multi-objective genetic algorithm. *Journal of Heat Transfer*, 133(2):021801, 2011.

[53] M.S. Kim, J. Lee, S.J. Yook, and K.S. Lee. Correlations and optimization of a heat exchanger with offset-strip fins. *International Journal of Heat and Mass Transfer*, 54:2073–2079, 2011.

[54] H. Najafi, B. Najafi, and P. Hoseinpoori. Energy and cost optimization of a plate and fin heat exchanger using genetic algorithm. *Applied Thermal Engineering*, 31(16):1839–1847, 2011.

[55] M. Yousefi, R. Enayatifar, A.N. Darus, and A.H. Abdullah. A robust learning based evolutionary approach for thermal-economic optimization of compact heat exchangers. *International Communications in Heat and Mass Transfer*, 39(11):1605–1615, 2012.

[56] V. Patel and V. Savsani. Optimization of a plate-fin heat exchanger design through an improved multi-objective teaching-learning based optimization (mo-itlbo) algorithm. *Chemical Engineering Research and Design*, 2014.

[57] J. Wen, H. Yang, X. Tong, K. Li, S. Wang, and Y. Li. Configuration parameters design and optimization for plate-fin heat exchangers with serrated fin by multi-objective genetic algorithm. *Energy Conversion and Management*, 117:482–489, 2016.

[58] H. Zarea and M. Keshavarzi. Multi-objective optimization of plate fin heat exchanger using evolutionary algorithm. *International Journal of Advanced Biotechnology and Research*, 7(1):1–10, 2016.

[59] D. Juan, Y. Man-Ni, and Y. Shi-Fang. Correlations and optimization of a heat exchanger with offset fins by genetic algorithm combining orthogonal design. *Applied Thermal Engineering*, 2016.

[60] T.A. Khan and W. Li. Optimal design of plate-fin heat exchanger by combining multi-objective algorithms. *International Journal of Heat and Mass Transfer*, 108:1560–1572, 2017.

[61] C. Liu, W. Bu, and D. Xu. Multi-objective shape optimization of a plate-fin heat exchanger using cfd and multi-objective genetic algorithm. *International Journal of Heat and Mass Transfer*, 111:65–82, 2017.

[62] P. Maghsoudi, S. Sadeghi, H. Khanjarpanah, and H.H. Gorgani. A comprehensive thermo-economic analysis, optimization and ranking of different microturbine plate-fin recuperators designs employing similar and dissimilar fins on hot and cold sides with nsga-ii algorithm and dea model. *Applied Thermal Engineering*, 130:1090–1104, 2018.

[63] R. Song and M. Cui. Single- and multi-objective optimization of a plate-fin heat exchanger with offset strip fins adopting the genetic algorithm. *Applied Thermal Engineering*, 2019.

[64] C. Yu, X. Xue, K. Shi, and M. Shao. A three-dimensional numerical and multi-objective optimal design of wavy plate-fins heat exchangers. *Processes*, 9(1):9, 2021.

[65] B.S. Mekki, J. Langer, and S. Lynch. Genetic algorithm based topology optimization of heat exchanger fins used in aerospace applications. *International Journal of Heat and Mass Transfer*, 170:121002, 2021.

[66] M. Cui and R. Song. Comprehensive performance investigation and optimization of a plate fin heat exchanger with wavy fins. *Thermal Science*, 26(3A):2261–2273, 2022.

[67] S. Li, Z. Deng, J. Liu, and D. Liu. Multi-objective optimization of plate-fin heat exchangers via non-dominated sequencing genetic algorithm (nsga-ii). *Applied Sciences*, 12(22):11792, 2022.

[68] Y. Guan, L. Wang, and H. Cui. Optimization analysis of thermodynamic characteristics of serrated plate-fin heat exchanger. *Sensors*, 23(8):4158, 2023.

[69] Y. Yang and Y. Li. General prediction of the thermal hydraulic performance for plate-fin heat exchanger with offset strip fins. *International Journal of Heat and Mass Transfer*, 78:860–870, 2014.

[70] F. Menter. Two-equation eddy-viscosity turbulence models for engineering applications. *AIAA Journal*, 32(8):1598 – 1605, 1994. Cited by: 13968; All Open Access, Green Open Access.

[71] M. Pendar, J. Páscoa, and R. Lima. Numerical investigation of automotive paint oven for improving the thermal efficiency. In *Fluids Engineering Division Summer Meeting*, volume 85840, page V002T05A032. American Society of Mechanical Engineers, 2022.

[72] H. Weller, G. Tabor, H. Jasak, and C. Fureby. A tensorial approach to computational continuum mechanics using object-oriented techniques. *Computers in Physics*, 12(6):620–631, 1998.

[73] S.V. Patankar and D.B. Spalding. Paper 5 - a calculation procedure for heat, mass and momentum transfer in three-dimensional parabolic flows. In S. Patankar, A. Pollard, A. Singhal, and S. Vanka, editors, *Numerical Prediction of Flow, Heat Transfer, Turbulence and Combustion*, pages 54–73. Pergamon, 1983.

[74] L. Guo, F. Qin, J. Chen, Z. Chen, and Y. Zhou. Influence of geometrical factors and pressing mould wear on thermal-hydraulic characteristics for steel offset strip fins at low reynolds number. *International Journal of Thermal Sciences*, 46(12):1285–1296, 2007.

[75] M. Grespan, A. Leonforte, M. Cavazzuti, L. Calò, and D. Angeli. Accurate reduced-order modelling of plate-fin heat exchangers. In *International Heat Transfer Conference Digital Library*. Begel House Inc., 2023.

[76] D. Marquardt. An algorithm for least-squares estimation of nonlinear parameters. *Journal of the Society for Industrial and Applied Mathematics*, 11(2):431–441, 1963.

[77] P. Virtanen et al. SciPy 1.0: Fundamental Algorithms for Scientific Computing in Python. *Nature Methods*, 17:261–272, 2020.

[78] W. Kays and A. London. *Compact Heat Exchangers*. 3rd ed. McGraw-Hill, 1984.

[79] M. Awad and Y. Muzychka. Models for pressure drop and heat transfer in air cooled compact wavy fin heat exchangers. *Journal Of Enhanced Heat Transfer*, 18(3):191–207, 2011.

[80] J. Stasiek, M. Collins, M. Ciofalo, and P. Chew. Investigation of flow and heat transfer in corrugated passages—i. experimental results. *International Journal of Heat and Mass Transfer*, 39(1):149–164, 1996.

[81] M. Kim, J. Lee, S. Yook, and K. Lee. Correlations and optimization of a heat exchanger with offset-strip fins. *International Journal of Heat and Mass Transfer*, 54(9):2073–2079, 2011.

[82] P. Forchheimer. Wasserbewegung durch boden. *Zeitschrift des Vereines Deutscher Ingenieure*, 45:1782–1788, 1901.

[83] D.P. Bertsekas. *Nonlinear Programming*. Athena Scientific, 1999.

[84] J. Nocedal and S.J. Wright. *Numerical Optimization*. Springer, 2 edition, 2006.

[85] J.C. Spall. *Introduction to Stochastic Search and Optimization*. Wiley, 2003.

[86] E.G. Talbi. *Metaheuristics: From Design to Implementation*. Wiley, 2009.

[87] J. Kennedy and R. Eberhart. Particle swarm optimization. In *Proceedings of the IEEE International Conference on Neural Networks*, volume 4, pages 1942–1948, Perth, Australia, 1995. IEEE.

[88] Y. Collette and P. Siarry. *Multiobjective Optimization: Principles and Case Studies*. Springer, Berlin, Heidelberg, 2004.

[89] D.E. Goldberg. *Genetic Algorithms in Search, Optimization, and Machine Learning*. Addison-Wesley, 1989.

[90] E. Wirsansky. *Hands-On Genetic Algorithms with Python*. Packt Publishing, 2020.

[91] K. Deb, A. Pratap, S. Agarwal, and T. Meyarivan. A fast and elitist multiobjective genetic algorithm: Nsga-ii. *IEEE Transactions on Evolutionary Computation*, 6(2):182–197, 2002.

[92] C.L. Hwang and K. Yoon. *Multiple Attribute Decision Making: Methods and Applications*. Springer, 1981.

[93] M. Yousefi, R. Enayatifar, and A.N. Darus. Optimal design of plate-fin heat exchangers by a hybrid evolutionary algorithm. *International Communications in Heat and Mass Transfer*, 39(2):258–263, 2012.

[94] F.A. Fortin, F.M. De Rainville, M.A. Gardner, M. Parizeau, and C. Gagné. Deap: Evolutionary algorithms made easy. *Journal of Machine Learning Research*, 13:2171–2175, 2012.